REPORT DOCUMENTATION PAGE

Form Approved
OMB No. 0704-0188

1. REPORT DATE *(DD-MM-YYYY)*	2. REPORT TYPE	3. DATES COVERED *(From - To)*
06-02-2009	Technical Paper	

4. TITLE AND SUBTITLE

A High-Order Transport Scheme for Collisional- Radiative and Nonequilibrium Plasma

5a. CONTRACT NUMBER

5b. GRANT NUMBER

5c. PROGRAM ELEMENT NUMBER

6. AUTHOR(S)
Michael G. Kapper (AFRL/RZSA)

5d. PROJECT NUMBER

5e. TASK NUMBER

5f. WORK UNIT NUMBER
23040256

7. PERFORMING ORGANIZATION NAME(S) AND ADDRESS(ES)

Texas Research Institute Austin, Inc.
9063 Bee Caves Road
Austin TX 78733-6201

8. PERFORMING ORGANIZATION REPORT NUMBER

AFRL-RZ-ED-TP-2009-028

9. SPONSORING / MONITORING AGENCY NAME(S) AND ADDRESS(ES)

Air Force Research Laboratory (AFMC)
AFRL/RZS
5 Pollux Drive
Edwards AFB CA 93524-7048

10. SPONSOR/MONITOR'S ACRONYM(S)

11. SPONSOR/MONITOR'S NUMBER(S)
AFRL-RZ-ED-TP-2009-028

12. DISTRIBUTION / AVAILABILITY STATEMENT

Approved for public release; distribution unlimited (PA #09052).

13. SUPPLEMENTARY NOTES
Dissertation for presentation to University of Ohio Dissertation Committee

14. ABSTRACT
A series of shock tube experiments performed in the 1970s at the Institute for Aerospace Studies, University of Toronto, led in the discovery of instabilities in relaxing shock structures in noble gases under hypervelocity conditions. The instabilities were oscillatory in nature and found to affect the entire shock structure including the translational front, induction zone, and electron avalanche. Theoretical models were first developed in order to reproduce the length and time scales of the observed quasi-equilibrium state, and later extended to include unsteady plasmadynamic simulations that verified the influence of pressure oscillations in one dimension. Despite these attempts, a complete explanation for the oscillations nor a quantitative analysis of the multi-dimensional shock structure has been provided to date. This dissertation builds upon previous modeling efforts, extending the numerical simulations to a high level of accuracy and detail so that coupling of complex wave phenomena and nonequilibrium effects can be well resolved. This has necessitated the development of a numerical capability aimed at relaxing shock layers and other unsteady, high-enthalpy nonequilibrium plasmas and is the focus of much of this work. The plasma is described as a two-temperature, single fluid with the electronic states convected as separate species. Solution of the convective transport is handled via upwind shock-capturing techniques, extended to third-order on general curvilinear meshes.

15. SUBJECT TERMS

16. SECURITY CLASSIFICATION OF:			17. LIMITATION OF ABSTRACT	18. NUMBER OF PAGES	19a. NAME OF RESPONSIBLE PERSON
					Michael Kapper
a. REPORT	b. ABSTRACT	c. THIS PAGE	SAR	214	19b. TELEPHONE NUMBER *(include area code)*
Unclassified	**Unclassified**	**Unclassified**			N/A

A HIGH-ORDER TRANSPORT SCHEME FOR COLLISIONAL-RADIATIVE AND NONEQUILIBRIUM PLASMA

DISSERTATION

Presented in Partial Fulfillment of the Requirements for

the Degree of Philosophy in the Graduate

School of the Ohio State University

By

Michael Gino Kapper, M.S.

* * * * *

The Ohio State University
2009

Dissertation Committee:

Professor John Yu, Adviser

Professor Walter Lempert

Professor Igor Adamovich

Professor Mohammed Samimy

Dr. Jean-Luc Cambier

Approved by

_____

Adviser
Mechanical Engineering Graduate Program

ABSTRACT

A series of shock tube experiments performed in the 1970s at the Institute for Aerospace Studies, University of Toronto, led in the discovery of instabilities in relaxing shock structures in noble gases under hypervelocity conditions. The instabilities were oscillatory in nature and found to affect the entire shock structure including the translational front, induction zone, and electron avalanche. Theoretical models were first developed in order to reproduce the length and time scales of the observed quasi-equilibrium state, and later extended to include unsteady plasmadynamic simulations that verified the influence of pressure oscillations in one dimension. Despite these attempts, a complete explanation for the oscillations nor a quantitative analysis of the multi-dimensional shock structure has been provided to date.

This dissertation builds upon previous modeling efforts, extending the numerical simulations to a high level of accuracy and detail so that coupling of complex wave phenomena and nonequilibrium effects can be well resolved. This has necessitated the development of a numerical capability aimed at relaxing shock layers and other unsteady, high-enthalpy nonequilibrium plasmas and is the focus of much of this work. The plasma is described as a two-temperature, single fluid with the electronic states convected as separate species. Solution of the convective transport is handled via upwind shock-capturing techniques, extended to third-order on general curvilinear meshes. A collisional-radiative model describing the kinetics of excitation and ionization and reverse processes allows for a non-Boltzmann distribution of the excited levels. The solver is developed within a parallelized software architecture, implemented entirely in Java and capable or execution on distributed memory machines.

The numerical solver is developed in a systematic fashion with much emphasis placed

on code validation. The transport schemes are benchmarked using standard test cases. The collisional-radiative model is benchmarked as well on a steady flow fields before considering unsteady calculations.

Numerical simulations of ionizing shocks in argon are conducted to gain insight to the shock structure and help determine the source of the oscillations observed in the experiment. Solutions presented in the form of simulated interferograms provide a direct comparison with experimental interferograms enabling identification of key wave structures. Results show that the instabilities are caused by a resonance pattern of longitudinal and transverse waves that give rise to ionization cells that are analogous to detonation cells. Furthermore, a mechanism is proposed for the oscillations which takes into account the unsteady wave phenomena coupled with the collisional-radiative kinetics.

ACKNOWLEDGMENTS

I would like to acknowledge the many people who have helped in making this dissertation possible. I would first like to thank my adviser Prof. John Yu for his help and support during my time at OSU. He has proved to be a respectable running partner whether it be jogging around Antrim Park Lake or running laps at Jesse Owens Memorial Stadium. I would also like to thank Prof. Walter Lempert, Prof. Igor Adamovich, and Prof. Mohammed Samimy for serving on my committee and their valuable input to my research. I am grateful to Dr. Jean-Luc Cambier, who has given my research a sense of direction, allowing me to tackle problems of real interest. His attention to detail and discerning eye has served to greatly improve the quality of my work. He has also been an excellent teacher, always willing to sharing his experiences and wisdom.

I would like to acknowledge the various professors and colleagues who have inspired me to achieve more, including Prof. Periklis Papadopoulos of SJSU for being my first CFD professor and helping to spring-board my career in numerical methods as well as Prof. Edward Overmann of the OSU math department for his contagious enthusiasm for numerical methods. I would like to thank Dr. Hung T. Huynh of NASA Glenn Research Center for sharing his clear and elegant description of Riemann solvers, reconstruction methods, and limiters. I thank AFRL alumnus Mr. Jay Levine for his deep interest and support of CFD at the AFRL. I would also like to acknowledge Mr. Levine as being the first to inspire me to pursue a doctorate. I thank Dr. Leonid Pekker for many enlightening discussions about physics.

This research was supported by AFOSR laboratory task 02PR05COR.

VITA

January 15, 1978.....Born in Hayward, California

June, 2000.....B.S., Chemistry
University of California at Berkeley

October, 2000–June, 2003.....Engineer, Guerra Technologies, Inc
San José, CA

June, 2005.....M.S., Mechanical Engineering
San José State University
San José, CA

July, 2003–present.....Mechanical engineer
Air Force Research Laboratory
Edwards AFB, CA

PUBLICATIONS

M. Kapper and J.-L. Cambier. A High-Order Scheme for Collisional-Radiative and Non-Equilibrium Plasma. In *Proceedings of the 3rd International Workshop of High Temperature Gases in Atmospheric Entry*, Heraklion, Greece, 30 September–3 October 2008 (ESA SP-667, January 2009).

J.-L. Cambier, M. Carroll, and M. Kapper. Development of a Hybrid Model for Nonequilibrium High-Energy Plasmas. In *Proceedings of the 35th Plasmadynamics and Lasers Conference*, Portland, OR, June 2004. AIAA.

FIELDS OF STUDY

Major Field: Mechanical engineering

TABLE OF CONTENTS

LIST OF TABLES

LIST OF FIGURES

LIST OF SYMBOLS

Latin Symbols

a	thermal sound speed, abscissa for Gaussian quadrature, specific Helmholtz function
A	flux Jacobian matrix, Helmholtz function per unit volume
$\mathscr{A}$	area
B	banded matrix
$\vec{B}$	magnetic flux density (magnetic induction)
c	speed of light in vacuum
c_a	Alfvén wave speed
c_f	fast magnetosonic wave speed
c_p	specific heat at constant pressure
c_s	slow magnetosonic wave speed
c_v	specific heat at constant volume
E	energy density
$\vec{E}$	electric field
$\vec{E}^*$	electric field including pondermotive force, i.e. $\vec{E} + \vec{u} \times \vec{B}$
f	distribution function, oscillator strength
F	vector flux density of the fluid
$\mathbb{F}$	DFT matrix
$\ddot{F}$	tensor flux density of the fluid
g	specific Gibbs function, degeneracy
g_{ij}	covariant metric coefficient
g^{ij}	contravariant metric coefficient
$\bar{g}$	gaunt factor

$\vec{g}_i$	covariant basis vector
$\vec{g}^i$	contravariant basis vector
G	Gibbs function density
h	Planck constant, specific enthalpy
H	enthalpy density
$\vec{H}$	magnetic field strength
$h_\circ$	specific stagnation enthalpy
$H_\circ$	stagnation enthalpy density
h_f	specific enthalpy of formation
$\hbar, \hbar$	Planck constant
I	identity matrix, ionization potential
J	Jacobian matrix, angular momentum quantum number
$\vec{j}$	electric current
k_B	Boltzmann constant
K	quantum number
$\vec{l}$	left eigenvector
ℓ	length
L	matrix of left eigenvectors
m	mass
$\vec{m}$	momentum density
M	similarity transformation matrix
n	number density, principal quantum number
$\vec{P}$	momentum transfer operator
p	pressure
$p_\circ$	sum of thermal and magnetic pressures
Q	vector of conserved quantities
$\vec{r}$	right eigenvector
R	gas constant, matrix of right eigenvectors
$\mathscr{R}$	universal gas constant
S	entropy density

s	specific entropy
t	time
u	velocity component in x-direction
$\vec{u}$	mass-average velocity
v	specific volume, velocity component in y-direction
V	vector of primitive variables, Vandermonde matrix
$\vec{V}$	diffusion velocity field
$\mathscr{V}$	volume
w	velocity component in z-direction, weight for Gaussian quadrature
$\vec{w}$	velocity w.r.t. laboratory coordinates
W	vector of characteristic variables
$\vec{W}$	relative velocity field
x	specie mole fraction
y	specie mass fraction
Z	particle charge, partition function

Greek Symbols

α	characteristic wave strength, ionization fraction, plasma diffusivity
$\vec{\beta}$	normalized magnetic field
$\epsilon_\circ$	dielectric constant, permittivity of vacuum
η	plasma diffusivity
δ	finite-difference approximation
Δ	forward-difference operator: $(\cdot)_R - (\cdot)_L$
η	plasma diffusivity
γ	adiabatic exponent (ratio of specific heats)
κ	thermal diffusivity, wave number
λ	eigenvalue
λ_D	Debye length
Λ	diagonal matrix of eigenvalues, optical escape factor
μ	momentum transfer operator

$\mu_\circ$ magnetic permeability

ν_{rs} collision frequency between species r and s

ω plasma frequency, general source term

Ω vector of source terms

$\ddot{\Pi}$ tensor momentum flux density of the fluid (Maxwell stress tensor)

ρ mass density, plasma resistivity

$\dot{\rho}$ rate of denisty change

σ collision cross section, plasma conductivity

τ relaxation time scale

ε specific internal energy

ξ number of optical electrons

Superscripts

$'$ rate of energy density production/destruction

* excited state

$^\circ$ standard reference state

^{n} time level

^{A} allowed transition

^{F} forbidden transition

^{P} parity-forbidden transition

^{S} spin-forbidden transition

Subscripts

$_c$ conservative form, capture

$_e$ electron specie component

$_i$ mesh index in x- or ξ-direction, ion specie component

$_j$ mesh index in y- or η-direction

$_k$ mesh index in z- or ζ-direction

$_h$ heavy (atom) specie component

$_{n}$ specie component, normal component

$_{N}$ north

$_{p}$ primitive form, periodic

$_{s}$ general specie component

$_{L}$ left state

$_{R}$ right state

$_{\nu}$ photon

$_{x}$ vector component in x-direction

$_{y}$ vector component in y-direction

$_{z}$ vector component in z-direction

$_{\xi}$ vector component in ξ-direction

$_{\eta}$ vector component in η-direction

$_{\zeta}$ vector component in ζ-direction

$_{\parallel}$ parallel component

$_{\perp}$ perpendicular component

CHAPTER 1

INTRODUCTION

As a proven complement to experimental results, flowfield simulation has become an integral component in the engineering process, providing valuable insight to observed phenomena. In particular, modeling of nonequilibrium plasma flows has emerged as a key technology for many critical aerospace applications, including aerodynamic flow control, re-entry and hypersonic air-breathing vehicles, as well as capillary discharge and electric propulsion devices. As applied to such cases, modeling can aid in improved aerodynamic performance, thermal protection systems, combustion enhancement, and thruster efficiency among others.

The complexity of such high enthalpy flows is as vast as the range of characterizing conditions, from highly collisional regimes encountered in shock layers, to supersonic base flows that give rise to near-vacuum states. These flows are dominated by nonlinear wave phenomena and nonequilibrium plasma conditions, requiring an accurate description of the transport processes along with generalized equations of state that can account for a non-Boltzmann distribution of states.

In relaxing shock layers, for example, plasma transport through the nonlinear compression shock results in conversion of bulk kinetic energy to random thermal energy which is then distributed between the various internal modes of the plasma through collisions. If the time scales of such collisions are comparable to the convective times scales to be resolved, then the resulting nonequilibrium states of the plasma must be evaluated through the use kinetic models.

In stark contrast to collision-dominated shocks, flows through nonlinear rarefaction waves can be nearly collisionless, resulting in a cold plasma. While such plasmas may be unable to relax through collisions, radiation emission and absorption becomes important and must

be accounted for.

Furthermore, when unsteady flow effects are considered, coupling between the plasma transport and nonequilibrium effects becomes especially important. In many cases the dynamics of the flow can depend heavily upon accurate treatment of the thermophysical properties, requiring accurate and complete descriptions of the equation of state. The sensitivity can be quite pronounced, as nonlinearities can amplify small changes. The equation of state in turn depends on the local conditions as determined by the transport, for which correct temperature jumps through shocks and temperature drops in rarefactions, for example, should be accurately computed.

With this in mind, it is the focus of this research not to include as much nonequilibirum complexity as possible, but rather to focus on developing a relatively complete model of the nonequilibrium effects considered and to ensure proper coupling with transport phenomena. In particular, the current work is limited to monatomic gases so that nonequilibrium effects of the electronic states can be studied in some detail. The approach will be very systematic, starting from an accurate treatment of the plasma transport, described by a two-temperature, single-fluid model, which is then coupled with a collisional-radiative model that includes the kinetics of excitation and ionization and all reverse processes, allowing a non-Boltzmann distribution of the bound electronic states. Particular emphasis will be placed on validation through benchmarks, ensuring proper coupling between transport and kinetics. In particular, the numerical model developed in this work will be validated against the shock tube studies described in the following section.

1.1 UTIAS experiments

Shock tubes have been and continue to be an invaluable tool in providing thermochemical data for gases under non-equilibrium conditions. They are able to generate gasdynamic phenomena with time scales on the order of relaxation times necessary to achieve thermodynamic equilibrium. For gasdynamic processes occurring more rapidly than relaxation processes, the gas will be left in a state of non-equilibrium, thereby allowing measurement of reaction rates and collision cross sections in a controlled environment.

Due to its simplicity as a monatomic gas and its relative abundance, argon in particular has extensively been studied in the context of shock tubes. Without an energy sink for

rotational or vibrational modes or dissociative processes, high shock speeds and associated temperature jumps are easily attainable, making it ideal to study electronic excitation and ionization kinetics. The first experiments on ionization relaxation in argon were carried out by Petschek and Byron [85], the results of which were used to benchmark theoretical models in subsequent work. The structure of an ionizing shock wave in argon was first calculated by Biberman and Yakubov [11] whose results are shown in Figure 1.1. These results indicate a compression shock at $x = 0$ cm through which the argon gas is rapidly heated (within several mean-free paths) to temperatures above 2 eV. At these temperatures, there exist atoms with sufficient thermal energy to excite and ionize other argon atoms through inelastic collisions. The electrons produced by these collisions are then heated through thermalization with ground state atoms, indicated by the initial sharp gradient of T_e from 0–0.75 cm. Once a sufficient number of *priming* electrons have been liberated, they themselves begin to dominate inelastic collisions due to their high velocity in comparison with that of the atoms. Electron production and temperature steadily increase until just before 4 cm, at which point the rate of inelastic collisions increases exponentially, resulting in an electron avalanche. The distance between the compression shock and the peak ionization fraction in the avalanche is known as the relaxation or induction length. The heavy-particle temperature then rapidly drops due to the large number of electrons and the large cross section for thermalization through Coulomb collisions.

Combination of such experimental data with theoretical calculations has yielded approximate values for cross sections and rates associated with excitation and ionization. Knowledge of key parameters from experimental data such as the relaxation length and ionization fraction allow for the tailoring of rates used in theoretical calculations until agreement is achieved. In particular, it has been found that atom-atom cross sections for excitation from ground state have the greatest influence on the shock structure and the relaxation length. Since the gas down stream of the shock is not ionized, atom-atom collisions immediately following the compression shock generate the initial priming electrons which in turn become the dominant ionizing species once sufficient number densities have been obtained. Table 1.1 offers some values of the atom-atom cross sections used in previous studies. The range of values exceeds an order of magnitude and indicates the relative uncertainty in this particular cross section.

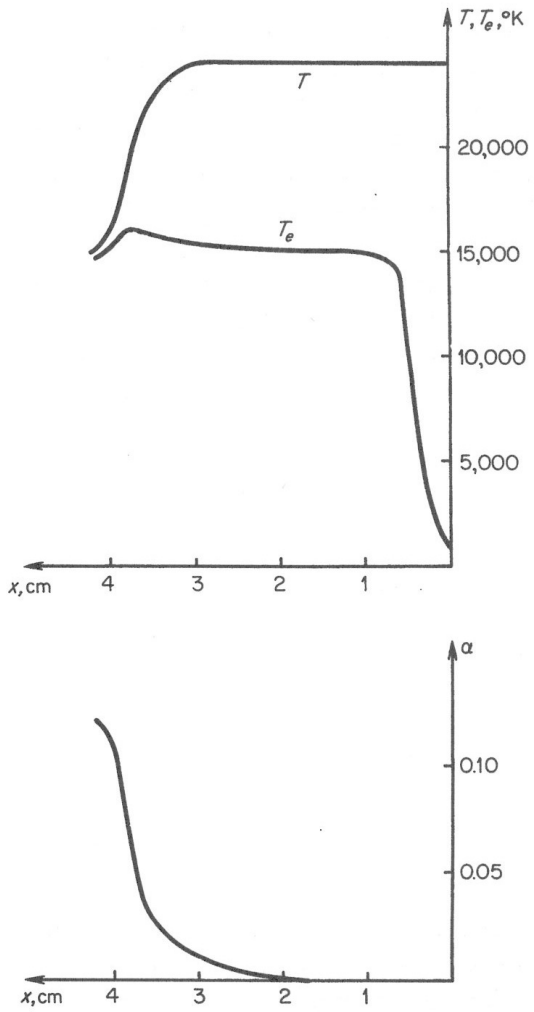

Figure 1.1: Distribution of electron and atom temperatures and degree of ionization in a shock wave in argon on the assumption that the initial electrons are formed by atom-atom collisions. The Mach number is 16, the pressure ahead of the shock 10 mm Hg, and the initial temperature 293 K. Taken from [128].

Authors	σ^a [m^2/eV]
Harwell and Jahn [49]	7×10^{-23}
Morgan and Morrison [80]	7×10^{-24}
Kelly [60]	1.2×10^{-23}
Merilo and Morgan [76]	1.2×10^{-23}
McLaren and Hobson [72]	2.5×10^{-24}
Glass and Liu [42]	$1 - 2 \times 10^{-23}$

Table 1.1: Atom-atom cross section parameters for excitation from ground state used in various attempts to reproduce the shock structure in argon.

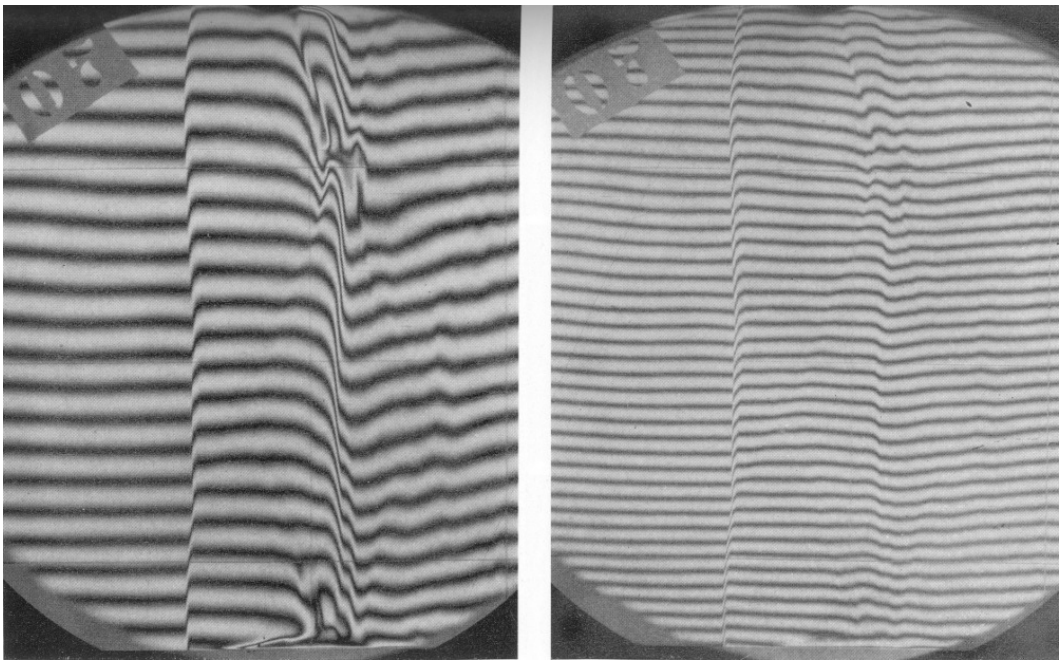

Figure 1.2: Experimental interferogram of argon shock structure at Ma 14.7 from [42]. First fringe shift from the left is the compression shock which is followed by the electron avalanche approximately 4.4 cm upwind. Flow is from right to left.

Of the numerous studies conducted and results obtained, it was not until the shock tube experiments conducted at the Institute for Aerospace Studies, University of Toronto, [42] showed that under certain conditions, a definite dynamical behavior could be associated with a strong ionizing shock in argon. It was discovered that the translational shock front propagating in pure argon "develops sinusoidal instabilities which affect the entire shock structure including the ionization relaxation region, the electron cascade front, and the final quasi-equilibrium state" (cf. Figure 1.2). The authors noted similarities between the oscillating shock front of the ionizing argon shock and detonation shock waves and sought techniques for suppressing the ionization instabilities that could also be applicable to detonation waves. While it was found that small amounts of impurities including molecular hydrogen, nitrogen, and oxygen were suitable in quenching the oscillations, a valid explanation for their existence nor a concrete link to detonation phenomena was found.

Attempts to duplicate these anomalies numerically were not made until the transient, one-dimensional simulations of Cambier [21] were able to show a definite coupling between the ionization kinetics and the gasdynamics through pressure sources. It was found that

pressure spikes in the electron avalanche region are reflected down stream to the compression shock, thereby causing fluctuations in the shock temperature and speed. This mechanism is similar to that found in detonation waves, furthering the case for a link between the two. The further significance is that it introduced yet another criterion to gauge the quality of theoretical models against experimental data. An accurate model should be able to reproduce the oscillations of the experimental results to the same degree. Despite these efforts, the work was never extended to simulate the instabilities of a multi-dimensional ionizing shock.

1.2 Scope and overview

It is the primary focus of this work to develop a numerical method for the transport of nonequilibrium plasma as described by a collisional-radiative model that can be applied to study the structure of multidimensional ionizing shocks in argon. Modeling such a structure requires high-order transport solvers to resolve the dynamical nature of the shock structure as well as a detailed chemical kinetics scheme to solve the processes of nonequilibrium ionization. The ability to accurately do so would be a significant contribution to the coupling of gasdynamic and collisional-radiative modeling. This would also open the door to many problems of interest including re-entry dynamics including base flows, rapid expansion of plasmas, RF plasmas, laser-plasma interaction, etc.

The plasma is described by the two-temperature, single-fluid equations with treatment of the electronic states as individual as formulated in Chapter 2. A numerical formulation based on a finite-volume discretization is given in Chapter 3. Treatment of the convective transport is discussed in some detail, beginning in Chapter 4 with a third-order reconstruction scheme for which the stability analysis in Chapter 5 is performed. The convection scheme is benchmarked against several standard test cases in Chapter 6 as applied to the Euler and ideal MHD equations. The collisional-radiative model developed for argon is presented in Chapter 9.

Numerical results of the Glass and Liu shock tube experiments are presented in Chapter 10 in terms of one- and two-dimensional simulations. Both steady and unsteady 1D simulations are used to establish the cross sections and rates that are best able to reproduce the experimental relaxation length and ionization fractions. Two-dimensional simulations

are then preformed to determine the actual shock structure. As an extension to external flow, the solver is then applied to flow around a circular cylinder in Chapter 11.

The parallel framework that serves as the backbone of the numerical solver is presented in Chapter 12. It is developed entirely in Java and is capable of execution on distributed memory machines.

CHAPTER 2

GOVERNING EQUATIONS

The governing set of equations at the foundation of the current research are presented in this chapter. They include all of the relevant physics to be modeled, including convective and diffusive transport, wave (acoustic) phenomena, chemical kinetics, and so on. Of critical importance is the coupling of these effects and how they are accounted for in the formulation and resulting numerical implementation.

In particular, a self-consistent formulation between convective transport and wave phenomena is crucial. This is important, for example, to ensure proper jump conditions across shock waves and other discontinuities that are necessary for accurate calculation of the reaction rates needed for the collisional-radiative model. As a result, added emphasis will be placed on accurate treatment of the convective terms.

The plasmas to be investigated are assumed to be sufficiently collisional such that the continuum hypothesis is valid. As a result, a Maxwellian distribution of the velocity is taken, allowing a fluid description of the plasma. The resulting fluid equations are presented here in conservation form and are hyperbolic in nature. It is from the hyperbolic nature of these equations that numerical formulations will be be developed. The diffusive and kinetic processes will be treated as source terms that can be updated independently[1]of the convective terms.

We begin by introducing the general form of the governing equations and some properties. We then get into the specifics in which we introduce the two-temperature (2T) equations which we finally couple with electromagnetic effects.

[1]Within a time step.

2.1 Conservative formulation

The governing equations are presented here in differential form to facilitate their derivation. They will be cast into integral form in the following chapter which will serve as the basis for the numerical finite-volume formulation. The flow equations in divergence form can be expressed as

$$\frac{\partial Q}{\partial t} + \nabla \cdot \bar{\bar{F}} = \dot{\Omega}, \tag{2.1}$$

where Q is the vector of conserved quantities, $\bar{\bar{F}}$ is a second-order tensor containing the flux density of Q, and $\dot{\Omega}$ is a vector of source terms. The convention adopted in this work is that the mathematical nature of the left-hand side (LHS) of Eq. (2.1) will be strictly hyperbolic while $\dot{\Omega}$ contains all terms to the contrary. These terms may include diffusive, dispersive, chemical kinetics and other such processes, each of which must be dealt with appropriately. In particular, these processes may have associated time scales much smaller than that of the convective processes, and temporal resolution of these scales in both an efficient and accurate manner requires operator-splitting techniques to be employed. That is, the transport equations are solved independently of the source terms, which are in turn solved independently of each other. In such an approach, a change is computed for the convective contribution,

$$\left.\frac{\partial Q}{\partial t}\right|_{\text{conv}} = -\nabla \cdot \bar{\bar{F}} \tag{2.2}$$

followed by the contribution from the various source terms,

$$\left.\frac{\partial Q}{\partial t}\right|_{\text{cond}} = \dot{\Omega}_{\text{cond}}, \quad \left.\frac{\partial Q}{\partial t}\right|_{\text{diff}} = \dot{\Omega}_{\text{diff}}, \quad \left.\frac{\partial Q}{\partial t}\right|_{\text{chem}} = \dot{\Omega}_{\text{chem}}, \ldots \tag{2.3}$$

the combined sum of which gives the total change of the conserved variables,

$$\frac{\partial Q}{\partial t} = \left.\frac{\partial Q}{\partial t}\right|_{\text{conv}} + \left.\frac{\partial Q}{\partial t}\right|_{\text{cond}} + \left.\frac{\partial Q}{\partial t}\right|_{\text{diff}} + \left.\frac{\partial Q}{\partial t}\right|_{\text{chem}} + \ldots \tag{2.4}$$

2.1.1 Hyperbolic terms

Operator-splitting can be used to analyze individual contributions to the governing equations. In particular, operator-splitting is applied here to isolate the hyperbolic contribution to the governing equations, resulting in

$$\frac{\partial Q}{\partial t} + \nabla \cdot \bar{\bar{F}} = 0. \tag{2.5}$$

Taking the directional derivative of the LHS of Eq. (2.5) along an arbitrary direction $\hat{n}$ gives,

$$\frac{\partial Q}{\partial t} + \nabla_{\hat{n}} \cdot \bar{\bar{F}} = 0, \tag{2.6}$$

or equivalently,

$$\frac{\partial Q}{\partial t} + \nabla \cdot F_n = 0, \tag{2.7}$$

where $F_n = \hat{n} \cdot \bar{\bar{F}}$ is the vector of flux density in the n-direction. This form is particularly useful in the analysis of the governing equations and will be used extensively throughout this work. Upon application of the chain rule,

$$\frac{\partial F(Q)}{\partial n} = \left[\frac{\partial F}{\partial Q}\right] \frac{\partial Q}{\partial n} = A \frac{\partial Q}{\partial n}, \tag{2.8}$$

Eq. (2.6) can be expressed as

$$\frac{\partial Q}{\partial t} + A_n \frac{\partial Q}{\partial n} = 0, \tag{2.9}$$

where $A = \partial F / \partial Q$. This system is classified as hyperbolic if all eigenvalues of the Jacobian matrix A are real and has a complete set of right eigenvectors, $\vec{r}_i$. This work will deal only with systems for which the flux Jacobian matrix A can be diagonalized as,

$$A = R \Lambda L, \tag{2.10}$$

where Λ is a diagonal matrix of *real* eigenvalues and R and L are matrices of right and left eigenvectors, respectively. In general, diagonalization of the Jacobian matrix when expressed

in terms of the conserved quantities can be fairly complex. To facilitate diagonalization, the Jacobian is re-expressed through a similarity transformation,

$$A = \frac{\partial Q}{\partial V}\frac{\partial V}{\partial Q}\frac{\partial F}{\partial V}\frac{\partial V}{\partial Q} \tag{2.11}$$

$$= M A_p M^{-1} \tag{2.12}$$

provided by the transformation matrices,

$$M = \partial Q/\partial V \tag{2.13}$$

$$M^{-1} = \partial V/\partial Q. \tag{2.14}$$

Because A and A_p are similar, they share the same eigenvalues, although their eigenvectors span different eigenspaces. Their eigenvectors are related by

$$R = M R_p, \quad L = L_p M^{-1}. \tag{2.15}$$

The vector V can arbitrarily be defined, but will be taken as the vector of primitive variables as will later be shown (hence the subscript p in Eq. (2.12)). With such a diagonalization, Eq. (2.9) can be cast into characteristic form as,

$$\frac{\partial W}{\partial t} + \Lambda_n \frac{\partial W}{\partial n} = 0, \tag{2.16}$$

with $W = LQ$ and assuming A to be constant. In the transformation from Eq. (2.9) to Eq. (2.16), the hyperbolic system has been decoupled, and as a result, each characteristic equation can be solved independently of each other.[2] The exact form of Q, V, and F, as well as their resulting diagonalization, to be used in the current research are the subject of the following sections, which include the basic flow equations coupled with the bi-temperature and magnetohydrodynamic models, for which the form of $\dot{\Omega}$ will also be derived.

[2]This is a necessary step if the solution technique involves nonlinear operators, such as limiters.

2.2 Two-temperature model

For flows that can be described by very high Mach numbers, the air may become appreciably ionized. For such cases in which ionization results from a hot plasma, an equation for the electron energy is also required. As the atoms in the fluid are ionized and an electron gas is formed, electrons rapidly thermalize with each other, and a Maxwellian distribution and associated electron temperature T_e can be assumed if the electrons are sufficiently collisional. The slow energy exchange between between electrons and the heavy particles, however, means that the two species, in general, cannot be described by the same temperature. As a result, a two-temperature (2T) model in which the electron thermal energy is convected independently of the total energy is necessary.

Such a model can be achieved by augmenting the governing equations for the bulk fluid with the electron fluid equations. Incorporation of the full electron mass, momentum, and energy equations leads to a two-fluid (2F) description of the plasma. This can be computationally restrictive as the electron conservation equations introduce the electron thermal velocity, a_e, which can be several orders of magnitude greater than that of the heavy particles and must be resolved nonetheless. In the single-fluid (1F) approach, on the other hand, the electron momentum equation is used to simplify the electron energy equation to a linear convection equation. As a result, the electron momentum equation is implicitly satisfied and the electron thermal velocity vanishes. In order to highlight key assumptions, the single-fluid, two-temperature model is derived here from the full two-fluid description of the plasma.

2.2.1 Two-fluid equations

For collision-dominated flows, the heavy particles are well-defined by a single fluid, with continuity, momentum, and energy equations,

$$\frac{\partial \rho_s}{\partial t} + \nabla \cdot (\rho_h \vec{u}_h) = \dot{\rho}_s \tag{2.17}$$

$$\frac{\partial \rho_h \vec{u}_h}{\partial t} + \nabla \cdot (\rho_h \vec{u}_h \vec{u}_h) + \nabla p_h = \vec{\mu}_{eh} + n_i e Z_i (\vec{E} + \vec{u}_h \times \vec{B}) \tag{2.18}$$

$$\begin{aligned} \frac{\partial}{\partial t}\left[\rho_h \left(\varepsilon_h + \frac{1}{2}\vec{u}_h \cdot \vec{u}_h\right)\right] + \nabla \cdot \left[\rho_h \vec{u}_h \left(\varepsilon_h + \frac{1}{2}\vec{u}_h \cdot \vec{u}_h\right)\right] + \nabla \cdot (\vec{u}_h p_h) \\ = \vec{u}_h \cdot \vec{\mu}_{eh} - n_i e Z_i \vec{u}_h \cdot \vec{E} - \nabla \cdot (\bar{\bar{\kappa}}_h \nabla T_h) - \dot{q}_h^{\mathrm{CR}} \end{aligned} \tag{2.19}$$

respectively. Each heavy particle specie s contributes to the total mass density,

$$\rho_h = \sum_{s \neq e} \rho_s \tag{2.20}$$

which in this work can be an atom, ion, or electronically-excited level. Thermal conductivity is given by κ and $\dot{q}_h^{\mathrm{CR}}$ denotes energy changes dues to collisional-radiative processes, while $\vec{\mu}$ is the momentum transfer function between heavy particles and electrons.

The continuity, momentum, and energy equations for the electron fluid are given by

$$\frac{\partial \rho_e}{\partial t} + \nabla \cdot (\rho_e \vec{u}_e) = \dot{\rho}_e \tag{2.21}$$

$$\frac{\partial \rho_e \vec{u}_e}{\partial t} + \nabla \cdot (\rho_e \vec{u}_e \vec{u}_e) + \nabla p_e = \vec{\mu}_{he} + n_e e (\vec{E} + \vec{u}_e \times \vec{B}) \tag{2.22}$$

$$\begin{aligned} \frac{\partial}{\partial t}\left[\rho_e \left(\varepsilon_e + \frac{1}{2}\vec{u}_e \cdot \vec{u}_e\right)\right] + \nabla \cdot \left[\rho_e \vec{u}_e \left(\varepsilon_e + \frac{1}{2}\vec{u}_e \cdot \vec{u}_e\right)\right] + \nabla \cdot (\vec{u}_e p_e) \\ = \vec{u}_e \cdot \vec{\mu}_{he} - n_e e \vec{u}_e \cdot \vec{E} - \nabla \cdot (\bar{\bar{\kappa}}_e \nabla T_e) - \dot{q}_e^{\mathrm{CR}} \end{aligned} \tag{2.23}$$

respectively. Here, $\vec{\mu}_{he}$ is the momentum transfer function between electrons and heavy particles which is equal in magnitude but opposite in sign to $\vec{\mu}_{eh}$.

The key assumption in the two-temperature model is that both the heavy particle and electron bulk velocities can be described by the same velocity, i.e. $u \approx u_e \approx u_h$. This assumption is a direct consequence of charge neutrality and is valid when considering length scales greater than the Debye length. Making use of this condition, the overall continuity equation becomes

$$\frac{\partial \rho}{\partial t} + \nabla \cdot (\rho \vec{u}) = 0 \tag{2.24}$$

while the heavy-particle and electron momentum equations can be combined into an overall momentum equation,

$$\frac{\partial \rho \vec{u}}{\partial t} + \nabla \cdot (\rho \vec{u} \vec{u}) + \nabla p = Q\vec{E} + \vec{j}_c \times \vec{B}, \tag{2.25}$$

with the total mass density $\rho = \rho_e + \rho_h$ and the the total charge density $Q = en_e + e\sum n_i Z_i$. Furthermore, the heavy-particle and electron energy equations can be combined into an overall energy equation,

$$\frac{\partial E}{\partial t} + \nabla \cdot (\vec{u} H_\circ) + \nabla p = \vec{j}_c \cdot \vec{E} - \nabla \cdot (\bar{\bar{\kappa}}_h \nabla T_h) - \nabla \cdot (\bar{\bar{\kappa}}_e \nabla T_e) - \dot{q}_{\text{CR}} \tag{2.26}$$

where E is the total energy,

$$E = \varepsilon_h + \varepsilon_e + \frac{1}{2}\rho \vec{u} \cdot \vec{u} \tag{2.27}$$

and $H_\circ = E + p$ is the stagnation enthalpy density.

2.2.2 Generalized Ohm's law

Although the assumption of charge neutrality in the 2T model precludes the possibility of convection currents, conduction currents can still be present due to variations in the specie drift velocities. As derived from the 2F equations, the generalized Ohm's law provides an expression for the conduction current [109],

$$\vec{j}_c = \sigma \left\{ \vec{E} + \vec{u} \times \vec{B} + \frac{\nabla p_e}{n_e e} - \frac{\vec{j} \times \vec{B}}{n_e e} \right\}. \tag{2.28}$$

2.2.3 Electron fluid

Note that the electron energy equation is a function of the electron pressure p_e. The eigenvalues of such a system includes the thermal sound speed of the electron gas which is prohibitively stiff. It is therefore necessary to remove this dependency and reduce the electron energy equation to a linear advection equation in eigenspace. We begin this process by first recasting the electron continuity and momentum equations in non-conservative form which will then be used to simplify the electron energy equation. Furthermore, electromagnetic

effects will be neglected.

Conservation of electron mass

The electron continuity equation in divergence form is given by Eq. (2.21),

$$\frac{\partial \rho_e}{\partial t} + \nabla \cdot (\rho_e \vec{u}) = \dot{\rho}_e \tag{2.29}$$

where $\dot{\rho}_e$ is the rate of change of electron density due to ionization and recombination. Expanding the divergence term,

$$\frac{\partial \rho_e}{\partial t} + \vec{u} \cdot \nabla \rho_e + \rho_e \nabla \cdot \vec{u} = \dot{\rho}_e, \tag{2.30}$$

the non-conservative form is found to be

$$\frac{D\rho_e}{Dt} + \rho_e \nabla \cdot \vec{u} = \dot{\rho}_e \tag{2.31}$$

with the material derivative defined as

$$\frac{D}{Dt} \equiv \frac{\partial}{\partial t} + \vec{u} \cdot \nabla. \tag{2.32}$$

Conservation of electron momentum

The momentum equation in divergence form is given by

$$\frac{\partial \rho_e \vec{u}}{\partial t} + \nabla \cdot (\rho_e \vec{u}\vec{u}) + \nabla p_e = \vec{\mu}_{he}. \tag{2.33}$$

where $\vec{\mu}_e$ is the momentum transfer function between the electron and heavy species. Substitution into the momentum equation and carrying out the indicated operations on the LHS yields

$$\rho_e \frac{\partial \vec{u}}{\partial t} + \vec{u}\frac{\partial \rho_e}{\partial t} + \rho_e(\vec{u} \cdot \nabla)\vec{u} + \vec{u}\nabla \cdot (\rho_e \vec{u}) + \nabla p_e = \vec{\mu}_{he} \tag{2.34}$$

in which the second and fourth terms are the convective terms of the continuity equation, Eq. (2.31), yielding

$$\rho_e \frac{D\vec{u}}{Dt} + \nabla p_e = \vec{\mu}_{he} - \dot{\rho}_e \vec{u}. \tag{2.35}$$

Conservation of electron energy

The energy equation is represented in divergence form as

$$\frac{\partial}{\partial t}\left[\rho_e\left(\varepsilon_e + \frac{1}{2}\vec{u}\cdot\vec{u}\right)\right] + \nabla\cdot\left[\rho_e\left(\varepsilon_e + \frac{1}{2}\vec{u}\cdot\vec{u}\right)\vec{u}\right] + \nabla\cdot(\vec{u}p_e) = \vec{u}_{he}\cdot\vec{\mu} - \nabla\cdot\vec{q}_e - \dot{q}_{\text{CR}} \tag{2.36}$$

where $\nabla\cdot\vec{q}_e$ is the electron heat condution. Separating the internal energy from the kinetic energy, for which the indicated operations are carried out,

$$\frac{\partial}{\partial t}(\rho_e\varepsilon_e) + \nabla\cdot(\rho_e\varepsilon_e\vec{u}) + \frac{1}{2}(\vec{u}\cdot\vec{u})\frac{\partial\rho_e}{\partial t} + \frac{1}{2}\rho_e\frac{\partial}{\partial t}(\vec{u}\cdot\vec{u}) + \frac{1}{2}\rho_e\vec{u}\cdot\nabla(\vec{u}\cdot\vec{u}) + \frac{1}{2}(\vec{u}\cdot\vec{u})\nabla\cdot(\rho_e\vec{u}) + p_e\nabla\cdot\vec{u} + \vec{u}\cdot\nabla p_e = \vec{u}_{he}\cdot\vec{\mu} - \nabla\cdot\vec{q}_e - \dot{q}_{\text{CR}} \tag{2.37}$$

and upon regrouping terms,

$$\frac{\partial}{\partial t}(\rho_e\varepsilon_e) + \nabla\cdot(\rho_e\varepsilon_e\vec{u}) + \frac{1}{2}(\vec{u}\cdot\vec{u})\left[\frac{\partial\rho_e}{\partial t} + \nabla\cdot(\rho_e\vec{u})\right] + \frac{1}{2}\rho_e\frac{D}{Dt}(\vec{u}\cdot\vec{u}) + \vec{u}\cdot\nabla p_e + p_e\nabla\cdot\vec{u} = \vec{u}_{he}\cdot\vec{\mu} - \nabla\cdot\vec{q}_e - \dot{q}_{\text{CR}} \tag{2.38}$$

and noting that

$$\frac{1}{2}\rho_e\frac{D}{Dt}(\vec{u}\cdot\vec{u}) = \vec{u}\cdot\rho_e\frac{D\vec{u}}{Dt}$$

$$\frac{\partial}{\partial t}(\rho_e \varepsilon_e) + \nabla \cdot (\rho_e \varepsilon_e \vec{u}) + \frac{1}{2}(\vec{u} \cdot \vec{u}) \left[\frac{\partial \rho_e}{\partial t} + \nabla \cdot (\rho_e \vec{u}) \right] + \vec{u} \cdot \left[\rho_e \frac{D\vec{u}}{Dt} + \nabla p_e \right] + p_e \nabla \cdot \vec{u}$$
$$= \vec{u}_{he} \cdot \vec{\mu} - \nabla \cdot \vec{q}_e - \dot{q}_{\text{CR}} \quad (2.39)$$

it is found that the third and fourth terms on the LHS of Eq. (2.39) contain expressions involving the continuity and momentum equations, (2.29) and (2.35), respectively. Making the appropriate substitutions, the energy equation reduces to

$$\frac{\partial}{\partial t}(\rho_e \varepsilon_e) + \nabla \cdot (\rho_e \varepsilon_e \vec{u}) = -p_e \nabla \cdot \vec{u} + \dot{\omega} \quad (2.40)$$

where

$$\dot{\omega} = \frac{1}{2}\dot{\rho}_e \vec{u} \cdot \vec{u} - \nabla \vec{q}_e - \dot{q}_{\text{CR}} \quad (2.41)$$

in which the second term has been obtained under the assumption, $\vec{V}_e \gg \vec{u}$.

The result is that the electron energy equation has been reduced to a linear convection equation, for which the electron sound speed does not play a role. The trade-off, however, is that the source term containing the velocity divergence $p_e \nabla \cdot \vec{u}$ is in non-conservative form, and may present severe numerical difficulties where the flow gradients are not resolved, degrading solutions at shocks and other discontinuities. A solution to this problem is possible and was first presented in [15]. Expressing the LHS of Eq. (2.40) in non-conservative form with the aid of Eq. (2.31),

$$\rho_e \frac{D\varepsilon_e}{Dt} + p_e \nabla \cdot \vec{u} = \dot{\omega} - \dot{\rho}_e \varepsilon_e \quad (2.42)$$

and noting that the from the continuity equation Eq. (2.31),

$$\begin{aligned} \nabla \cdot \vec{u} &= -v_e \frac{D\rho_e}{Dt} + v_e \dot{\rho}_e \\ &= \rho_e \frac{Dv_e}{Dt} + v_e \dot{\rho}_e \end{aligned} \quad (2.43)$$

where v_e is the specific electronic volume, the velocity divergence term can be eliminated from Eq. (2.42), yielding

$$\rho_e \frac{D\varepsilon_e}{Dt} + \rho_e p_e \frac{Dv_e}{Dt} = \dot{\omega} - \varepsilon_e \dot{\rho}_e - \frac{p_e}{\rho_e}\dot{\rho}_e \tag{2.44}$$

The LHS of Eq. (2.44) can be related to the entropy through the 1$^{\text{st}}$ law of thermodynamics in advection form, namely

$$\rho_e \frac{D\varepsilon_e}{Dt} + \rho_e p_e \frac{Dv_e}{Dt} = \rho_e T_e \frac{Ds_e}{Dt} \tag{2.45}$$

resulting in

$$\rho_e T_e \frac{Ds_e}{Dt} = \dot{\omega} - \dot{\rho}_e h_e, \tag{2.46}$$

where $h_e = \varepsilon_e + p_e/\rho_e$ is the specific electronic enthalpy. Dividing through by T_e,

$$\rho_e \frac{Ds_e}{Dt} = \frac{1}{T_e}(\dot{\omega} - \dot{\rho}_e h_e) \tag{2.47}$$

and adding the continuity equation Eq. (2.31) with a factor s_e,

$$\rho_e \frac{\partial s_e}{\partial t} + \rho_e \vec{u} \cdot \nabla s_e + s_e \left[\frac{\partial \rho_e}{\partial t} + \nabla \cdot (\rho_e \vec{u}) - \dot{\rho}_e \right] = \frac{1}{T_e}(\dot{\omega} - \dot{\rho}_e h_e) \tag{2.48}$$

the conservative formulation is obtained for $\rho_e s_e$,

$$\frac{\partial \rho_e s_e}{\partial t} + \nabla \cdot (\rho_e s_e \vec{u}) = \frac{1}{T_e}(\dot{\omega} - \dot{\rho}_e h_e) + \dot{\rho}_e s_e \tag{2.49}$$

This form of the energy equation is free of any non-conservative spatial operators and so is best-suited for shock-capturing schemes. The electron entropy function is given by the ideal gas isentropic relation,

$$s_e \equiv \frac{p_e}{\rho_e^{\gamma_e}} = \text{constant} \tag{2.50}$$

since electrons lack an internal structure and the assumption of constant specific heats is valid.

The electron entropy above presents a problem as it is ill-defined for cases in which the ionization fraction tends to zero. This can be remedied by introducing a pseudo-entropy variable defined as

$$\hat{s}_e \equiv \frac{p_e}{\rho^{\gamma_e}} \tag{2.51}$$

which is well-defined for all ionization fractions. Since the electron gas is calorically-perfect,

$$p_e = (\gamma_e - 1)\rho_e \varepsilon_e, \tag{2.52}$$

so that $\hat{s}_e$ can also be defined as

$$\hat{s}_e \equiv (\gamma_e - 1)\frac{\rho_e \varepsilon_e}{\rho^{\gamma_e}} \tag{2.53}$$

The replacement of $\rho_e s_e$ with $\rho \hat{s}_e$ as a conserved variable is trivial as can be seen when inserted into the convection equation, (and can be verified by direct calculation)

$$\begin{aligned}
\frac{\partial \rho \hat{s}_e}{\partial t} + \nabla \cdot (\rho \hat{s}_e \vec{u}) &= \frac{\partial}{\partial t}\left(\frac{p_e}{\rho^{\gamma_e - 1}}\right) + \nabla \cdot \left(\frac{p_e}{\rho^{\gamma_e - 1}}\vec{u}\right) \\
&= (1 - \gamma_e)\frac{p_e}{\rho^{\gamma_e}}\frac{\partial \rho}{\partial t} + \frac{1}{\rho^{\gamma_e - 1}}\frac{\partial p_e}{\partial t} + \vec{u} \cdot \nabla \frac{p_e}{\rho^{\gamma_e - 1}} + \frac{p_e}{\rho^{\gamma_e - 1}} \nabla \cdot \vec{u} \\
&= (1 - \gamma_e)\frac{p_e}{\rho^{\gamma_e}}\frac{D\rho}{Dt} + \frac{\gamma_e - 1}{\rho^{\gamma_e - 1}}\left(\frac{\partial E_e}{\partial t} + \nabla \cdot \vec{u} E_e\right) \\
&= \frac{\gamma_e - 1}{\rho^{\gamma_e - 1}}\dot{\omega}
\end{aligned} \tag{2.54}$$

where the overall momentum equation, $D\rho/Dt + \rho \nabla \cdot \vec{u} = 0$, has been used as well as Eq. (2.40) in conjunction with Eq. (2.52). Note that in addition to being better conditioned, Eq. (2.54) has the advantage of also being a simpler expression than Eq. (2.49). This results from the fact that $d\rho = 0$ while $d\rho_e \neq 0$. Thus if the source terms are computed with $\rho_e \varepsilon$ as the conservative variable, an update to the electronic entropy function may be obtained after the source term is multiplied by the factor $(\gamma_e - 1)/\rho^{\gamma_e - 1}$. This result is verified by differentiating Eq. (2.53), i.e.

$$d(\rho\hat{s}_e) = \frac{(\gamma_e - 1)}{\rho^{\gamma_e - 1}} d(\rho_e \varepsilon_e) \tag{2.55}$$

2.2.4 Thermophysical properties

With the electron entropy equation, Eq. (2.54), combined with the bulk equations of motion and total energy, the two-temperature model takes the following form,

$$Q = \begin{pmatrix} \rho_1 \\ \vdots \\ \rho_n \\ \rho u \\ \rho v \\ \rho w \\ E \\ \rho\hat{s}_e \end{pmatrix}, \quad V = \begin{pmatrix} \rho_1 \\ \vdots \\ \rho_n \\ u \\ v \\ w \\ p \\ p_e \end{pmatrix}, \quad F_n = \begin{pmatrix} \rho_1 v_n \\ \vdots \\ \rho_n v_n \\ \rho u v_n + n_x p \\ \rho v v_n + n_y p \\ \rho w v_n + n_z p \\ (E + p) v_n \\ \rho\hat{s}_e v_n \end{pmatrix} \tag{2.56}$$

In order to close the 2T system, the thermal pressure must be related to the conserved quantities via appropriate equations of state (EOS). The relations are paramount in determining the differential relations that are necessary to develop the flux Jacobian matrix and corresponding eigensystem. First, the partial derivatives of the total and electron thermal pressures with respect to the conserved quantities are derived, followed by the partial derivatives of the total energy and electron entropy function with respect to the primitive variables.

Pressure derivatives

The plasma is assumed to behave as an ideal gas in which case an exact expression for the total pressure of all species is obtained from Dalton's law of partial pressures,

$$p = p_h + p_e, \tag{2.57}$$

where the heavy particles obey a thermally-perfect EOS,

$$p_h = T_h \sum_{s \neq e} \rho_s R_s, \tag{2.58}$$

while a direct relationship between the electron pressure and entropy function has previously been defined (cf. Eq. (2.51)), giving

$$p_e = S_e \rho^{\gamma_e - 1}. \tag{2.59}$$

Differentiating Eqs. (2.58) and (2.59),

$$dp_h = dT_h \sum_{s \neq e} \rho_s R_s + T_h \sum_{s \neq e} R_s d\rho_s \tag{2.60}$$

$$dp_e = \rho^{\gamma_e - 1} dS_e + (\gamma_e - 1) \frac{p_e}{\rho} d\rho, \tag{2.61}$$

and combining with Eq. (2.57),

$$dp = dT_h \sum_{s \neq e} \rho_s R_s + T_h \sum_{s \neq e} R_s d\rho_s + \rho^{\gamma_e - 1} dS_e + (\gamma_e - 1) \frac{p_e}{\rho} d\rho, \tag{2.62}$$

an expression for the differential pressure is obtained. While the electron pressure has been expressed solely in terms of the conserved quantities, the heavy species contain a temperature dependence, which must be expressed in terms of the energy—a conservative variable. The total energy is expressed as the sum of the specie internal energies, kinetic energy, and, in the presence of magnetic fields, the magnetic pressure.

$$E = \sum_{s \neq e} \rho_s \varepsilon_s + \rho_e \varepsilon_e + \frac{\vec{m} \cdot \vec{m}}{2\rho} + \frac{\vec{B} \cdot \vec{B}}{2\mu_\circ} \tag{2.63}$$

Since the electrons lack an internal structure, the electron fluid obeys a calorically-perfect EOS, permitting a direct relationship between the electron internal energy and pressure,

$$\rho_e \varepsilon_e = \frac{p_e}{\gamma_e - 1}, \tag{2.64}$$

which, in combination with Eq. (2.63), gives

$$E = \sum_{s \neq e} \rho_s \varepsilon_s + \frac{p_e}{\gamma_e - 1} + \frac{\vec{m} \cdot \vec{m}}{2\rho} + \frac{\vec{B} \cdot \vec{B}}{2\mu_\circ} \tag{2.65}$$

Differentiating this expression,

$$dE = \sum_{s \neq e} \rho_s d\varepsilon_s + \sum_{s \neq e} \varepsilon_s d\rho_s + \frac{dp_e}{\gamma_e - 1} + \vec{u} \cdot d\vec{m} - \frac{1}{2}\vec{u} \cdot \vec{u} d\rho + \frac{1}{\mu_\circ}\vec{B} \cdot d\vec{B}, \tag{2.66}$$

and noting that for the (thermally-perfect) heavy species,

$$c_{v,s} = \left(\frac{\partial \varepsilon_s}{\partial T_h}\right)_v \quad \xrightarrow[\text{ideal gas}]{c_{v,s}=f(T)} \quad d\varepsilon_s = c_{v,s} dT_h \tag{2.67}$$

the desired differential form of T_h is found to be

$$dT_h = \frac{1}{\sum\limits_{s \neq e} \rho_s c_{v,s}} \left[dE + \frac{1}{2}\vec{u} \cdot \vec{u} d\rho - \vec{u} \cdot d\vec{m} - \frac{1}{\mu_\circ}\vec{B} \cdot d\vec{B} - \sum_{s \neq e} \varepsilon_s d\rho_s - \frac{dp_e}{\gamma_e - 1} \right] \tag{2.68}$$

Inserting Eq. (2.68) into (2.62) and again applying (2.61), the expression for the differential pressure can finally be expressed entirely in terms of the conserved quantity differentials,

$$\begin{aligned} dp = (\gamma_h - 1) \left[dE + \frac{1}{2}\vec{u} \cdot \vec{u} d\rho - \vec{u} \cdot d\vec{m} - \frac{1}{\mu_\circ}\vec{B} \cdot d\vec{B} - \sum_{s \neq e} \varepsilon_s d\rho_s - \frac{\rho^{\gamma_e - 1}}{\gamma_e - 1} dS_e \right] \\ + T_h \sum_{s \neq e} R_s d\rho_s + \rho^{\gamma_e - 1} dS_e + (\gamma_e - \gamma_h)\frac{p_e}{\rho} d\rho \end{aligned} \tag{2.69}$$

where

$$\gamma_h - 1 \equiv \frac{\sum\limits_{s \neq e} \rho_s R_s}{\sum\limits_{s \neq e} \rho_s c_{v,s}} \tag{2.70}$$

From Eqs. (2.61) and (2.69), the resulting pressure derivatives can now be defined.

$$P_E \equiv \left(\frac{\partial p}{\partial E}\right)_{q \neq E} = \gamma_h - 1 \tag{2.71}$$

$$P_{S_e} \equiv \left(\frac{\partial p}{\partial S_e}\right)_{q\neq S_e} = \rho^{\gamma_e - 1}\left(1 - \frac{\gamma_h - 1}{\gamma_e - 1}\right) \tag{2.72}$$

$$P_{\vec{m}} \equiv \left(\frac{\partial p}{\partial \vec{m}}\right)_{q\neq \vec{m}} = -(\gamma_h - 1)\vec{u} \tag{2.73}$$

$$P_{\vec{B}} \equiv \left(\frac{\partial p}{\partial \vec{B}}\right)_{q\neq \vec{B}} = -(\gamma_h - 1)\frac{\vec{B}}{\mu_\circ} \tag{2.74}$$

$$P_{\rho_e} \equiv \left(\frac{\partial p}{\partial \rho_e}\right)_{q\neq \rho_e} = (\gamma_e - \gamma_h)\frac{p_e}{\rho} + \frac{1}{2}(\gamma_h - 1)\vec{u}\cdot\vec{u} \tag{2.75}$$

$$P_{\rho_{s\neq e}} \equiv \left(\frac{\partial p}{\partial \rho_{s\neq e}}\right)_{q\neq \rho_{s\neq e}} = P_{\rho_e} - (\gamma_h - 1)\varepsilon_s + \frac{p_s}{\rho_s} \tag{2.76}$$

$$P_\rho \equiv \left(\frac{\partial p}{\partial \rho}\right)_{q\neq \rho} = \sum y_s P_{\rho_s} = P_{\rho_e} - (\gamma_h - 1)\sum_{s\neq e} y_s\varepsilon_s + \frac{p - p_e}{\rho} \tag{2.77}$$

Energy derivatives

Similar to the approach taken in the previous section, we can find the partial derivatives of the total energy and electron entropy function with respect to the primitive variables. Contrary to inserting the expression found for dT_h from the energy equation into the pressure equation, the pressure equation is rearranged to find dT_h which is then inserted into the energy equation. Differentiating the energy equation with respect to the primitive variables $(\rho_s, \vec{u}, \vec{B}, p, p_e)$, the following expression is obtained.

$$dE = dT_h \sum_{s\neq e}\rho_s c_{v,s} + \sum_{s\neq e}\varepsilon_s d\rho_s + \frac{dp_e}{\gamma_e - 1} + \rho\vec{u}\cdot d\vec{u} + \frac{1}{2}\vec{u}\cdot\vec{u}d\rho + \frac{1}{\mu_\circ}\vec{B}\cdot d\vec{B} \tag{2.78}$$

Rearranging the primitive variable equivalent of Eq. (2.62),

$$dT_h = \frac{1}{\sum\limits_{s\neq e}\rho_s R_s}\left[dp - T_h\sum_{s\neq e} R_s d\rho_s - dp_e\right] \tag{2.79}$$

and inserting into Eq. (2.78),

$$dE = \frac{1}{\gamma_h - 1}\left[dp - T_h \sum_{s\neq e} R_s d\rho_s - dp_e\right] + \sum_{s\neq e}\varepsilon_s d\rho_s + \frac{dp_e}{\gamma_e - 1} + \rho\vec{u}\cdot d\vec{u} + \frac{1}{2}\vec{u}\cdot\vec{u}d\rho + \frac{1}{\mu_\circ}\vec{B}\cdot d\vec{B}, \quad (2.80)$$

an expression for the differential energy is obtained from which the partial derivatives of the total energy with respect to the primitive variables are defined.

$$E_p \equiv \left(\frac{\partial E}{\partial p}\right)_{v\neq p} = \frac{1}{\gamma_h - 1} \quad (2.81)$$

$$E_{p_e} \equiv \left(\frac{\partial E}{\partial p_e}\right)_{v\neq p_e} = \frac{1}{\gamma_e - 1} - \frac{1}{\gamma_h - 1} \quad (2.82)$$

$$E_{\vec{u}} \equiv \left(\frac{\partial E}{\partial \vec{u}}\right)_{v\neq \vec{u}} = \rho\vec{u} \quad (2.83)$$

$$E_{\vec{B}} \equiv \left(\frac{\partial E}{\partial \vec{B}}\right)_{v\neq \vec{B}} = \frac{1}{\mu_\circ}\vec{B} \quad (2.84)$$

$$E_{\rho_e} \equiv \left(\frac{\partial E}{\partial \rho_e}\right)_{v\neq \rho_e} = \frac{1}{2}\vec{u}\cdot\vec{u} \quad (2.85)$$

$$E_{\rho_{s\neq e}} \equiv \left(\frac{\partial E}{\partial \rho_{s\neq e}}\right)_{v\neq \rho_{s\neq e}} = E_{\rho_e} + \varepsilon_s - \frac{p_s}{(\gamma_h - 1)\rho_s} \quad (2.86)$$

Electron pressure and entropy function derivatives

The electron pressure derivatives,

$$P_{eS_e} \equiv \left(\frac{\partial p_e}{\partial S_e}\right)_{q\neq S_e} = \rho^{\gamma_e - 1} = \frac{p_e}{S_e} \quad (2.87)$$

$$P_{e\rho_s} \equiv \left(\frac{\partial p_e}{\partial \rho_s}\right)_{q\neq \rho_s} = (\gamma_e - 1)\frac{p_e}{\rho} \quad (2.88)$$

$$P_{e\rho} \equiv \left(\frac{\partial p_e}{\partial \rho}\right)_{q\neq \rho} = P_{e\rho_s} \quad (2.89)$$

$$P_{e\vec{m}} \equiv \left(\frac{\partial p_e}{\partial \vec{m}}\right)_{q\neq \vec{m}} = 0 \quad (2.90)$$

$$P_{e\,\vec{B}} \equiv \left(\frac{\partial p_e}{\partial \vec{B}}\right)_{q\neq\vec{B}} = 0 \tag{2.91}$$

$$P_{e\,E} \equiv \left(\frac{\partial p_e}{\partial E}\right)_{q\neq E} = 0 \tag{2.92}$$

and entropy function derivatives,

$$S_{e\,\rho_s} \equiv \left(\frac{\partial S_e}{\partial \rho_s}\right)_{v\neq\rho_s} = (1-\gamma_e)\frac{p_e}{\rho^{\gamma_e}} = (1-\gamma_e)\frac{S_e}{\rho} \tag{2.93}$$

$$S_{e\,\rho} \equiv \left(\frac{\partial S_e}{\partial \rho}\right)_{v\neq\rho} = S_{e\,\rho_s} \tag{2.94}$$

$$S_{e\,p_e} \equiv \left(\frac{\partial S_e}{\partial p_e}\right)_{v\neq p_e} = \rho^{1-\gamma_e} \tag{2.95}$$

$$S_{e\,\vec{u}} \equiv \left(\frac{\partial S_e}{\partial \vec{u}}\right)_{v\neq\vec{u}} = 0 \tag{2.96}$$

$$S_{e\,\vec{B}} \equiv \left(\frac{\partial S_e}{\partial \vec{B}}\right)_{v\neq\vec{B}} = 0 \tag{2.97}$$

$$S_{e\,p} \equiv \left(\frac{\partial S_e}{\partial p}\right)_{v\neq p} = 0 \tag{2.98}$$

are defined via Eq. (2.61).

2.2.5 Two-temperature eigensystem

With the thermodynamics properties derived, it is now possible to derive the eigensystem for the two-temperature model. The complete 2T eigensystem is given in Appendix A.

2.3 Two-Temperature MHD Model

With the presence of electrically charged species, the fluid has the ability to conduct electricity, and in the presence of electromagnetic fields, body forces which act on the fluid will be created and energy will be exchanged within the fluid. In order to take these effects into account, the bi-temperature fluid transport equations Eqs. (2.1) and (2.56) and must be coupled with Maxwell's equations,

$$\nabla \cdot \vec{E} = \frac{\rho_e}{\epsilon_\circ} \tag{2.99}$$

$$\nabla \cdot \vec{B} = 0 \tag{2.100}$$

$$\nabla \times \vec{E} = \frac{\partial \vec{B}}{\partial t} \tag{2.101}$$

$$\nabla \times \vec{B} = \mu_\circ \vec{J} + \mu_\circ \epsilon_\circ \frac{\partial \vec{E}}{\partial t} \tag{2.102}$$

The resulting two-temperature MHD equations can be expressed in the following vector form ([65],[15]),

$$Q = \begin{pmatrix} \rho_1 \\ \vdots \\ \rho_n \\ \rho u \\ \rho v \\ \rho w \\ B_x \\ B_y \\ B_z \\ E \\ \rho \hat{s}_e \end{pmatrix}, \quad V = \begin{pmatrix} \rho_1 \\ \vdots \\ \rho_n \\ u \\ v \\ w \\ B_x \\ B_y \\ B_z \\ p \\ p_e \end{pmatrix}, \quad F_n = \begin{pmatrix} \rho_1 v_n \\ \vdots \\ \rho_n v_n \\ \rho u v_n + n_x p_\circ - B_x B_n/\mu_\circ \\ \rho v v_n + n_y p_\circ - B_y B_n/\mu_\circ \\ \rho w v_n + n_z p_\circ - B_z B_n/\mu_\circ \\ v_n B_x - u B_n \\ v_n B_y - v B_n \\ v_n B_z - w B_n \\ v_n (E + p_\circ) - B_n (\vec{v} \cdot \vec{B})/\mu_\circ \\ v_n S_e \end{pmatrix} \tag{2.103}$$

where $p_\circ$ is the sum of the thermal and magnetic pressures,

$$p_\circ = p + \frac{\vec{B} \cdot \vec{B}}{2\mu_\circ}, \tag{2.104}$$

and the total energy is given by

$$E = \sum_{s \neq e} \rho_s \varepsilon_s + \rho_e \varepsilon_e + \frac{\vec{m} \cdot \vec{m}}{2\rho} + \frac{\vec{B} \cdot \vec{B}}{2\mu_\circ}. \tag{2.105}$$

2.4 Eigensystem

As done for the two-temperature hydrodynamic equations, the 2T MHD eigensystem is presented in Appendix A.

CHAPTER 3

NUMERICAL FORMULATION

With the governing equations detailed in the previous chapter, attention is here turned to developing a suitable numerical formulation. In particular, the discretization approach resulting from a finite-volume (FV) formulation is described. Focus will then be extended to the hyperbolic convection terms and the shock-capturing method will be detailed. Solution techniques for the diffusion terms and chemical kinetics will be described in Chapters 7 and 9, respectively.

3.1 Finite-volume formulation

While their derivation was carried out in divergence form, the governing equation are here cast into integral form to ensure a conservative discretization. From Reynold's transport theorem,

$$\int_{V(t_2)} Q dV - \int_{V(t_1)} Q dV + \int_{t_1}^{t_2} \oint_{S(t)} \hat{n} \cdot \bar{\bar{F}} dS dt = \int_{t_1}^{t_2} \int_{V(t)} \dot{\Omega} dV dt, \tag{3.1}$$

the integral form of the governing equations is obtained. Defining

$$F_n \equiv \hat{n} \cdot \bar{\bar{F}} = n_x F_x + n_y F_y + n_z F_z \tag{3.2}$$

as the flux normal to the surface described by the unit vector, $\hat{n}$, and assuming that all variables are continuous in time, Eq. 3.1 reduces to

$$\frac{d}{dt} \int_V Q dV + \oint_S F_n dS = \int_V \dot{\Omega} dV. \tag{3.3}$$

Introducing the volume-average quantities,

$$\bar{Q} \equiv \frac{1}{V}\int_V Q dV, \quad \dot{\bar{\Omega}} \equiv \frac{1}{V}\int_V \dot{\Omega} dV, \tag{3.4}$$

further simplification can be made, yielding

$$\frac{dQ}{dt} + \frac{1}{V}\oint_S F_n dS = \dot{\Omega}, \tag{3.5}$$

in which the bars have been dropped with the implication that all quantities are volume averages. Equation (3.5) serves as the basis for finite-volume (FV) schemes adopted in this work.

Before proceeding, Eq. (3.5) is *operator split* such that the contribution of the source terms to the change in the conserved quantities will be treated independently of the contribution of the convective terms. The splitting results in two equations,

$$\left.\frac{dQ}{dt}\right|_{\text{conv}} = -\frac{1}{V}\oint_S F_n dS \quad \text{and} \quad \left.\frac{dQ}{dt}\right|_{\text{src}} = \dot{\Omega}, \tag{3.6}$$

the combination of which yields the total change in Q,

$$\frac{dQ}{dt} = \left.\frac{dQ}{dt}\right|_{\text{conv}} + \left.\frac{dQ}{dt}\right|_{\text{src}}. \tag{3.7}$$

3.2 Semi-discete approach

Although a number of techniques exist to discretize Eq. (3.5), the one adopted here is a term-by-term treatment, in which the spatial operator is discretized first followed by the temporal derivative. Known as the semi-discrete approach, it is straight-forward, allowing flexibility. We begin by discretizing the spatial domain into N-sided polyhedra[1] which we refer to here as cells, such that the surface integral can be replaced by the summation,

$$\oint_S F_n dS \rightarrow \sum_{s=1}^{N} F_s A_s \tag{3.8}$$

where F_s is the flux normal to surface s and A_s is the area of surface s. This results in a coupled system of ODE's of the form

[1] Polyhedra in 3D, polygons in 2D, etc.

$$\frac{dQ}{dt} = -\frac{1}{V}\sum_s F_s A_s \tag{3.9}$$

for all cells in the domain. The flux function F_s at the surface between two cells, L and R, may be approximated via a numerical flux function,

$$\hat{F}_s = \frac{1}{2}(F_L + F_R) - \Phi, \tag{3.10}$$

which is a combination of a nondissipative centered approximation and a numerical diffusion function, Φ. The numerical flux function can be tailored depending on the form of Φ. In particular, an *upwind* bias may be introduced by letting Φ take the form

$$\Phi = \frac{1}{2}|A_s|(Q_R - Q_L) \tag{3.11}$$

with the flux Jacobian as defined through the diagonalization

$$|A_s| \equiv R|\Lambda|L \tag{3.12}$$

as detailed in Chapter 2. The exact form of $|A_s|$ follows from the necessary condition for pure upwinding,

$$F_s = \begin{cases} F_L & \text{if } |\Lambda| = \Lambda \\ F_R & \text{if } |\Lambda| = -\Lambda \end{cases}, \tag{3.13}$$

which can be achieved only in the case that A_s from Eq. (3.11) satisfies

$$F_R - F_L = A_s(Q_R - Q_L), \tag{3.14}$$

the solution of which yields the Roe-average states [96]. Such a linearization of the flux Jacobian also satisfies the Rankine-Hugoniot jump conditions and is able to capture stationary discontinuities exactly. Note that the Roe-average values are obtainable for the bi-temperature gasdynamic equations in the case that all species can be described by a calorically-ideal EOS. The bi-temperature MHD equations are further restricted to polytropic species with an adiabatic exponent of 2 [17], which consequently represents a phys-

ically meaningless state. However, approximations are available and can have a negligible effect as determined through numerical experiments.

As with all numerical flux functions, the upwind approximation does have its share of shortcomings, requiring special attention under certain flow conditions. Although details are not provided here, stabilizing techniques similar to the approaches found in [25], [92], and [47] have been implemented in this work.

3.3 Time-Marching

Once the spatial fluxes have been evaluated, the conserved quantities can be integrated in time via an appropriate time-marching method. While implicit integration techniques will be applied to the various source terms (c.f. Chapters 7 and 9), integration of the convective terms has been limited to explicit methods. Several such time-marching methods have been implemented and tested, including multi-step and predictor-corrector schemes. Introducing the operator $L(Q) = -1/V \sum_s F_s A_s$, Eq. (3.1) can be expressed as

$$\frac{dQ}{dt} = L(Q). \tag{3.15}$$

Integration from discrete time levels n to $n+1$,

$$\int_{t_n}^{t_{n+1}} (dQ = L(Q)dt), \tag{3.16}$$

can be approximated in a number of ways, several of which are provided as follows.

Explicit Euler

The explicit Euler scheme given by

$$Q^{n+1} = Q^n + \Delta t L(Q^n) \tag{3.17}$$

is perhaps the simplest integration techniques, resulting in global first-order accuracy.

Adams-Bashforth

The second-order Adams-Bashforth (AB2) scheme is given by

$$Q^{n+1} = Q^n - \frac{1}{2}\Delta t L(3Q^n - Q^{n-1}) \tag{3.18}$$

can provide better stability than the Euler explicit method, especially in convection-dominated problems. The AB2 scheme requires the storage of the solution at two distinct time levels, n and $n+1$. One possible implementation approach is to store Q^n explicitly, while Q^{n-1} is stored implicitly in the linear combination, $3Q^n - Q^{n-1}$. This can present advantages over storing as the fluxes must be evaluated for $3Q^n - Q^{n-1}$ as opposed to Q^{n-1}.

Runge-Kutta

Runge-Kutta schemes are of the predictor-corrector type which require multiple evaluations of the operator L per time step. This may be undesirable in a parallel implementation as each evaluation of L requires communication between blocks in order to update information at the boundaries. The second-order variant (RK2), also known as modified Euler, is given below.

$$\tilde{Q}^{n+1} = Q^n + \Delta t L(Q^n), \tag{3.19a}$$

$$Q^{n+1} = Q^n + \frac{1}{2}\Delta t L(Q^n + \tilde{Q}^{n+1}). \tag{3.19b}$$

$$\tag{3.19c}$$

CHAPTER 4

RECONSTRUCTION

Accurate solution of the transport equations is necessary in order to reproduce such complex wave structures such as those seen in the argon shock tube results as discussed in Chapter 1. In particular, the ionization begins with a small but significant number of priming electrons just after the compression shock. The convection of these priming electrons and excited species farther upstream of the shock is determined by the evaluation of the flux F in Eq. (2.1). A low-order evaluation of the flux may lead to excessive diffusion of these species, resulting in a delay in the electron avalanche, thereby altering the induction length. Therefore it is desirable to have an advection scheme which introduces as minimal amount of diffusion as possible, while maintaining a numerically stable and oscillation-free solution.

The approach taken here begins with the finite-volume method described in the previous chapter and proceeds via the steps outlined in Figure 4.1. In the standard finite-volume approach, the conservative variables are stored as averaged values over each computational cell. These values are then used to *reconstruct* higher-order representations based on polynomial, logarithmic, and other such approximations. The reconstruction determines the overall accuracy of the scheme and therefore is a key element of the numerical transport process. The principle function of the reconstruction scheme is to obtain accurate values at the interfaces between cells. These values, combined with an appropriate Riemann solver, are used to evolve the variables in characteristic phase-space, giving a flux quantity at each cell interface. Once the flux values have been determined, the variables are then projected to the new time level via a time-marching scheme.

The purpose of the chapter is to describe the reconstruction scheme to be used in the present research. A one-dimensional formulation is presented first, followed by a two-

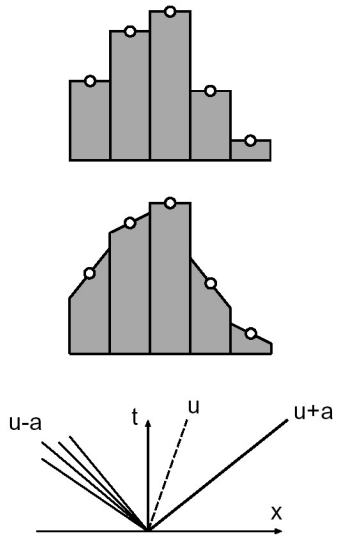

Figure 4.1: Numerical approach: projection, reconstruction, and evolution (taken from [89]).

dimensional extension based on piecewise-quadric surfaces. Formulated from the method of undetermined coefficients, the proposed reconstruction scheme can provide true multi-dimensional reconstruction on arbitrary meshes. Implementation of boundary conditions is briefly considered along with limiters.

4.1 One-dimensional formulation

As applied to a three-point stencil from a 1D finite-volume discretization, the method of undetermined coefficients seeks a fit of the cell average values to a quadratic polynomial which defines the profile of the parabola,

$$u(x) = c_1 + c_2 x + c_3 x^2, \tag{4.1}$$

as determined by the following conditions,

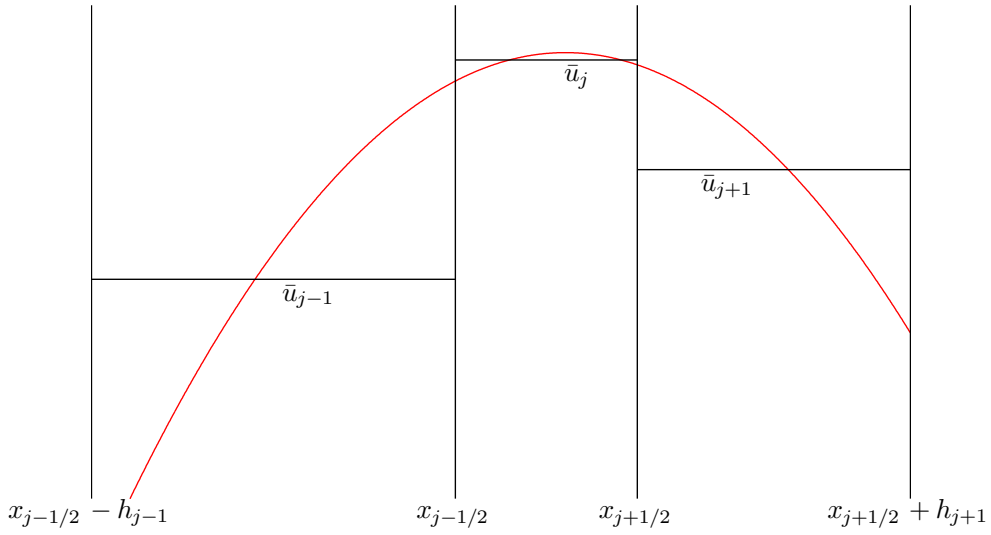

Figure 4.2: One-dimensional parabolic interpolation on a non-uniform mesh.

$$\frac{1}{h_{j+1}} \int_{x_{j+1/2}}^{x_{j+1/2}+h_{j+1}} u(x)\, dx = \bar{u}_{j+1} \tag{4.2a}$$

$$\frac{1}{h_j} \int_{x_{j-1/2}}^{x_{j+1/2}} u(x)\, dx = \bar{u}_j \tag{4.2b}$$

$$\frac{1}{h_{j-1}} \int_{x_{j-1/2}-h_{j-1}}^{x_{j-1/2}} u(x)\, dx = \bar{u}_{j-1}, \tag{4.2c}$$

where h_j is the width of cell j as illustrated in Figure 4.1. Introducing normalization parameters based on the ratio of the left and right cell widths *w.r.t.* that of the center cell,

$$r_{j-1} = \frac{h_{j-1}}{h_j} \qquad r_{j+1} = \frac{h_{j+1}}{h_j},$$

the system can be rewritten as

$$\frac{1}{2r_{j+1}}\int_{1}^{1+2r_{j+1}} u(\xi)\ d\xi = \bar{u}_{j+1} \tag{4.3a}$$

$$\frac{1}{2}\int_{-1}^{1} u(\xi)\ d\xi = \bar{u}_{j} \tag{4.3b}$$

$$\frac{1}{2r_{j-1}}\int_{-1-2r_{j-1}}^{-1} u(\xi)\ d\xi = \bar{u}_{j-1} \tag{4.3c}$$

with corresponding polynomial, $u(\xi) = c_1 + c_2\xi + c_3\xi^2$. This leads to the following linear system which must be solved for each cell I_j.

$$\begin{bmatrix} 1 & -1-r_{j-1} & 1+2r_{j-1}+\frac{4}{3}r_{j-1}^2 \\ 1 & 0 & \frac{1}{3} \\ 1 & 1+r_{j+1} & 1+2r_{j+1}+\frac{4}{3}r_{j+1}^2 \end{bmatrix} \begin{bmatrix} c_1 \\ c_2 \\ c_3 \end{bmatrix} = \begin{bmatrix} \bar{u}_{j-1} \\ \bar{u}_{j} \\ \bar{u}_{j+1} \end{bmatrix} \tag{4.4}$$

The first term on the LHS is the corresponding Vandermonde coefficient matrix, V, which can easily be inverted to obtain

$$V_j^{-1} = \begin{bmatrix} -\frac{1+r_{j+1}}{3|V|} & 1-\frac{2+r_{j-1}+r_{j+1}}{3|V|} & -\frac{1+r_{j-1}}{3|V|} \\ -\frac{2(1+r_{j+1})(1+2r_{j+1})}{3|V|} & -\frac{2(r_{j-1}-r_{j+1})(3+2r_{j-1}+2r_{j+1})}{3|V|} & \frac{2(1+r_{j-1})(1+2r_{j-1})}{3|V|} \\ \frac{1+r_{j+1}}{|V|} & -\frac{2+r_{j-1}+r_{j+1}}{|V|} & \frac{1+r_{j-1}}{|V|} \end{bmatrix} \tag{4.5}$$

with determinant,

$$|V| = \frac{4}{3}(1+r_{j-1})(1+r_{j+1})(1+r_{j-1}+r_{j+1}). \tag{4.6}$$

Obtaining the coefficients of the reconstruction polynomial then becomes a simple matrix-vector multiplication,

$$\begin{bmatrix} c_1 \\ c_2 \\ c_3 \end{bmatrix} = \begin{bmatrix} \\ V_j^{-1} \\ \\ \end{bmatrix} \begin{bmatrix} \bar{u}_{j-1} \\ \bar{u}_{j} \\ \bar{u}_{j+1} \end{bmatrix}. \tag{4.7}$$

An example reconstruction polynomial obtained from Eq. (4.7) is plotted in figure 4.1.

Since constructing the fluxes at the cell interfaces (cf. Eq. (3.10)) is of primary concern,

the value of the interpolated polynomial at the locations $u_{j\pm n/2}$, $n = 1, 2, \ldots$ is desired. In the normalized reference frame, the values of the polynomial at the faces of cell j are defined by

$$u_{L,j} \equiv u_{j-1/2} = u(-1) = c_1 - c_2 + c_3, \tag{4.8}$$

$$u_{R,j} \equiv u_{j+1/2} = u(+1) = c_1 + c_2 + c_3, \tag{4.9}$$

where $u_{L,j}$ is the interpolated value at the left cell interface, resulting from the interpolation based in cell j, while $u_{R,j}$ is the interpolated value at the right cell interface, resulting from the interpolation based in cell j. Vectorization is accomplished via

$$u_j^L = \begin{bmatrix} 1 & 1 & 1 \end{bmatrix} \begin{bmatrix} & V_j^{-1} & \end{bmatrix} \begin{bmatrix} \bar{u}_{j-1} \\ \bar{u}_j \\ \bar{u}_{j+1} \end{bmatrix}, \tag{4.10}$$

$$u_j^R = \begin{bmatrix} 1 & -1 & 1 \end{bmatrix} \begin{bmatrix} & V_j^{-1} & \end{bmatrix} \begin{bmatrix} \bar{u}_{j-1} \\ \bar{u}_j \\ \bar{u}_{j+1} \end{bmatrix}. \tag{4.11}$$

Uniform mesh

In the case of uniform mesh spacing, the Vandermonde matrix reduces to

$$V = \begin{bmatrix} 1 & -2 & \frac{13}{3} \\ 1 & 0 & \frac{1}{3} \\ 1 & 2 & \frac{13}{3} \end{bmatrix}, \quad V^{-1} = \begin{bmatrix} -\frac{1}{24} & \frac{13}{12} & -\frac{1}{24} \\ -\frac{1}{4} & 0 & \frac{1}{4} \\ \frac{1}{8} & -\frac{1}{4} & \frac{1}{8} \end{bmatrix} \tag{4.12}$$

yielding left and right states,

$$u_L = \frac{1}{6}(2\bar{u}_{j-1} + 5\bar{u}_j - \bar{u}_{j+1}), \tag{4.13}$$

$$u_R = \frac{1}{6}(2\bar{u}_{j+1} + 5\bar{u}_j - \bar{u}_{j-1}). \tag{4.14}$$

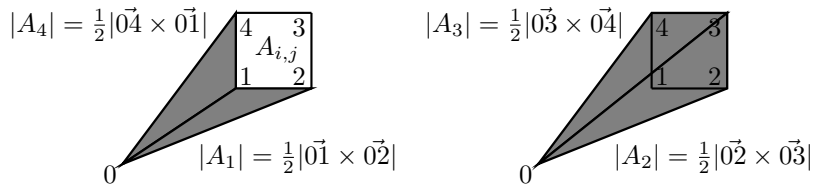

Figure 4.3: General area representation based on arbitrary point. Shaded regions are absolute values of the areas $A_1 \dots A_4$.

This formulation is equivalent to the fourth scheme of van Leer (cf. [115, 54]).

4.2 Two-dimensional formulation

The method of undetermined coefficients is easily generalized to 2D. The second-order polynomial which defines a quadric paraboloid in two dimensions is given by

$$u(x, y) = c_1 + c_2 x + c_3 y + c_4 x^2 + c_5 y^2 + c_6 xy. \tag{4.15}$$

To determine the coefficients, this polynomial is integrated over each cell in the stencil.

$$\frac{1}{A_{i,j}} \int_{I_{i,j}} u(x, y)\ dx\ dy = \bar{u}_{i,j} \tag{4.16}$$

To evaluate the integral, we rely on a coordinate transformation from the physical to the natural domain using isoparametric elements defined by bi-linear shape functions as given in Appendix B. The integral in Eq. (4.16) is transformed to

$$\frac{1}{A_{i,j}} \int_{-1}^{1} \int_{-1}^{1} u(\xi, \eta)|J_{i,j}|\ d\xi\ d\eta = \bar{u}_{i,j} \tag{4.17}$$

with associated polynomial,

$$u(\xi, \eta) = c_1 + c_2 \xi + c_3 \eta + c_4 \xi^2 + c_5 \eta^2 + c_6 \xi\eta. \tag{4.18}$$

Integration of Eq. (4.17) with Eq. 4.18 yields

$$\bar{u}_{i,j} = \sum_{k=1}^{6} c_k v_k, \tag{4.19}$$

where

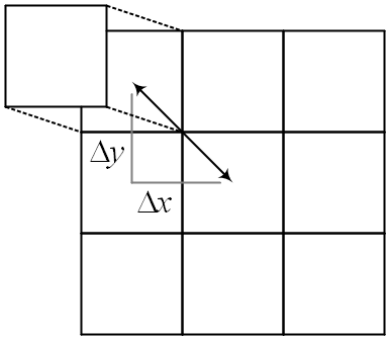

Figure 4.4: Two-dimensional interpolation stencil.

$$v_1 = 1 \tag{4.20a}$$

$$v_2 = \frac{1}{3A_{i,j}} \sum_{n=1}^{4} A_n (x_n + x_{n+1}) \tag{4.20b}$$

$$v_3 = \frac{1}{3A_{i,j}} \sum_{n=1}^{4} A_n (y_n + y_{n+1}) \tag{4.20c}$$

$$v_4 = \frac{1}{12A_{i,j}} \sum_{n=1}^{4} A_n \left[x_n^2 + x_{n+1}^2 + (x_n + x_{n+1})^2 \right] \tag{4.20d}$$

$$v_5 = \frac{1}{12A_{i,j}} \sum_{n=1}^{4} A_n \left[y_n^2 + y_{n+1}^2 + (y_n + y_{n+1})^2 \right] \tag{4.20e}$$

$$v_6 = \frac{1}{12A_{i,j}} \sum_{n=1}^{4} A_n \left[x_n y_n + x_{n+1} y_{n+1} + (x_n + x_{n+1})(y_n + y_{n+1}) \right] \tag{4.20f}$$

with $\sum A_n$ being equivalent to the cell area,

$$A_{i,j} = \underbrace{\tfrac{1}{2}(\vec{01} \times \vec{02})}_{A_1} + \underbrace{\tfrac{1}{2}(\vec{02} \times \vec{03})}_{A_2} + \underbrace{\tfrac{1}{2}(\vec{03} \times \vec{04})}_{A_3} + \underbrace{\tfrac{1}{2}(\vec{04} \times \vec{01})}_{A_4} \tag{4.21}$$

A geometric description of A is provided in Figure 4.2 which can be determined from any arbitrary point P_0.

In order to establish a well-defined system, a stencil of six cells is necessary—one cell for each coefficient. However, in order to preserve symmetry on a logically-indexed mesh, a nine cell stencil as illustrated in Figure 4.4 is chosen, resulting in the linear system,

$$\begin{bmatrix} & & & \\ v_{1,i-1,j-1} & v_{2,i-1,j-1} & \cdots & v_{6,i-1,j-1} \\ \vdots & \vdots & & \vdots \\ v_{1,i,j} & v_{2,i,j} & \cdots & v_{6,i,j} \\ \vdots & \vdots & & \vdots \\ v_{1,i+1,j+1} & v_{2,i+1,j+1} & \cdots & v_{6,i+1,j+1} \\ & & & \end{bmatrix} \begin{bmatrix} c_1 \\ c_2 \\ c_3 \\ c_4 \\ c_5 \\ c_6 \end{bmatrix} = \begin{bmatrix} \bar{u}_{i-1,j-1} \\ \bar{u}_{i,j-1} \\ \bar{u}_{i+1,j-1} \\ \bar{u}_{i-1,j} \\ \bar{u}_{i,j} \\ \bar{u}_{i+1,j} \\ \bar{u}_{i-1,j+1} \\ \bar{u}_{i,j+1} \\ \bar{u}_{i+1,j+1} \end{bmatrix}. \tag{4.22}$$

The above system is over-determined, which can be solved using a least-squares formulation,

$$V\vec{c} = \vec{u} \tag{4.23}$$

$$V^T DV\vec{c} = V^T D\vec{u} \tag{4.24}$$

$$\vec{c} = (V^T DV)^{-1} V^T D\vec{u} \tag{4.25}$$

where, D is a diagonal matrix of weights to apply to each cell in the stencil. The elements of D have been chosen such that the diagonal cells of the stencil are given minimal weight, while maintaining a well-conditioned system. Once the coefficients have been determined, the quadric surface results from Eq. 4.18. A generic example is provided in Figure 4.5.

4.2.1 Flux Calculation

Once the quadric surface has been determined, evaluation of the interface values becomes a simple line integral of the parabolic function resulting from the intersection of the quadric surface with the cell interface. Since the parabolas are determined using second-order polynomials, the integrals can be evaluated exactly using three-point Gaussian quadratures.

4.3 Limiters

When applied to highly nonlinear wave phenomena such as shocks, the interpolation scheme will inherently develop oscillations leading to catastrophic failure of the reconstruction. To

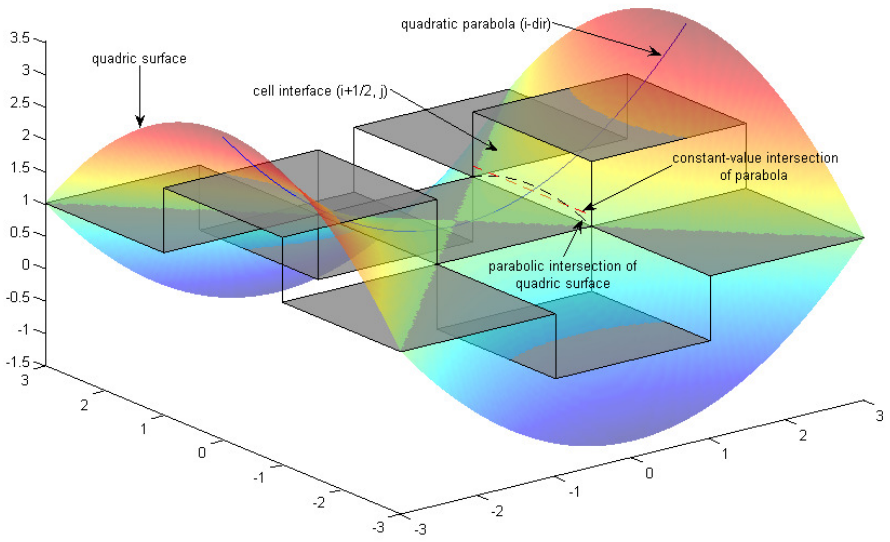

Figure 4.5: Two-dimensional quadric surface interpolation on a uniform mesh.

remedy this, the monotonicity-preserving (MP) limiters of Suresh and Huynh [107] have been implemented in the reconstruction. MP limiters enforce monotonicity in the reconstruction scheme by modifying interpolated point values at cell interfaces. As applied to the 1D interpolation on a uniform mesh, the reconstructed value u_L in Eq. (4.13) is modified according to

$$u_L \leftarrow \text{median}(u_L,\ \bar{u}_j,\ u^{\text{MP}}) \tag{4.26}$$

with $u^{\text{MP}} = \bar{u}_j + \text{minmod}[\bar{u}_{j+1} - \bar{u}_j,\ \alpha(\bar{u}_j - \bar{u}_{j-1})]$. The MP limiter has been implemented in the current work with $\alpha = 2$.

CHAPTER 5

NUMERICAL STABILITY

The reconstruction procedure detailed in the previous chapter is just one component of the semi-discrete approach. In order to complete the numerical convection scheme, the reconstruction must be combined with an appropriate time-marching method. The suitability of the integration scheme is dependent upon the spatial discretization, making it necessary to analyze the numerical scheme as a whole. In general it must determined if the given scheme is consistent with the physical model and under what conditions it is stable—only then can convergence be ensured.

In particular, the stability analysis performed here will be based on discretization of the model linear advection equation,

$$\frac{\partial u}{\partial t} + a\frac{\partial u}{\partial x} + a\frac{\partial u}{\partial y} = 0, \tag{5.1}$$

with a constant advection speed $a > 0$. Consistent with the semi-discrete approach, the spatial derivatives of Eq. (5.1) will first be discretized,

$$\frac{d\vec{u}}{dt} = L\vec{u}, \tag{5.2}$$

requiring a vectorization of the reconstruction scheme. It is important to note that when combined with the monotonicity-preserving limiters discussed in Chapter 4 Section 4.3, the reconstruction scheme cannot be linearized. However, the base interpolation scheme will be considered independently of the limiters, resulting in two coupled sets of ODE's that will be analyzed separately. The ODE's will then be discretized in time yielding the desired set of OΔE's,

$$\vec{u}^{n+1} = S\vec{u}^{n}. \tag{5.3}$$

to advance the solution from time level n to $n+1$. The conditions for stability of Eq. 5.3 as based on the Lax-Richtmyer theorem require the eigenvalue of maximum magnitude of S be bounded by the unit circle,

$$\sigma_{\max} \leq 1. \tag{5.4}$$

In what follows, the form of L will be determined along with its eigenvalues, λ. Making use of the so-called $\lambda - \sigma$ relation [68], the eigenvalues of S will be derived without the explicit form of S. To facilitate analysis, all discretizations are performed on equispaced Cartesian grids with periodic boundary conditions.

5.1 Finite-difference approximation

A finite-difference (FD) approximation to the spatial derivatives of Eq. (5.1) can be made based on the reconstruction procedure of the previous chapter. In particular, an upwind approximation results from differencing the interpolated cell interface values given by Eq. 4.13,

$$\left(\frac{\partial u}{\partial x}\right)_j = u_{R,j} - u_{R,j-1} + O(\Delta x^?) \tag{5.5}$$

$$= \frac{1}{6\Delta x}[2\bar{u}_{j+1} + 5\bar{u}_j - \bar{u}_{j-1} - (2\bar{u}_j + 5\bar{u}_{j-1} - \bar{u}_{j-2})] + O(\Delta x^?) \tag{5.6}$$

$$= \frac{1}{6\Delta x}(2\bar{u}_{j+1} + 3\bar{u}_j - 6\bar{u}_{j-1} + \bar{u}_{j-2}) + O(\Delta x^?). \tag{5.7}$$

The truncated term in Eq. 5.7 can be found from Fourier error analysis by comparing the exact derivative of $u = e^{i\kappa x}$,

$$\frac{\partial e^{i\kappa x}}{\partial x} = i\kappa e^{i\kappa x}, \tag{5.8}$$

with the approximate derivate of discrete function $u_j = e^{i\kappa j\Delta x}$,

$$(\delta_x e^{i\kappa j\Delta x})_j = \frac{2e^{i\kappa\Delta x(j+1)} + 3e^{i\kappa\Delta x(j)} - 6e^{i\kappa\Delta x(j-1)} + e^{i\kappa\Delta x(j-2)}}{6\Delta x} \tag{5.9}$$

$$= \frac{(e^{-i\kappa 2\Delta x} - 6e^{-i\kappa\Delta x} + 3 + 2e^{i\kappa\Delta x})e^{i\kappa j\Delta x}}{6\Delta x}. \tag{5.10}$$

where κ is the modified wave number. Comparing the right-hand sides of Eqs. 5.8 and 5.10 yields a modified wave number,

$$\kappa^* = \frac{3 + \cos 2\kappa\Delta x - 4\cos\kappa\Delta x + i(8\sin\kappa\Delta x - \sin 2\kappa\Delta x)}{6i\Delta x}, \tag{5.11}$$

that approximates the exact wave number to third order accuracy as revealed by the series expansion of Eq. 5.11,

$$\kappa^* = \kappa + \frac{\kappa^4\Delta x^3}{12i} + \ldots, \tag{5.12}$$

confirming third-order accuracy of Eq. (5.7). As such, the scheme including monotonicity-preserving limiters shall be referred to as MP3.

The modified wave number along with the modified phase speed, $a^*/a = \kappa^*/\kappa$, are plotted in Figure 5.1. The third-order scheme requires approximately 19 points per wavelength (PPW) to maintain an error in phase speed of less than 0.1% or 10 PPW for an error of less than 1%.

5.2 1D stability

Spatial discretization of the model equation using Eq. (5.7) on an uniform 1D mesh with M cells results in the spatial discretization operator,

$$L = \frac{a}{\Delta x}\frac{1}{6}\begin{bmatrix} -3 & -2 & & & -1 & 6 \\ 6 & -3 & -2 & & & -1 \\ -1 & 6 & -3 & -2 & & \\ & \ddots & \ddots & \ddots & \ddots & \\ & & -1 & 6 & -3 & -2 \\ -2 & & & -1 & 6 & -3 \end{bmatrix} \tag{5.13}$$

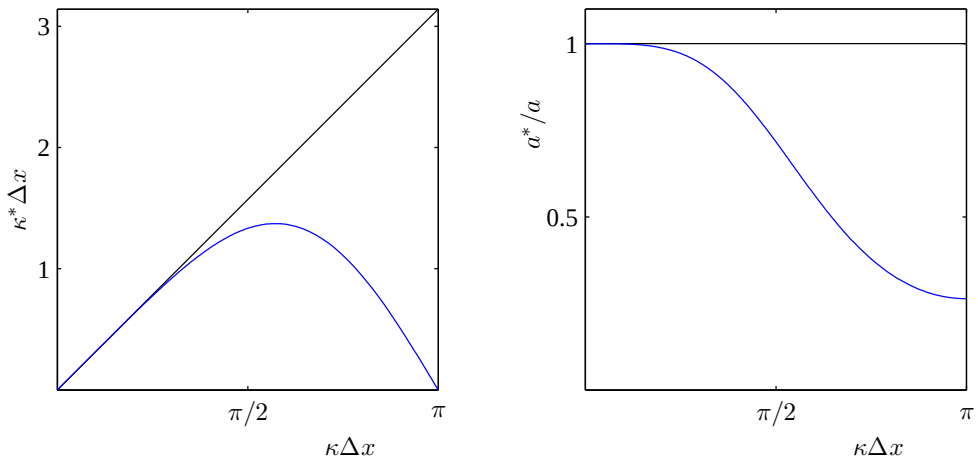

Figure 5.1: Modified wave number and phase error for 3$^{\text{rd}}$-order backward difference operator.

which may conveniently be expressed in banded matrix notation as

$$L = \frac{a}{\Delta x}\frac{1}{6}B_p(M:-1,6,-3,-2,0), \tag{5.14}$$

in which B_p denotes a periodic banded or circulant matrix. Because it is circulant, the eigenvalues of L can be found from a 1D discrete Fourier transform (DFT),

$$\lambda_j = \sum_{m=0}^{M-1} e^{-2\pi ijm/M} L_{1j}, \quad j = 0, 1, \ldots, M-1. \tag{5.15}$$

The linear operator resulting from the MP limiter is also considered here and is given by

$$L = \frac{a}{\Delta x}\frac{1}{6}\begin{bmatrix} -3 & & & & -2 & 5 \\ 5 & -3 & & & & -2 \\ -2 & 5 & -3 & & & \\ & \ddots & \ddots & \ddots & \ddots & \\ & & -2 & 5 & -3 & \\ & & & -2 & 5 & -3 \end{bmatrix} \tag{5.16}$$

Though not detailed here, its derivation is similar to that of the third-order FD approximation.

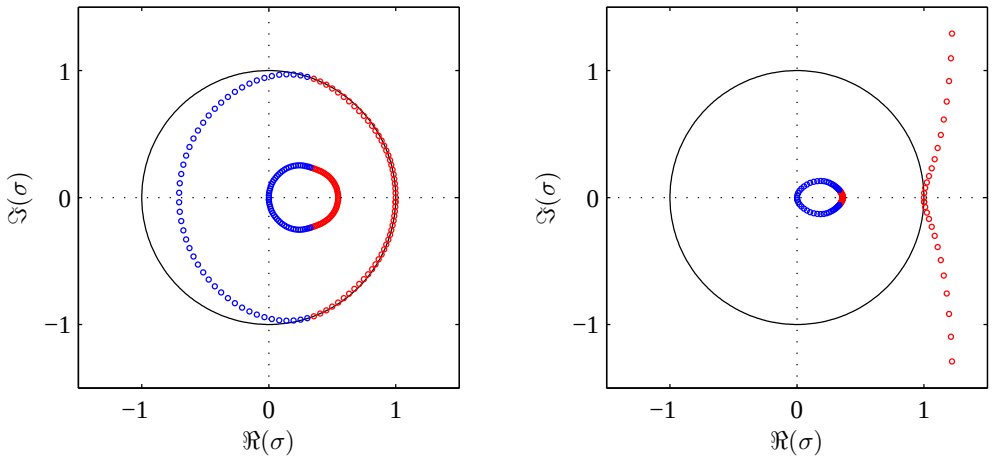

Figure 5.2: Stability plot for the 1D MP3-AB2 scheme with CFL= 0.58. The 3^{rd}-order interpolation is stable (*left*), while the limiter is not (*right*).

2^{nd}-order Adams-Bashforth

Once the eigenvalues of L have been computed, the eigenvalues of S follow from the $\lambda - \sigma$ relation, which are given by

$$\sigma^2 - \left(1 + \frac{3}{2}\lambda\Delta x\right)\sigma + \frac{1}{2}\lambda\Delta x = 0. \tag{5.17}$$

for the 2^{nd}-order Adams-Bashforth (AB2) scheme [68]. As a multi-step scheme, AB2 gives rise to two σ-eigenvalues for each λ-eigenvalue.

The eigenvalues for the 1D AB2-MP3 scheme have been plotted for a CFL number of 0.58 in Figure 5.2 and for a CFL number of 0.1 in Figure 5.3. The base interpolation scheme is clearly stable for CFL= 0.58 as all of the eigenvalues lie within the unit circle in the complex plane. The MP limiter function, on the other hand, is not stable at this CFL number. Even as the CFL number is decreased to 0.1, the limiter function is still unstable, with eigenvalues from the principle σ-root lying outside the unit circle.

2^{nd}-order Runge-Kutta

The second-order Runge-Kutta (RK2) scheme is a two-step, predictor-corrector scheme which has one principal σ root given by

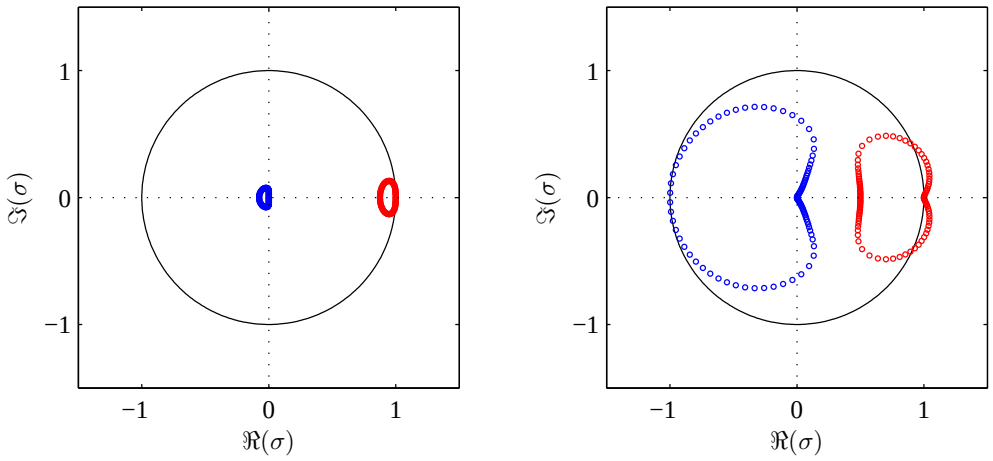

Figure 5.3: Stability plot for the MP3-AB2 scheme with CFL= 0.1. Despite the small value of the CFL number, the limiter (*right*) remains unstable, although mildly so. It is interesting to note that the spurious root is stable while the principal root is not. The 3^{rd}-order interpolation is given on the left.

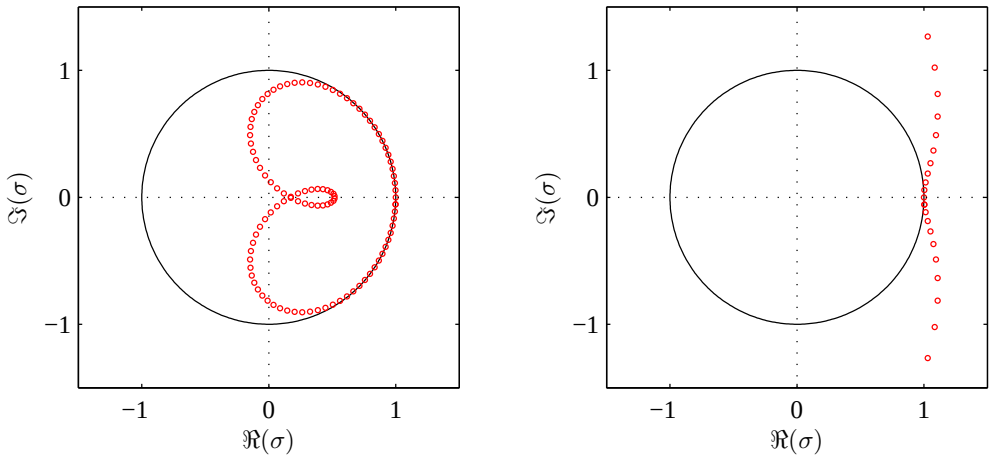

Figure 5.4: Stability plot for the 1D RK2-AB2 scheme with CFL= 0.1. The 3^{rd}-order interpolation is stable (*left*), while the limiter is not (*right*).

$$\sigma - 1 - \lambda\Delta x - \frac{1}{2}\lambda^2\Delta x^2 = 0. \tag{5.18}$$

From Figures 5.4 and 5.5, the base interpolation scheme is stable for CFL= 0.9. As with the AB2 scheme, the MP limiter function is not stable, even as the CFL number is decreased to 0.1.

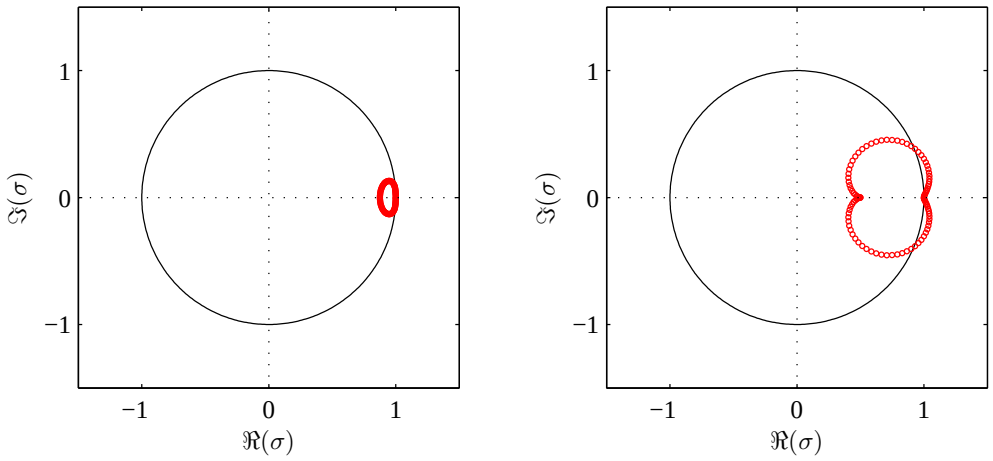

Figure 5.5: Stability plot of the 3[rd]-order interpolation scheme with RK2 for CFL= 0.1. Despite the small value of the CFL number, the limiter (*right*) remains unstable, although mildly so. The 3^{rd}-order interpolation is given on the left.

5.3 2D stability

As applied to an $M \times M$ mesh with $\Delta x = \Delta y$ and periodic boundary conditions, vectorization of the 2D reconstruction scheme results in a $M^2 \times M^2$ block circulant matrix with circulant blocks (BCCB),

$$C = \begin{pmatrix} C_0 & C_1 & & & C_{M-2} & C_{M-1} \\ C_{M-1} & C_0 & C_1 & & & C_{M-2} \\ C_{M-2} & C_{M-1} & C_0 & C_1 & & \\ & \ddots & \ddots & \ddots & \ddots & \\ & & C_{M-2} & C_{M-1} & C_0 & C_1 \\ C_1 & & & C_{M-2} & C_{M-1} & C_0 \end{pmatrix}, \tag{5.19}$$

where $C_{M-2} = -\frac{1}{6} I_M$, $C_{M-1} = I_M$, $C_1 = -\frac{1}{3} I_M$, and

$$C_0 = \frac{1}{6} B_p(M : -1, 6, -6, -2, 0), \tag{5.20}$$

for the third-order FD approximation (I_M indicates a $M \times M$ identity matrix). Diagonalization of a BCCB is given by ([32])

$$C = (\mathbb{F}_M \otimes \mathbb{F}_M)^{-1} \Lambda (\mathbb{F}_M \otimes \mathbb{F}_M) \tag{5.21}$$

where Λ is the diagonal matrix of eigenvalues of C and $\mathbb{F}_M$ is the $M \times M$ discrete Fourier transform (DFT) matrix,

$$\mathbb{F}_M = \begin{bmatrix} 1 & 1 & \cdots & 1 \\ 1 & w^1 & \cdots & w^{M-1} \\ 1 & w^2 & \cdots & w^{2(M-1)} \\ \vdots & \vdots & & \vdots \\ 1 & w^{M-1} & \cdots & w^{(M-1)(M-1)} \end{bmatrix} \tag{5.22}$$

where $w = e^{-2\pi i/M}$. The eigenvalues of C can be found from the 2D DFT,

$$\sigma_{jk} = \sum_{n=0}^{M-1} \sum_{m=0}^{M-1} e^{-2\pi i j n/M} e^{-2\pi i k m/M} g_{nm}, \quad n, m = 0, 1, \ldots, M-1 \tag{5.23}$$

where g_{nm} are the elements of matrix G, of which the n^{th} row corresponds to the first row of the n^{th} circulant matrix C_n in Eq. 5.19,

$$G = \begin{pmatrix} C_{0,11} & C_{0,12} & \cdots & C_{0,1M} \\ C_{1,11} & C_{1,12} & \cdots & C_{1,1M} \\ 0 & 0 & \cdots & 0 \\ \vdots & \vdots & & \vdots \\ 0 & 0 & \cdots & 0 \\ C_{M-2,11} & C_{M-2,12} & \cdots & C_{M-2,1M} \\ C_{M-1,11} & C_{M-1,12} & \cdots & C_{M-1,1M} \end{pmatrix} \tag{5.24}$$

The matrix operator for the limiter function can be found in a similar manner.

2^{nd}-order Adams-Bashforth

The results for the 2D AB2-MP3 scheme plotted in Figures 5.6 and 5.7 indicate that stability decreases by a factor of two for all cases as compared with the 1D scheme.

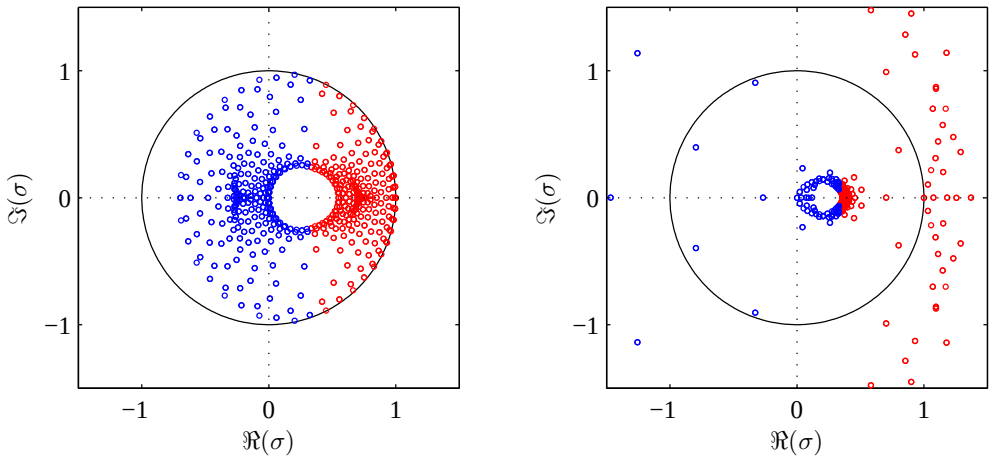

Figure 5.6: Stability plot for the 2D AB2-MP3 scheme with CFL= 0.29. The 3^{rd}-order interpolation is stable (*left*), while the limiter is not (*right*).

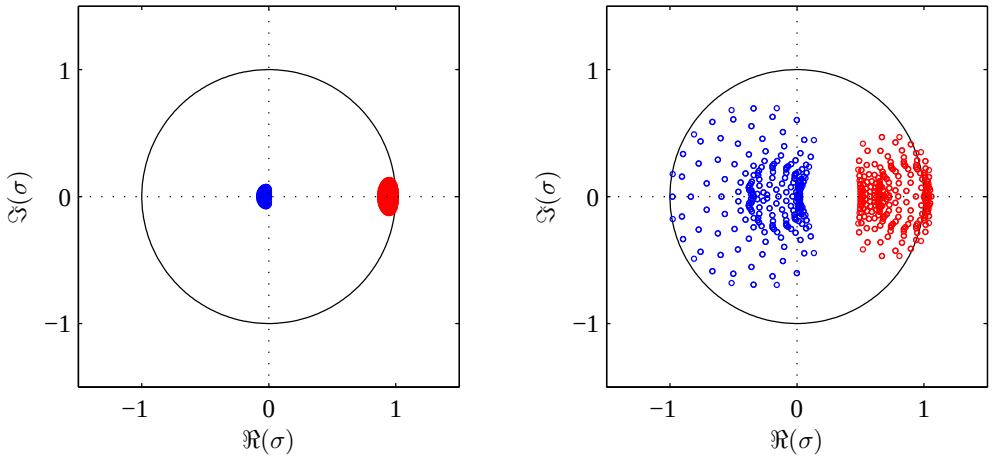

Figure 5.7: Stability plot for the 2D AB2-MP3 scheme with CFL= 0.05. The limiter (*right*) remains unstable at this CFL number. The 3^{rd}-order interpolation is given on the left.

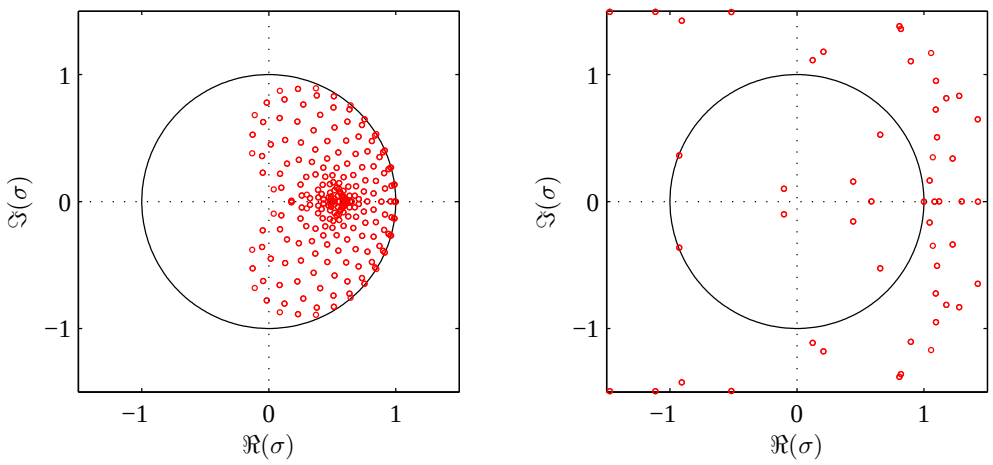

Figure 5.8: Stability plot for the 2D RK2-MP3 scheme with CFL= 0.45.

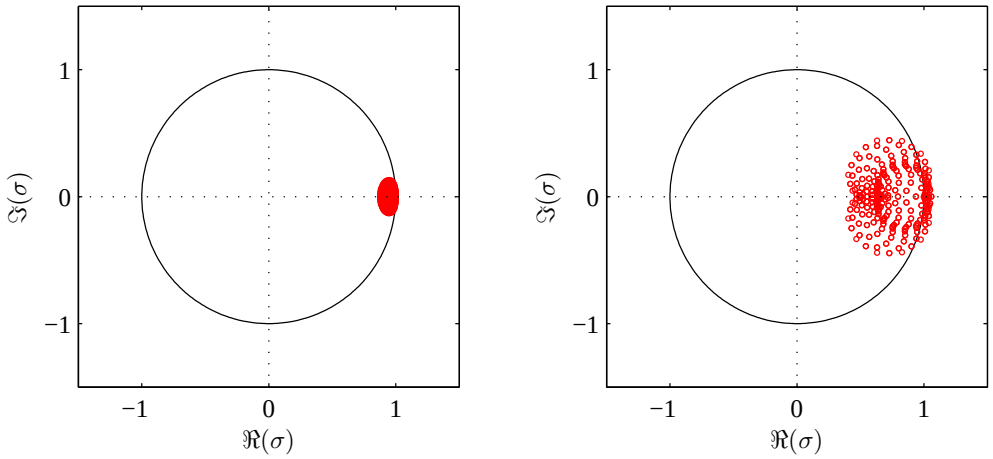

Figure 5.9: Stability plot for the 2D RK2-MP3 scheme with CFL= 0.05. The limiter (*right*) remains unstable at this CFL number. The 3^{rd}-order interpolation is given on the left.

2^{nd}-order Runge-Kutta

The stability plots for the 2D MP3-RK2 scheme are given in Figures 5.8 and 5.9. As for the 2D AB2-MP3 scheme, the 2D RK2-MP3 scheme is stable up to only half the value of the CFL number as found for its 1D counterpart.

While these results demonstrate a clear advantage of the AB2-MP3 scheme over the RK2-MP3 scheme based on the third-order differencing scheme, the results are inconclusive with respect to the MP limiters in regards to their stability. This has warranted numerical

experiments that have indicated the AB2-MP3 scheme to be more efficient when considering multiple factors, including parallelization implementation and communication overhead. As such, the AB2-MP3 scheme has been applied to the convective transport equations in the current research.

CHAPTER 6

BENCHMARKS

Benchmarks are essential in validating the performance of the numerical algorithms as applied to physical processes under known and controlled conditions. Assembled here is a collection of one- and two-dimensional test cases that have been well-documented in the literature. All problems have been solved using upwind Riemann solvers and the 3^{rd}-order scheme detailed in Chapter 4 to increase accuracy. Problems in gasdynamics are presented first followed by two magnetohydrodynamic cases.

6.1 Woodward-Colella blastwave

Blastwaves can generally be described as a strong and sudden release of energy, resulting in regions characterized by extreme temperatures and pressures. The severity of the conditions is further compounded when two blastwaves interact. The reconstruction scheme must deal with pressure and temperature jumps of several orders of magnitude while preserving monotonicity and preserving critical features. In particular, when the shock fronts of the blastwaves interact, the resulting contact discontinuity is difficult to resolve. The initial conditions for the left, middle, and right states are given by,

$$\begin{pmatrix} \rho_L \\ u_L \\ p_L \end{pmatrix} = \begin{pmatrix} 1 \\ 0 \\ 10^3 \end{pmatrix}, \quad \begin{pmatrix} \rho_M \\ u_M \\ p_M \end{pmatrix} = \begin{pmatrix} 1 \\ 0 \\ 10^{-2} \end{pmatrix}, \quad \begin{pmatrix} \rho_R \\ u_R \\ p_R \end{pmatrix} = \begin{pmatrix} 1 \\ 0 \\ 10^2 \end{pmatrix} \tag{6.1}$$

for a polytropic gas with an adiabatic exponent of 7/5. As can be seen in Figure 6.1, the middle contact is well resolved by the scheme with the use of a slope-steepening technique

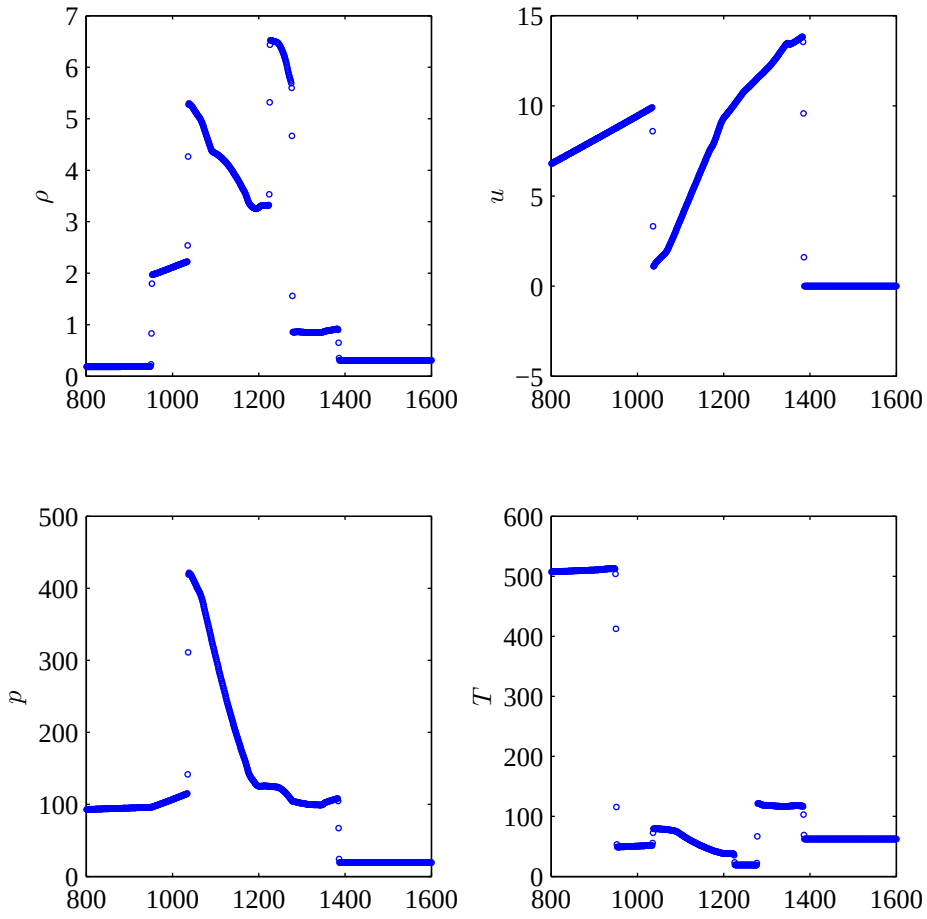

Figure 6.1: Numerical solution of Woodward-Colella blastwave problem as computed with 1600 cells.

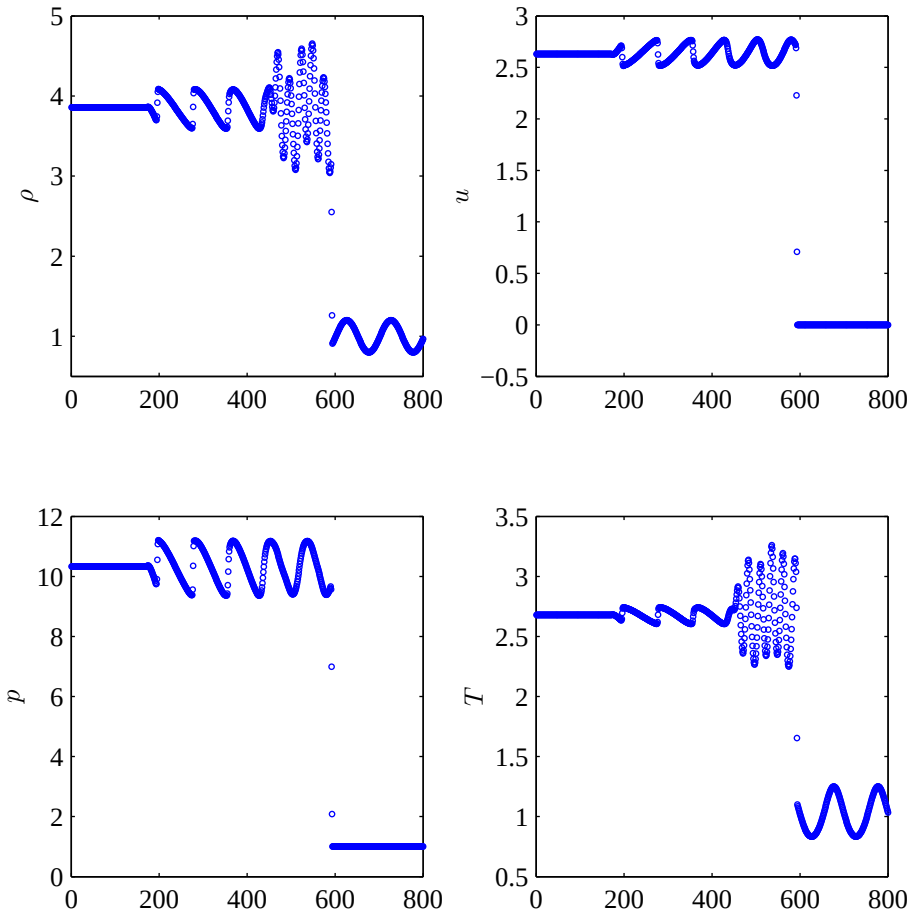

Figure 6.2: Numerical solution of the Shu-Osher problem as computed with 800 cells.

similar to that of [25] and [54].

6.2 Shu-Osher shock-entropy wave interaction

The ability of a numerical scheme to resolve smooth flow disturbances is also of concern. This becomes especially critical in boundary layers and other highly turbulent regions where entropy waves are prevalent. The Shu-Osher problem [104] has extensively been used to simulate a shock passing through an entropy disturbance which can be thought of as a one-dimensional analog to the shock-vortex interaction problem. The initial conditions for the

left and right states are given by,

$$\begin{pmatrix} \rho_L \\ u_L \\ p_L \end{pmatrix} = \begin{pmatrix} 3.857143 \\ 2.629369 \\ 10.33333 \end{pmatrix}, \quad \begin{pmatrix} \rho_R \\ u_R \\ p_R \end{pmatrix} = \begin{pmatrix} 1 + 0.2\sin(5x - 25) \\ 0 \\ 1 \end{pmatrix} \tag{6.2}$$

for a polytropic gas with an adiabatic exponent of 7/5. As can be seen in Figure 6.2, the entropy waves are well-defined after compression by the shock.

6.3 Emery wind tunnel

Another case popularized by Colella and Woodward [25], this problem has been simulated extensively in the literature to test various solvers' ability to properly capture the flow around the 90° corner of a forward-facing step. The resultant sonic rarefaction fan emanating from this corner flow may be strong enough to produce negative densities if a positivity-preserving scheme is not utilized. The standard Harten-type entropy fix [100] is sufficient to ensure positivity as well as avoid sonic rarefactions. An key feature of this problem is the Kelvin-Helholtz (KH) instabilities which originate at the triple point of the Mach stem. While the KH structures themselves are physical in nature, it is how they are initiated that is an artifact of the numerical solver. The inability of Riemann solvers to capture slow-moving shocks exactly creates oscillations which serve as a forcing function that acts as artificial turbulence. These features are purely numerical in nature and result from the inability of Riemann solvers to capture slow-moving shocks exactly. Despite artificial dissipation as prescribed in [25], the oscillations and subsequent vortices persist.

The initial conditions are everywhere identical, with a Mach 3 flow described by a polytropic gas with an adiabatic exponent of 7/5 traversing from the left inlet to the sonic outflow boundary at the opposite end. Results are presented in Figures 6.3–6.6 in the form of infinite-fringe interferograms and were obtained using a total of 252 computational domains, each consisting of 75×75 cells for which $\Delta x = \Delta y$.

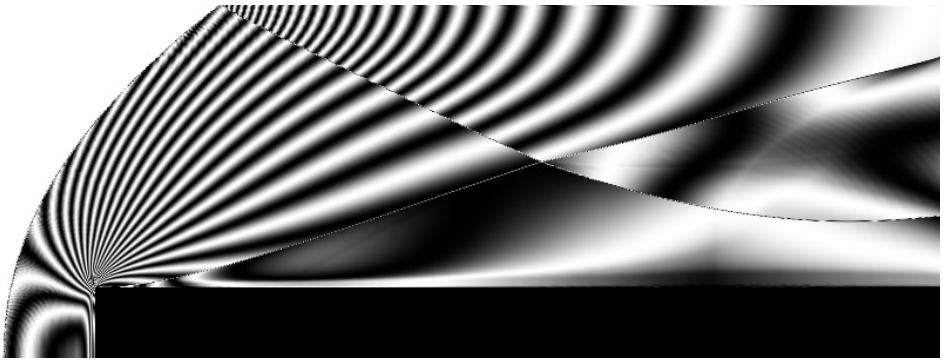

Figure 6.3: Emery solution at $t = 1$.

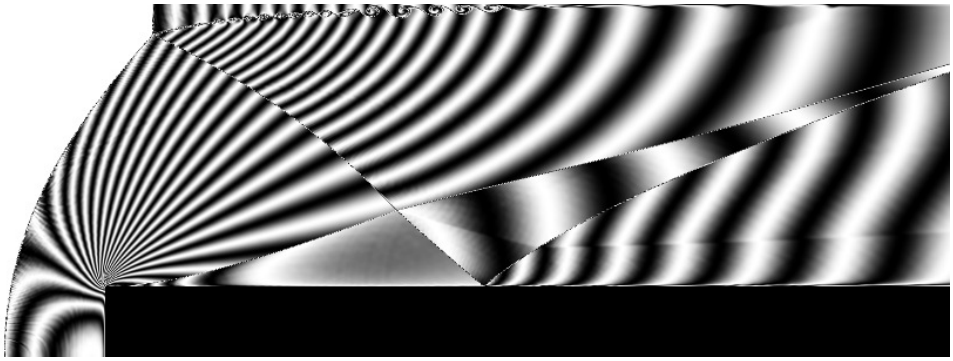

Figure 6.4: Emery solution at $t = 2$.

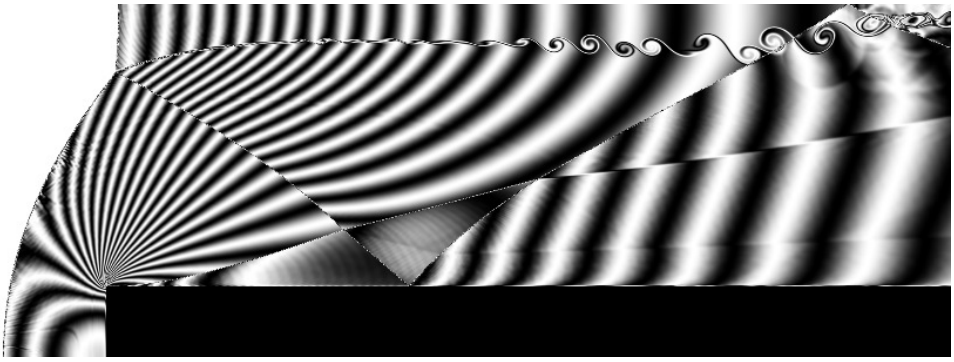

Figure 6.5: Emery solution at $t = 3$.

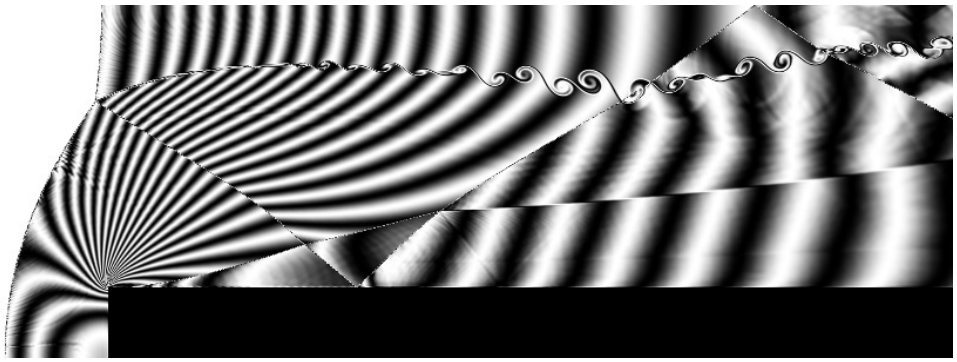

Figure 6.6: Emery solution at $t = 4$.

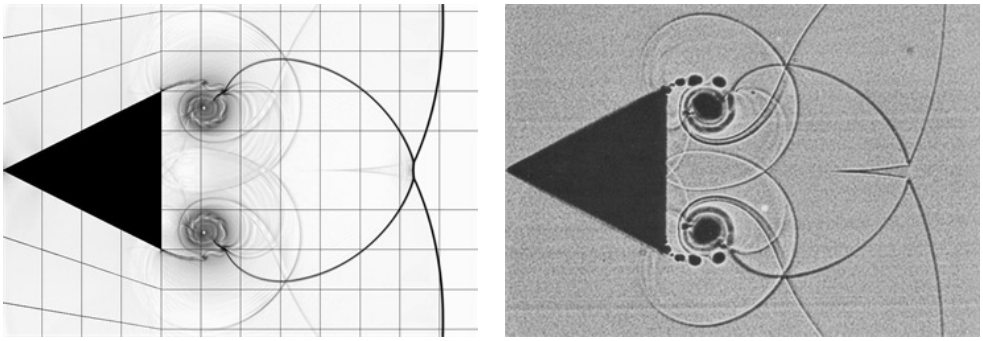

Figure 6.7: Simulated Schlieren (*left*) of Schardin's problem as compared with experiment (*right*) from [36].

6.4 Schardin's problem

Schardin's problem involves air flow past a symmetric wedge at Mach 1.3. This problem has been simulated using a polytropic gas with an adiabatic exponent of 7/5 on a mesh with $400k$ cells that included half of the wedge. The numerical Schlieren in Figure 6.7 shows excellent agreement with the experimental results.

6.5 Shock diffraction down a step

Shock diffraction down a 90° step has been a popular problem for comparing numerical and experimental results. This particular problem chosen here is due to Bazhenova [10], involving a Mach 5.09 shock. The numerical results presented in Figure 6.8 have been computed assuming an adiabatic exponent of 7/5. The numerical results are able to reproduce all of the experimental flow features accurately. Soultions were obtained on a 1.2M cell mesh with

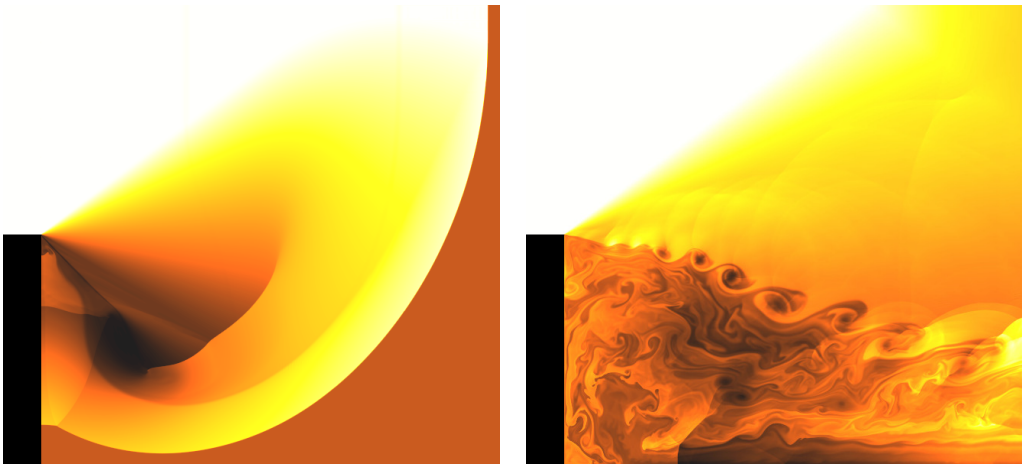

Figure 6.8: Density plot of a Mach 5.09 shock diffracting down a 90° step. Results (*left*) compare favorably with experimental results [10] and previous numerical simulations [92]. The right frame shows the intricate flow field at a much later time. Colormap: ρ_{min} ρ_{max}

$\Delta x = \Delta y$.

6.6 Rayleigh-Taylor instability

Rayleigh-Taylor instability can occur at the interface of two fluids of differing densities if the heavier fluid is accelerated into the lighter one. The instabilities are initiated here at a contact surface, across which the fluid pressure is constant but mass density is discontinuous. The initial conditions are given by

$$\begin{pmatrix} \rho_L \\ u_L \\ v_L \\ p_L \end{pmatrix} = \begin{pmatrix} 2 \\ 0 \\ -0.025\cos(8\pi x) \\ 2y+1 \end{pmatrix}, \quad \begin{pmatrix} \rho_U \\ u_U \\ v_U \\ p_U \end{pmatrix} = \begin{pmatrix} 1 \\ 0 \\ -0.025a\cos(8\pi x) \\ y+3/2 \end{pmatrix} \tag{6.3}$$

on the domain $0 \le x \le 1/4$, $0 \le y \le 1$ where the subscripts U and L denote the upper and lower fluids respectively. The numerical setup here is slightly different from similar RT simulations presented in the literature (see [122]), in that the left and right boundaries here are periodic, while the top and bottom boundaries are reflecting. The results in Figure 6.6 show many fine-scale structures emanating from the contact surface. As the flow develops,

and mixing increases, Kelvin-Helmholtz instabilities are also apparent as shear layers develop. While the flow is undoubtedly unstable, it is unclear to what extent, if any, these structures are numerical in origin. It has been stated that higher complexity of the fine-scale structures is an indication of less diffusive solvers [122], but the work of [98] may suggest other influences, including numerical effects (e.g. grid effects).

6.7 Brio-Wu MHD shocktube

The Brio-Wu shock tube problem [17] is a magnetohyrdodynamic extension of Sod's gas-dynamic problem. Magnetic fields both normal and tangential to the flow generate several MHD wave structures, including fast and slow magnetosonic shocks and rarefactions as well as a compound wave. This problem demonstrates the true complexity of the fact that the waves cannot all be described as strictly being either linearly degenerate or genuinely nonlinear. From Figure 6.10 it can be seen that the solver has problems capturing the compound wave structure as well as the tail of the slow rarefaction wave, typical of compressive limiters. Also noteworthy is the ability of the slope-steepening to capture the contact in 2 cells.

6.8 Orszag-Tang MHD vortex

When considering MHD problems in more than one spatial dimension, enforcement of $\nabla \cdot \vec{B}$ is no longer automatic and may require special attention. The Orszag-Tang MHD vortex is one example of a problem which has been used to test a solvers ability to satisfy the divergence-free condition. The solution is obtained on the domain $0 \leq x \leq 1$, $0 \leq y \leq 1$ with the density and pressure initially equal everywhere with values $25/36\pi$ and $5/12\pi$, and the velocity and magnetic fields described by $[-\sin(2\pi y), \sin(2\pi y)]$ and $[-\sin(2\pi y), \sin(4\pi x)]$, respectively. The magnetic fields specified by the inital conditions are able to twist the fluid into a vortical structure via the Lorentz force. The boundary conditions are periodic. Critical to this problem is enforcement of the $\nabla \cdot \vec{B}$ condition as required by the MHD equations. While there are several well-known methods for implementing this condition, including Hodge projection ([14]), constrained transport ([38]), and the 8-wave formulation ([87],[86]), the solution presented in Figure 6.11 was obtained without using any of these methods. In this particular test case, the standard Roe FDS approximate Riemann solver

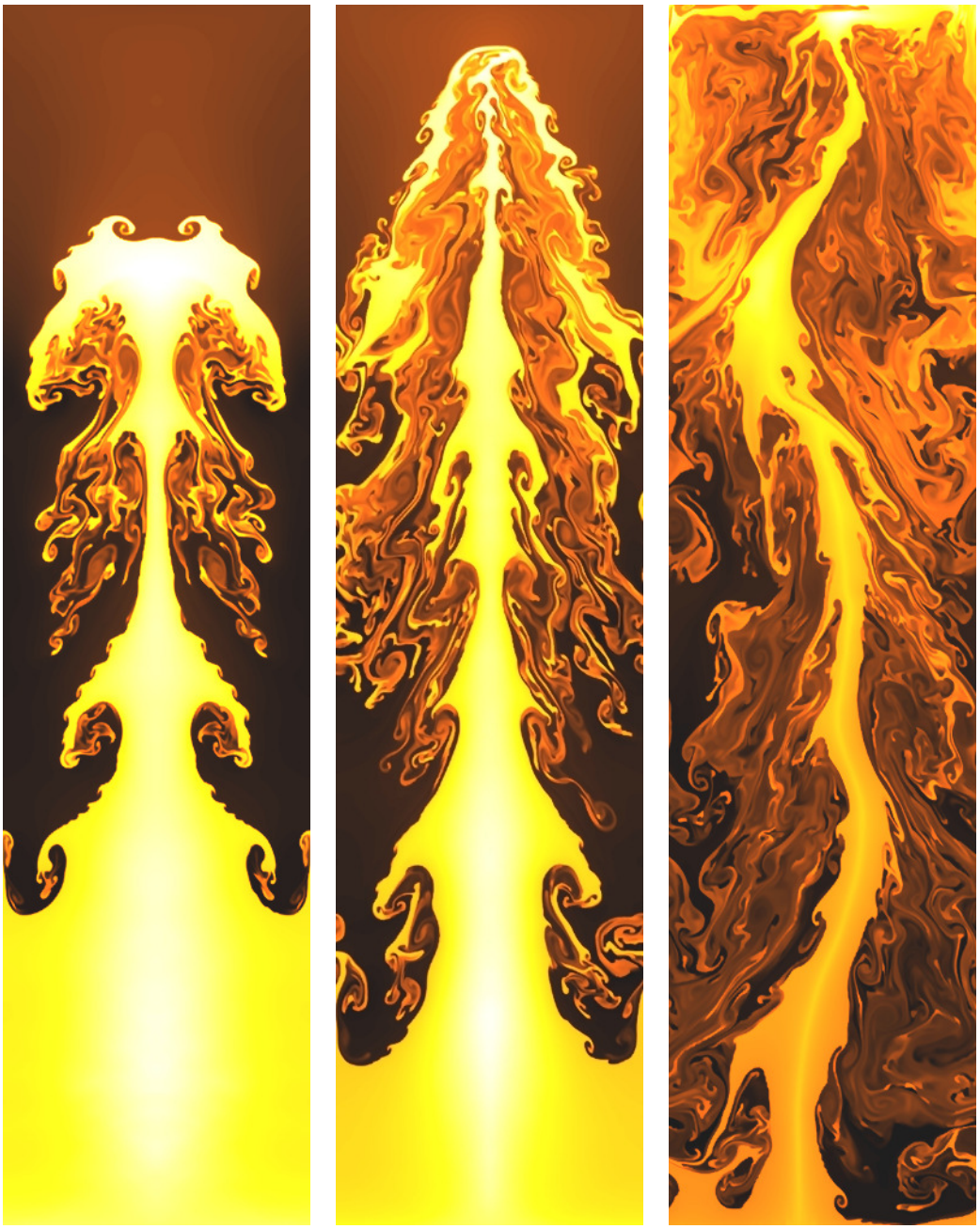

Figure 6.9: Rayleigh-Taylor instability at three different times as computed on a 400×1600 cell mesh with $\Delta x = \Delta y$. In the third frame, portions of the contact surface have reflected from the upper boundary. Colormap: ρ_{min} ρ_{max}

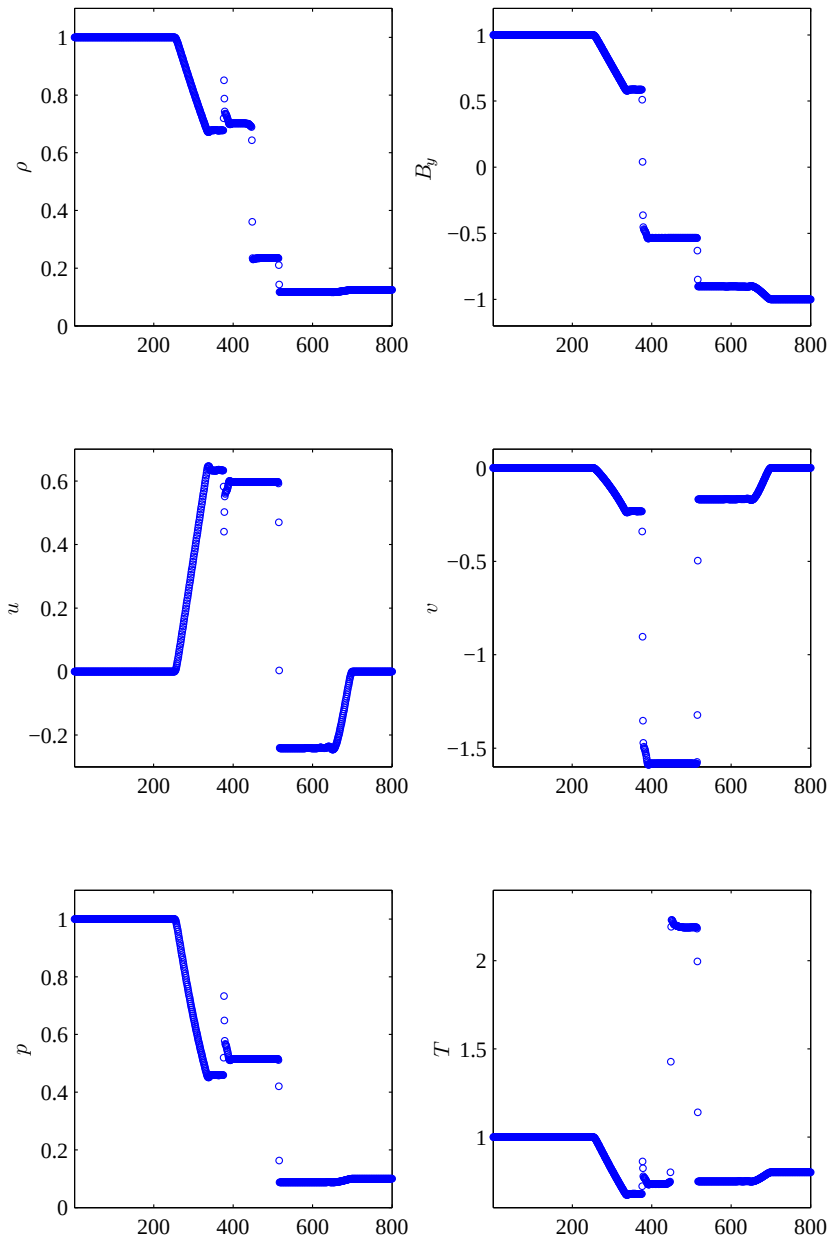

Figure 6.10: Numerical results for Brio-Wu MHD shocktube as computed with 800 cells.

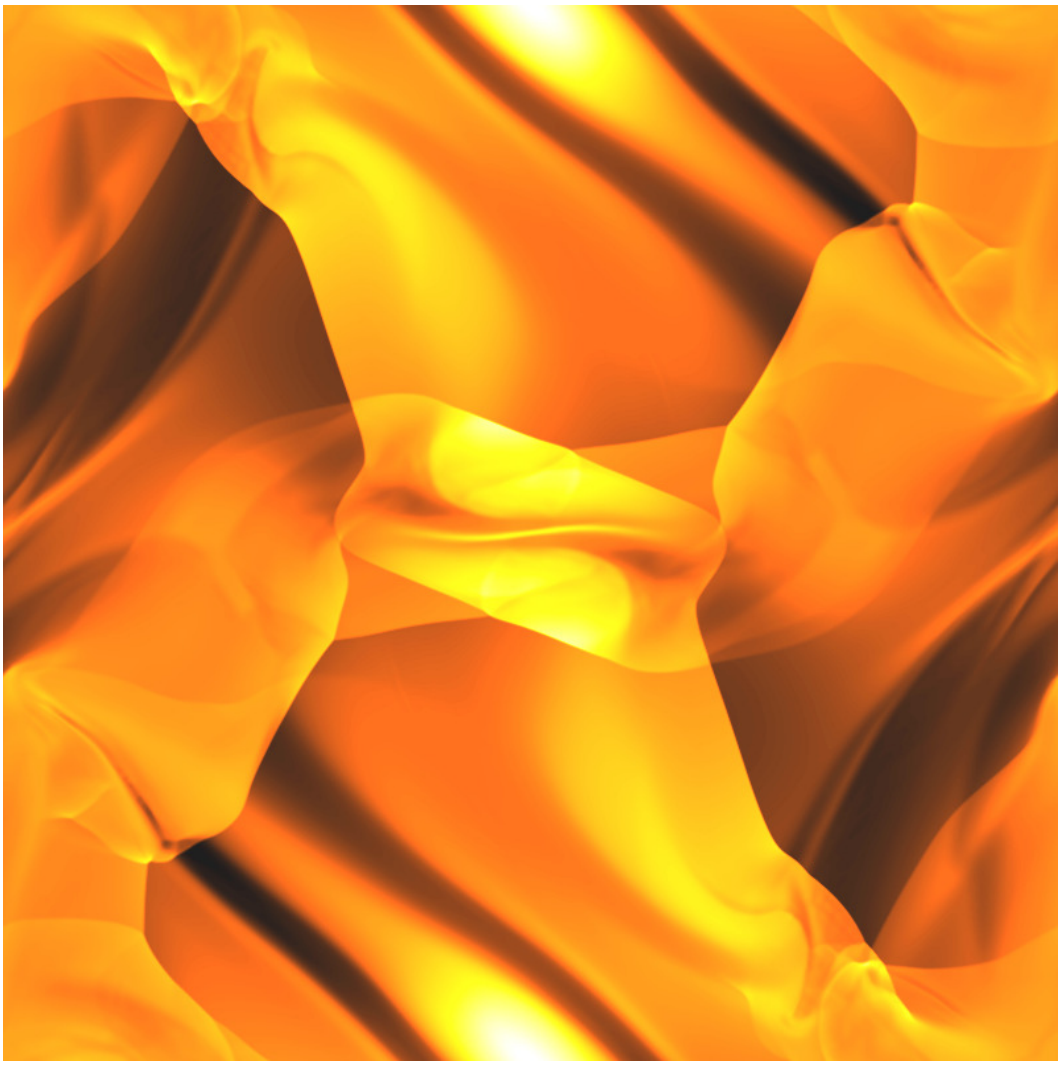

Figure 6.11: Orszag-Tang MHD vortex as computed on an 800×800 cell mesh with $\Delta x = \Delta y$. Colormap: ρ_{min} ρ_{max}

has been replaced with the highly diffusive HLLE [37] Riemann solver. It is well known that errors in the divergence of the magnetic flux density can be artificially diffused away [69]. The HLLE solver provides a significant amount of diffusion, effectively stabilizing the solution.

CHAPTER 7

DIFFUSION PROCESSES

It has been shown to be a natural conclusion to separate the physical models based on their mathematical classification as being hyperbolic, parabolic, etc. The individual processes resulting from this decomposition are then solved independently of each other using the operator splitting technique. In this chapter, attention is shifted from the convective terms of the governing equations to the source terms. In particular, diffusion processes are parabolic in nature and are considered here. In particular, an implicit solver for electron heat conduction is detailed.

7.1 Governing equations

Relative to the convective speeds studied in this work, thermal diffusion of the heavy particles is negligible. The diffusion speed of electrons on the other hand may be significant as a result of their large thermal velocity. As such, all diffusion processes involving electrons must be considered. This includes thermal diffusion, the governing equations of which may be expressed as a finite-volume discretization,

$$\frac{\partial E}{\partial t} = \frac{1}{V} \sum_{s} F_{n_s} A_s \tag{7.1}$$

with the flux F_{n_s} normal to cell interface s given by

$$F_{n_s} = \kappa_s \frac{\partial T}{\partial \hat{n}_s} \tag{7.2}$$

with κ_s being the scalar thermal conductivity taken at s. The difference is approximated using the states immediately to the left and right of s,

$$\frac{\partial T}{\partial \hat{n}_s} \approx \frac{(T_R - T_L)}{\Delta n} \tag{7.3}$$

while the thermal conductivity at s is taken as a simple arithmetic average,

$$\kappa_s \approx \frac{1}{2}(\kappa_L + \kappa_R). \tag{7.4}$$

In the following sections, the one- and two-dimensional form of the governing equations are derived, assuming the conductivity to be a function of temperature. The exact form of the thermal conductivity for an electron fluid will be given in Section 7.4.

7.2 One-dimensional case

The one-dimensional heat equation will be described here in detail. To facilitate analysis, the heat equation is recast into differential form, yielding

$$\frac{\partial E}{\partial t} = \frac{\partial}{\partial x}\left(\kappa_s \frac{\partial T}{\partial x}\right) \tag{7.5}$$

and upon application of the chain rule to the LHS, an expression for the time rate of change of the temperature is obtained,

$$\frac{\partial E}{\partial T}\frac{\partial T}{\partial t} = \frac{\partial}{\partial x}\left(\kappa_s \frac{\partial T}{\partial x}\right) \tag{7.6}$$

Assuming a one-dimensional discretization on a uniformly-spaced mesh, the spatial derivatives can be approximated by finite-differences, thereby reducing the PDE to a system of ODE's,

$$\frac{dT_i}{dt} = \frac{(E_T)_i^{-1}}{\Delta x}\left[\kappa_{i+1/2}\frac{(T_{i+1} - T_i)}{\Delta x} + \kappa_{i-1/2}\frac{(T_i - T_{i-1})}{\Delta x}\right] \tag{7.7}$$

for $i = 1, 2, \cdots, M$ where

$$E_T = \text{diag}\left(\ldots, \frac{dE_i}{dT_i}, \ldots\right) \tag{7.8}$$

For an ideal gas, the definition of the specific heat yields $dE_i/dT_i = \rho_i c_{v,i}$. Rearranging,

$$\frac{dT_i}{dt} = \frac{(E_T)_i^{-1}}{\Delta x^2}\left[\kappa_{i-1/2}T_{i-1} - (\kappa_{i-1/2} + \kappa_{i+1/2})T_i + \kappa_{i+1/2}T_{i+1}\right] \tag{7.9}$$

the system of equations can be written in matrix notation as

$$\frac{\partial \vec{T}}{\partial t} = \Phi \vec{T} \tag{7.10}$$

where Φ is a tridagonal matrix and $\vec{T}$ is the spatial vector of temperatures,

$$\Phi = \frac{E_T^{-1}}{\Delta x^2}\begin{bmatrix} \ddots & \ddots & & \ddots & \\ & \kappa_{i-1/2} & -(\kappa_{i-1/2} & & \kappa_{i+1/2} \\ & & +\kappa_{i+1/2}) & & \\ & \ddots & & \ddots & \ddots \end{bmatrix}, \quad \vec{T} = \begin{bmatrix} \vdots \\ T_{i-1} \\ T_i \\ T_{i+1} \\ \vdots \end{bmatrix} \tag{7.11}$$

The above discretization has resulted in a reduction of the original PDE into a system of ODE's. The choice for discretization in time, however, is still open to consideration. Since electron diffusion is such a rapid process, the above system is stiff in comparison with the bulk convection. This implies that an implicit time marching scheme can be advantageous. Evaluating the RHS of Eq. (7.10) at time $t + \Delta t$,

$$\frac{\Delta \vec{T}}{\Delta t} = \Phi^{n+1}\vec{T}^{n+1} \tag{7.12}$$

a temporal discretization is obtained, where $T^n = T(t)$, $T^{n+1} = T(t + \Delta t)$, and $\Phi^{n+1} = \Phi(\vec{T}^{n+1})$. As usual, Δ is the forward difference operator. Linearization of the RHS is obtained through a Taylor series expansion, yielding

$$\frac{\Delta \vec{T}}{\Delta t} = \Phi \vec{T} + \frac{\partial(\Phi \vec{T})_i}{\partial T_j}\Delta \vec{T} \tag{7.13}$$

in which the superscripts have been dropped with the implication that all terms are evaluated at time n. Isolating the energy difference,

$$\Delta\vec{T} = (I - \Delta t J)^{-1} \Delta t \Phi \vec{T} \tag{7.14}$$

the final expression is obtained which is used to compute the change in energy. The Jacobian, $J = \partial(\Phi\vec{T})_i/\partial T_j$ is a tridiagonal matrix,

$$J = \begin{bmatrix} & & & & \\ \ddots & \ddots & \ddots & & \\ & a_i & b_i & c_i & \\ & & \ddots & \ddots & \ddots \\ & & & & \end{bmatrix} \tag{7.15}$$

with elements

$$a_i = \frac{E_T^{-1}}{\Delta x^2}\left[\frac{\partial \kappa_{i-1/2}}{\partial T_{i-1}}(T_{i-1} - T_i) - \kappa_{i-1/2}\right] \tag{7.16}$$

$$\begin{aligned} b_i = \frac{E_T^{-1}}{\Delta x^2}\Bigg[&\frac{\partial \kappa_{i-1/2}}{\partial T_{i-1}}(T_{i-1} - T_i) - \kappa_{i-1/2} \\ &+ \frac{\partial \kappa_{i+1/2}}{\partial T_i}(T_{i+1} - T_i) - \kappa_{i+1/2}\Bigg] \end{aligned} \tag{7.17}$$

$$c_i = \frac{E_T^{-1}}{\Delta x^2}\left[\frac{\partial \kappa_{i+1/2}}{\partial T_{i+1}}(T_{i+1} - T_i) - \kappa_{i+1/2}\right] \tag{7.18}$$

Note that the Jacobian can also be expressed in terms of Φ and Q only,

$$J = \Phi + \frac{\partial \Phi}{\partial Q} Q \tag{7.19}$$

Defining $\Psi \equiv (\partial\Phi/\partial Q)Q$, the Jacobian can compactly be expressed as

$$J = \Phi + \Psi \tag{7.20}$$

with the explicit form of Ψ easily found by subtracting Φ from J,

$$\Psi = \frac{E_T^{-1}}{\Delta x^2}\begin{bmatrix} \ddots & \ddots & \ddots \\ \frac{\partial \kappa_{i-1/2}}{\partial T_{i-1}}(T_{i-1}-T_i) & \left(\frac{\partial \kappa_{i-1/2}}{\partial T_i}(T_{i-1}-T_i)\right. & \frac{\partial \kappa_{i+1/2}}{\partial T_{i+1}}(T_{i+1}-T_i) \\ & \left. + \frac{\partial \kappa_{i+1/2}}{\partial T_i}(T_{i+1}-T_i)\right) & \\ \ddots & \ddots & \ddots \end{bmatrix} \tag{7.21}$$

This splitting of the Jacobian is key to developing a condition for stability as derived in the following section.

7.3 Stability

The practical reason for using an implicit method is for its added stability over explicit methods, thereby allowing the solution to be advanced by larger time steps per iteration. Since the thermal diffusion equation is nonlinear, however, stability is not unconditional. Linearization has precluded the solution from being advanced to regions beyond which such an approximation is valid. As such, a criterion for an optimal time step must be determined as to maximize solver efficiency while avoiding oscillations or even catastrophic instability.

The solution of Eq. (7.14) at time $t + \Delta t$ is given by

$$\vec{T}^{n+1} = (I - \Delta t J)^{-1}[I - \Delta t J + \Delta t \Phi]\vec{T}^n \tag{7.22}$$

or equivalently

$$\vec{T}^{n+1} = (I - \Delta t(\Phi + \Psi))^{-1}[I - \Delta t \Psi]\vec{T}^n \tag{7.23}$$

after application of Eq. (7.19). Introducing $\Theta \equiv (I - \Delta t(\Phi + \Psi))^{-1}[I - \Delta t \Psi]$ such that

$$\vec{T}^{n+1} = \Theta \vec{T}^n, \tag{7.24}$$

it is evident that stability of the above system can only be guaranteed if the eigenvalues of Θ,

$$\lambda_i^{\Theta} = \frac{1 - \Delta t \lambda_i^{\Phi}}{1 - \Delta t(\lambda_i^{\Phi} + \lambda_i^{\Psi})} \tag{7.25}$$

satisfy the condition

$$|\lambda_i^{\Theta}| \leq 1, \forall i \tag{7.26}$$

The strict evaluation of this criterion requires the eigenvalues of Φ and Ψ be determined from recursion formulas, adding severe complexity to the analysis. This is avoidable, however, as a reasonable estimate can readily be found by assuming that the function $\kappa_i, \forall i$ in Φ as well as the function $\partial \kappa_{i+1/2}/\partial T_i (T_{i+1/2} - T_{i+1/2}), \forall i$ in Ψ can be replaced by *representative*[1] constant parameters ϕ and ψ, such that

$$\Phi \to \phi \frac{E_T^{-1}}{\Delta x^2} B(M:1,-2,1), \quad \Psi \to \psi \frac{E_T^{-1}}{\Delta x^2} B(M:1,-2,1). \tag{7.27}$$

The eigenvalues of Eq. (7.25) can then be approximated as

$$\lambda_i^{\Phi} \approx -4\phi \frac{E_T^{-1}}{\Delta x^2} \left[\sin^2 \left(\frac{i\pi}{2(M+1)} \right) \right], \quad \lambda_i^{\Psi} \approx -4\psi \frac{E_T^{-1}}{\Delta x^2} \left[\sin^2 \left(\frac{i\pi}{2(M+1)} \right) \right] \tag{7.28}$$

where $B(M:1,-2,1)$ is banded matrix notation for a tridiagonal matrix with the main diagonal composed of 2's while the entries of both the subdiagonal and superdiagonal are 1. Note that ϕ is necessarily positive while ψ is not. Returning to the stability condition,

$$-1 \geq \frac{1 - \Delta t \lambda_i^{\Psi}}{1 - \Delta t(\lambda_i^{\Phi} + \lambda_i^{\Psi})} \leq 1 \tag{7.29}$$

it is now evident that for $\lambda_i^{\Phi} > 0$,

$$-1 \geq \frac{1 - \Delta t |\lambda_i^{\Psi}|}{1 - \Delta t |\lambda_i^{\Psi}| + \Delta t |\lambda_i^{\Phi}|} \leq 1 \tag{7.30}$$

the system is unconditionally stable, while for $\lambda_i^{\Psi} < 0$,

[1] This approach can be found in [106] for example.

$$-1 \geq \frac{1 + \Delta t|\lambda_i^{\Psi}|}{1 + \Delta t|\lambda_i^{\Psi}| + \Delta t|\lambda_i^{\Phi}|} \leq 1 \tag{7.31}$$

it is found that

$$\Delta t \leq \frac{2}{2|\lambda_i^{\Psi}| - |\lambda_i^{\Phi}|} \tag{7.32}$$

which holds true *iff* the denominator is positive, i.e. $2|\lambda_i^{\Psi}| > |\lambda_i^{\Phi}|$. In other words, as $|\lambda_i^{\Phi}| \rightarrow 2|\lambda_i^{\Psi}|$, $\Delta t \rightarrow 0$, and as a result, $|\lambda_i^{\Phi}|$ can safely be neglected. Neglecting this eigenvalue greatly simplifies the condition, but the drawback is a more restrictive time step. The condition can be restated as

$$\Delta t \leq \frac{1}{|\lambda_i^{\Psi}|} \tag{7.33}$$

for which Eq. (7.28) can be applied, yielding

$$\Delta t \leq \frac{1}{\left|-4\psi \frac{E_T^{-1}}{\Delta x^2} \sin^2\left(\frac{i\pi}{2(M+1)}\right)\right|}. \tag{7.34}$$

7.4 Thermal conductivity

Constitutive equations for the thermal conductivity are necessary to obtain closure for the diffusion equation. In the case of electron heat transfer, the thermal conductivity for a fully-ionized plasma takes the form

$$\kappa_e \approx 1.44 \times 10^{-10} \frac{T_e^{5/2}}{\ln \Lambda} \ [\mathrm{W/m \cdot K}] \tag{7.35}$$

with the Coulomb logarithm given by

$$\Lambda = 1.24 \times 10^7 \frac{T_e^{3/2}}{n_e^{1/2}}. \tag{7.36}$$

7.5 Benchmarks

In order to validate the thermal diffusion solver, a test problem was created which demonstrates the importance of electron heat conduction in a fully-ionized plasma. The problem

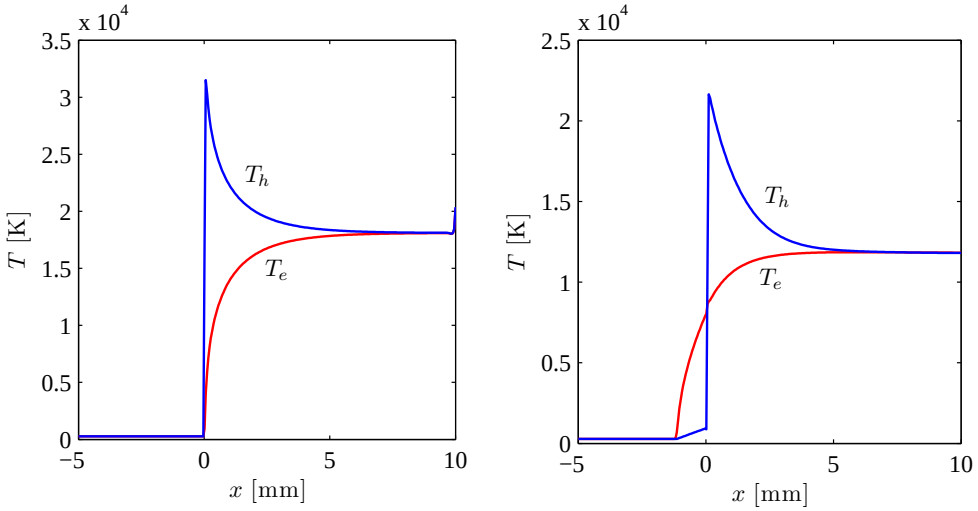

Figure 7.1: Thermal diffusion benchmarks—fully-ionized argon plasma (Ar^+, e^-) without (*left*) and with (*right*) electron heat conduction. The shock is created by reflection of a uniform flow from an adiabatic wall located at $x = 10$ mm

setup consists of a uniform one-dimensional flow field described by

$$\begin{pmatrix} p_\infty \\ u_\infty \\ T_\infty \end{pmatrix} = \begin{pmatrix} 4.13 \text{ Pa} \\ 4700 \text{ m/s} \\ 275 \text{ K} \end{pmatrix} \tag{7.37}$$

composed of e^- and Ar^+ species with equal number densities (fully ionized) impinging upon an adiabatic wall[2]. The shock structure resulting from the reflection of the plasma from the wall is given in Figure 7.5 for cases with and without electron heat conduction. The results show that without conduction, the shock travels at approximately Mach 19 while with conduction, this value decreases to approximately 16. This is a significant difference and demonstrates the amount of thermal energy that is diffused by the electrons across the shock. The pre-shock electron temperature profile reflects the nonlinear dependence ($\kappa \sim T_e^{5/2}$) and is consistent with the analytical solutions presented in [128].

A point of interest is the plasma *overheating* that results when the shock reflects from the wall for the case without heat conduction. This is purely a numerical anomaly and results from a known deficiency of approximate Riemann solvers (cf. [82] and [75]). Although its treatment is not addressed nor implemented here, the electron heat conduction is significant

[2]Coulombic thermalization is also considered and is detailed in Section 9.5.

enough to diffuse away this anomaly and minimize any adverse effects.

Also noteworthy is the discontinuous profile of the electron temperature across the shock. While adiabatic compression of the electrons across the shock may lead to such a jump, thermal diffusion should be significant enough to smooth out the profile. It has yet to be determined whether this jump is indeed physical in nature or is a numerical artifact.

CHAPTER 8

NEAR-VACUUM FLOWS

Under certain flow conditions, a situation may occur in which the internal energy becomes a small fraction of the total energy. For example, in cases of rapid expansions, the kinetic energy may dominate the total energy of the system as the internal energy quickly drops. As the kinetic energy is subtracted from the total energy, substantial errors in the internal energy and subsequent pressure may result[1]. This problem is further compounded in cases in which the density approaches zero, as small fluctuations in this variable can lead to large errors in the fluid temperature.

While the choice of solver can have some impact in such cases [81], the root of the problem lies in the conditioning of the governing equations. This problem has been addressed in the literature with several approaches being proposed. In [24], the internal energy is convected independently of the total energy which is a technique that can be found in mature CFD codes. The drawback is that the formulation is no longer conservative and can result in significant errors.

Another approach has been to modify the reconstruction scheme to include a bound on the internal and kinetic energies [51]. While this technique is able to preserve positivity of the governing equations, it does not address the conditioning problem of the system.

The approach taken here is to augment the transport equations with entropy conservation in a similar fashion as done in [62]. This in effect is a way to convect the internal energy independently of the total energy while preserving the conservation property of the governing equations. Such an approach, however, is limited to flows that are isentropic, namely non-shocked polytropic gases. However, this approach can be extended to include real gas effects

[1] This problem can be even more dramatic if the MHD equations are considered with a strong magnetic field, in which case the magnetic pressure can be a dominant term as well.

through the inclusion of relaxation parameters, assuming near-equilibrium conditions. The formulation of the governing equations are presented first followed by benchmarks on a standard rarefaction test case.

8.1 Formulation

The purpose of this section is to augment the the continuity, momentum, and energy equations with an entropy equation in conservation form. The derivation is entirely analogous to that of the electron energy equation for the 2T model presented in Chapter 2. For simplicity, a single component fluid will be considered. For a polytropic gas, the entropy equation can be expressed in conservative form as

$$\frac{\partial \rho s}{\partial t} + \nabla \cdot (\vec{u} \rho s) = 0 \tag{8.1}$$

with $s = p/\rho^{\gamma}$. Incorporating this into the governing equations, the entropy-augmented Euler equations can be expressing in vector form as

$$\frac{\partial Q}{\partial t} + \nabla \cdot F_n = 0 \tag{8.2}$$

where

$$Q = \begin{pmatrix} \rho_1 \\ \vdots \\ \rho_n \\ \rho u \\ \rho v \\ \rho w \\ E \\ S \end{pmatrix}, \quad V = \begin{pmatrix} \rho_1 \\ \vdots \\ \rho_n \\ u \\ v \\ w \\ p \\ p \end{pmatrix}, \quad F_n = \begin{pmatrix} v_n \rho_1 \\ \vdots \\ v_n \rho_n \\ v_n \rho u + n_x p \\ v_n \rho v + n_y p \\ v_n \rho w + n_z p \\ v_n (E + p) \\ v_n S \end{pmatrix} \tag{8.3}$$

and $S = \rho s$. The flux Jacobian of the system is analogous to Eq. (A.4) and is given by

$$A_x = \frac{\partial F}{\partial Q} =$$

$$\begin{pmatrix}
u(1-y_1) & \dots & -uy_1 & y_1 & 0 & 0 & 0 & 0 \\
\vdots & \ddots & \vdots & \vdots & \vdots & \vdots & \vdots & \vdots \\
-uy_n & \dots & u(1-y_n) & y_n & 0 & 0 & 0 & 0 \\
-uv & \dots & -uv & v & u & 0 & 0 & 0 \\
-uw & \dots & -uw & w & 0 & u & 0 & 0 \\
P_{\rho_1} - \vec{u}\cdot\vec{u} & \dots & P_{\rho_n} - \vec{u}\cdot\vec{u} & P_{m_x} + 2u & P_{m_y} & P_{m_z} & P_E & P_S \\
\mathcal{A}_{\rho_1,E} & \dots & \mathcal{A}_{\rho_n,E} & \mathcal{A}_{m_x,E} & uP_{m_y} & uP_{m_z} & u(1+P_E) & uP_S \\
-uS/\rho & \dots & -uS/\rho & S/\rho & 0 & 0 & 0 & u
\end{pmatrix}$$

where

$$\mathcal{A}_{\rho_i,E} = uP_{\rho_i} - u(E+p)/\rho,$$

$$\mathcal{A}_{m_x,E} = uP_{m_x} + (E+p)/\rho.$$

The similarities with the 2T extend to the diagonalization of the flux Jacobian, resulting in an analogous eigensystem as well. The right and left eigenvectors for the entropy-augmented Euler equations can be deduced from Eqs. (A.11) and (A.15), respectively. In addition, the Roe-averaged states $\tilde{Q}$ can be found from a linearization of the definition of the flux Jacobian,

$$\Delta F = A(\tilde{Q})\Delta Q, \tag{8.4}$$

and are given by

$$\tilde{\rho} = \sqrt{\rho_{\mathrm{L}}\rho_{\mathrm{R}}} \tag{8.5}$$

$$\tilde{u} = \frac{\sqrt{\rho_{\mathrm{L}}}u_{\mathrm{L}} + \sqrt{\rho_{\mathrm{R}}}u_{\mathrm{R}}}{\sqrt{\rho_{\mathrm{L}}} + \sqrt{\rho_{\mathrm{R}}}} \tag{8.6}$$

$$\tilde{h}_{\circ} = \frac{\sqrt{\rho_{\mathrm{L}}}h_{\circ\mathrm{L}} + \sqrt{\rho_{\mathrm{R}}}h_{\circ\mathrm{R}}}{\sqrt{\rho_{\mathrm{L}}} + \sqrt{\rho_{\mathrm{R}}}} \tag{8.7}$$

$$\tilde{S} = \frac{\sqrt{\rho_{\mathrm{L}}}S_{\mathrm{R}} + \sqrt{\rho_{\mathrm{R}}}S_{\mathrm{L}}}{\sqrt{\rho_{\mathrm{L}}} + \sqrt{\rho_{\mathrm{R}}}} \tag{8.8}$$

Note that with the inclusion of both the energy and entropy equations, there are two distinct possibilities for computing the Roe-average pressure and sound speed for isentropic flows. The first option is to compute the sound speed and pressure from the stagnation enthalpy according to

$$\tilde{a} = (\gamma - 1)\left(\tilde{h}_{\circ} - \frac{1}{2}\tilde{u}^2\right)^{1/2} \tag{8.9}$$

$$\tilde{p} = \frac{\tilde{\rho}\tilde{a}^2}{\gamma}. \tag{8.10}$$

Alternatively, the values may be derived from the entropy,

$$\tilde{p} = \tilde{S}\tilde{\rho}^{\gamma-1} \tag{8.11}$$

$$\tilde{a} = \left(\frac{\gamma\tilde{p}}{\tilde{\rho}}\right)^{1/2} \tag{8.12}$$

To ensure consistency, Eq. (8.11) must be used if the left and right pressure states were computed from the entropy variable as well. If the left and right pressure states were computed from the internal energy, on the other hand, the sound speed should be derived from the Roe average stagnation enthalpy.

8.2 Benchmarks

One of the most common benchmarks to test a solver's ability to properly capture high velocity/low density flows is the *1-2-3* problem, so-called due to the initial ratio of density

to momentum to energy, respectively [37]. This test case simulates two retracting pistons and the low pressure/density region that results. The left and right states are defined by,

$$\begin{pmatrix} \rho_{\mathrm{L}} \\ u_{\mathrm{L}} \\ p_{\mathrm{L}} \end{pmatrix} = \begin{pmatrix} 1 \\ -2 \\ 0.4 \end{pmatrix}, \quad \begin{pmatrix} \rho_{\mathrm{R}} \\ u_{\mathrm{R}} \\ p_{\mathrm{R}} \end{pmatrix} = \begin{pmatrix} 1 \\ 2 \\ 0.4 \end{pmatrix} \tag{8.13}$$

for a polytropic gas with an adiabatic exponent of 5/3. The deficiency of numerical solvers in duplicating the exact solution is a conditioning problem inherent in the governing equations. At very low densities, relatively small changes in the pressure and density can lead to large errors in temperature as can be seen in Figure 8.2. However, if the pressure is obtained directly from the entropy function, $p/\rho^{\gamma-1}$, this problem is essentially eliminated as can be seen in Figure 8.2.

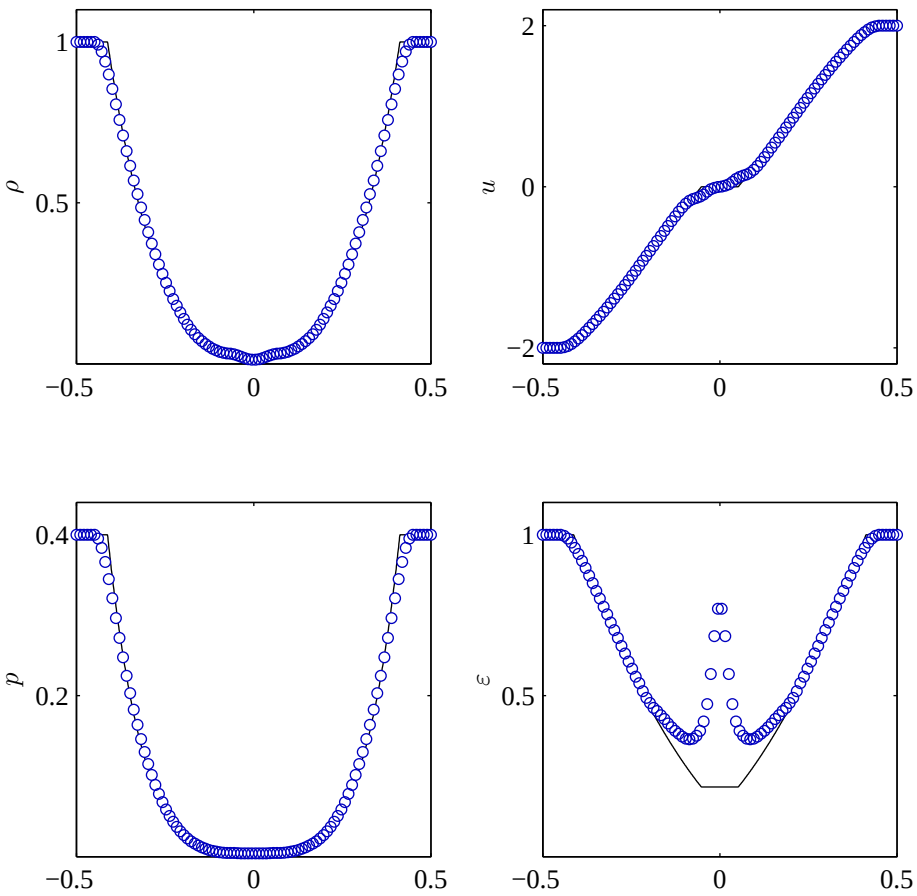

Figure 8.1: Solution to Einfeldt's *1-2-3* problem as obtained with conservation of energy. Symbols (∘) denote numerical solution while solid line (—) is the exact solution.

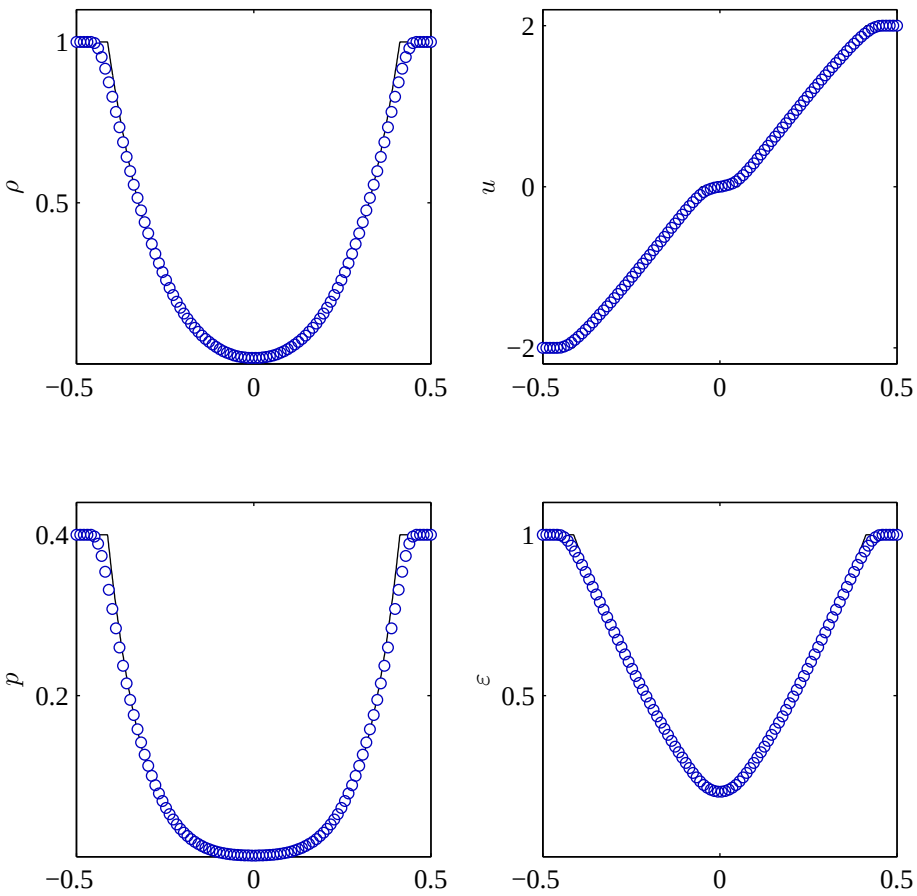

Figure 8.2: Solution to Einfeldt's *1-2-3* problem as obtained with conservation of entropy. Symbols (∘) denote numerical solution while solid line (—) is the exact solution.

CHAPTER 9

COLLISIONAL-RADIATIVE MODEL

In this chapter, the collisional-radiative model developed for monatomic argon is detailed. The CR model functions as a generalized equation of state for the electronic energy modes. It is used to compute the populations of the excited levels through detailed kinetic relations for excitation and ionization, and reverse processes, allowing for non-Boltzmann distribution of bound electronic states. Rates are computed from collision cross sections of the associated processes under the assumption of a Maxwellian electron energy distribution function (EEDF).

The CR model presented here draws upon the previous work of Vlček [117] and Bultel *et al.* [19] both of which are specific to argon. The model includes the first 31 excited levels of neutral argon, for which a partial Grotrian is provided in Figure 9.1, as well as the ground states of the singly-charged ion. Population of the states beyond the lower lying levels is negligible for the plasma conditions considered, as verified by equilibrium considerations. Level grouping is not considered, as the approach here is to look in detail at the influence of the lower lying states.

As the CR model will be validated on the UTIAS shock tube experiments in the following chapter, assumptions made herein are based on the plasma conditions of the experiments where ever necessary. This includes number densities up to 10^{24} [m$^-$3] and temperatures just above 1 eV.

9.1 Rate equations

The processes to be included can be represented by the following rate equations,

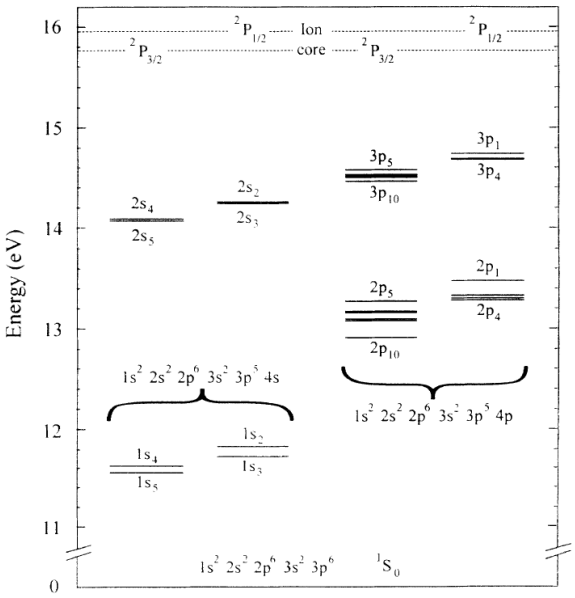

Figure 9.1: Partial Grotrian diagram for neutral argon taken from [99].

$$Ar(i) + e^- \underset{F_{ji}}{\overset{C_{ij}}{\rightleftharpoons}} Ar(j) + e^- \tag{9.1}$$

$$Ar(i) + Ar(1) \underset{L_{ji}}{\overset{K_{ij}}{\rightleftharpoons}} Ar(j) + Ar(1) \tag{9.2}$$

$$Ar(i) + e^- \underset{O_i}{\overset{S_i}{\rightleftharpoons}} Ar^+ + e^- + e^- \tag{9.3}$$

$$Ar(i) + Ar(1) \underset{W_i}{\overset{V_i}{\rightleftharpoons}} Ar^+ + Ar(1) + e^- \tag{9.4}$$

$$Ar(i) + h\nu_{ij} \underset{A_{ij}}{\overset{(1-\Lambda_{ij})A_{ij}}{\rightleftharpoons}} Ar(j) \tag{9.5}$$

$$Ar(i) + h\nu \underset{R_i}{\overset{(1-\Lambda_i)R_i}{\rightleftharpoons}} Ar^+ + e^- \tag{9.6}$$

where the rate coefficients defined in [117] are summarized in Table 9.1. The convention has been adopted that takes $j > i$ so that C_{ij} and K_{ij} represent the rates for excitation from level i to j while F_{ji} and L_{ji} are the rates for de-excitation from level j to i. The levels considered in the present model include only those up to the $3p^5 3d$ and $3p^5 5s$ manifolds (cf. Table 9.2). This implies that ionization and recombination should proceed from and to only these low-lying levels; although levels beyond this manifold are more that 1 eV away

Rate Coefficient	Process
C_{ij}	collisional excitation by electrons
K_{ij}	collisional excitation by ground state atoms
F_{ji}	collisional de-excitation by electrons
L_{ji}	collisional de-excitation by ground state atoms
S_i, V_i	collisional ionization
O_i, W_i	three-body recombination
R_i	radiative recombination
A_{ij}	transition probability/spontaneous emission (Einstein coefficient)
Λ_{ij}	bound-bound optical escape factor
Λ_i	bound-free optical escape factor
k_{ei}	electron-ion collisions
k_{en}	electron-neutral collisions
k_{brems}	bremsstrahlung emission

Table 9.1: Rate coefficients for collisional-radiative model.

from the ionization limit, the combination of small energy gap and large cross-section makes the ionization from these levels extremely rapid, certainly with time scales much below the time resolution needed in the current research. Thus the lower-lying states provide the bottleneck to the ionization regime and most of the energy in bound states.

Note that neutral argon has two ionization potentials owing to the fact that the levels of argon are split according to two possible configurations for the core angular momentum j_c.

Neutral argon has two ionization potentials corresponding to two possible configurations for the core angular momentum j_c. As ionization and recombination can proceed only between levels having the same value of j_c, the populations of the two lowest lying levels of Ar^+ must be accounted for individually. In the current model, these two levels are treated as separate species and convected as such.

Considered here are plasmas for which a Maxwellian electron energy distribution function (EEDF) is valid,

$$f(\varepsilon)\ d\varepsilon = \frac{2}{\pi^{1/2}} \frac{\varepsilon^{1/2}}{(k_{\text{B}} T_e)^{3/2}} e^{-\varepsilon/k_{\text{B}} T_e}\ d\varepsilon, \tag{9.7}$$

which has been normalized according to

$$\int_0^\infty f(\varepsilon)\ d\varepsilon = 1. \tag{9.8}$$

i	$\varepsilon(i)$ [eV]	g_i	j_c	$n\ell[K]_J$	i	$\varepsilon(i)$ [eV]	g_i	j_c	$n\ell[K]_J$
1	0	1	1.5	[Mg]$3p^6$	18	13.903	5	1.5	$3d[3/2]_2$
2	11.548	5	1.5	$4s[3/2]_2$	19	13.979	9	1.5	$3d[7/2]_4$
3	11.624	3	1.5	$4s[3/2]_1$	20	14.013	7	1.5	$3d[7/2]_3$
4	11.723	1	0.5	$4s'[1/2]_0$	21	14.063	5	1.5	$3d[5/2]_2$
5	11.828	3	0.5	$4s'[1/2]_1$	22	14.068	5	1.5	$3d[3/2]_1$
6	12.907	3	1.5	$4p[1/2]_1$	23	14.090	3	1.5	$5s[3/2]_2$
7	13.076	7	1.5	$4p[5/2]_3$	24	14.099	7	1.5	$5s[5/2]_3$
8	13.095	5	1.5	$4p[5/2]_2$	25	14.153	3	1.5	$3d[3/2]_1$
9	13.153	3	1.5	$4p[3/2]_1$	26	14.214	5	0.5	$5s'[1/2]_0$
10	13.172	5	1.5	$4p[3/2]_2$	27	14.234	5	0.5	$3d'[5/2]_2$
11	13.273	1	1.5	$4p[1/2]_0$	28	14.236	7	0.5	$5s'[1/2]_1$
12	13.283	3	0.5	$4p'[3/2]_1$	29	14.241	1	0.5	$3d'[3/2]_2$
13	13.302	5	0.5	$4p'[3/2]_2$	30	14.255	3	0.5	$3d'[5/2]_3$
14	13.328	3	0.5	$4p'[1/2]_1$	31	14.304	3	0.5	$3d'[3/2]_1$
15	13.480	1	0.5	$4p'[1/2]_0$	∞	15.760	4	1.5	[Mg]$3p^5$
16	13.845	1	1.5	$3d[1/2]_0$	∞'	15.937	2	0.5	[Mg]$3p^5$
17	13.864	3	1.5	$3d[1/2]_1$					

Table 9.2: Argon levels considered in current CR model.

The rate coefficients are computed using the EEDF according to

$$k = \frac{\bar{v}}{(k_{\text{B}}T)^2} \int_{\varepsilon_\circ}^{\infty} \sigma(\varepsilon)\varepsilon e^{-\varepsilon/k_{\text{B}}T}\, d\varepsilon \tag{9.9}$$

where $\varepsilon_\circ$ is the threshold energy and $\bar{v}$ is the mean thermal velocity,

$$\bar{v} = \left(\frac{8k_{\text{B}}T}{\pi\mu}\right)^{1/2}, \tag{9.10}$$

with μ being the reduced mass. The reverse rates are then computed from the principle of detailed balance. For excitation processes this takes the form

$$k_{ji} = k_{ij}\frac{g_i}{g_j}e^{\varepsilon_{ij}/k_{\text{B}}T} \tag{9.11}$$

where $\varepsilon_{ij} = \varepsilon_j - \varepsilon_i$ is the energy difference of the upper and lower levels. The temperature in Eq. (9.11) is taken to be that of the the impact species. For processes involving a third body, the reverse rates are computed via

$$k_i^r = k_i \frac{Z_i}{Z_+ Z_e} \tag{9.12}$$

where Z_e is the electron partition function,

$$Z_e = 2\left(\frac{2\pi m_e k_{\mathrm{B}} T_e}{h^2}\right)^{3/2} \tag{9.13}$$

while the ratio of partition functions for Ar and Ar^+ can be approximated as[1]

$$\frac{Z_i}{Z_+} \approx \frac{g_i}{g_+} e^{I_i/k_{\mathrm{B}}T} \tag{9.14}$$

with I_i being the ionization potential of the i^{th} excited state, allowing Eq. (9.12) to be written as

$$k_i^r = k_i \frac{g_i}{g_+} \frac{1}{2} \left(\frac{h^2}{2\pi m_e k_{\mathrm{B}} T_e}\right)^{3/2} e^{I_i/k_{\mathrm{B}}T}. \tag{9.15}$$

Note that the exponential temperature dependence in Eq. (9.15) is a function of the third body—T is taken to be either the electron or heavy particle temperature for cases in which the third body is an electron or atom, respectively.

In addition to species production rates, the second moment with respect to energy is also necessary as it determines the energy production rate for a given process,

$$k' = \frac{\bar{v}}{(k_{\mathrm{B}}T)^2} \int_{\varepsilon_\circ}^{\infty} \sigma(\varepsilon)\varepsilon^2 e^{-\varepsilon/k_{\mathrm{B}}T}\, d\varepsilon \tag{9.16}$$

In practice, all rate coefficients and their derivatives are computed *a priori* and tabulated as a function of temperature which is used in the code. This is possible due to the assumption of a known distribution function.

The remainder of this section is devoted to calculation of the cross sections and associated rates used in the CR model. For further details, the reader is directed to [19] and [117].

9.1.1 Atom impact processes

Cross sections for atom-atom collisions are typically several orders of magnitude less than their electron-atom counterpart since for a given translational temperature, $\bar{v}_e \gg \bar{v}_a$. However, with the absence of electrons immediately behind the compression shock, atom-atom collisions are the only means for initial electron production and result in the necessary

[1] Assuming $m_{Ar} \approx m_{Ar^+}$.

i	j	β^*_{ij} [m^2/eV]	f_{ij}
1	3	1.10×10^{-23}	6.78×10^{-02}
1	5	3.95×10^{-23}	2.56×10^{-01}
1	17	9.58×10^{-26}	1.00×10^{-03}
1	23	3.10×10^{-24}	3.40×10^{-02}
1	25	8.55×10^{-24}	9.51×10^{-02}
1	30	1.59×10^{-24}	1.80×10^{-02}
1	31	6.92×10^{-24}	7.94×10^{-02}

Table 9.3: Atom impact excitation parameters for allowed transitions from ground state Ar.

i	j	β^*_{ij} [m^2/eV]
2	3	1.79×10^{-24}
2	4	4.80×10^{-26}
2	5	4.80×10^{-26}
3	4	4.80×10^{-26}
3	5	4.80×10^{-26}
4	5	1.79×10^{-24}

Table 9.4: Atom impact excitation parameters for intra-4s transitions.

priming electrons that eventually trigger inelastic electron collisions.

Excitation from ground state in particular plays a significant role in determining the overall induction length, i.e. the distance between shock-front and electron avalanche. In addition, the excitation rates have a profound influence on the dynamics of the simulation. It will be shown that pressure waves initiated at the electron avalanche are exacerbated for undervalued cross sections while excessive values can lead to over damping of the system. The sharp sensitivity of the convection-kinetics coupling highlights the need for accurate determination of the heavy particle cross sections.

The cross sections for excitation from ground state have been determined from Drawin's model,

$$\sigma^a_{ij}(\varepsilon) = 4\pi a_\circ^2 \left(\frac{\varepsilon_1^{\mathrm{H}}}{\varepsilon_{ij}}\right)^2 \frac{m_{Ar}}{m_H} \xi^2 f_{ij} \frac{2m_e}{m_{Ar}+m_e} \frac{\varepsilon/\varepsilon_{ij} - 1}{\left(1 + \frac{2m_e}{m_{Ar}+m_e}(\varepsilon/\varepsilon_{ij} - 1)\right)^2} \tag{9.17}$$

where I_H is the ionization potential of the hydrogen atom and ξ is the number of optical electrons. For the energy ranges under consideration, Eq. (9.17) is well-approximated by a

linear function,

$$\sigma_{1j}^{a}(\varepsilon) = \beta_{1j}^{*}(\varepsilon - \varepsilon_{ij}), \tag{9.18}$$

where

$$\beta_{1j}^{*} = 4\pi a_{\circ}^{2} \frac{(\varepsilon_{1}^{\mathrm{H}})^{2}}{\varepsilon_{ij}^{3}} \xi^{2} f_{ij} \frac{2m_e}{m_H} \tag{9.19}$$

The inner $3p^5 4s$ manifold transitions, however, take the form [19]

$$\sigma_{ij}^{a}(\varepsilon) = \beta_{ij}^{*} \frac{\varepsilon - \varepsilon_{ij}}{\varepsilon_{ij}^{2.26}} \tag{9.20}$$

All necessary parameters are given in Table 9.3.

Less sensitive are the ionization cross sections—we remark that decreasing these values by an order of magnitude did not have any significant effect on the induction length or flow dynamics. The cross section for ionization from ground state argon is taken from [50],

$$\sigma_{1}^{a}(\varepsilon) = 1.8 \times 10^{-25} (\varepsilon - 15.760)^{1.3} \ [\mathrm{m}^2], \tag{9.21}$$

while the formula of Drawin has been applied for all other levels,

$$\sigma_{i}^{a}(\varepsilon) = 4\pi a_{\circ}^{2} \left(\frac{I_H}{I_i}\right)^{2} \frac{m_{Ar}}{m_H} \xi^{2} \frac{2m_e}{m_{Ar} + m_e} \frac{\varepsilon/I_i - 1}{\left(1 + \frac{2m_e}{m_{Ar}+m_e}(\varepsilon/I_i - 1)\right)^{2}}. \tag{9.22}$$

9.1.2 Electron impact processes

Once a sufficient number of priming electrons have been generated by heavy particle impact and their temperature increased by thermalization, electron impact processes begin to become important and eventually dominate the kinetics. The rates associated with processes are critical in determining the magnitude of the electron avalanche and associated ionization fraction. The cross sections for ionization and excitation processes can be computed using Drawin's formulas,

The cross sections for electron-impact excitation are due to Zatsarinny and Bartschat [126],[125]. These include excitation from the ground and $4s$ levels to all levels below the

	s	p	d	f
a	1.06	2	3/2	3/2
b	0.23	1	3	1
c	1	1	2/3	2/3
d	1	1	1	1

Table 9.5: Electron-impact ionization parameters as taken from [35].

Valence electron shell, $n\ell$	$r_{n\ell}$ [m]	$g_{n\ell} \times I_{n\ell}$ [eV]
$4s$	2.49×10^{-10}	7.40
$5s$	6.35×10^{-10}	6.35
$4p$	3.40×10^{-10}	31.00
$3d$	4.36×10^{-10}	13.60

Table 9.6: Radii of Ar valence electron and reduced weighting factors for $\xi = 1$ as taken from [35] and [34].

$5p$ manifold. For all other transitions, Drawin's formulas

$$\sigma_{ij}^{e}(\varepsilon) = 4\pi a_{\circ}^{2} \begin{cases} \alpha_{ij}^{A} f_{ij}(u_{ij}-1)/u_{ij}^{2}\,(I_H/\varepsilon_{ij})^2 \ln(1.25\beta_{ij}u_{ij}) & \text{allowed} \\ \alpha_{ij}^{P}(u_{ij}-1)/u_{ij}^{2} & \text{parity forbidden} \\ \alpha_{ij}^{S}(u_{ij}^{2}-1)/u_{ij}^{5} & \text{spin forbidden} \end{cases} \tag{9.23}$$

have been used systematically with $\alpha_{ij}^{A} f_{ij} = 1$, $\alpha_{ij}^{P} = 1$, and $\alpha_{ij}^{S} = 1$.

Cross sections for electron-impact ionization from the excited levels have been determined based on the work of Deutsch *et al.* [34] via

$$\sigma_i(\varepsilon) = g_{n\ell}\pi r_{n\ell}^{2}\xi_{n\ell} f(\varepsilon) \tag{9.24}$$

where $g_{n\ell}$ are the reduced weighting factors, $r_{n\ell}$ are the radii of the valence electron, and

$$f_i(\varepsilon) = d\frac{I_i}{\varepsilon}\left(\frac{\varepsilon/I_i - 1}{\varepsilon/I_i + 1}\right)^{a}\left[b + c\left(1 - \frac{I_i}{2\varepsilon}\right)\ln(2.7 + (\varepsilon/I_i - 1)^{1/2})\right]. \tag{9.25}$$

The necessary parameters for Eqs. (9.24) and (9.25) are given in Tables 9.5 and 9.6.

9.1.3 Pressure ionization

Particular attention must be paid when considering ionization and recombination in plasmas defined by relatively high densities. This is due to nonideal effects for which interactions between particles can lead to an effective lowering of the ionization potential. As a consequence, the rates must be considered as functions of pressure as well. Griem [44] used Debye theory to predict a decrease in the ionization potential that is inversely proportional to the Debye length,

$$\Delta\varepsilon_{\infty,m} = \frac{(m+1)e^2}{4\pi\epsilon_\circ\lambda_D}, \tag{9.26}$$

where λ_D is the Debye length[2],

$$\lambda_D = \left(\frac{\epsilon_\circ k_\mathrm{B} T_e}{N_e e^2}\right)^{1/2}. \tag{9.27}$$

For the shock tube conditions under consideration, the lowering of the ionization potential was found to be small, yielding a drop of 0.08 eV for an electron temperature of 1 eV and number density of 10^{23} m^{-3}. As a result, the effects of pressure ionization were not accounted for.

9.2 Photorecombination

In the absence of a third body, the energy released in recombination is liberated as radiation. Photorecombination is a significant loss mechanism and plays an important role in radiative cooling. The cross section for photorecombination can be found from the cross section for photoionization under equilibrium conditions [128],

$$\sigma_{c,i}(\nu) = \frac{g_n}{g_+}\frac{h^2\nu^2}{m_e^2 v_e^2 c^2}\sigma_{\nu,i}(\nu). \tag{9.28}$$

Utilizing the relation $h\nu = m_e v^2/2 + \varepsilon_i = \varepsilon + \varepsilon_i$, the cross section associated with the ground state is given by

[2] neglecting the effect of ions

$$\sigma_1(\varepsilon) = \frac{g_1}{g_+}\frac{(\varepsilon+\varepsilon_1)^2}{2\varepsilon m_e c^2}\begin{cases} 3.5\times10^{-21} & 0 \le \varepsilon \le 2\varepsilon_1^{\mathrm{H}} - \varepsilon_1 \\ 2.8\times10^{-20}\left(\dfrac{\varepsilon_1^{\mathrm{H}}}{\varepsilon+\varepsilon_1}\right)^3 & \varepsilon > 2\varepsilon_1^{\mathrm{H}} - \varepsilon_1 \end{cases} \tag{9.29}$$

while all others are computed using

$$\sigma_i(\varepsilon) = \gamma_i(n_{pqn,\ell})\frac{g_i}{g_+}\frac{(\varepsilon+\varepsilon_i)^2}{2\varepsilon m_e c^2}\begin{cases} 2\times10^{-22} & 0 \le \varepsilon \le 0.59\varepsilon_1^{\mathrm{H}} - \varepsilon_1 \\ 7.91\times10^{-22}\left(\dfrac{\varepsilon_i}{\varepsilon_1^{\mathrm{H}}}\right)^{5/2}\left(\dfrac{\varepsilon_1^{\mathrm{H}}}{\varepsilon+\varepsilon_i}\right)^3 & \varepsilon > 0.59\varepsilon_1^{\mathrm{H}} - \varepsilon_i \end{cases}. \tag{9.30}$$

The parameter $\gamma_i(n_{pqn,\ell})$ takes the values 0.0763, 0.0458, 0.0305, and 0.0915 for $i = 2$, 3, 4, and 5, respectively [117].

Estimation of the mean-free path as based on the representative shock tube plasma conditions indicates that radiation from bound-free transitions to the ground state are absorbed locally while the mean-free paths for transitions to the $4s$ manifold are greater by several orders of magnitude. Thus, radiation from bound-free transitions is assumed to escape completely.

9.3 Bremsstrahlung emission

Free-free transitions have been incorporated in the model via Kramer's formula [128] for *Bremsstrahlung* emission,

$$\frac{\partial E_e}{\partial t} = -\frac{16\pi^2}{3\sqrt{3}}\frac{\bar{v}_e Z_{\mathrm{eff}}^2 e^6 \bar{g}}{m_e h(4\pi\epsilon_\circ c)^3} n_+ n_e \tag{9.31}$$

$$= -1.42\times10^{-40} Z_{\mathrm{eff}}^2 T_e^{1/2} n_+ n_e \quad [\mathrm{J}\cdot\mathrm{m}^{-3}\cdot\mathrm{s}^{-1}] \tag{9.32}$$

where $\bar{g}$ is the gaunt factor taken to be unity and the effective charge Z_{eff}^2 is taken to be 1.67 [42]. Bremsstrahlung emission resulting from neutral atoms is 1-2 orders of magnitude less than for ions and has therefore been neglected. The plasma is assumed to be optically thin to all Bremsstrahlung emission.

lower level	upper level	mean-free path [m]
$3p^6$	$4s[1/2]_1$	3.59×10^{-2}
$3p^6$	$4s'[1/2]_1$	9.47×10^{-3}
$3p^6$	$3d[1/2]_1$	2.41
$3p^6$	$5s[3/2]_1$	7.11×10^{-2}
$3p^6$	$3d[3/2]_1$	2.54×10^{-2}
$3p^6$	$5s'[1/2]_1$	1.34×10^{-1}
$3p^6$	$3d'[3/2]_1$	3.05×10^{-2}

Table 9.7: Estimated mean-free paths for bound-bound transitions to ground state for $T =$ 1 eV and $n_{3p^6} = 10^{24}$ m^{-3}.

9.4 Bound-bound transitions

In addition to photorecombination and Bremsstrahlung, bound-bound transitions are a significant source of radiative cooling of the plasma. The photoionization cross section for a given bound-bound transition may be estimated by [128],

$$\sigma_{ij} = \frac{1}{\nu_{ij}} \int \sigma_{\nu,ij} \, d\nu = 2.65 \times 10^{-6} \frac{f_{ij}}{\nu_{ij}} \text{ [m}^2\text{]} \tag{9.33}$$

where the absorption oscillator strength is given by

$$f_{\text{abs}} = \frac{g_j}{g_i} \frac{A_{ji}}{3\gamma}. \tag{9.34}$$

Contributions to the parameter γ have been assumed to result from a combination of natural and pressure line broadening,

$$\gamma = \gamma_{\text{nat}} + \gamma_{\text{col}} \tag{9.35}$$

given by

$$\gamma_{\text{nat}} = \frac{8\pi^2 e^2 \nu^2}{3mc^3} = 2.47 \times 10^{-22} \nu^2 \text{ [s}^{-1}\text{]} \tag{9.36}$$

and

$$\gamma_{\text{col}} = \frac{2}{\tau_{\text{col}}} = 2\sigma \bar{v} n \tag{9.37}$$

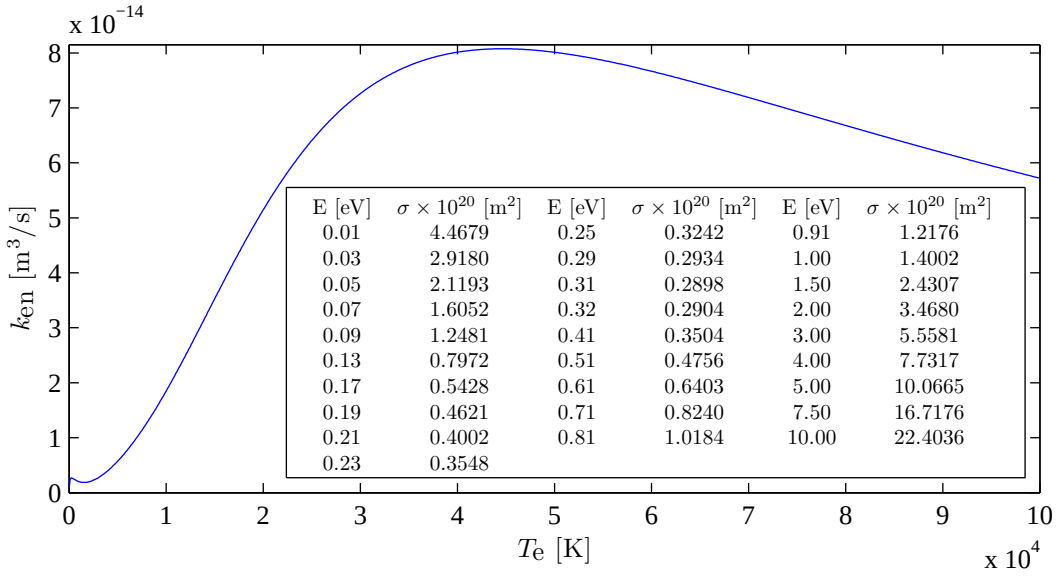

E [eV]	$\sigma \times 10^{20}$ [m^2]	E [eV]	$\sigma \times 10^{20}$ [m^2]	E [eV]	$\sigma \times 10^{20}$ [m^2]
0.01	4.4679	0.25	0.3242	0.91	1.2176
0.03	2.9180	0.29	0.2934	1.00	1.4002
0.05	2.1193	0.31	0.2898	1.50	2.4307
0.07	1.6052	0.32	0.2904	2.00	3.4680
0.09	1.2481	0.41	0.3504	3.00	5.5581
0.13	0.7972	0.51	0.4756	4.00	7.7317
0.17	0.5428	0.61	0.6403	5.00	10.0665
0.19	0.4621	0.71	0.8240	7.50	16.7176
0.21	0.4002	0.81	1.0184	10.00	22.4036
0.23	0.3548				

Figure 9.2: Electron-neutral collision rate as computed from the theoretical cross sections (table) computed in [71].

respectively. The collision periodicity τ_{col} and the collision cross section σ have been tallied for neutral argon-argon collisions. The radiation cross sections Eq. (9.33) have been estimated using the oscillator strengths and transition probabilities from [95] along with representative plasma conditions of the shock tube experiments. The resulting mean-free paths for bound-bound transitions to ground state given in Table 9.7 are below the length scales of the shock tube dimensions for most of the levels. It has therefore been assumed that all bound-bound radiation to the ground level from the excited states is absorbed. For all other transitions, the mean-free path is several orders of magnitude greater than the dimensions of the shock tube and the associated radiation is assumed to escape.

9.5 Elastic collisions

Elastic collisions are incorporated into the CR implicit solver as well. This strong coupling permits more accurate and stable calculations. The energy transfer between electrons and neutrals is computed as

$$\frac{\partial E_e}{\partial t} = -\frac{\partial E_h}{\partial t} = n_e n_n \frac{3}{2} k_{\text{B}} (T_h - T_e) \frac{2m_e}{m_{Ar}} k_{en} \tag{9.38}$$

For electron-neutral collisions, the theoretical cross section of McEachran and Stauffer [71] have been utilized. These are reproduced in Figure 9.2 along with the associated rates. The Coulomb collision rates, $\bar{k}_{ei}$, have been computed using the energy-averaged properties [78],

$$\frac{\partial E_e}{\partial t} = -\frac{\partial E_h}{\partial t} = n_e n_n \frac{3}{2} k_{\mathrm{B}} (T_h - T_e) \frac{2m_e}{m_{Ar}} k_{en} \tag{9.39}$$

$$\bar{k}_{ei} = \bar{v}_e \bar{Q}_{ei} \tag{9.40}$$

$$\bar{Q}_{ei} = 5.85 \times 10^{-10} \frac{\ln \Lambda}{T_e^2} \ [\mathrm{m}^2] \tag{9.41}$$

$$\Lambda = 1.24 \times 10^7 \left(\frac{T_e^3}{n_e} \right)^{1/2} \tag{9.42}$$

where $\bar{Q}_{ei}$ is the momentum-averaged cross section, and Λ is the Coulomb logarithm. The energy transfer equation for electron-ion collsions is similar to Eq. 9.39 and is given by

$$\frac{\partial E_e}{\partial t} = -\frac{\partial E_h}{\partial t} = n_e n_i \frac{3}{2} k_{\mathrm{B}} (T_h - T_e) \frac{2m_e}{m_{Ar^+}} k_{ei} \tag{9.43}$$

9.6 Numerical formulation

The coupled system of linear rate equations for the CR model is expressed in vector form via

$$\frac{dQ_{CR}}{dt} = \dot{\Omega} \tag{9.44}$$

where

$$Q_{CR} = \begin{pmatrix} n_{3p^6} \\ n_{4s[3/2]_2} \\ n_{4s[3/2]_1} \\ \vdots \\ n_{n\ell[K]_J} \\ n_{Ar^+(j_c=3/2)} \\ n_{Ar^+(j_c=1/2)} \\ E_h \\ E_e \end{pmatrix}, \quad \dot{\Omega} = \begin{pmatrix} \dot{\omega}_{3p^6} \\ \dot{\omega}_{4s[3/2]_2} \\ \dot{\omega}_{4s[3/2]_1} \\ \vdots \\ \dot{\omega}_{n\ell[K]_J} \\ \dot{\omega}_{Ar^+(j_c=3/2)} \\ \dot{\omega}_{Ar^+(j_c=1/2)} \\ \dot{\omega}_{E_h} \\ \dot{\omega}_{E_e} \end{pmatrix} \tag{9.45}$$

Note that the conservative variables used in the CR formulation are not the same as those previously detailed in Chapter 2. However, conversion between the two vectors is accomplished via the simple transformation,

$$Q = MQ_{CR} \tag{9.46}$$

where

$$M = \begin{pmatrix} m_{Ar} & & & & & & & \\ & \ddots & & & & & & \\ & & m_{Ar} & & & & & \\ & & & m_{Ar^+} & & & & \\ & & & & m_{Ar^+} & & & \\ & & & & & 1 & 1 & \\ & & & & & & \frac{\gamma_e - 1}{\rho^{\gamma_e - 1}} \end{pmatrix} \tag{9.47}$$

The components of $\dot{\Omega}$ are obtained after combining the rate equations for all processes, the exact form of which are as follows.

Ar levels

$$\begin{aligned}\dot{\omega}_{n_k} \equiv \frac{\partial n_k}{\partial t} = &\sum_{i<k} n_i(n_e C_{ik} + n_1 K_{ik} + (1-\Lambda_{ki})A_{ki}) - \sum_{j<k} n_k(n_e F_{kj} + n_1 L_{kj} + A_{kj}) \\ &- \sum_{j>k} n_k(n_e C_{kj} + n_1 K_{kj} + (1-\Lambda_{jk})A_{jk}) + \sum_{i>k} n_i(n_e F_{ik} + n_1 L_{ik} + A_{ik}) \\ &+ n_+ n_e(n_1 W_k + n_e O_k + R_k) - n_k(n_e S_k + n_1 V_k + (1-\Lambda_k)R_k)\end{aligned} \tag{9.48}$$

Ar^+

$$\dot{\omega}_{n_+} \equiv \frac{\partial n_+}{\partial t} = \sum_i n_i(n_e S_i + n_1 V_i + (1-\Lambda_i)R_i) - n_+ n_e \sum_i (n_1 W_i + n_e O_i + R_i) \tag{9.49}$$

Heavy-particle energy

$$\begin{aligned}\dot{\omega}_{E_h} \equiv \frac{\partial E_h}{\partial t} = &\; n_1 \sum_i \sum_{j>i} \varepsilon_{ij}(n_j L_{ji} - n_i K_{ij}) && \text{from (9.2)} \\ &+ n_1 \sum_i I_i(n_e n_+ W_i - n_i V_i) && \text{from (9.4)} \\ &- 3\rho_e n_n k_{\mathrm{B}}(T_h - T_e)\frac{k_{en}}{m_{Ar}} && \text{from (9.39)} \\ &- 3\rho_e n_+ k_{\mathrm{B}}(T_h - T_e)\frac{\bar{k}_{ei}}{m_{Ar^+}} && \text{from (9.43)}\end{aligned} \tag{9.50}$$

Electron energy

$$\begin{aligned}\dot{\omega}_{E_e} \equiv \frac{\partial E_e}{\partial t} = &\; n_e \sum_i \sum_{j>i} \varepsilon_{ij}(n_j F_{ji} - n_i C_{ij}) && \text{from (9.1)} \\ &+ n_e \sum_i I_i(n_e n_+ O_i - n_i S_i) && \text{from (9.3)} \\ &+ \sum_i ((n_i(1-\Lambda_i) - n_e n_+)R_i') && \text{from (9.6)} \\ &- n_+ n_e \frac{16\pi^2}{3\sqrt{3}} \frac{\bar{v}_e Z_{\mathrm{eff}}^2 e^6 \bar{g}}{m_e h(4\pi\epsilon_o c)^3} && \text{from (9.31)} \\ &+ 3\rho_e n_n k_{\mathrm{B}}(T_h - T_e)\frac{k_{en}}{m_{Ar}} && \text{from (9.39)} \\ &+ 3\rho_e n_+ k_{\mathrm{B}}(T_h - T_e)\frac{\bar{k}_{ei}}{m_{Ar^+}} && \text{from (9.43)}\end{aligned} \tag{9.51}$$

A necessary condition in closure of the above system is the assumption of quasi-neutrality,

which in this instance takes the form

$$n_e = n_{Ar^+(j_c=3/2)} + n_{Ar^+(j_c=1/2)}. \tag{9.52}$$

It is important to note that since ionization and recombination proceed to and from either $Ar^+(j_c = 3/2)$ or $Ar^+(j_c = 1/2)$, the rates associated with such processes are functions of j_c as well, such that

$$S_i,\ O_i,\ W_i,\ V_i,\ R_i = f(j_c). \tag{9.53}$$

Due to inevitable stiffness in the above system, the CR kinetics are solved implicitly, the algorithm for which is detailed in Appendix D.

CHAPTER 10

UTIAS SHOCK TUBE EXPERIMENTS

While conducting shock tube experiments at the Institute for Aerospace Studies, University of Toronto (UTIAS), Brimelow [16] discovered instabilities in the translational shock front of a strong ionizing shock in argon. The discovery set off a series of experiments that extended the research to various Mach numbers and other noble gases, including krypton and xenon. The UTIAS experiments were unique in that it was the first time instabilities were observed in an ionizing shock. The instabilities, which were observed as aberrations in the translational shock front and electron avalanche, were labeled as *sinusoidal* and an explanation for their existence was not determined.

These experiments provided invaluable data for which to benchmark theoretical and numerical models, including databases. Measurements were taken in the form of interferograms from which the total mass and electron number densities were derived. From this data, key parameters for describing the shock structure can be ascertained, including the peak ionization fraction, α, and the relaxation length, ℓ, as measured from the shock front to the location of peak ionization.

Glass and Liu [42] provided a theoretical model that was used in the analysis of the resulting shock structure based on the conditions of several of the UTIAS experiments. In particular, they determined the relaxation length to be a function of the excitation cross sections by atom-atom, σ^a, and electron-atom, σ^e, impact; the elastic cross sections for electron-neutral, σ^{en}, and Coulomb, σ^{ei} collisions; and the combined radiation losses, q_{rad}:

$$\ell = \ell(\sigma^a, \sigma^e, \sigma^{en}, \sigma^{ei}, q_{\text{rad}}) \tag{10.1}$$

Of these, the atom-atom excitation cross sections were found to have the largest influence

on the relaxation length, which currently maintain an association with the largest amount of uncertainty.

The work of Cambier [21] extended the model to include one-dimensional transient effects and found that pressure pulses initiated by the electron avalanche would propagate downstream, increasing the pressure of the compression shock. The consequential increase in shock intensity was found to shorten the relaxation length and raise the peak ionization fraction. This phenomenon necessitated the addition of a new parameter τ to describe the periodicity of shock fluctuations.

Here, the collisional-radiative model detailed in the previous chapter is combined with the transport equations in order to match the experimental results of the UTIAS shock tube experiments presented by Glass and Liu. We proceed by first simplifying the governing equations to a steady-state form to develop a baseline for the collisional-radiative cross sections. Transient simulations are then performed in one- and two-dimensions to determine the effect of the cross sections on the dynamical behavior of the ionizing shock.

10.1 Steady-state simulations

Although the data provided by the UTIAS experiments are *snapshots* of dynamic behavior, steady-state calculations can nonetheless provide valuable insight to the shock structure. Such numerical experiments were carried out in [42] and are important in the current analysis as well to determine the atom-atom impact excitation cross sections.

With the conditions downstream of the shock known along with the shock Mach number, the Rankine-Hugoniot relations were applied to determine the post shock conditions. A shooting method was then used to determine the steady-state shock structure, with the post shock conditions serving as the initial values.

The steady-state form can be found by canceling the time-dependent term from the differential form of the governing equations (cf. Eq. (2.9)),

$$\cancelto{0}{\frac{\partial Q}{\partial t}} + A\frac{\partial F}{\partial x} = \dot{\Omega}, \tag{10.2}$$

reducing the system to a set of ODE's,

Case	Reference	Ma_s	$p_\circ$ [torr]	$T_\circ$ [K]	ℓ [cm]	α
1	1	15.9	5.14	293.6	2.00	0.14
2	2	16.1	5.15	295.9	1.90	0.15
3	3	16.5	5.12	296.6	1.80	0.16
4	4	13.0	5.01	296.6	8.90	0.06
7	7	14.7	4.08	297.8	4.40	0.106

Table 10.1: Shock tube cases studied by Glass and Liu.

$$\frac{dQ}{dx} = A^{-1}\dot{\Omega}. \tag{10.3}$$

The inverse of the flux Jacobian in Eq. (10.3) can be computed efficiently if the analytical form of the eigensystem is known (see Appendix A), such that

$$\frac{dQ}{dx} = R\Lambda^{-1}L\dot{\Omega}. \tag{10.4}$$

The matrix product on the RHS of Eq. (10.4) can be computed in approximately $2N^2$ operations. The inverse of Λ is well-defined as long as the flow velocity does not approach zero.

Glass and Liu applied their steady-state model in the analysis of four different cases in pure argon which are summarized in Table 10.1[1]. In a similar fashion, Eq. (10.4) has been applied to the same four cases, the results of which are presented in terms of total mass density ρ, electron number density n_e, and ionization fraction α. As there exists a fair amount of uncertainty associated with the atom-atom excitation cross sections σ^a, these were varied until an acceptable agreement between the theoretically-predicted and experimentally-observed relaxation lengths was achieved. Exact agreement for all cases could not be achieved with a fixed value for σ^a. However, good agreement was obtained for the intermediate cases, corresponding to Mach numbers 14.7, 15.9, and 16.1, the results of which are summarized in Table 10.2.

As mentioned in Section 9.1.1, the atom-atom impact excitation cross sections have been approximated as linear functions of energy as based on the model of Drawin. Tuning these cross sections was therefore a matter of modifying their slopes. This was accomplished by

[1]Although not modeled by Glass and Liu, information was provided on the relaxation length and ionization fraction of a Mach 14.7 shock that we also consider here as case 7.

Case	Experiment [cm]	Theory [cm]
1	2.00	2.09
2	1.90	1.88
3	1.80	1.61
4	8.90	10.6
7	4.40	4.48

Table 10.2: Comparison between experimental and steady-state numerical relaxation lengths for ionizing shock in argon.

i	j	β^*_{ij} [m^2/eV]
1	3	9.35×10^{-25}
1	5	3.36×10^{-24}
1	17	8.14×10^{-27}
1	23	2.64×10^{-25}
1	25	7.27×10^{-25}
1	30	1.35×10^{-25}
1	31	5.88×10^{-25}

Table 10.3: Tuned atom impact excitation parameters for allowed transitions from ground state Ar.

multiplying β^*_{1j} in Eq. 9.18 by a factor of 0.085. That is, the current results indicate that Drawin's model over-predicts these cross sections by more than a factor of 10. The modified parameters are summarized in Table 10.3. In comparison with values previously obtained in the literature (cf. Table 1.1), it is evident that the cross sections used here are at the lower end of the spectrum, matching most closely with the values obtained by McLaren and Hobson [72].

10.1.1 Effect of upper levels

In an effort to quantify the influence of the upper levels on the overall shock structure, simulations were first performed taking into account the $4s$ manifold of Ar exclusively, followed by systematic inclusion of higher manifolds, including the $4p$, $5s$ and $3d$. Numerical results obtained with levels of only the $4s$ manifold given in Figure 10.1 show satisfactory prediction of the induction length, but poor reproduction of the radiative cooling region as indicated by the slow drop-off in electron number density, indicating an under-prediction in radiative losses. This is as expected as the the plasma has been assumed to be optically-thick for all transitions to ground state Ar (cf. Section 9.4), resulting in no radiative losses due to

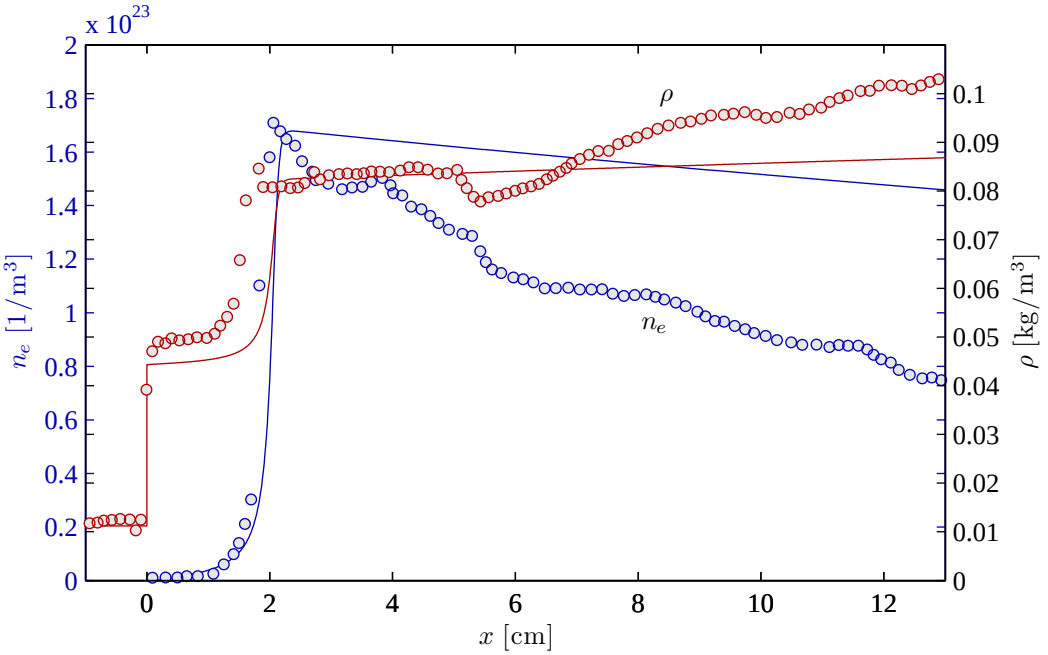

Figure 10.1: Comparison of experimental (∘) and numerical (–) results for Ma 15.9 shock in argon in terms of total mass density ρ and electron number density n_e. Numerical results were obtained using only levels of the $4s$ manifold of Ar.

bound-bound transitions since intra-$4s$ transitions are forbidden. As a result, all radiative losses in this case are due to free-free and free-bound transitions only.

When the levels of the $4p$ manifold are included in the CR model, the numerical prediction of the radiative cooling region drastically improves as indicated by the results in Figure 10.2. The difference clearly represents the direct influence of the 32 allowed transitions within the $4p$ manifold as well as those between the $4s$ and $4p$ manifolds on the radiative cooling region.

Figure 10.2 illustrates the the effects of additional levels, this time with inclusion of levels from the $5s$ and $3d$ manifolds. The results clearly indicate an asymptotic approach of the numerical solution to the experimental results as more levels are included and hence the full extent of radiative losses due to bound-bound transitions are realized.

Similar behavior can also be observed through the influence of additional levels on the ionization fraction as evident in Figure 10.4. As more levels are added, the ionization fraction approaches the experimentally-observed value. Also apparent is the effect of the upper levels on the induction length. Addition of the upper levels increases radiation losses in

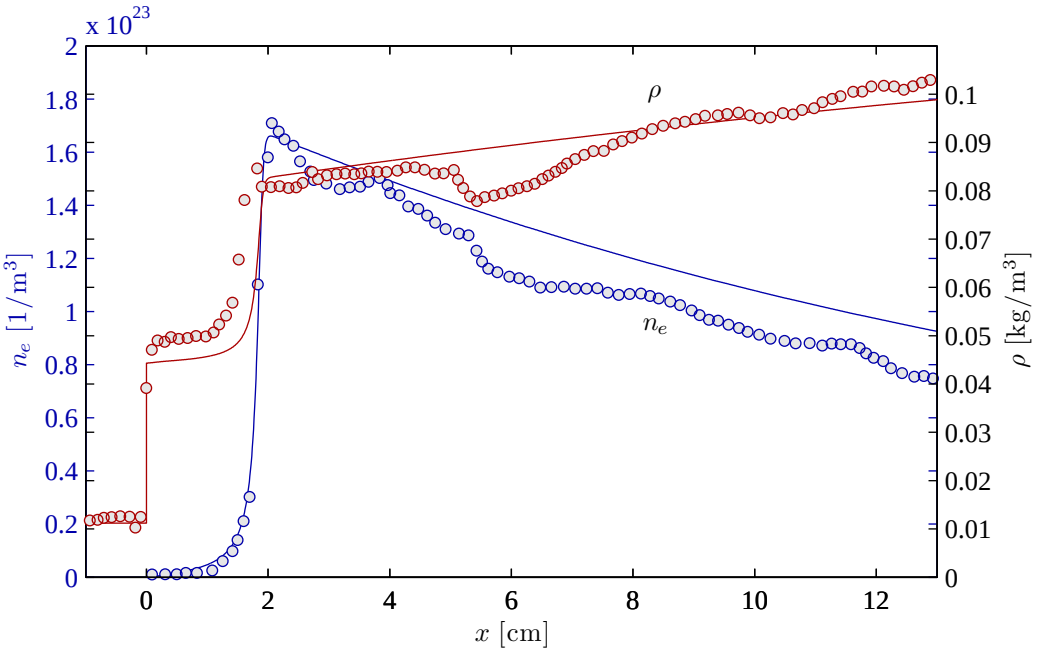

Figure 10.2: Comparison of experimental (∘) and numerical (–) results for Ma 15.9 shock in argon in terms of total mass density ρ and electron number density n_e. Numerical results were obtained using levels of the $4s$ and $4p$ manifolds of Ar.

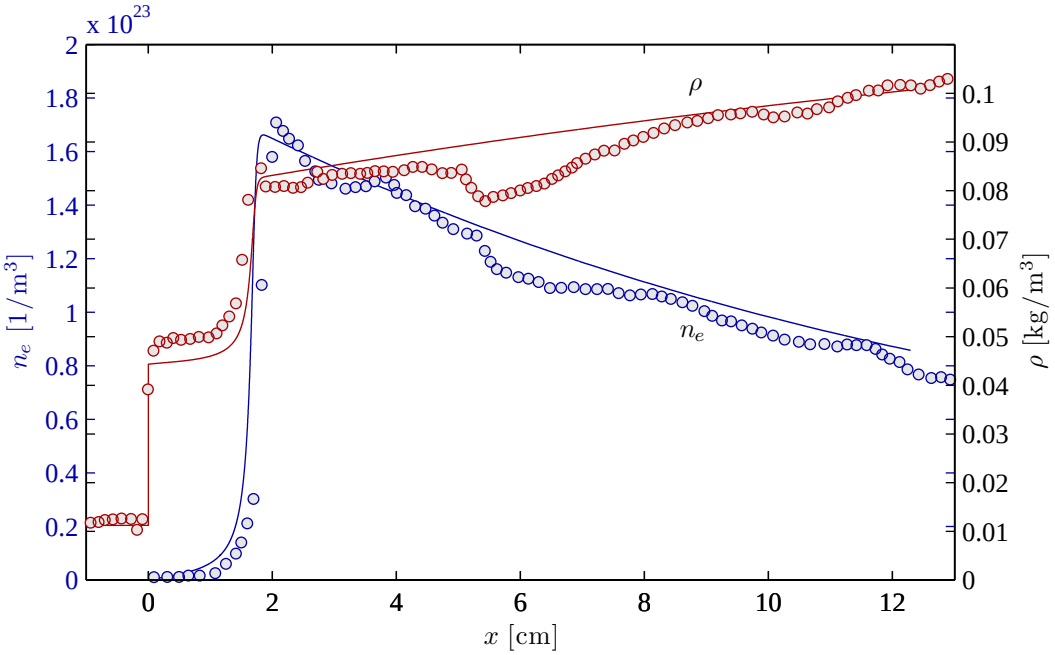

Figure 10.3: Comparison of experimental (∘) and numerical (–) results for Ma 15.9 shock in argon in terms of total mass density ρ and electron number density n_e. Numerical results were obtained using levels of the $4s$, $4p$, $5s$, and $3d$ manifolds of Ar.

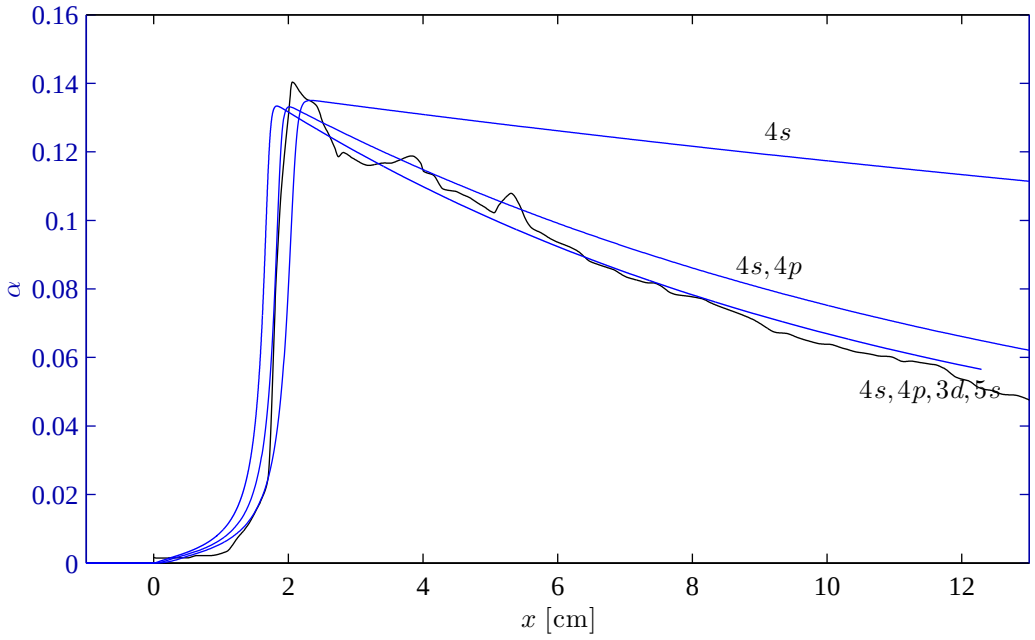

Figure 10.4: Effect of upper levels on the ionizing shock structure as indicated by the ionization fraction. With the inclusion of more levels, the numerical ionization fraction (–) approaches the experimental results (–).

the induction region, thereby delaying the onset of the electron avalanche. It should be noted that the ionization fractions as derived from the experimental data for this particular case, Ma = 15.9, as well as for the case of Ma = 16.1 in [42] do not coincide with the respective total mass and electron number densities provided. As a consequence, the experimental ionization fractions plotted for comparison have been computed directly from the plasma densities. Results for the remaining three cases (2,3,4) have been provided in Appendix E.

10.1.2 Shock structure

Details of the electron and heavy-particle temperature profiles along with the Boltzmann and Saha equivalence temperatures provided in Figure 10.4 help illustrate the influence of the various CR processes and to separate the shock structure into several distinct regions. The first region, easily identifiable by a sharp spike in electron temperature just behind the compression shock, indicates the initial production of priming electrons which are rapidly thermalized by the heavy particles. The excitation temperatures based on a Boltzmann distribution,

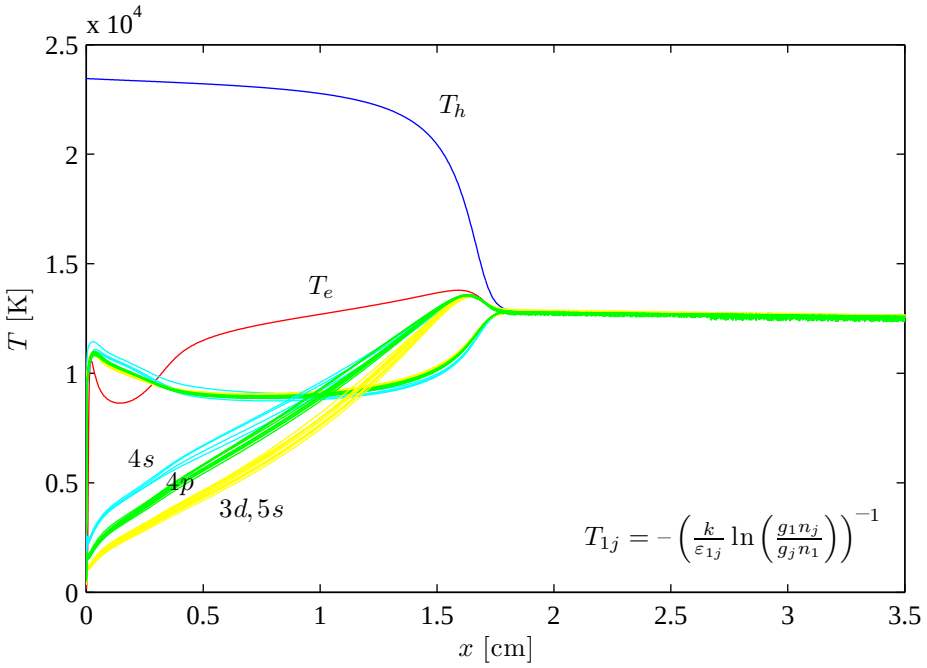

Figure 10.5: Details of the Mach 15.9 ionizing shock structure in terms of electron, heavy particle, and excitation temperatures. The bottom profiles labeled $4s$, $4p$, and $3d$, $5s$ are of the Saha equivalence temperatures of the respective manifolds, while the upper profiles, characterized by a sharp rise accompanied by an overshoot, are of the Boltzmann equivalence temperatures.

$$T_{1j} \equiv -\left(\frac{k_{\mathrm{B}}}{\varepsilon_{1j}} \ln\left(\frac{g_1 n_j}{g_j n_1}\right)\right)^{-1}, \tag{10.5}$$

surpass the electron temperature, indicating over-population of the excited states and confirming that the priming electrons are generated via *Ar*-*Ar* inelastic collisions.

The spike is quickly followed by a dip in electron temperature, signaling a shift from heavy-particle dominated kinetics to electron-impact processes. That is, as the electron population becomes more significant, the electrons themselves become responsible for the bulk of excitation and ionization processes. As a result, thermal energy of the free electrons is transferred to the bound electronic modes as well as liberating more electrons. The dip is the result of this energy transfer which cannot be compensated for by thermalization with heavy-particles. The excitation temperature declines as well, and stabilizes significantly below the electron temperature. This indicates that ionization is rapid from the excited levels under these conditions, causing an under-population of the excited levels, and hence the deviation from T_e.

After this, the electron temperature recovers from the dip and increases steadily as energy is transferred from the heavy-particles to the free electrons at a slightly higher rate than which the electrons lose energy through inelastic collisions. In this region, electron production begins to ramp up exponentially, triggering rapid thermalization with the heavy-particles and the resulting electron avalanche. The avalanche results in complete thermalization between the heavy-particles and electrons, as the energy reserves of the heavy particles becomes exhausted. All levels finally reach Boltzmann and Saha equilibrium and the plasma is well-described by a single temperature.

It is worth noting that the spread of excitation temperatures throughout the shock structure is quite small, indicating Boltzmann equilibrium among the excited levels with respect to the ground state. This indicates a rapid exchange between the excited levels, with the result that the plasma may be approximated by a three-temperature model under such conditions.

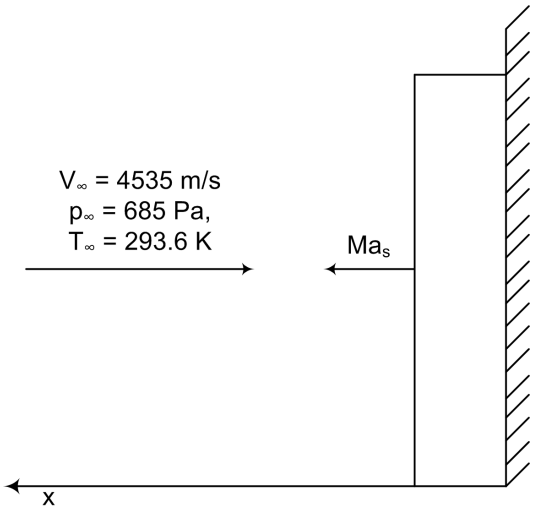

Figure 10.6: Numerical setup for unsteady 1D shock tube simulations.

10.2 Unsteady 1D simulations

With the CR model validated against experimental data for the steady-state case, the unsteady solver was then applied to determine the effect of the kinetics on the dynamic behavior of the system. Initial work on such unsteady effects verified the exsistence of oscillations in the form of longitudinal pulsations in the direction of flow [21]. Building upon this work, similar numerical experiments are carried out here, albeit with the more detailed CR model.

The conditions of the shock tube experiments were simulated numericaly by impinging argon gas upon a wall, thereby initiating a shock that would propagate against the oncoming flow as illustrated in Figure 10.6. The freestream conditions provided in the figure were those used to reproduce the Mach 15.9 shock of case 1. Note that such conditions correspond to a shock with an initial strength of Mach 19. As the shock reflects from the wall, its Mach number decreases as the thermal energy is quickly converted to electronic energy in the form of bound excited states as well as free electrons, until a quasi-steady limit is reached.

The results in Figures 10.7 and 10.8 clearly show oscillations, characteristic of the experimental results, that appear as undamped, periodic fluctuations in both the shock Mach number as well as the induction length, with a periodicity of approximately 32.5 μsec. The oscillations do not vary smoothly as evident in the discontinuous shifts of the induction length, signaling strong non-linear behavior. In fact, this behavior is well approximated by

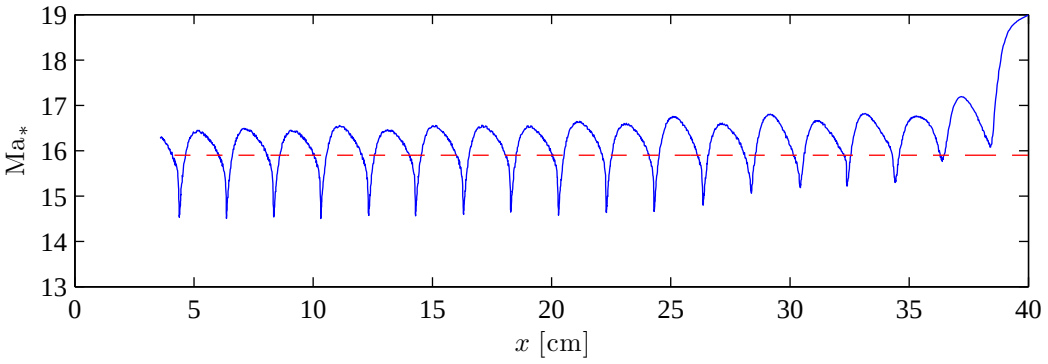

Figure 10.7: Instantaneous Mach number as a function of distance from the wall located at 40 cm for Mach 15.9 case.

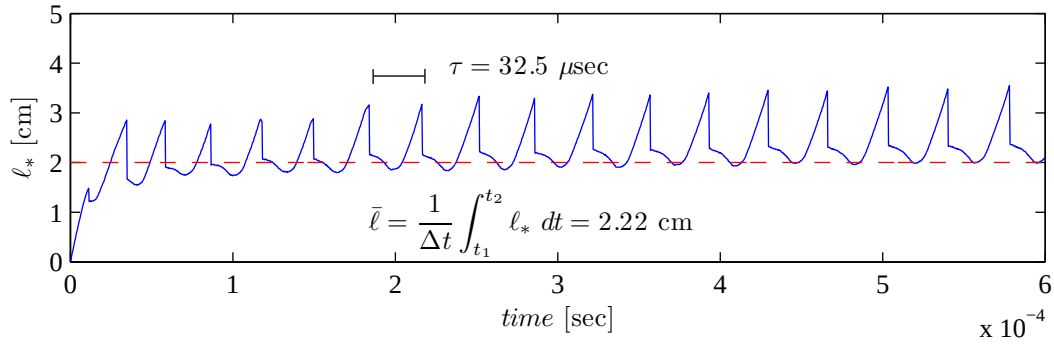

Figure 10.8: Instantaneous induction length as a function of time for Mach 15.9 case. Dashed red line indicates the experimentally observed value of 2 cm. The fluctuation periodicity is 32.5 μsec, with an induction length of 2.22 cm averaged over one period.

the square-wave model for detonations [39] in which the kinetics are assumed to be frozen below a certain threshold, but infinitely fast above, reaching equilibrium instantaneously. This necessitates introduction of an average induction length defined over one period,

$$\bar{\ell} = \frac{1}{\Delta t}\int_{t_1}^{t_2} \ell_* dt, \tag{10.6}$$

with ℓ_* being the instantaneous induction length. In regards to the discontinuous change in the induction length exhibited in this particular case, there is evidence that these anomalies have a physical origin. From the experimental results, it can be seen that in certain regions the ionization fraction rises before taking a sharp dip after which it spikes until the peak of the avalanche is realized.

10.2.1 Fluctuation mechanism

A semiquantitative description of the fluctuations can be extracted from the space-time plots given in Figure 10.2.1 as well as several snapshots illustrated in Figure 10.2.1. The plots clearly show pressure waves emerging from the electron avalanche that travel both towards and away from the compression shock. This is taken as the initiation of the fluctuation cycle. The forward-moving wave overtakes the shock, thereby increasing its temperature and speed.[2] The resulting high temperature region generated behind the shock is separated from the previous post-shock region by a contact wave that can be seen as traveling away from the shock as it accelerates. Identification of the contact waves is trivial as they are present in the mass density plot but absent in the pressure plot.

The temperature jump across the contact wave is crucial. Due to the exponential dependence on temperature, a relatively small jump can accelerate the kinetics and cause the electron avalanche to form much sooner than its quasi-equilibrium position. This discontinuous shift in the electron avalanche evident in Figure 10.2.1 is entirely analogous to the mechanism for detonation wave fluctuations proposed by Alpert and Toong [2].

This theory of the fluctuation mechanism can be confirmed by a simple estimation of the periodicity of the oscillations from basic wave theory. In [21] it was shown that the period can be approximated by

$$\tau = \bar{\ell}\left(\frac{1}{a_2 - u_2} + \frac{1}{u_2}\right), \tag{10.7}$$

assuming that the pressure wave travels towards the shock with the nonlinear wave speed $a_2 - u_2$, while the entropy wave reflected from the shock travels with velocity u_2, where the subscript 2 denotes the post-shock state. With $u_2 = 1284$m/s and $a_2 = 2852$m/s taken as the post-shock fluid and sound speeds respectively, the estimated periodicity is 31.4μsec which agrees well with the observed value of 32.5μsec (cf. Figure 10.8).

10.2.2 Sensitivity to cross sections

Knowing the effect of the cross sections on the dynamics of the oscillations is crucial to a stability analysis. While an analytical approach to stability is not pursued here, semi-

[2]The interaction also produces a rarefaction wave due to the acceleration of the shock which is too weak to notice here.

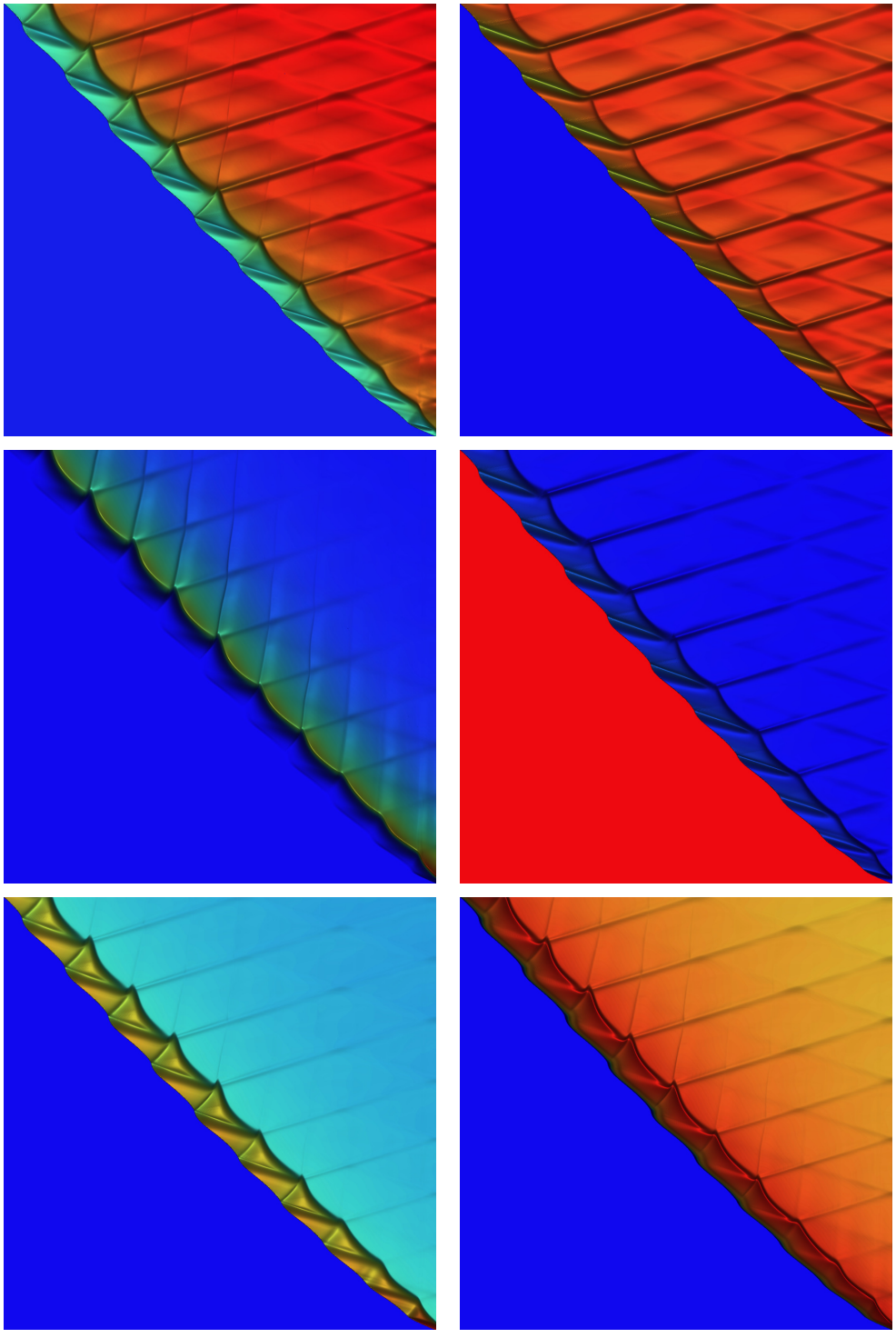

Figure 10.9: x-t diagrams for 1D Ma 14.7 case. Clockwise from top left: total density, total pressure, velocity, electronic temperature, heavy-particle temperature, and ionization fraction. Gradients are enhanced through shading effects. Colormap: *min* *max*

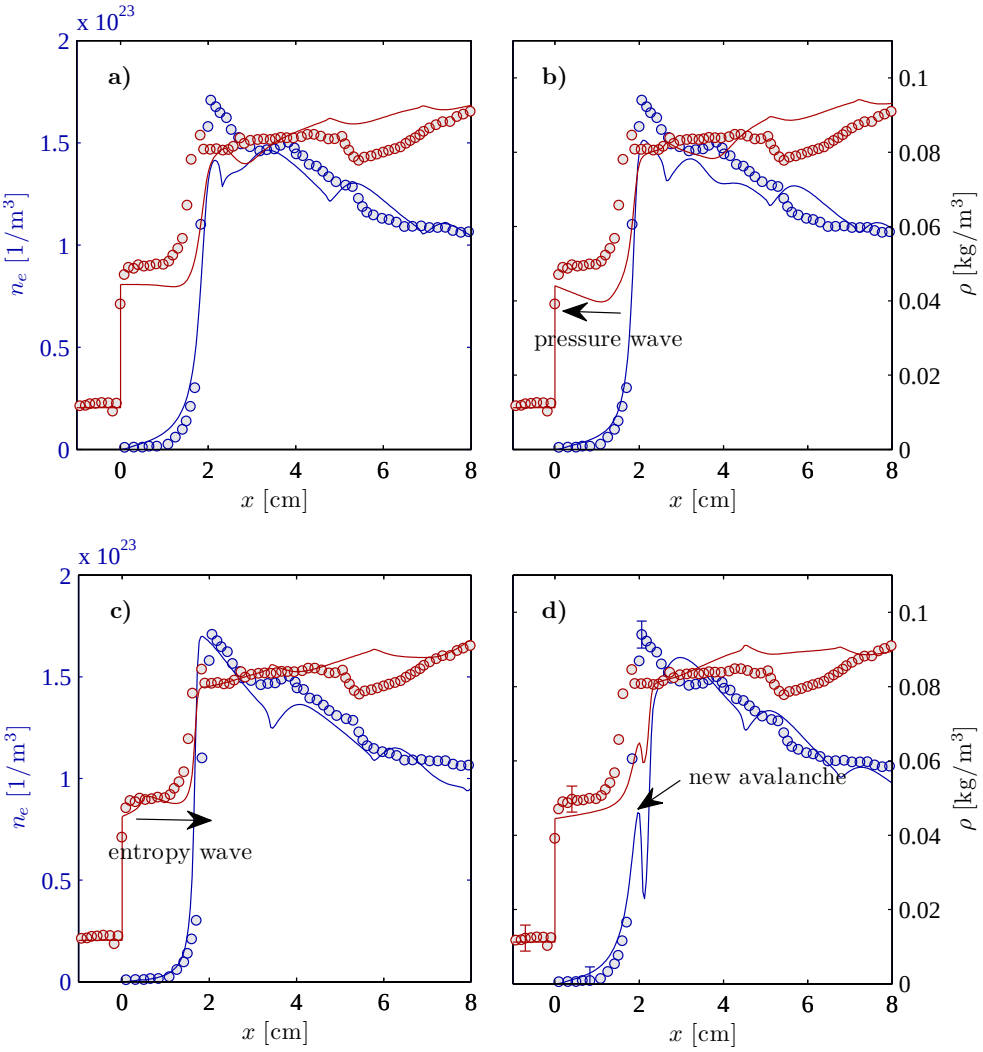

Figure 10.10: Dynamic evolution of 1D ionizing shock structure: a) quasi-equilibrium state b) pressure wave initiated at electron avalanche travels towards compression shock c) after overtaking shock, pressure wave is reflected as an entropy wave due to strengthening of shock d) sensitivity of excitation and ionization rates to temperature jump across entropy wave results in earlier onset of electron avalanche. The process then repeats.

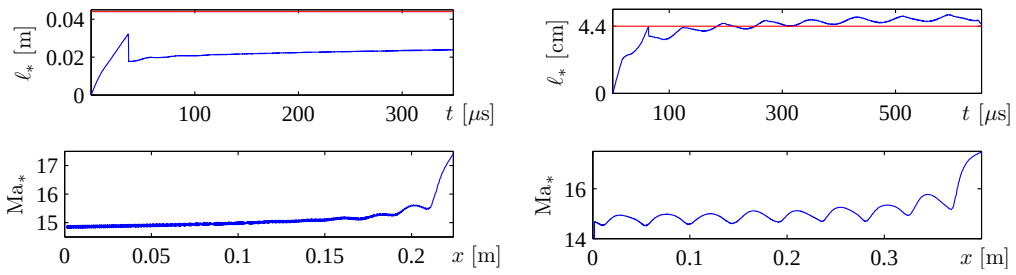

Figure 10.11: Sensitivity of 1D ionizing shock oscillation dynamics to cross sections. Left: Results using Drawin's atom-atom impact excitation cross sections. Right: Results obtained after decreasing electron-atom impact excitation cross sections by a factor of ten.

empirical considerations can serve as a valuable precursor to such studies.

As a first test, the Mach 14.7 case was run using the atom-atom impact excitation cross sections as computed from Drawin's formula, Eq. (9.17), without modification. As a reminder, the resulting rates are more than a factor of ten greater than those used to obtain the solutions with the experimentally-observed induction length. The results shown in Figure 10.2.2 indicate that increasing the atom-impact excitation cross sections by an order of magnitude, essentially halves the induction length. Furthermore, the influence on the oscillations is pronounced, resulting in significant damping to the point that the oscillations can no longer be sustained. The explanation for this is as follows. As the pressure wave emanating from the electron avalanche overtakes the compression shock, the heavy particle temperature increases. This in turn increases the atom-impact inelastic processes accordingly to their exponential dependence on T_h. The atom-impact inelastic processes thus act as an energy sink, effectively absorbing energy from the pressure wave and damping the oscillations.

In a separate test, the electron-atom impact excitation cross sections were reduced by a factor of ten. In this case the atom-atom impact excitation cross sections were also modified so that the induction length was close to 4.4 cm as seen in Figure 10.2.2. While the oscillations still persist in this case, a key observation is that the discontinuous change in the induction length (cf. Figure 10.7) has disappeared. Instead, the oscillations vary smoothly over the entire period of the fluctuation. The discontinuous shift is a nonlinear effect caused by the exponential temperature dependence of the rate equations and is well-approximated by the square-wave model for detonation phenomena as previously noted.

As the electron-impact cross sections are decreased, this nonlinear effect diminishes, and is overshadowed by other processes, such as thermalization. This slows the rate of onset of the electron avalanche and gives the fluid more time to "react" to the kinetics.

10.3 Unsteady 2D simulations

With a general understanding of the oscillation mechanism and resulting wave pattern observed in the unsteady 1D simulations, focus was then set upon extending the simulations and theory to a two-dimensional shock tube. With a second dimension, the oscillations observed in the 1D simulations are no longer confined to the longitudinal direction, leading to the possibility of transverse waves. While this opens the door to more complex wave interactions and structures, a systematic approach that extends the ideas of the previous section in a straight-forward manner is taken here.

The 2D simulations were conducted on the domain $0 \leq x \leq 54$ cm, $0 \leq y \leq 18$ cm, with a depth of 10 cm[3]. A general schematic is provided in Figure 10.3. The simulations were initiated in the same manner as the 1D simulations, with a high speed flow impinging upon a wall, resulting in a shock propagating in the opposite direction. The difference being, however, that the 2D simulations required an initial perturbation to initiate *disturbances* in the transverse direction. While such disturbances can have any number of origins in an actual shock tube[4], such disturbances must be explicitly included in the numerical experiment as small perturbations. Such perturbations must be sufficiently random and weak as to not overshadow the dynamics inherent in the model, yet strong enough to initiate pressure disturbances that can essentially be picked up and amplified by the (GE).

Simulations have been performed for two of the cases, including Mach 14.7 and 16.5. All simulations shown were run on a Cartesian mesh with $\Delta x = \Delta y = 0.33$ mm and have taken into account excited levels from only the $4s$ manifold of neutral argon. It was shown in the 1D simulations that although higher levels are required to obtain good agreement in the radiative cooling region, the induction zone is for the most part unaffected. Therefore, neglecting the levels beyond those conatined in the $4s$ manifold should have negligible effect on the overall dynamics.

[3]The actual width of the UTIAS shock tube was 17.78 cm with a depth of 10.16 cm [18].
[4]Including turbulence, boundary layer effects, wall irregularities, etc.

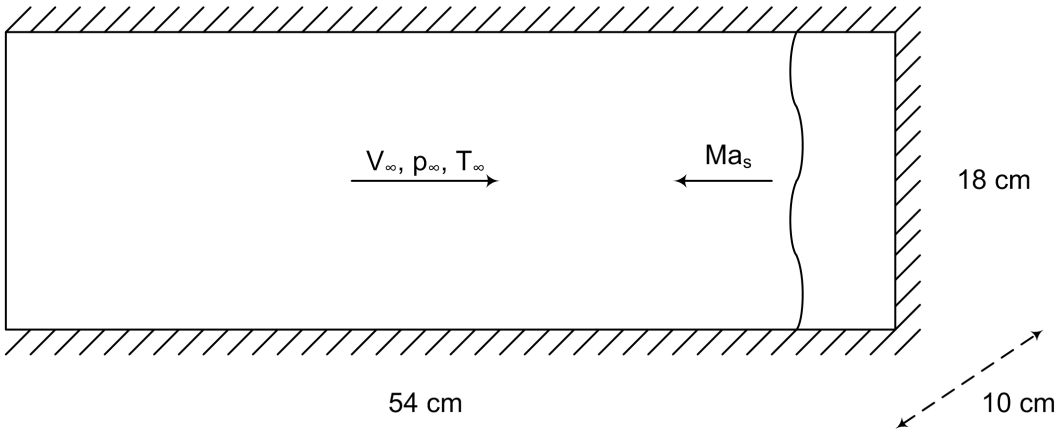

Figure 10.12: Numerical setup for 2D unsteady shock tube simulations.

10.4 Mach 16.5 case

Figure 10.13 shows the evolution of the Mach 16.5 ionizing shock from a nearly planar wave to a self-sustaining oscillating pattern. The initial perturbation, visible as a half-sine wave bulge in the shock front, generates transverse waves that are apparently random in nature. After propagating a few centimeters, however, the waves begin to oscillate with a resonant frequency, creating the strong incident and reflected shock pattern that is clearly visible.

Figure 10.4 provides snapshots of the same simulation at a later time as generated by two different visualization techniques. From the finite-fringe interferogram, it is clear that the simulations have produced corrugations in the shock front similar to the UTIAS experiments. The refractive index plot further reveals a well-defined structure behind the shock, having a periodic nature in the transverse direction. From an investigation of the wave structure it was determined that the shock front actually consists of incident and reflected shocks as well as Mach stems, the intersection of which forms a series of triple points. These nodes appear in a quite regular pattern in both the longitudinal and transverse directions, indicating a resonant phenomenon. The triple points are a source of significant vorticity, the trace of which, given in Figure 10.15, highlights a cellular structure, remarkably similar to detonation cells. These analogous *ionization* cells, bounded by the trace of triple points, initiate at the intersection of two triple points which causes a high-temperature node. This node can be thought of as a two-dimensional analog to the one-dimensional electron avalanche. The resulting pressure wave generated by the increase in electron number density at this point

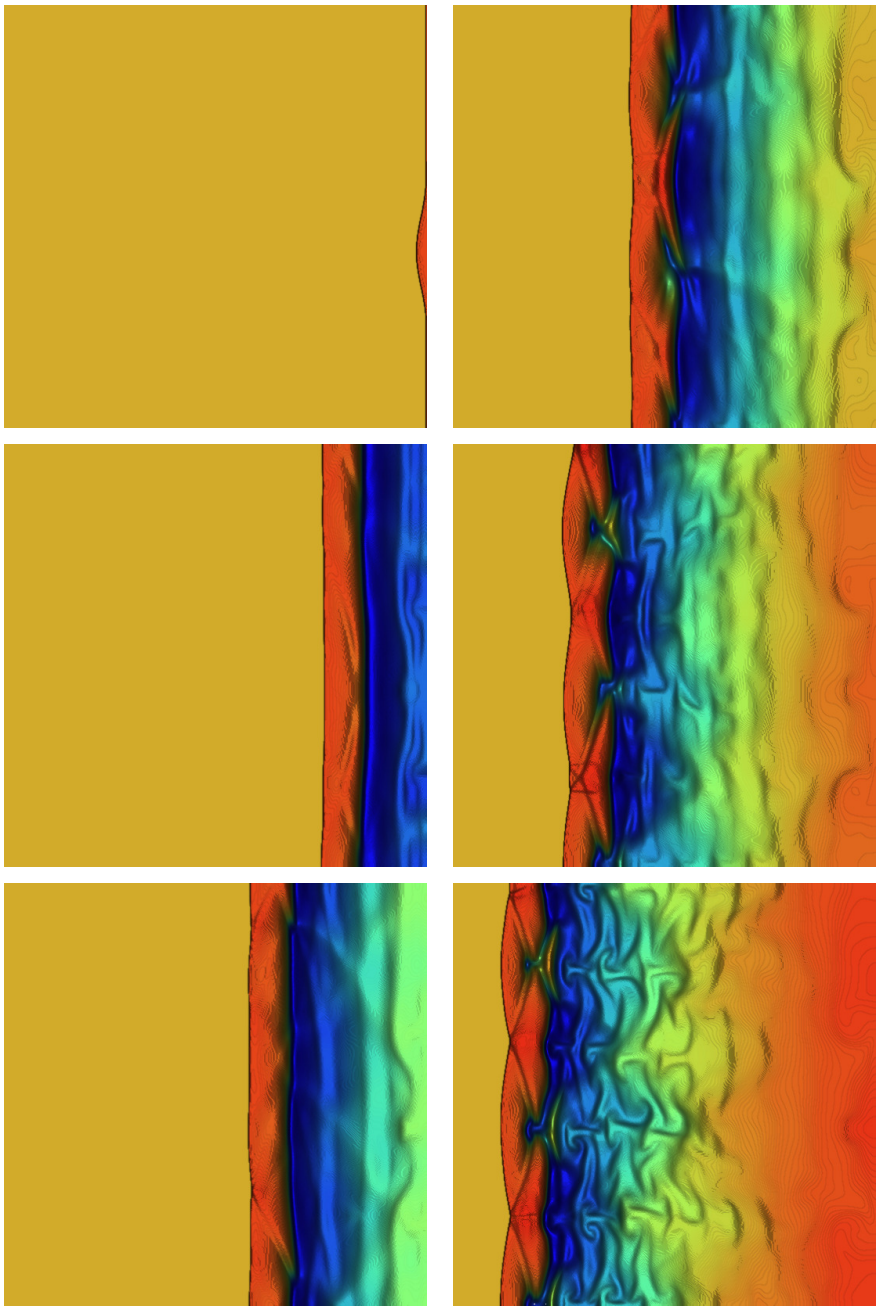

Figure 10.13: Evolution of Mach 16.5 shock, showing transition from 2D planar shock to oscillating shock. The perturbation seen in the first frame triggers transverse waves that initially appear random, but develop into a definite. Colormap: *min* *max*

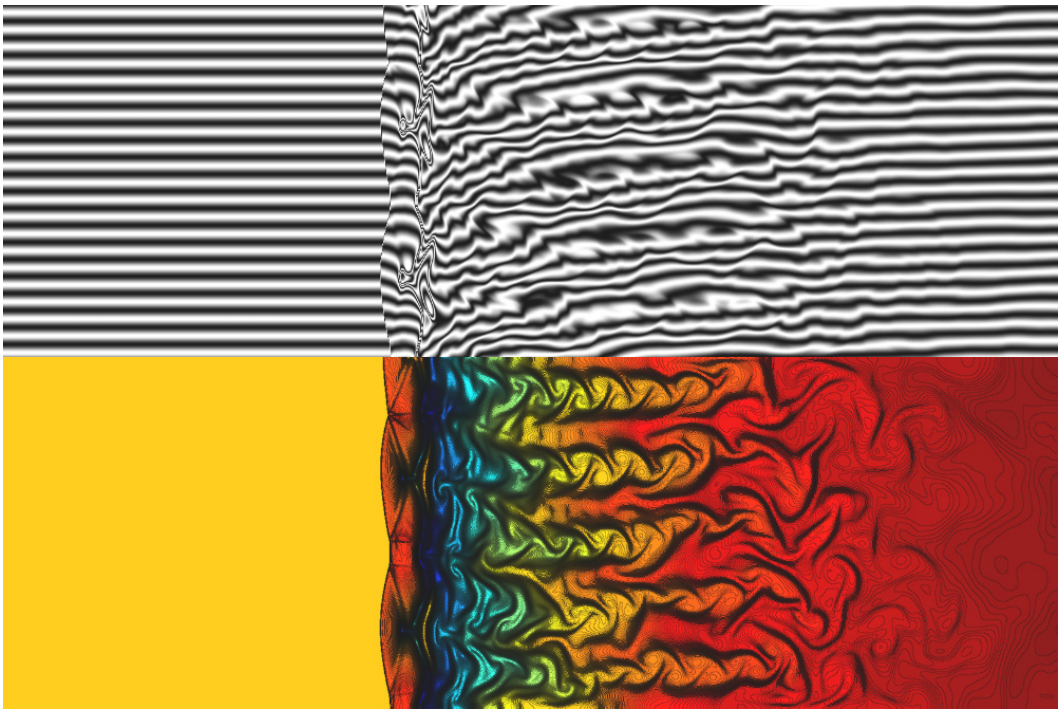

Figure 10.14: Simulated interferogram and refractive index for 2D Mach 16.5 shock. The shock front consists of incident and reflected shock waves. Colormap: *min* *max*

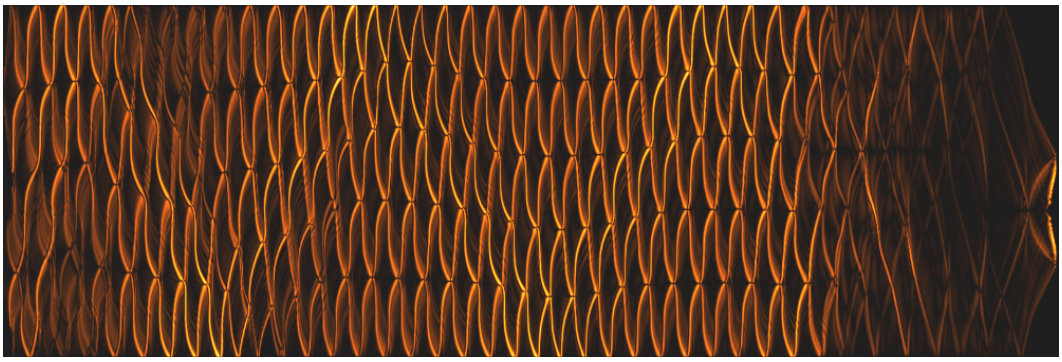

Figure 10.15: Trace of triple points for Mach 16.5 case exposing ionizing cell structure. Brighter regions correspond to stronger flow vorticity.

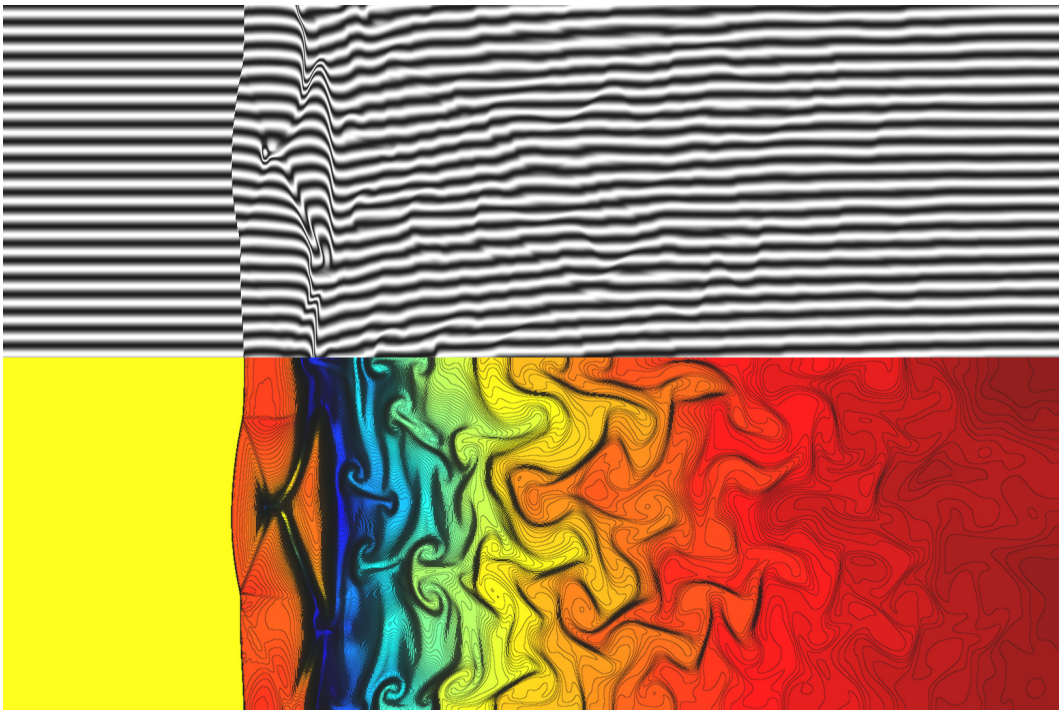

Figure 10.16: Simulated interferogram and refractive index for 2D Mach 14.7 shock. Colormap: *min* *max*

travels radially outward, as indicated by the trace of triple points.

10.5 Mach 14.7 case

The case of a Mach 14.7 shock was also simulated, and from the snapshots in Figure 10.16, as well as the simulated soot trace in Figure 10.5, it is clear that decreasing the Mach number has increased the cell size in both the longitudinal and transverse directions. A direct comparison of the experimental and simulated results for the Mach 14.7 case is presented in Figure 10.5. As can be seen, the shock structure is well-predicted by the numerical simulations, with similar relaxation lengths and discontinuous gradients in the electron avalanche region along the transverse direction.

A comparison between the shock structure of the refractive index and features of the experimental interferogram in Figure 10.19 indicate the two match well. Well enough, in fact, that a similar shock structure can be overlaid upon on the experimental results showing excellent agreement and compatibility with the visible structures. In particular, the pattern

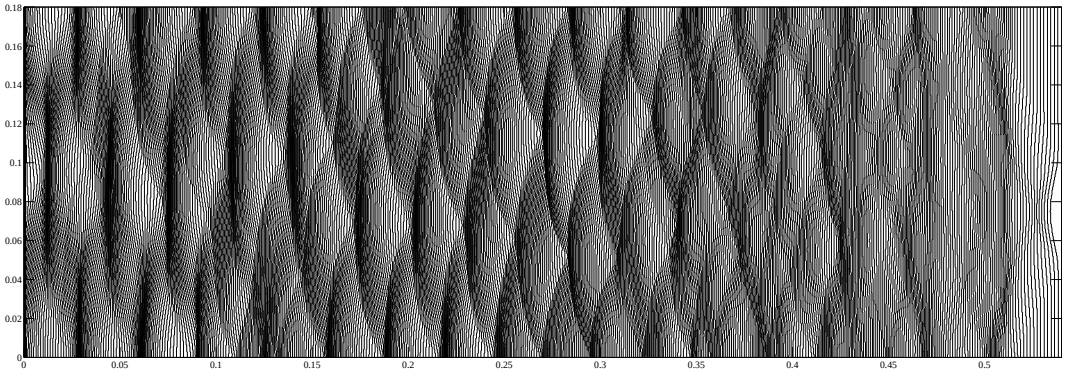

Figure 10.17: Numerical soot trace for Mach 14.7 case, exposing ionizing cell structure. Image was made by super-imposing instantaneous snapshots of the shock front.

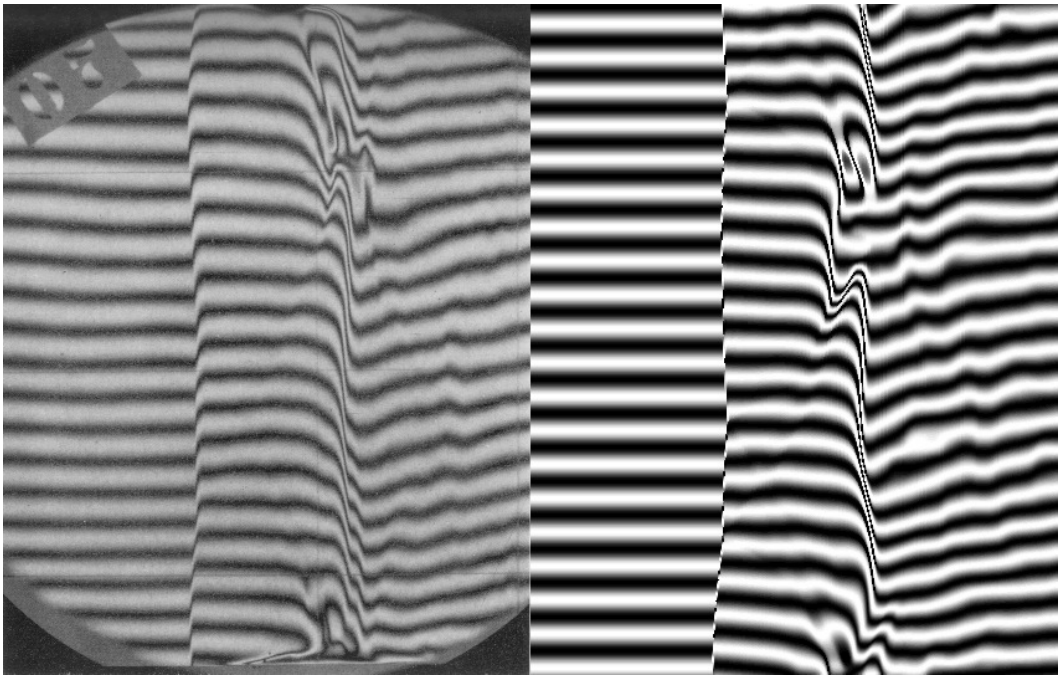

Figure 10.18: Direct comparison of experimental and numerical results for Mach 14.7 shock. Clearly evident are the corrugations in the compression shock as well as unique formation patterns in the electron avalanche which are accurately reproduced by the solver.

of incident and reflected shocks is clear in the fringe shifts of the interferogram.

10.5.1 Cell size approximation

Estimation of the 2D cell size was also provided in [21], based on an extension of the 1D periodicity calculation. In particular, it was determined that the longitudinal periodicity

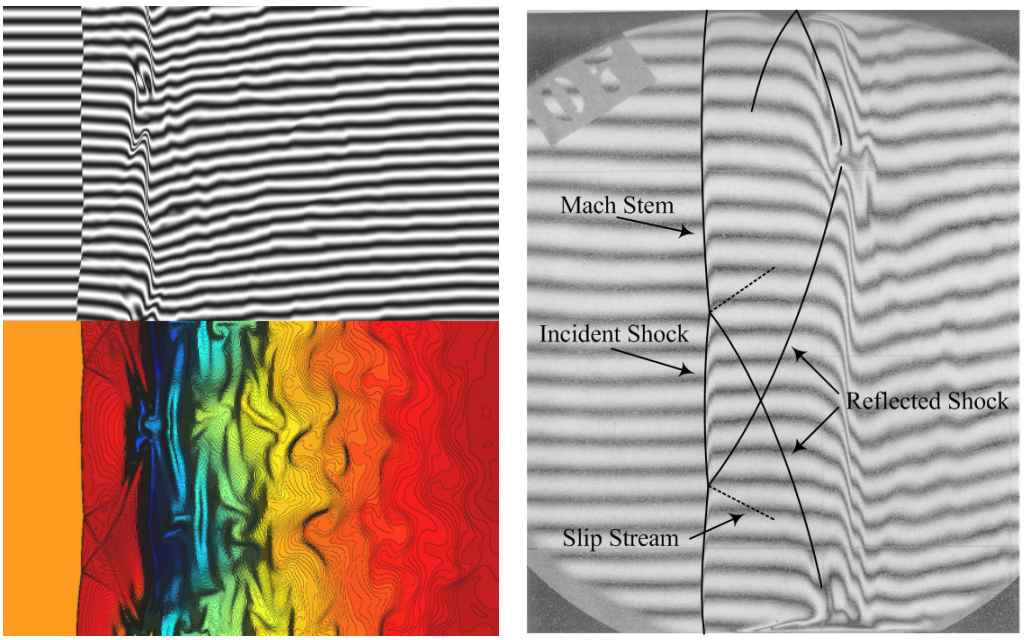

Figure 10.19: Details of the 2D ionizing shock structure for the Mach 14.7 case. The experimental shock structure can be inferred from a comparison of the simulated interferogram and refractive index plots. Incident and reflected shocks are evident in the shift in fringes in the induction zone.

must equal the transverse wave propagation time across the height (y-dir) of one complete cell. The cell width can therefore be estimated by

$$\delta \approx (a_2 + \cancelto{0}{v_2})\tau, \tag{10.8}$$

where the bulk velocity in the transverse direction behind the shock, v_2, is assumed to be zero. Using the periodicity as determined in the 1D Mach 15.9 simulations, the periodicity of the Mach 14.7 and 16.5 cases can roughly be approximated by

$$\tau' \simeq \frac{Ma}{Ma'}\frac{\ell'}{\ell}\tau. \tag{10.9}$$

From this it is found $\tau'_{Ma14.7} \simeq 77$ μsec and $\tau'_{Ma16.5} \simeq 28$ μsec. Plugging these values into Eq. 10.8 gives $\delta_{Ma14.7} \simeq (2658 \text{ m/s})(77\ \mu\text{sec}) \simeq 20$ cm and $\delta_{Ma16.5} \simeq (2973 \text{ m/s})(28\ \mu\text{sec}) \simeq 8.3$ cm. The predicted cell height for the Mach 16.5 case agrees favorably with the numerically-observed value of 7.2 cm, while there is a bit of over-prediction for the Mach 14.7 case with a maximum observed value of just under 14 cm.

CHAPTER 11

IONIZING FLOW PAST A CIRCULAR CYLINDER

Furthermore, with similar structures between ionizing shocks and detonation waves,

With the numerical solver proven capable of reproducing the detailed shock structure and dynamic behavior observed in the UTIAS shock tube experiments, it was a natural progression to apply the solver to other flow configurations. Of particular interest, an extension of the solver to external flows is suggested by a series of experiments performed by Lehr [64] of a projectile fired into a hydrogen-oxygen mixture, producing a detonation shock front with nearly identical oscillating wave patterns as that of the 1D ionizing shock simulations (cf. Figure 11.1). With such similar behavior between detonations and ionizing shocks as detailed in the previous chapter, the Lehr experiments open the possibility of oscillating ionizing shock fronts in external flow cases.

11.1 Numerical results

To test this theory, the flow solver has been applied to a single quadrant of a circular cylinder with a mesh defined by the transformation,

$$x = (R_x - (R_x - R_\circ)\xi)\cos\theta \tag{11.1}$$

$$y = (R_y - (R_y - R_\circ)\xi)\sin\theta \tag{11.2}$$

on the domain $\xi = [0, 1]$, $\theta = [\pi, 3\pi/2]$, with $R_x = 0.075$ m, $R_y = 0.14$ m, and $R_\circ = 0.05$ m. While relatively simple in nature, this particular transformation demonstrates the potential of the solver to handle non-orthogonal, curvilinear geometries. The topology of the grid and

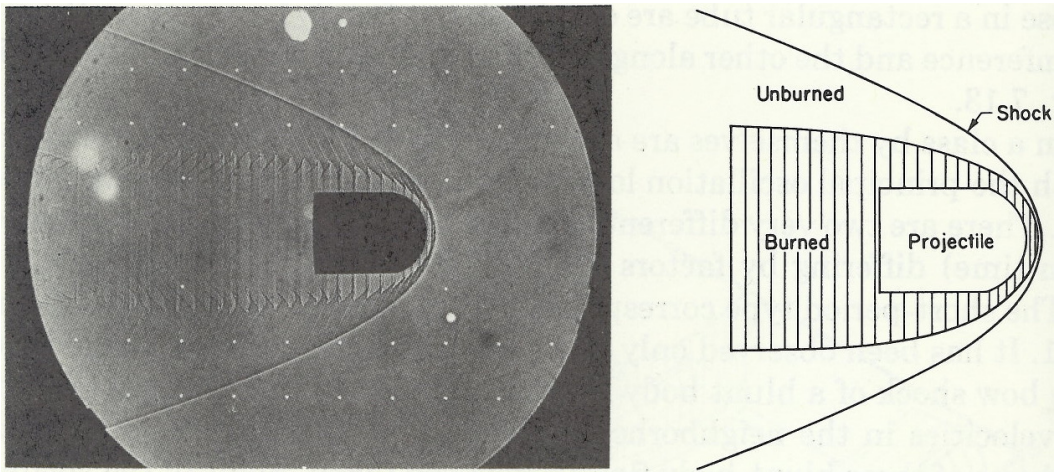

Figure 11.1: Lehr's detonation experiment of a projectile traveling through hydrogen-oxygen mixture. Taken from [39].

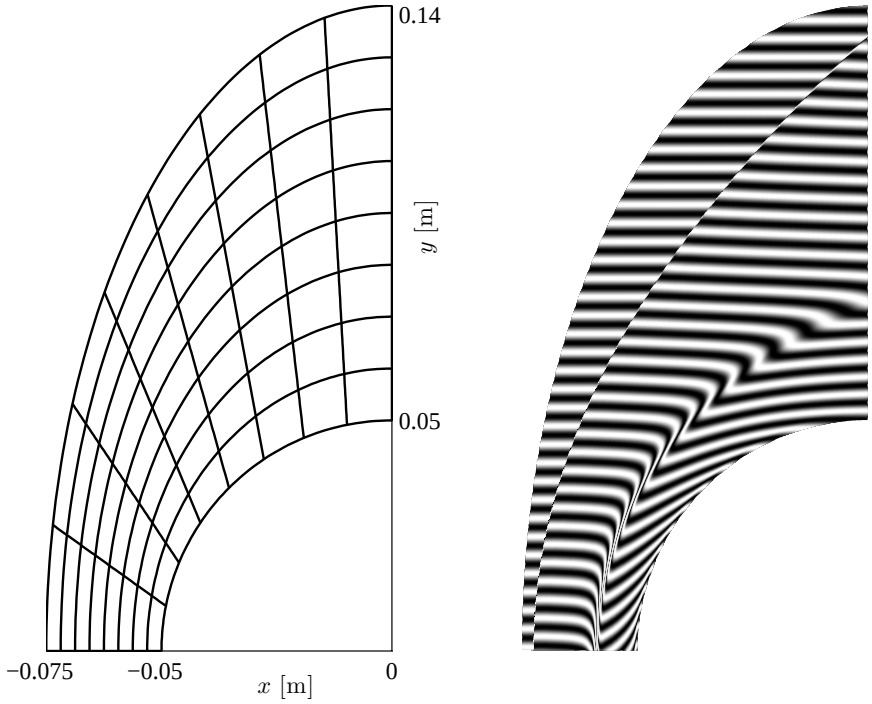

Figure 11.2: Mesh used in computation of fow around cyinder and simulated interferogram.

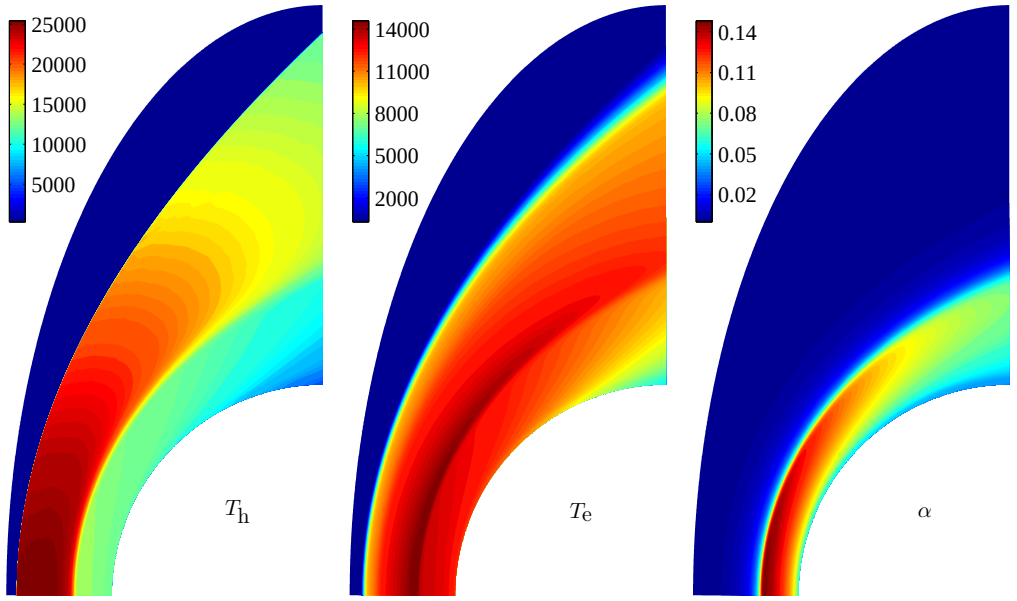

Figure 11.3: Heavy particle and electron temperatures and ionization fraction for fow around cyinder.

resulting domain decomposition are given in Figure 11.2. The actual mesh consisted of 144 domains, each containing 50×50 cells.

Results for a shock of Mach 18.1 are given in Figure 11.3 for which the free stream conditions are given by

$$\begin{pmatrix} u_\infty \\ p_\infty \\ T_\infty \end{pmatrix} = \begin{pmatrix} 5292 \text{ [m/s]} \\ 4.08 \text{ [torr]} \\ 297.8 \text{ [K]} \end{pmatrix}. \tag{11.3}$$

The simulation was performed taking into account only the $4s$ manifold as in the 2D unsteady shock tube experiments presented in the previous chapter. The conditions result in a relaxation length of 1.45 cm along the stagnation line as seen in Figure 11.4.

The results in Figures 11.3 represent a truly steady-state solution in which there are no oscillations or fluctuations. Such a steady solution is not entirely unexpected and may be described as follows. As compared with the pressure waves generated by the heat release and specie production in the Lehr experiments, the pressure waves generated by the electron avalanche are relatively weak. As a consequence, any pressure disturbances are quickly convected past the cylinder, without the possibility of interacting with the compression

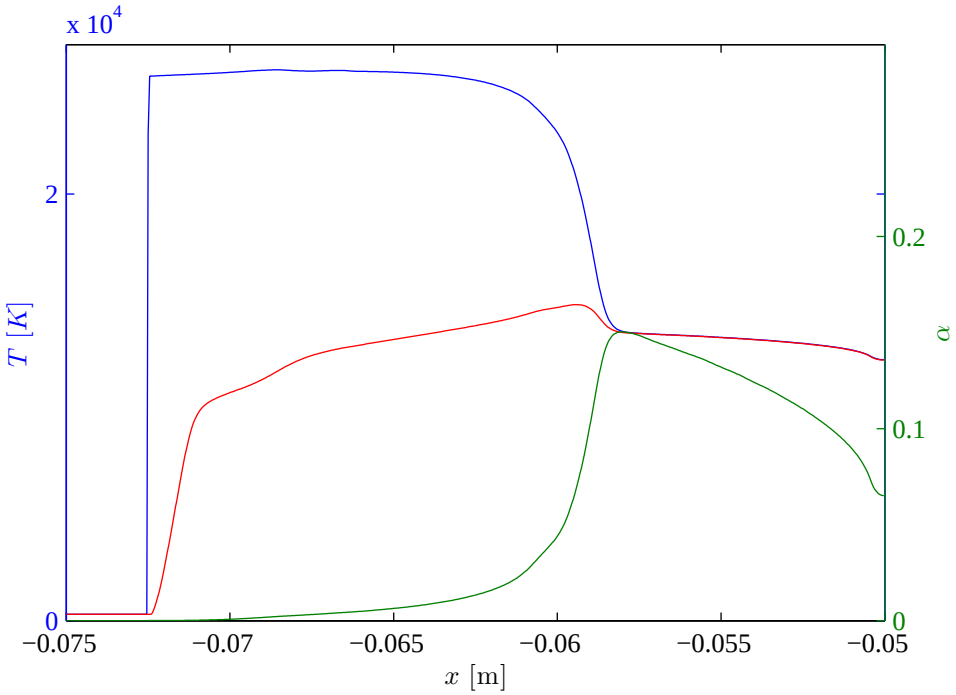

Figure 11.4: Temperature profiles and ionization fraction taken at $\theta = 0$ for flow past cylinder.

shock. This result, however, does not preclude the possibility of such oscillations for external flows involving other geometries. Increasing the bluntness of the geometry may serve to *trap* the pressure waves so that they are able to overtake the shock. Investigation of alternate geometries is planned as a part of future work.

11.2 Excitation temperatures

With the number densities of all the excited states known, the degree of non-equilibrium can be assessed in terms of the excitation temperature between levels i and j as defined in terms of the Boltzmann distribution,

$$T_{ij} \equiv -\left(\frac{k_{\mathrm{B}}}{\varepsilon_{ij}} \ln\left(\frac{g_i n_j}{g_j n_i}\right)\right)^{-1} \tag{11.4}$$

As can be seen from Figure 11.5, the excited states are over-populated just behind the compression shock but quickly reach near equilibrium with the electron temperature shortly thereafter. Equilibrium holds constant until the flow passes near the top of the cylinder at

which point the plasma cools as it expands, resulting in an over-population of the excited states once again.

Although not modeled beyond the apex of the cylinder, the flow will continue to expand rapidly in such a region, resulting in a cold plasma far from equilibrium conditions. The rapid expansion will lead to near-vacuum conditions, making the CR model especially important as the population of the levels will be far from Boltzmann equilibrium. Accurate simulation of the flow conditions in this radiative cooling region is not trivial and, if not treated properly, the governing equations may lead to erroneous temperature prediction. This is a result of the near-vacuum conditions leading to poor conditioning of the governing equations as discussed in Chapter 8. Application of the techniques discussed therein to this problem is planned as a part of future work.

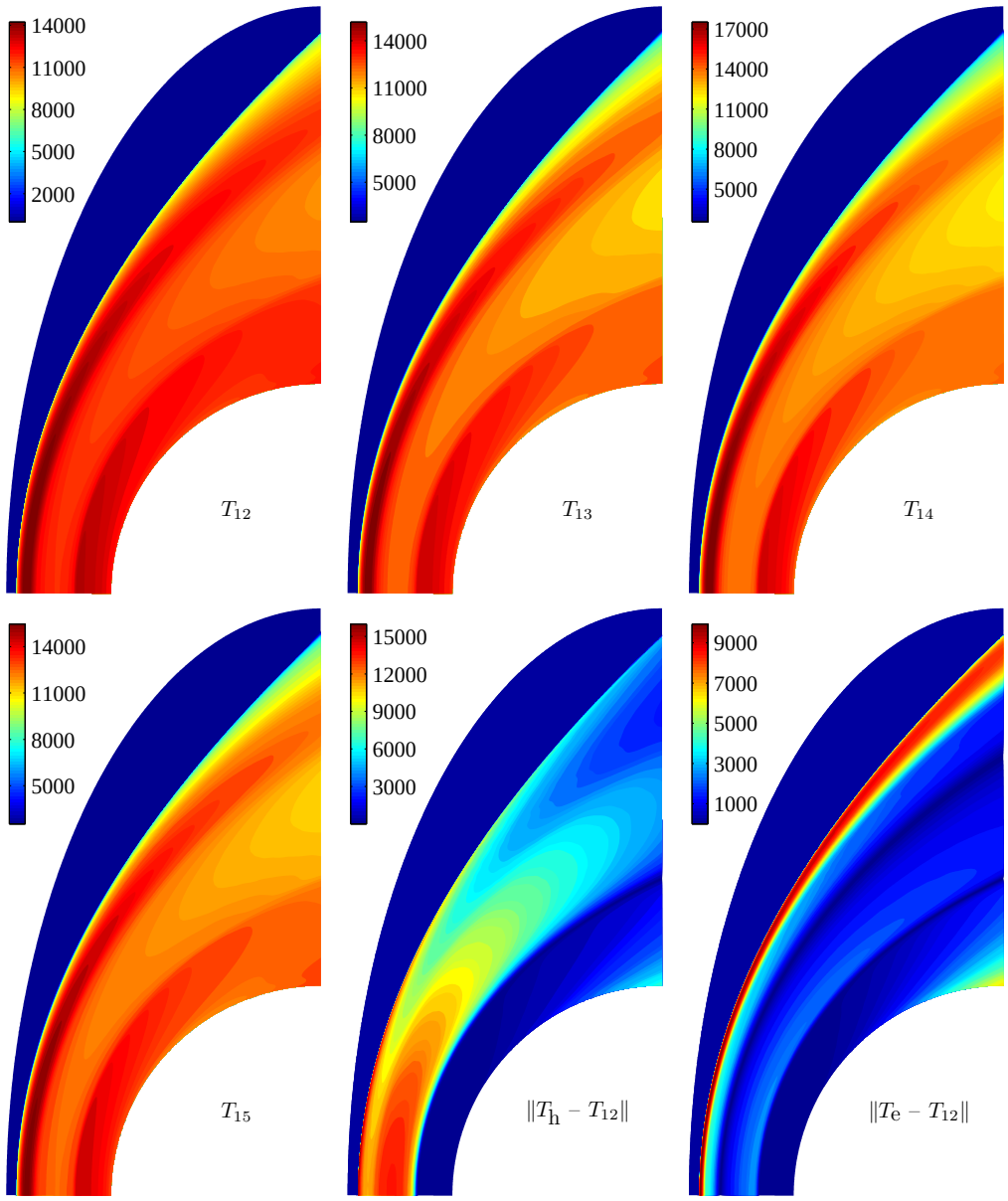

Figure 11.5: Equivalence temperatures of the first four excited levels relative to the ground state.

CHAPTER 12

PARALLEL FRAMEWORK

12.1 Introduction

Java is a highly attractive language for developing high performance computing (HPC) applications. Extensive thread support is built into the language, allowing programs to harness the power of multi-core and symmetric multiprocessing (SMP) hardware. The Remote Method Invocation (RMI) API allows seamless interaction with remote objects, simplifying the development of distributed applications. Java is inherently object-oriented, allowing key abstraction of various network environments. And its platform independence makes it ideal for distributing applications over heterogeneous computing platforms, thus maximizing hardware resources.

Making extensive use of these features, we have developed a distributed framework tailored for explicitly parallel, Single Program, Multiple Data (SPMD) programming applications on clustered networks. In particular, the framework is aimed at solving hyperbolic conservation laws and other problems in which parallelization can be accomplished via domain decomposition—the process by which the physical or solution domain is divided into multiple computation domains (see Figure 12.1). These computation domains encompass instruction sets necessary for advancing the solution in time or achieving a steady-state solution and are executed concurrently and asynchronously through an iterative cycle with only periodic communication and synchronization requirements. Furthermore, the domain decomposition is overlapping such that each domain can communicate by exchanging boundary information with its neighbors.

The framework is implemented 100% in Java, maintaining independence of computing platforms for which the Java Virtual Machine (JVM) is available. This maximizes available

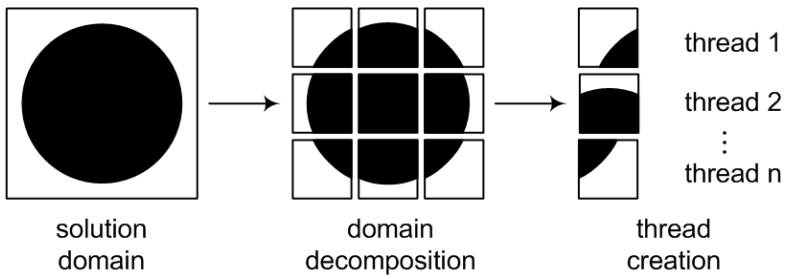

Figure 12.1: Domain decomposition process. Solution domain is decomposed into multiple computation domains from which new threads are created.

computing resources with a minimum of programming effort and required maintenance. The framework relies upon Java threads in order to optimize performance on shared-memory machines. Each computation domain executes within its own lightweight process (LWP), created by spawning new threads. The resulting threadpool is distributed over multiple servers. Communication between different servers is based on the client-server paradigm and relies upon the Remote Method Invocation (RMI) API for network-based communication. RMI is used to exchange boundary information from one domain object to another over the network. Communication must be synchronized and is implemented using concurrency constructs that encapsulate Java monitors.

12.2 Architecture

Java's distributed computing model is based upon the client-server paradigm. Objects distributed over client and server machines communicate with each other through Remote Method Invocation (RMI) protocols, allowing seamless interaction between applications. Programming with distributed objects greatly simplifies the development process and provides a natural extension of object-oriented programming to distributed environments. Because of its inherent simplicity, RMI is used as the basis for designing the framework around the client-server paradigm. Employing a request-response protocol, orchestrated with the aide of concurrency constructs, the framework allows interaction and communication between computation domains distributed over a network. Here we discuss the roles of clients and servers within the framework and extensions to a multi-tier implementation.

12.2.1 Client

From the user's point-of-view, the client is the access point into the entire framework. By means of a Graphical User Interface (GUI), the client allows remote-steering of simulations by the user. The user is able to configure, modify, and visualize the problem and solution in real time, all in a user-friendly environment. Before a simulation is initiated, problem-dependent tasks such as the set-up and initialization of boundary conditions, initial conditions, and numerical solvers can be configured through the client.

12.2.2 Server

Servers are responsible for the relevant program execution. This entails funneling critical I/O, communication between domains, synchronization, and execution of the domain threads. These tasks are divided between two different types of servers, masters and slaves. Master servers accept incoming requests and initialize slave servers for the client. Their primary function is to distribute the computation domains to slave servers and provide periodic barrier synchronization between iteration cycles. Masters in turn initialize slave servers that respond to synchronization signals from their master to begin a cycle of program execution, returning signals when completed.

A simple master-slave interaction is demonstrated in Figure 12.2. A master server distributes computation domains among multiple slave machines and requests for the advancement of the solution for a given time step. During this time, the servers may communicate with each other, requesting critical I/O such as domain boundary information. The client then awaits for their successful completion via signals from each of the servers, at which time it may request for solution results. The entire process is then repeated until the final solution is achieved.

This two-tier model demonstrates horizontal scalability, in which the bottom tier is expanded to accommodate the computational load requested by the master. This assumes that the master has direct access to all possible hardware resources. However, this may not always be the case. A master may want to tap into the resources of a Beowulf cluster for example, but may only do so through the head node of the cluster. In such a scenario, the head node assumes a dual role of accepting part of the computational workload from

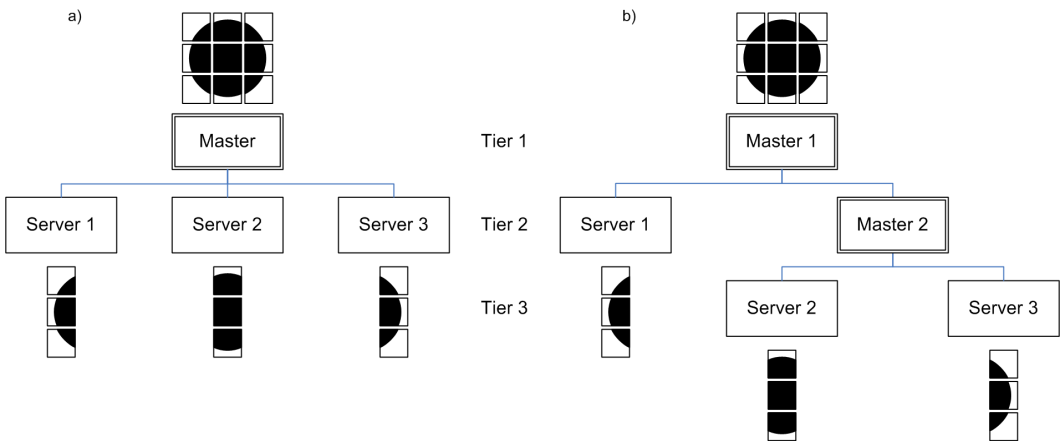

Figure 12.2: Master-slave configurations. In (a), a single Master node distributes workload among 3 slaves. In (b), Master 2 controls Slaves 1 and 2, but is itself a slave to Master 1.

the master as well as distributing the load to its available nodes. This is an example of a three-tier model and is depicted in 12.3 below.

In order to support both horizontal and vertical scalability, the framework has been generalized to a multi-tiered, client-master-slave model. In a multi-tier network, servers can simultaneously function as both masters and slaves, far more hardware and networking environments can be used. Furthermore, horizontal scalability cannot be sustained indefinitely, and will eventually present a bottleneck for massively-parallel applications. Vertical scalability can be used to funnel I/O through multiple tiers, effectively reducing I/O bandwidth at each tier. The disadvantage is that multiple requests may need to be made in order to obtain the same response, increasing network latency time.

12.2.3 Tree Model

In the current architecture, the multi-tier client-server paradigm is implemented through a tree-based abstraction. As illustrated in Figure 12.3, each node in the system can be represented as either a *Root*, *Branch*, or *Leaf* object. The standard tree terminology is also adopted in the following descriptions, including parent, child, sibling, etc.

Root

The *Root* node is the information focal point of the tree data structure. As such, for every network tree there can exist a single root node. It functions as a global master by

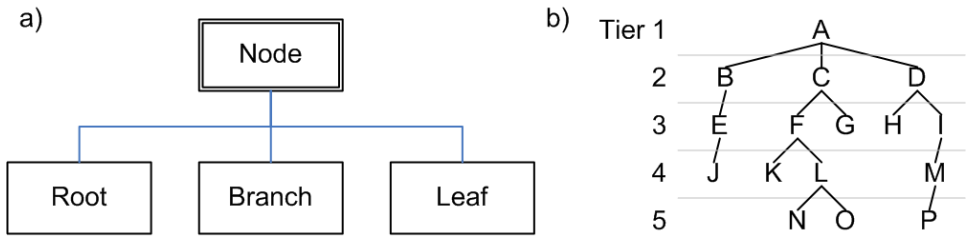

Figure 12.3: Tree abstraction. (a) *Root*, *Branch*, and *Leaf* are subclasses of *Node*. (b) Example configuration: A represents the *Root* node; B, C, D, E, F, I, L, and M represent *Branch* nodes; and J, G, H, K, N, O, and P represent *Leaf* nodes.

synchronizing its child nodes. It is also the access point for the client to the entire framework. The root node can have as children any combination of branches or leaves. The root node has no parents but listens for data requests from the client for such tasks as visualization. The Root node is used as a central location for configuration files as well as mapping information about which domains belong to which servers.

Leaf

Terminal nodes in the network tree are called leaves and cannot have child Nodes. The primary function of a leaf is to host computational domains which handle the computational workload.

Branch

A branch assumes the same responsibilities as those of both root and leaf nodes. The branch must wait until signaled by its parent node (either a *Root* or *Branch* node) and in turn must signal its child nodes (either *Leaf* or other *Branch* nodes) and finally wait for its children to finish their tasks. While it is possible, it is not necessary for a branch node to have computational domains. If it does, however, it must also signal and wait for the domains.

12.3 Communication

With computation domains distributed over a multi-tiered, heterogeneous network, communication becomes of critical importance. In the current framework, there are three primary types of information which must be communicated between different nodes in the network. These include

(i) boundary information shared between domains

(ii) global information

(iii) signals for thread communication and cooperation

In all three cases, Java RMI is the protocol used to establish a connection between the nodes, allowing objects to interact and share data. Here we provide details on the exchange process of boundary and global data. Thread communication is an integral part of the synchronization process and is discussed in the next section.

12.3.1 Boundary Communication

Continuity of the solution domain is left fragmented after the domain decomposition process. To restore continuity, each computation domain must exchange its boundary information with its neighbors during program execution. For time-accurate simulations, this translates into one or more boundary communications per time step.

In the current framework, boundary information is passed from one domain to another within buffer objects. Source buffers are used to store boundary information which originates on the local domain and is to be sent to the remote domain. The domain on the receiving end of the source buffer stores it locally as a ”target” buffer. The information from the target buffer is then used to fill the ghost cells of that domain. This process is illustrated in Figure 12.4.

A partial listing of the Buffer class implemented in the current framework is given below. Along with fields for storing the boundary information of the domain, the Buffer class also contains all necessary information to ensure that data is transferred and received in the proper order. This includes information about the source and target pairs for the domain, cell, and face indices. Encapsulating this information within the Buffer class greatly simplifies implementation of dynamic load balancing. Sending this information each exchange may seem extraneous and unnecessary, but the overhead is negligible since the performance limitation is based on the time it takes to make a remote call overshadows the time it takes to transfer the extra data. This ”connectivity” information tells the local domain how to fill the buffer and how the remote domain extracts data from the buffer is determined a priori

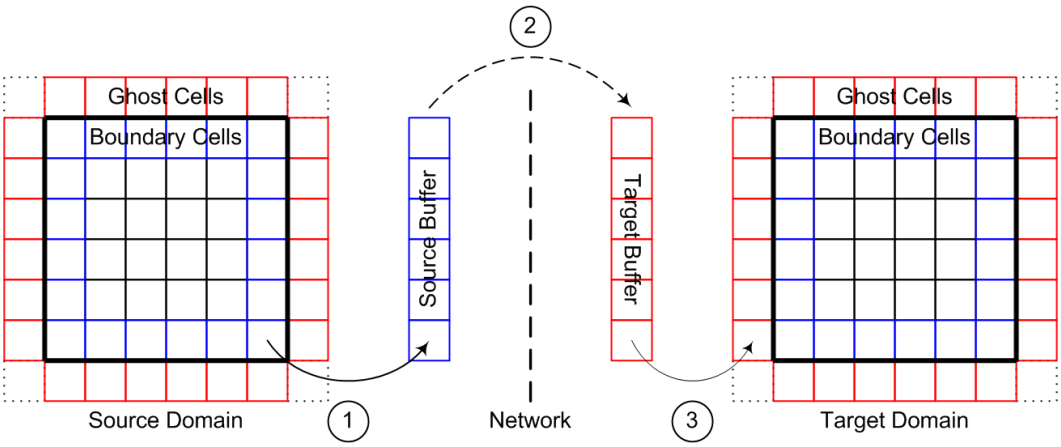

Figure 12.4: Domain Buffers are used to transfer data from the boundary layers of the source domain over the network and into the ghost layers of the target domain.

by the preprocessor. To be transferable via the RMI protocol, the *Buffer* class implements *java.io.Serializable*.

Before a method call is made to transfer the data, a check is in place to determine if the source and target domains exist within the same JVM. If so, a remote method call is initiated, otherwise a local call is made.

Listing 12.1: Buffer

```
public class DomainBuffer implements java.io.Serializable
{
    public int sourceDomain;
    public int targetDomain;

    public int sourceFace[];
    public int targetFace[];

    public int sourceCell[][];
    public int targetCell[][];

    public double[][][][][] Q;

    ...
```

}

Buffer objects can either be pushed from the source domain to the target domain by a *set()* method or pulled from the source domain by the target domain by a *get()* method. This may seem like a trivial choice, but proper implementation of the two methods can be quite different, with one resulting in performance gains over the other. To analyze the differences between a push and a pull, we present two scenarios. The first case represents a push by the source domain while the second is a pull by the target domain. Both cases represent the steps taken by each domain during a complete time step with all domains assumed to be synchronized at the start the iteration.

Cycle I:

(i) Begin time step n.

(ii) Fill ghost cells with target buffer data.

(iii) Advance solution to time n+1

(iv) Fill source buffer with boundary cell data corresponding to time level n+1.

(v) Send source buffer to target domains.

(vi) End Iteration.

Cycle II:

(i) Begin time step n.

(ii) Get buffer from source domain.

(iii) Fill ghost cells with target buffer data.

(iv) Advance solution to time n+1

(v) Fill source buffer with boundary cell data corresponding to time level n+1.

(vi) End Iteration.

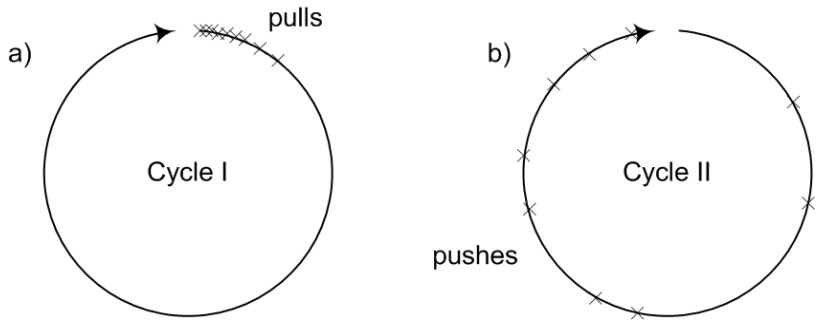

Figure 12.5: Push vs. Pull. Domain buffers can be transferred by either (a) a *pull* from the source domain by the target domain or (b) a *push* from the source domain to the target domain.

Note that the *push* at the end of the iteration by the source domain in Cycle I becomes a *pull* by the target domain at the beginning of the iteration in Cycle II. For the pull taking place at the beginning of the time step, it is more likely that all domains will attempt to get their boundary information at the same time, leading to a possible I/O bottleneck. This is less of an issue for a push, however, since it is less probable that all domains will finish their cycle at the exact same moment. This means that the domains will likely perform the push during a time when they would otherwise be idle, waiting for the final domain to finish its cycle. The chances for the remote calls being staggered in time is much greater, thus maintaining a higher level of asynchronicity. The degree of this effect is dependent upon how many domain threads are executing on each server and the thread scheduling characteristics of the operating system.

It is important to note that there exists the potential for synchronization issues with both of the above schemes. If either of the cases are not implemented properly, a critical race condition may ensue. In both scenarios, it is possible for the source domain to have completed its iteration before the target domain has even begun. In this situation, the target domain will attempt to fill its ghost cells with buffer data from an incorrect time step—the next one (n+1).

This race condition can be remedied by storing the buffers on each domain in a First-In-First-Out (FIFO) queue as illustrated in Figure 12.6. For Cycle I, as 12.6 illustrates, as source buffers are pushed to the target domain, they are added to the top of the buffer queue. The target domain then extracts these buffers from the bottom of the queue, ensuring

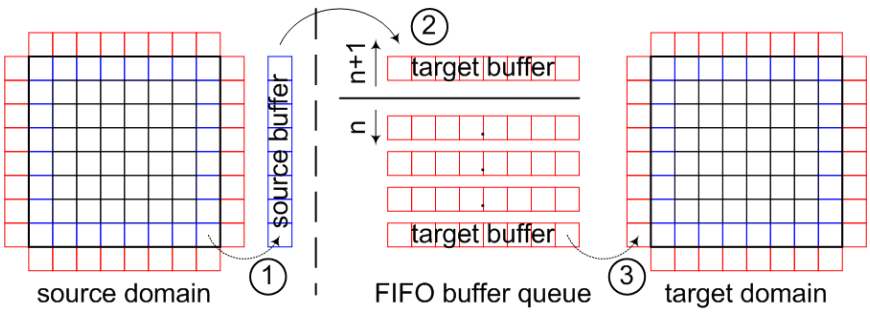

Figure 12.6: FIFO buffer queue. FIFO buffer queues on the receiving end of a push from the source domain are used to ensure correct synchronization of data between iterations.

that buffers of different time steps are effectively separated. The fix for Cycle II is similar, necessitating a FIFO buffer queue on the source domain from which the target domain *pulls*.

In the current framework, the buffer queue is implemented with the *java.util.-LinkedList* class that provides such FIFO access. Since the object can be accessed by more than one thread, we must ensure that its methods are synchronized. This is accomplished by creating the *LinkedList* object in conjunction with the *java.util.Collections.synchronizedList()* static method.

12.4 Synchronization

The end of Moore's Law has ushered in a new era of symmetric multiprocessor (SMP) and multi-core platforms. As a result, successful applications must be able to exploit inherent parallelism to take advantage of the processing power available from all cores/processors. As a thread-based language with support for mutual exclusion and thread cooperation built in, Java is ideal for developing parallel applications on shared-memory machines. Any object (and corresponding class) can be locked by a thread that enters either a synchronized method or synchronized statement of that object. Once inside a synchronized region, a thread blocks all others from accessing any field or method. While a thread maintains a lock on an object, inter-thread communication and coordination is possible through the wait/notify mechanism. A thread can either invoke the *wait()* method, in which case the thread releases its hold on the object and allows for the possibility that another thread may enter and obtain a lock, or it can invoke the *notify()* method as it leaves the synchronized region, to signal to awaiting threads that the object has become available.

The *wait/notify* mechanism provides the essentials for thread coordination, provided that critical sections are encapsulated within a synchronized region. For a domain decomposition-based parallelization scheme, a particular example of a critical section is code that accesses the buffer data objects. Since multiple buffers are accessed by multiple threads through *get/set* methods, explicitly encapsulating this critical code in synchronized regions can quickly lead to a complicated implementation that is difficult to understand. Furthermore, the *wait/notify* mechanism is a low level concurrency construct which does not guarantee against deadlock conditions.

As an alternative, the *wait/notify* mechanism itself can be encapsulated within a higher-level lock construct. Critical code can then interact with this construct, thereby invoking the *wait/notify* mechanism implicitly. The lock construct implemented in the current work is based on the BooleanLock utility of Paul Hyde [55]. BooleanLock is a shared class that encapsulates a boolean variable that can be accessed only through several synchronized methods. The boolean variable is a thread-safe condition variable upon which threads can wait for other thread to change its state to either true or false. Encapsulation of the *wait/notify* mechanism is provided in such a way that it is also thread safe, eliminating the possibility of deadlock conditions.

Listing 12.2: BooleanLock Utility

```
public class BooleanLock
{
    private boolean value;

    public synchronized boolean get()
    {   return value;
    }

    public synchronized void set(boolean value)
    {   this.value = value;
        notifyAll();
    }

    public synchronized void waitUntil(boolean value)
```

```
            throws InterruptedException
    {   while( this.value != value )
            wait();
    }

}
```

Within the framework, *BooleanLock* is used to synchronize several processes including initialization of the simulation, computation cycles, and visualization just to name a few. A unique lock is associated with each process for each thread. *BooleanLock* is further encapsulated within the *NodeSync* class listed below which is used directly within the framework. It provides methods to set, query, and wait on the state of individual threads as well as groups of threads. The *NodeSync* class also allows locks to be stored in *java.util.TreeMaps* so that they can easily be accessed through unique IDs.

Upon the completion of an iteration, each domain must wait for the final domain to complete its computations before the cycle can continue. This form of barrier synchronization is implemented by looping over all domain locks and waiting until each lock has been released. This is accomplished in the code by invoking *waitUntil(DOMAINS, RUNNING, false)* at any point in the code where all domains must be synchronized together.

Listing 12.3: NodeSync

```
public class NodeSync implements NodeSyncInterface
{
    private int Nchildren;
    private int Ndomains;
    private int Nproxies;

    private Lock[] clientLock;
    private Lock[] localLock;

    private Map<Integer, Lock[]>  childLock =
                                    new TreeMap<Integer, Lock[]>();
    private Map<Integer, Lock[]> domainLock =
```

```
                                    new TreeMap<Integer, Lock[]>();
private Map<Integer, Lock[]>  proxyLock =
                                    new TreeMap<Integer, Lock[]>();

...

public void set(Identifier identifier, int state, boolean value)
        throws RemoteException
{
    switch(identifier)
    {   case CLIENT:
            clientLock[state].set(value);
            break;
        case LOCAL:
            localLock[state].set(value);
            break;
        case CHILDREN:
            for(Lock[] lock : childLock.values())
                lock[state].set(value);
            break;
        case DOMAINS:
            for(Lock[] lock : domainLock.values())
                lock[state].set(value);
            break;
        case PROXIES:
            for(Lock[] lock : proxyLock.values())
                lock[state].set(value);
    }
}

public void set(Identifier identifier,
        int index, int state, boolean value)
        throws RemoteException
```

```
{
    switch(identifier)
    {   case CHILD:
            childLock.get(index)[state].set(value);
            break;
        case DOMAIN:
            domainLock.get(index)[state].set(value);
            break;
        case PROXY:
            proxyLock.get(index)[state].set(value);
            break;
    }
}

public boolean is(Identifier identifier, int state)
       throws RemoteException
{
    switch(identifier)
    {   case CLIENT:
            return clientLock[state].get();
        case PARENT:
            return parentLock[state].get();
        case LOCAL:
            return localLock[state].get();
    }
}

public boolean is(Identifier identifier, int index, int state)
        throws RemoteException
{
    switch(identifier)
    {   case CHILD:
            return childLock.get(index)[state].get();
```

```
            case DOMAIN:
                return domainLock.get(index)[state].get();
            case PROXY:
                return proxyLock.get(index)[state].get();
        }
    }

    public boolean are(Identifier identifier, int state)
            throws RemoteException
    {
        switch(identifier)
        {   case CHILDREN:
                for(Lock[] lock : childLock.values())
                    if( !lock[state].get() )
                        return false;
                return true;
            case DOMAINS:
                for(Lock[] lock : domainLock.values())
                    if( !lock[state].get() )
                        return false;
                return true;
            case PROXIES:
                for(Lock[] lock : proxyLock.values())
                    if( !lock[state].get() )
                        return false;
                return true;
        }
    }

    public void waitUntil(Identifier identifier,
            int state, boolean value)
            throws RemoteException, InterruptedException
    {
```

```
    switch(identifier)
    {   case CLIENT:
            clientLock[state].waitUntil(value);
            break;
        case LOCAL:
            localLock[state].waitUntil(value);
            break;
        case CHILDREN:
            for(Lock[] lock : childLock.values())
                lock[state].waitUntil(value);
            break;
        case DOMAINS:
            for(Lock[] lock : domainLock.values())
                lock[state].waitUntil(value);
            break;
        case PROXIES:
            for(Lock[] lock : proxyLock.values())
                lock[state].waitUntil(value);
    }
}

public void waitUntil(Identifier identifier,
        int index, int state, boolean value)
        throws RemoteException, InterruptedException
{
    switch(identifier)
    {   case CHILD:
            childLock.get(index)[state].waitUntil(value);
            break;
        case DOMAIN:
            domainLock.get(index)[state].waitUntil(value);
            break;
        case PROXY:
```

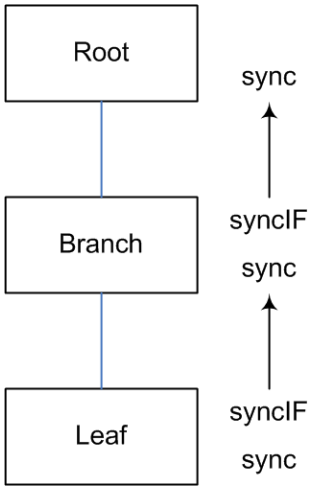

Figure 12.7: Synchronization convention. Synchronization calls between a child node and its parent are accomplished through the *Sync* implementation on the parent and the *Sync* interface of the child.

```
                proxyLock.get(index)[state].waitUntil(value);
        }
    }

}
```

The elegance of the *BooleanLock/NodeSync* combination is that it not only simplifies local thread coordination (reducing the chances of error-prone code), but it is easily extended to coordinate communication between remote threads via RMI. As can be seen from the NodeSync listings above, *NodeSyncInterface* extends java.rmi.Remote, making its implemented methods invokable from remote JVMs. Threads on one JVM can transparently set, query, and wait for thread states on an entirely different JVM. The *NodeSync* class is the basis for distributed-shared memory (DSM) computing in the current architecture.

Each Node in the network has its own local instance of *NodeSync* as well as a *NodeSyncInterface* proxy corresponding to the *NodeSync* implementation of its parent Node. As illustrated in the Figure 12.7, the convention adopted in the framework is for a Node to communicate with its parent through a *NodeSyncInterface* proxy. A Node then communicates with its child through its local *NodeSync* instance.

BooleanLock is just one example of a concurrency construct for barrier synchronization.

The following *IntergerLock* could also be used to synchronize multiple domains by incrementing an integer value as each domain obtains a lock and then decrementing the value upon release of the lock. This could result in a more efficient implementation.

Listing 12.4: IntegerLock

```
public class IntegerLock
{
    private int value;

    public synchronized int get()
    {   return value;
    }

    public synchronized void set(int value)
    {   this.value = value;
        notifyAll();
    }

    public synchronized void increment()
    {   value++;
        notifyAll();
    }

    public synchronized void decrement()
    {   value--;
        notifyAll();
    }

    public synchronized void waitUntil(int value)
            throws InterruptedException
    {   while( this.value != value )
            wait();
    }
```

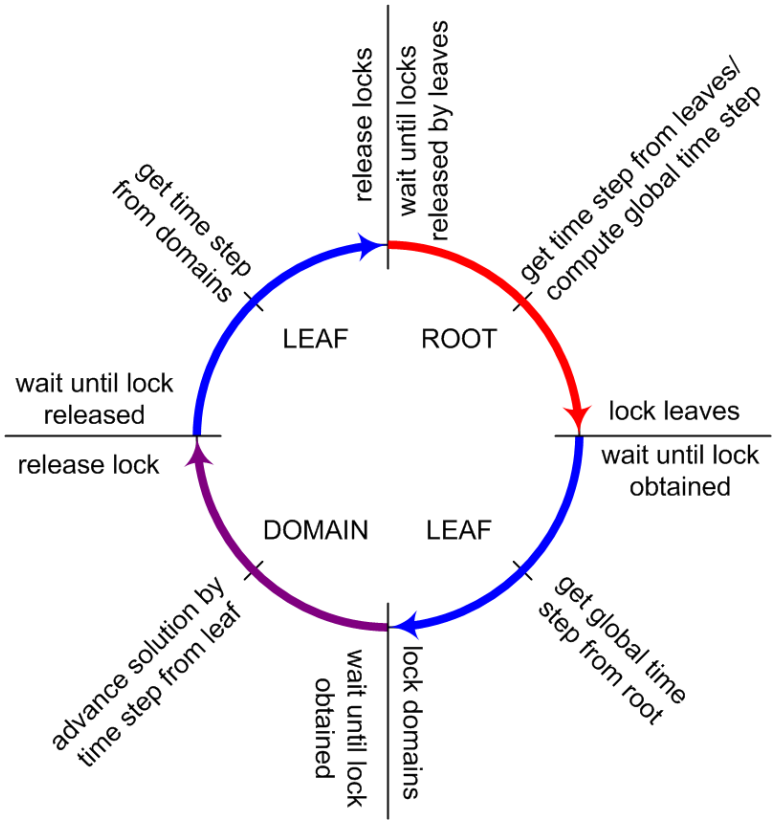

Figure 12.8: Global cylce. Interaction between *Root* and *Leaf* nodes and associated *Domain*s during a global cycle.

}

To demonstrate the usage of the *NodeSync* class, we detail a computation cycle in the current framework for a given network configuration. The example considered is a two-tier network structure, consisting of a *Root* node, a *Leaf* node, and multiple *Domains* as illustrated in Figure 12.8. The stages along with the corresponding methods invoked in *NodeSync*.

ROOT THREAD:

(i) wait until proxies have released their locks → *sync.waitUntil(PROXIES, RUNNING, false)*

(ii) get time step from proxies and compute global time step

(iii) lock each proxy → *sync.set(PROXIES, RUNNING, true)*

PROXY THREAD:

(i) wait until lock is obtained → *sync.waitUntil(PROXY, 0, RUNNING, true)*

(ii) get global time step

(iii) lock child Node (Leaf) → *sync.set(CHILD, 0, RUNNING, true)*

(iv) wait until child has released its lock → *sync.waitUntil(CHILD, 0, RUNNING, true)*

(v) get time step from child

(vi) release lock → *sync.set(PROXY, 0, RUNNING, false)*

LEAF THREAD:

(i) wait until lock is obtained → *syncIF.waitUntil(CHILD, 0, RUNNING, true)*

(ii) get global time step

(iii) lock domains → *sync.set(DOMAINS, RUNNING, true)*

(iv) wait until domains release their locks → *waitUntil(DOMAINS, RUNNING, false)*

(v) get time step from domains

(vi) release lock → *syncIF.set(CHILD, 0, RUNNING, false)*

DOMAIN THREADS:

(i) wait until lock is obtained → *sync.waitUntil(DOMAIN, n, RUNNING, true)*

(ii) get global time step

(iii) fill ghost cells from target buffers

(iv) advance solution by time step and calculate new time step

(v) fill source buffers with boundary data and push to neighbor domains

(vi) release lock → *sync.set(DOMAIN, n, RUNNING, false)*

CHAPTER 13

CONCLUSIONS

13.1 Achievements and contributions

The achievements of the present work can be distinctly categorized in terms of both capability and application. In the case of the former, this work has been successful in introducing a numerical capability for plasmadynamic simulation that can resolve both transport phenomena and nonequilibrium effects to a high level of degree. Many advanced ideas have been incorporated including nonstandard formulations of the governing equations, such as entropy transport, with the aim of obtaining as accurate a solution as possible. A fluid description of the plasma has allowed solution of the convective transport by shock-capturing Riemann solvers extended to third-order, thus enabling resolution of highly nonlinear wave phenomena. The third-order reconstruction scheme has been extended to two-dimensional general curvilinear coordinates, allowing reconstruction of the data by quadric surfaces. A collisional-radiative model for atomic argon has yielded a database for both elastic and inelastic collisions that incorporates the latest cross section data available in the literature.

Development of the code has been systematic, relying heavily upon benchmarks and stability analysis. Stability analysis has further led to better choices for numerical algorithms, in terms of efficiency and robustness. Performance has also been addressed and a novel parallel framework in Java has been developed in conjunction with the governing equations used in this work.

In regards to application, the current work has made significant contributions to the modeling of ionizing shock instabilities. In particular, the current research marks the first time that the instabilities in a two-dimensional ionizing shock have been verified through direct simulation. Simulations have produced details of the shock structure, previously

unknown, revealing structures that are nearly identical to detonation waves. This opens the door for further comparisons between the two phenomena, with the potential to increase understanding of

This has only been possible through a strong coupling between transport and kinetics, verifying the capability of the solver to resolve such flows. The instabilities have been shown to result from a sensitivity of the kinetics to local changes in the flow properties, and hence must be modeled with an accurate treatment of both unsteady transport phenomena and nonequilibrium kinetics.

The same cellular structure resulting from a highly exothermic detonation wave can be observed in an endothermic system. In a detonation system the temperature increase in the induction zone is provided by the energy release from the chemical bonds. In an ionizing shock, however, the heavy particles act as the source of energy that enables the rise in electron temperature. In either case it is this temperature rise to which the kinetics are sensitive to.

The numerical experiments have also resulted in an improved description of the kinetics. While previous attempts to model relaxing shocks in argon have relied on limited kinetic models, this work has applied a fairly detailed collisional-radiative model that has enabled some key conclusions to be drawn. While assuming the argon plasma to be optically-thin to all radiative transitions except to the ground state, it has been found that inclusion of excited levels from the $4s$, $4p$, $5s$, and $3d$ manifolds is sufficient to obtain excellent agreement with the experimental results for the radiative-cooling region. Results for the induction zone and electron avalanche regions, however, indicate that the levels beyond the $4s$ manifold have very little effect.

13.2 Suggestions for future work

While the solver has been applied to unsteady ionizing shock phenomena with excellent results, there is still room for improvement starting with the collisional-radiative model. In particular, it was shown in [19] that molecular argon processes including associative ionization, atomic-to-molecular ion conversion, and dissociative recombination can have a large effect on the overall kinetics. Such processes are sure to influence the relaxation scales associated with relaxing shock layers, including the relaxation length in the current

simulations. This is especially important when considering the atom-atom impact excitation cross sections. The two-step process of atom-atom impact excitation followed by atom-atom ionization is the only method considered in the current work for generating priming electrons just behind the compression shock. Inclusion of the molecular argon processes are sure to require modifications to the atom-atom impact cross sections and should be done so before any claims as to the proper value of the atom-atom impact excitation cross sections can be made.

Improvements can also be made to the collisional-radiative model by extending its nonequilibrium effects to include a non-Maxwellian electron energy distribution function. This may be important for a more accurate representation of the high-energy region (11–16 eV) of the distribution function from which electrons are selectively removed as determined by excitation and ionization thresholds.

Also an open issue is the opacity of the plasma to the various radiation sources involved. It has been assumed that all radiation from higher states to the ground level of argon are absorbed locally while radiation resulting from all other transitions escapes the system. These assumptions have been based on rough estimates of the radiation mean-free path, and in order to validate or nullify these assumptions, solution of the radiation transport equations should be coupled with the solver. While this can be quite a challenge even in two dimensions (let alone 3D), a one-dimensional implementation may be all that is necessary to verify these assumptions or to determine the proper escape factors if necessary.

Glass and Liu noted that with the existence of similar instabilities in both ionizing shocks and detonation waves, developing a stabilizing mechanism for one system may lead to similar for the other. While doping with hydrogen and other impurities were shown both experimentally and numerically [21] to suppress these instabilities, it would be of interest to determine if other approaches can lead to the same effect. In particular, studies can be done to determine if magnetohydrodynamic effects can be applied suppress these oscillations.

An attempt has been made to induce the same type of instabilities in an external flow situation. Although unsuccessful, an extension to alternate geometries could prove successful in generating oscillations and could lead to open the door to a new set of experiments for further code validation.

The UTIAS experiments also resulted in unique boundary layer phenomena caused by

the interaction of viscous and nonequilibrium effects. While water vapor impurities on the surface of the shock tube were known to exacerbate these effects [], a straight-forward inclusion of the viscous terms in the governing equations should allow for the direct simulation of the boundary layer. Reproducing such effects and validating a viscous solver can result in a capability for accurate determination of boundary layers necessary for prediction of heat fluxes, drag, etc.

APPENDIX A

EIGENSYSTEM

A.1 Two-Temperature eigensystem

With the thermodynamics properties derived, it is now possible to derive the eigensystem for the two-temperature model. The final vector form of the two-temperature model results when the electron energy equation is combined with the overall conservation equations,

$$Q = \begin{pmatrix} \rho_1 \\ \vdots \\ \rho_n \\ \rho u \\ \rho v \\ \rho w \\ E \\ \rho \hat{s}_e \end{pmatrix}, \quad V = \begin{pmatrix} \rho_1 \\ \vdots \\ \rho_n \\ u \\ v \\ w \\ p \\ p_e \end{pmatrix}, \quad F_n = \begin{pmatrix} \rho_1 v_n \\ \vdots \\ \rho_n v_n \\ \rho u v_n + n_x p \\ \rho v v_n + n_y p \\ \rho w v_n + n_z p \\ (E+p) v_n \\ \rho \hat{s}_e v_n \end{pmatrix} \tag{A.1}$$

With these vectors, the determination of the flux Jacobian matrix A and its corresponding eigensystem (cf. Eq.(2.10)) can be found in a staright-forward manner. The similarity matrices defined by Eqs. (2.14) and (2.14) are found to be

$$M = \frac{\partial Q}{\partial V} = \begin{pmatrix} 1 & \dots & 0 & 0 & 0 & 0 & 0 & 0 \\ \vdots & \ddots & \vdots & \vdots & \vdots & \vdots & \vdots & \vdots \\ 0 & \dots & 1 & 0 & 0 & 0 & 0 & 0 \\ u & \dots & u & \rho & 0 & 0 & 0 & 0 \\ v & \dots & v & 0 & \rho & 0 & 0 & 0 \\ w & \dots & w & 0 & 0 & \rho & 0 & 0 \\ E_{\rho_1} & \dots & E_{\rho_n} & E_u & E_v & E_w & E_p & E_{p_e} \\ S_{e\rho_1} & \dots & S_{e\rho_n} & S_{eu} & S_{ev} & S_{ew} & S_{ep} & S_{ep_e} \end{pmatrix} \tag{A.2}$$

and

$$M^{-1} = \frac{\partial V}{\partial Q} = \begin{pmatrix} 1 & \dots & 0 & 0 & 0 & 0 & 0 & 0 \\ \vdots & \ddots & \vdots & \vdots & \vdots & \vdots & \vdots & \vdots \\ 0 & \dots & 1 & 0 & 0 & 0 & 0 & 0 \\ -u/\rho & \dots & -u/\rho & 1/\rho & 0 & 0 & 0 & 0 \\ -v/\rho & \dots & -v/\rho & 0 & 1/\rho & 0 & 0 & 0 \\ -w/\rho & \dots & -w/\rho & 0 & 0 & 1/\rho & 0 & 0 \\ P_{\rho_1} & \dots & P_{\rho_n} & P_{m_x} & P_{m_y} & P_{m_z} & P_E & P_{S_e} \\ P_{e\rho_1} & \dots & P_{e\rho_n} & P_{em_x} & P_{em_y} & P_{em_z} & P_{eE} & P_{eS_e} \end{pmatrix} \tag{A.3}$$

The conservative variable flux Jacobian matrix is found to be

$$A_x = \frac{\partial F}{\partial Q} =$$

$$\begin{pmatrix} u(1-y_1) & \dots & -uy_1 & y_1 & 0 & 0 & 0 & 0 \\ \vdots & \ddots & \vdots & \vdots & \vdots & \vdots & \vdots & \vdots \\ -uy_n & \dots & u(1-y_n) & y_n & 0 & 0 & 0 & 0 \\ -uv & \dots & -uv & v & u & 0 & 0 & 0 \\ -uw & \dots & -uw & w & 0 & u & 0 & 0 \\ P_{\rho_1} - \vec{u}\cdot\vec{u} & \dots & P_{\rho_n} - \vec{u}\cdot\vec{u} & P_{m_x} + 2u & P_{m_y} & P_{m_z} & P_E & P_{S_e} \\ \mathcal{A}_{\rho_1,E} & \dots & \mathcal{A}_{\rho_n,E} & \mathcal{A}_{m_x,E} & uP_{m_y} & uP_{m_z} & u(1+P_E) & uP_{S_e} \\ -uS_e/\rho & \dots & -uS_e/\rho & S_e/\rho & 0 & 0 & 0 & u \end{pmatrix} \tag{A.4}$$

where

$$\mathcal{A}_{\rho_i,E} = uP_{\rho_i} - u(E+p)/\rho$$

$$\mathcal{A}_{m_x,E} = uP_{m_x} + (E+p)/\rho.$$

from which the primitive variable Jacobian can be obtained using the similarity transformation,

$$A_{p_x} = M^{-1}A_xM = \begin{pmatrix} u & \dots & 0 & \rho_1 & 0 & 0 & 0 & 0 \\ \vdots & \ddots & \vdots & \vdots & \vdots & \vdots & \vdots & \vdots \\ 0 & \dots & u & \rho_n & 0 & 0 & 0 & 0 \\ 0 & \dots & 0 & u & 0 & 0 & 1/\rho & 0 \\ 0 & \dots & 0 & 0 & u & 0 & 0 & 0 \\ 0 & \dots & 0 & 0 & 0 & u & 0 & 0 \\ 0 & \dots & 0 & \rho a^2 & 0 & 0 & u & 0 \\ 0 & \dots & 0 & \gamma_e p_e & 0 & 0 & 0 & u \end{pmatrix} \tag{A.5}$$

Since the eigenvalues of A_{p_x} are $u, u \pm a$, the thermal speed of sound can be determined using the following matrix identity,

$$|A_x| = |A_{p_x}| = \prod_i^n \lambda_i = u^{n-2}(u+a)(u-a) \quad \longrightarrow \quad a^2 = u^2 - \frac{|A_{xp}|}{u^{n-2}} \tag{A.6}$$

yielding,

$$a^2 = \sum y_s P_{\rho_s} + (\varepsilon + p/\rho - \vec{u}\cdot\vec{u}/2)P_E + \hat{s}_e P_{S_e} \tag{A.7}$$

The subsequent right eigenvectors are given by

$$R_p = \begin{pmatrix} 1 & \dots & 0 & y_1 & 0 & 0 & y_1 & 0 \\ \vdots & \ddots & \vdots & \vdots & \vdots & \vdots & \vdots & \vdots \\ 0 & \dots & 1 & y_n & 0 & 0 & y_n & 0 \\ 0 & \dots & 0 & -a/\rho & 0 & 0 & a/\rho & 0 \\ 0 & \dots & 0 & 0 & 1 & 0 & 0 & 0 \\ 0 & \dots & 0 & 0 & 0 & 1 & 0 & 0 \\ 0 & \dots & 0 & a^2 & 0 & 0 & a^2 & 0 \\ 0 & \dots & 0 & \gamma_e p_e/\rho & 0 & 0 & \gamma_e p_e/\rho & 1 \end{pmatrix} \tag{A.8}$$

which can be inverted to obtain the left eigenvectors,

$$L_p = \begin{pmatrix} 1 & \dots & 0 & 0 & 0 & 0 & -y_1/a^2 & 0 \\ \vdots & \ddots & \vdots & \vdots & \vdots & \vdots & \vdots & \vdots \\ 0 & \dots & 1 & 0 & 0 & 0 & -y_n/a^2 & 0 \\ 0 & \dots & 0 & -\rho/2a & 0 & 0 & 1/2a^2 & 0 \\ 0 & \dots & 0 & 0 & 1 & 0 & 0 & 0 \\ 0 & \dots & 0 & 0 & 0 & 1 & 0 & 0 \\ 0 & \dots & 0 & \rho/2a & 0 & 0 & 1/2a^2 & 0 \\ 0 & \dots & 0 & 0 & 0 & 0 & -\gamma_e p_e/\rho a^2 & 1 \end{pmatrix} \tag{A.9}$$

The eigenvalues which are identical for both the conservative and primitive Jacobians are given by

$$\Lambda = \begin{pmatrix} u & \dots & 0 & 0 & 0 & 0 & 0 & 0 \\ \vdots & \ddots & \vdots & \vdots & \vdots & \vdots & \vdots & \vdots \\ 0 & \dots & u & 0 & 0 & 0 & 0 & 0 \\ 0 & \dots & 0 & u-a & 0 & 0 & 0 & 0 \\ 0 & \dots & 0 & 0 & u & 0 & 0 & 0 \\ 0 & \dots & 0 & 0 & 0 & u & 0 & 0 \\ 0 & \dots & 0 & 0 & 0 & 0 & u+a & 0 \\ 0 & \dots & 0 & 0 & 0 & 0 & 0 & u \end{pmatrix} \tag{A.10}$$

The eigensystem is transformed from the primitive back to the conservative formulation once again using the similarity matrices. The conservative right eigenvectors are found to be

$$R_n = T^{-1}R_x = \begin{pmatrix} 1 & \dots & 0 & y_1 & 0 & 0 & y_1 & 0 \\ \vdots & \ddots & \vdots & \vdots & \vdots & \vdots & \vdots & \vdots \\ 0 & \dots & 1 & y_n & 0 & 0 & y_n & 0 \\ u & \dots & u & u-\xi_x a & \eta_x\rho & \zeta_x\rho & u+\xi_x a & 0 \\ v & \dots & v & v-\xi_y a & \eta_y\rho & \zeta_y\rho & v+\xi_y a & 0 \\ w & \dots & w & w-\xi_z a & \eta_z\rho & \zeta_z\rho & w+\xi_z a & 0 \\ E_{\rho_1} & \dots & E_{\rho_n} & \mathcal{H}^- & E_{v_\eta} & E_{v_\zeta} & \mathcal{H}^+ & E_{p_e} \\ S_{e\rho_1} & \dots & S_{e\rho_n} & \mathcal{H}_e & 0 & 0 & \mathcal{H}_e & S_{ep_e} \end{pmatrix} \tag{A.11}$$

where

$$\mathcal{H}^{\pm} = \sum y_s E_{\rho_s} + \frac{\gamma_e p_e}{\rho} E_{p_e} + a^2 E_p \pm \frac{a}{\rho} E_{v_\xi} \tag{A.12}$$

and

$$\mathcal{H}_e = \sum y_s S_{e\rho_s} + \frac{\gamma_e p_e}{\rho} S_{ep_e} = \frac{S_e}{\rho} \tag{A.13}$$

while the conservative left eigenvectors take the form,

Conservative left eigenvector matrix (x-dir)

$$L_x = L_{p_x} M^{-1} =$$

$$\begin{pmatrix}
1 - y_1 \frac{P_{\rho_1}}{a^2} & \dots & -y_1 \frac{P_{\rho_n}}{a^2} & -y_1 \frac{P_{m_x}}{a^2} & -y_1 \frac{P_{m_y}}{a^2} & -y_1 \frac{P_{m_z}}{a^2} & -y_1 \frac{P_E}{a^2} & -y_1 \frac{P_{S_e}}{a^2} \\
\vdots & \ddots & \vdots & \vdots & \vdots & \vdots & \vdots & \vdots \\
-y_n \frac{P_{\rho_1}}{a^2} & \dots & 1 - y_n \frac{P_{\rho_n}}{a^2} & -y_n \frac{P_{m_x}}{a^2} & -y_n \frac{P_{m_y}}{a^2} & -y_n \frac{P_{m_z}}{a^2} & -y_n \frac{P_E}{a^2} & -y_n \frac{P_{S_e}}{a^2} \\
\frac{P_{\rho_1} + au}{2a^2} & \dots & \frac{P_{\rho_n} + au}{2a^2} & \frac{P_{m_x} - a}{2a^2} & \frac{P_{m_y}}{2a^2} & \frac{P_{m_z}}{2a^2} & \frac{P_E}{2a^2} & \frac{P_{S_e}}{2a^2} \\
-v/\rho & \dots & -v/\rho & 0 & 1/\rho & 0 & 0 & 0 \\
-w/\rho & \dots & -w/\rho & 0 & 0 & 1/\rho & 0 & 0 \\
\frac{P_{\rho_1} - au}{2a^2} & \dots & \frac{P_{\rho_n} - au}{2a^2} & \frac{P_{m_x} + a}{2a^2} & \frac{P_{m_y}}{2a^2} & \frac{P_{m_z}}{2a^2} & \frac{P_E}{2a^2} & \frac{P_{S_e}}{2a^2} \\
P_{e\rho_1} - \frac{\gamma_e p_e P_{\rho_1}}{\rho a^2} & \dots & P_{e\rho_n} - \frac{\gamma_e p_e P_{\rho_n}}{\rho a^2} & -\frac{\gamma_e p_e P_{m_x}}{\rho a^2} & -\frac{\gamma_e p_e P_{m_y}}{\rho a^2} & -\frac{\gamma_e p_e P_{m_z}}{\rho a^2} & -\frac{\gamma_e p_e P_E}{\rho a^2} & P_{eS_e} - \frac{\gamma_e p_e P_{S_e}}{\rho a^2}
\end{pmatrix} \tag{A.14}$$

Conservative left eigenvector matrix (n-dir)

$$L_n = L_x T = \begin{pmatrix} 1 - y_1 \frac{P_{\rho_1}}{a^2} & \dots & -y_1 \frac{P_{\rho_n}}{a^2} & -y_1 \frac{P_{m_x}}{a^2} & -y_1 \frac{P_{m_y}}{a^2} & -y_1 \frac{P_{m_z}}{a^2} & -y_1 \frac{P_E}{a^2} & -y_1 \frac{P_{S_e}}{a^2} \\ \vdots & \ddots & \vdots & \vdots & \vdots & \vdots & \vdots & \vdots \\ -y_n \frac{P_{\rho_1}}{a^2} & \dots & 1 - y_n \frac{P_{\rho_n}}{a^2} & -y_n \frac{P_{m_x}}{a^2} & -y_n \frac{P_{m_y}}{a^2} & -y_n \frac{P_{m_z}}{a^2} & -y_n \frac{P_E}{a^2} & -y_n \frac{P_{S_e}}{a^2} \\ \frac{P_{\rho_1} + a v_\xi}{2a^2} & \dots & \frac{P_{\rho_n} + a v_\xi}{2a^2} & \frac{P_{m_x} - \xi_x a}{2a^2} & \frac{P_{m_y} - \xi_y a}{2a^2} & \frac{P_{m_z} - \xi_z a}{2a^2} & \frac{P_E}{2a^2} & \frac{P_{S_e}}{2a^2} \\ -v_\eta/\rho & \dots & -v_\eta/\rho & \eta_x/\rho & \eta_y/\rho & \eta_z/\rho & 0 & 0 \\ -v_\zeta/\rho & \dots & -v_\zeta/\rho & \zeta_x/\rho & \zeta_y/\rho & \zeta_z/\rho & 0 & 0 \\ \frac{P_{\rho_1} - a v_\xi}{2a^2} & \dots & \frac{P_{\rho_n} - a v_\xi}{2a^2} & \frac{P_{m_x} + \xi_x a}{2a^2} & \frac{P_{m_y} + \xi_y a}{2a^2} & \frac{P_{m_z} + \xi_z a}{2a^2} & \frac{P_E}{2a^2} & \frac{P_{S_e}}{2a^2} \\ P_{e\rho_1} - \frac{\gamma_e p_e P_{\rho_1}}{\rho a^2} & \dots & P_{e\rho_n} - \frac{\gamma_e p_e P_{\rho_n}}{\rho a^2} & -\frac{\gamma_e p_e P_{m_x}}{\rho a^2} & -\frac{\gamma_e p_e P_{m_y}}{\rho a^2} & -\frac{\gamma_e p_e P_{m_z}}{\rho a^2} & -\frac{\gamma_e p_e P_E}{\rho a^2} & P_{eS_e} - \frac{\gamma_e p_e P_{S_e}}{\rho a^2} \end{pmatrix} \tag{A.15}$$

A.2 Two-Temperature MHD eigensystem

As done for the two-temperature hydrodynamic equations, the eigensystem is now presented for the two-temperature MHD equations. Although not strictly hyperbolic, the MHD equations are always diagonalizable. In the absence of magnetic fields, the fast magnetoacoustic waves become thermal acoustic waves while the Alfvén waves collapse onto the slow magnetoacoustic waves, producing the shear waves of the basic fluid equations [97]. This may lead to singularities in the eigensystem and was first addressed by Brio and Wu [17] in their development on an upwind solver. Renormalization parameters were introduced that were further refined by Roe and Balsara *et. al.* [97] and Barth [6].

$$Q = \begin{pmatrix} \rho_1 \\ \vdots \\ \rho_n \\ \rho u \\ \rho v \\ \rho w \\ B_x \\ B_y \\ B_z \\ E \\ S_e \end{pmatrix}, \quad V = \begin{pmatrix} \rho_1 \\ \vdots \\ \rho_n \\ u \\ v \\ w \\ B_x \\ B_y \\ B_z \\ p \\ p_e \end{pmatrix}, \quad F_n = \begin{pmatrix} \rho_1 v_n \\ \vdots \\ \rho_n v_n \\ \rho u v_n + n_x p_\circ - B_x B_n/\mu_\circ \\ \rho v v_n + n_y p_\circ - B_y B_n/\mu_\circ \\ \rho w v_n + n_z p_\circ - B_z B_n/\mu_\circ \\ v_n B_x - u B_n \\ v_n B_y - v B_n \\ v_n B_z - w B_n \\ v_n (E + p_\circ) - B_n (\vec{v} \cdot \vec{B})/\mu_\circ \\ v_n S_e \end{pmatrix} \tag{A.16}$$

Similarity transformation matrices

$$M = \frac{\partial Q}{\partial V} =$$

$$\begin{pmatrix}
1 & \dots & 0 & 0 & 0 & 0 & 0 & 0 & 0 & 0 & 0 \\
\vdots & \ddots & \vdots & \vdots & \vdots & \vdots & \vdots & \vdots & \vdots & \vdots & \vdots \\
0 & \dots & 1 & 0 & 0 & 0 & 0 & 0 & 0 & 0 & 0 \\
u & \dots & u & \rho & 0 & 0 & 0 & 0 & 0 & 0 & 0 \\
v & \dots & v & 0 & \rho & 0 & 0 & 0 & 0 & 0 & 0 \\
w & \dots & w & 0 & 0 & \rho & 0 & 0 & 0 & 0 & 0 \\
0 & \dots & 0 & 0 & 0 & 0 & 1 & 0 & 0 & 0 & 0 \\
0 & \dots & 0 & 0 & 0 & 0 & 0 & 1 & 0 & 0 & 0 \\
0 & \dots & 0 & 0 & 0 & 0 & 0 & 0 & 1 & 0 & 0 \\
E_{\rho_1} & \dots & E_{\rho_n} & E_u & E_v & E_w & E_{B_x} & E_{B_y} & E_{B_z} & E_p & E_{p_e} \\
S_{e\rho_1} & \dots & S_{e\rho_n} & S_{eu} & S_{ev} & S_{ew} & S_{eB_x} & S_{eB_y} & S_{eB_z} & S_{ep} & S_{ep_e}
\end{pmatrix} \tag{A.17}$$

$$M^{-1} = \frac{\partial V}{\partial Q} =$$

$$\begin{pmatrix}
1 & \dots & 0 & 0 & 0 & 0 & 0 & 0 & 0 & 0 & 0 \\
\vdots & \ddots & \vdots & \vdots & \vdots & \vdots & \vdots & \vdots & \vdots & \vdots & \vdots \\
0 & \dots & 1 & 0 & 0 & 0 & 0 & 0 & 0 & 0 & 0 \\
-\frac{u}{\rho} & \dots & -\frac{u}{\rho} & \frac{1}{\rho} & 0 & 0 & 0 & 0 & 0 & 0 & 0 \\
-\frac{v}{\rho} & \dots & -\frac{v}{\rho} & 0 & \frac{1}{\rho} & 0 & 0 & 0 & 0 & 0 & 0 \\
-\frac{v}{\rho} & \dots & -\frac{v}{\rho} & 0 & 0 & \frac{1}{\rho} & 0 & 0 & 0 & 0 & 0 \\
0 & \dots & 0 & 0 & 0 & 0 & 1 & 0 & 0 & 0 & 0 \\
0 & \dots & 0 & 0 & 0 & 0 & 0 & 1 & 0 & 0 & 0 \\
0 & \dots & 0 & 0 & 0 & 0 & 0 & 0 & 1 & 0 & 0 \\
P_{\rho_1} & \dots & P_{\rho_n} & P_{m_x} & P_{m_y} & P_{m_z} & P_{B_x} & P_{B_y} & P_{B_z} & P_p & P_{p_e} \\
P_{e\rho_1} & \dots & P_{e\rho_n} & P_{em_x} & P_{em_y} & P_{em_z} & P_{eB_x} & P_{eB_y} & P_{eB_z} & P_{ep} & P_{ep_e}
\end{pmatrix} \tag{A.18}$$

Conservative flux Jacobian matrix

$$A = \frac{\partial F}{\partial Q} = \begin{pmatrix} u(1-y_1) & \dots & -uy_1 & y_1 & 0 & 0 & 0 & 0 & 0 & 0 & 0 \\ \vdots & \ddots & \vdots & \vdots & \vdots & \vdots & \vdots & \vdots & \vdots & \vdots & \vdots \\ -uy_n & \dots & u(1-y_n) & y_n & 0 & 0 & 0 & 0 & 0 & 0 & 0 \\ P_{\rho_1} - u^2 & \dots & P_{\rho_n} - u^2 & P_{m_x} + 2u & P_{m_y} & P_{m_z} & P_{B_x} - \frac{B_x}{\mu_\circ} & P_{B_y} + \frac{B_y}{\mu_\circ} & P_{B_z} + \frac{B_z}{\mu_\circ} & P_E & P_{S_e} \\ -uv & \dots & -uv & v & u & 0 & -\frac{B_y}{\mu_\circ} & -\frac{B_x}{\mu_\circ} & 0 & 0 & 0 \\ -uw & \dots & -uw & w & 0 & u & -\frac{B_z}{\mu_\circ} & 0 & -\frac{B_x}{\mu_\circ} & 0 & 0 \\ \frac{vB_x - uB_y}{\rho} & \dots & \frac{vB_x - uB_y}{\rho} & \frac{B_y}{\rho} & -\frac{B_x}{\rho} & 0 & -v & u & 0 & 0 & 0 \\ \frac{wB_x - uB_z}{\rho} & \dots & \frac{wB_x - uB_z}{\rho} & \frac{B_z}{\rho} & 0 & -\frac{B_x}{\rho} & -w & 0 & u & 0 & 0 \\ & & & & \longleftarrow \partial f_E / \partial Q \longrightarrow & & & & & & \\ -\frac{u}{\rho} S_e & \dots & -\frac{u}{\rho} S_e & \frac{1}{\rho} S_e & 0 & 0 & 0 & 0 & 0 & 0 & u \end{pmatrix} \tag{A.19}$$

where

$$\frac{\partial f_E}{\partial Q} = \begin{pmatrix} uP_{\rho_1} - [u(E+p_\circ) - B_x(\vec{u}\cdot\vec{B})/\mu_\circ]/\rho \\ \vdots \\ uP_{\rho_n} - [u(E+p_\circ) - B_x(\vec{u}\cdot\vec{B})/\mu_\circ]/\rho \\ uP_{m_x} + \left(E + p_\circ - B_x^2/\mu_\circ\right)/\rho \\ uP_{m_y} - \frac{B_x B_y}{\rho\mu_\circ} \\ uP_{m_z} - \frac{B_x B_z}{\rho\mu_\circ} \\ uP_{B_x} - \vec{u}\cdot\vec{B}/\mu_\circ \\ u(P_{B_y} + B_y/\mu_\circ) - vB_x/\mu_\circ \\ u(P_{B_z} + B_z/\mu_\circ) - wB_x/\mu_\circ \\ u(1+P_E) \\ uP_{S_e} \end{pmatrix}^T$$

Primitive flux Jacobian matrix

$$A_{p_x} = M^{-1} A_x M =$$

$$\begin{pmatrix}
u & \dots & 0 & \rho_1 & 0 & 0 & 0 & 0 & 0 & 0 & 0 \\
\vdots & \ddots & \vdots & \vdots & \vdots & \vdots & \vdots & \vdots & \vdots & \vdots & \vdots \\
0 & \dots & u & \rho_n & 0 & 0 & 0 & 0 & 0 & 0 & 0 \\
0 & \dots & 0 & u & 0 & 0 & 0 & \frac{B_y}{\rho\mu_\circ} & \frac{B_z}{\rho\mu_\circ} & \frac{1}{\rho} & 0 \\
0 & \dots & 0 & 0 & u & 0 & 0 & -\frac{B_x}{\rho\mu_\circ} & 0 & 0 & 0 \\
0 & \dots & 0 & 0 & 0 & u & 0 & 0 & -\frac{B_x}{\rho\mu_\circ} & 0 & 0 \\
0 & \dots & 0 & 0 & 0 & 0 & u & 0 & 0 & 0 & 0 \\
0 & \dots & 0 & B_y & -B_x & 0 & 0 & u & 0 & 0 & 0 \\
0 & \dots & 0 & B_z & 0 & -B_x & 0 & 0 & u & 0 & 0 \\
0 & \dots & 0 & \rho a^2 & 0 & 0 & 0 & 0 & 0 & u & 0 \\
0 & \dots & 0 & \gamma_e p_e & 0 & 0 & 0 & 0 & 0 & 0 & u
\end{pmatrix} \tag{A.20}$$

where a^2 is the thermal sound speed and is independent of the magnetic pressure,

$$a^2 = \sum y_s P_{\rho_s} + (\varepsilon + p/\rho - \vec{u} \cdot \vec{u}/2) P_E + \hat{s}_e P_{S_e} \tag{A.21}$$

Diagonal matrix of eigenvalues

$$\mathbf{\Lambda} = \begin{pmatrix} u & \dots & 0 & 0 & 0 & 0 & 0 & 0 & 0 & 0 & 0 & 0 \\ \vdots & \ddots & \vdots & \vdots & \vdots & \vdots & \vdots & \vdots & \vdots & & & \\ 0 & \dots & u & 0 & 0 & 0 & 0 & 0 & 0 & 0 & 0 & 0 \\ 0 & \dots & 0 & u & 0 & 0 & 0 & 0 & 0 & 0 & 0 & 0 \\ 0 & \dots & 0 & 0 & u - c_s & 0 & 0 & 0 & 0 & 0 & 0 & 0 \\ 0 & \dots & 0 & 0 & 0 & u + c_s & 0 & 0 & 0 & 0 & 0 & 0 \\ 0 & \dots & 0 & 0 & 0 & 0 & u - c_f & 0 & 0 & 0 & 0 & 0 \\ 0 & \dots & 0 & 0 & 0 & 0 & 0 & u + c_f & 0 & 0 & 0 & 0 \\ 0 & \dots & 0 & 0 & 0 & 0 & 0 & 0 & u - \frac{B_x}{\sqrt{\rho}} & 0 & 0 & 0 \\ 0 & \dots & 0 & 0 & 0 & 0 & 0 & 0 & 0 & u + \frac{B_x}{\sqrt{\rho}} & 0 & 0 \\ 0 & \dots & 0 & 0 & 0 & 0 & 0 & 0 & 0 & 0 & u & 0 \\ 0 & \dots & 0 & 0 & 0 & 0 & 0 & 0 & 0 & 0 & 0 & u \end{pmatrix} \tag{A.22}$$

Conservative right eigenvector matrix

$$R_n = \begin{pmatrix}
1 & \dots & 0 & 0 & \alpha_f y_1 & \alpha_f y_1 & \alpha_s y_1 & \alpha_s y_1 & 0 & 0 & 0 \\
\vdots & \ddots & \vdots & \vdots & \vdots & \vdots & \vdots & \vdots & \vdots & \vdots & \vdots \\
0 & \dots & 1 & 0 & \alpha_f y_n & \alpha_f y_n & \alpha_s y_n & \alpha_s y_n & 0 & 0 & 0 \\
u & \dots & u & 0 & \alpha_f u + \mathcal{A}_f^x & \alpha_f u - \mathcal{A}_f^x & \alpha_s u + \mathcal{A}_s^x & \alpha_s u - \mathcal{A}_s^x & -(\hat{n}\times\vec{\beta})_x & (\hat{n}\times\vec{\beta})_x & 0 \\
v & \dots & v & 0 & \alpha_f v + \mathcal{A}_f^y & \alpha_f v - \mathcal{A}_f^y & \alpha_s v + \mathcal{A}_s^y & \alpha_s v - \mathcal{A}_s^y & -(\hat{n}\times\vec{\beta})_y & (\hat{n}\times\vec{\beta})_y & 0 \\
w & \dots & w & 0 & \alpha_f w + \mathcal{A}_f^z & \alpha_f w - \mathcal{A}_f^z & \alpha_s w + \mathcal{A}_s^z & \alpha_s w - \mathcal{A}_s^z & -(\hat{n}\times\vec{\beta})_z & (\hat{n}\times\vec{\beta})_z & 0 \\
0 & \dots & 0 & 0 & \sqrt{\frac{\mu_\circ}{\rho}}\mathcal{G}_f^x & \sqrt{\frac{\mu_\circ}{\rho}}\mathcal{G}_f^x & \sqrt{\frac{\mu_\circ}{\rho}}\mathcal{G}_s^x & \sqrt{\frac{\mu_\circ}{\rho}}\mathcal{G}_s^x & \sqrt{\frac{\mu_\circ}{\rho}}(\hat{n}\times\vec{\beta})_x & \sqrt{\frac{\mu_\circ}{\rho}}(\hat{n}\times\vec{\beta})_x & n_x \\
0 & \dots & 0 & 0 & \sqrt{\frac{\mu_\circ}{\rho}}\mathcal{G}_f^y & \sqrt{\frac{\mu_\circ}{\rho}}\mathcal{G}_f^y & \sqrt{\frac{\mu_\circ}{\rho}}\mathcal{G}_s^y & \sqrt{\frac{\mu_\circ}{\rho}}\mathcal{G}_s^y & \sqrt{\frac{\mu_\circ}{\rho}}(\hat{n}\times\vec{\beta})_y & \sqrt{\frac{\mu_\circ}{\rho}}(\hat{n}\times\vec{\beta})_y & n_y \\
0 & \dots & 0 & 0 & \sqrt{\frac{\mu_\circ}{\rho}}\mathcal{G}_f^z & \sqrt{\frac{\mu_\circ}{\rho}}\mathcal{G}_f^z & \sqrt{\frac{\mu_\circ}{\rho}}\mathcal{G}_s^z & \sqrt{\frac{\mu_\circ}{\rho}}\mathcal{G}_s^z & \sqrt{\frac{\mu_\circ}{\rho}}(\hat{n}\times\vec{\beta})_z & \sqrt{\frac{\mu_\circ}{\rho}}(\hat{n}\times\vec{\beta})_z & n_z \\
E_{\rho_1} & \dots & E_{\rho_n} & E_{p_e} & \mathcal{H}_f^+ & \mathcal{H}_f^- & \mathcal{H}_s^+ & \mathcal{H}_s^- & (\vec{v}\times\vec{\beta})\cdot\hat{n} & -(\vec{v}\times\vec{\beta})\cdot\hat{n} & B_x \\
S_{e\rho_1} & \dots & S_{e\rho_n} & S_{ep_e} & \mathcal{H}_e & \mathcal{H}_e & \mathcal{H}_e & \mathcal{H}_e & 0 & 0 & 0
\end{pmatrix} \tag{A.23}$$

$$\vec{\mathcal{A}}_{f,s} = \hat{n}\alpha_{f,s}c_{f,s} \mp \alpha_{s,f}c_{s,f}(\vec{\beta} - \hat{n}\beta_n)\mathrm{sgn}(B_n), \quad \vec{\mathcal{G}}_{f,s} = \pm\alpha_{s,f}a(\vec{\beta} - \hat{n}\beta_n) \tag{A.24}$$

$$\mathcal{H}^\pm = \alpha\left(\sum y_s E_{\rho_s} + \tfrac{\gamma_e p_e}{\rho}E_{p_e} + a^2 E_p + c^2 - a^2\right) \pm \vec{v}\cdot\vec{\mathcal{A}}, \quad \mathcal{H}_e = \sum y_s S_{e\rho_s} + \tfrac{\gamma_e p_e}{\rho}S_{ep_e} = \hat{s}_e \tag{A.25}$$

$$B_n = \hat{n}\cdot\vec{B}, \quad B^2 = B_x^2 + B_y^2 + B_z^2, \quad B_\perp = \sqrt{B^2 - B_n^2} \tag{A.26}$$

$$\vec{\beta} = \vec{B}/B_\perp, \quad \beta_n = B_n/B_\perp \tag{A.27}$$

$$a_*^2 = a^2 + \frac{B^2}{\rho\mu_\circ} = c_f^2 + c_s^2, \quad c_a^2 = \frac{B_n^2}{\rho\mu_\circ} \tag{A.28}$$

$$c_{f,s}^2 = \tfrac{1}{2}\left(a_*^2 \pm \sqrt{a_*^4 - 4a^2c_a^2}\right) \tag{A.29}$$

$$\alpha_f^2 = \tfrac{a^2 - c_s^2}{c_f^2 - c_s^2}, \quad \alpha_s^2 = \tfrac{c_f^2 - a^2}{c_f^2 - c_s^2} \tag{A.30}$$

Conservative left eigenvector matrix

$$
L = \left(\begin{array}{cccccc}
1 - y_1 \frac{P_{\rho_1}}{a^2} & \cdots & -y_1 \frac{P_{\rho_n}}{a^2} & -y_1 \frac{P_{m_x}}{a^2} & -y_1 \frac{P_{m_y}}{a^2} & -y_1 \frac{P_{m_z}}{a^2} \\
\vdots & \ddots & \vdots & \vdots & \vdots & \vdots \\
-y_n \frac{P_{\rho_1}}{a^2} & \cdots & 1 - y_n \frac{P_{\rho_n}}{a^2} & -y_n \frac{P_{m_x}}{a^2} & -y_n \frac{P_{m_y}}{a^2} & -y_n \frac{P_{m_z}}{a^2} \\
\frac{\alpha_f P_{\rho_1} - \vec{v}\cdot\vec{\mathcal{A}}_f}{2a^2} & \cdots & \frac{\alpha_f P_{\rho_n} - \vec{v}\cdot\vec{\mathcal{A}}_f}{2a^2} & \frac{\alpha_f P_{m_x} + A_f^x}{2a^2} & \frac{\alpha_f P_{m_y} + A_f^y}{2a^2} & \frac{\alpha_f P_{m_z} + A_f^z}{2a^2} \\
\frac{\alpha_f P_{\rho_1} + \vec{v}\cdot\vec{\mathcal{A}}_f}{2a^2} & \cdots & \frac{\alpha_f P_{\rho_n} + \vec{v}\cdot\vec{\mathcal{A}}_f}{2a^2} & \frac{\alpha_f P_{m_x} - A_f^x}{2a^2} & \frac{\alpha_f P_{m_y} - A_f^y}{2a^2} & \frac{\alpha_f P_{m_z} - A_f^z}{2a^2} \\
\frac{\alpha_s P_{\rho_1} - \vec{v}\cdot\vec{\mathcal{A}}_s}{2a^2} & \cdots & \frac{\alpha_s P_{\rho_n} - \vec{v}\cdot\vec{\mathcal{A}}_s}{2a^2} & \frac{\alpha_s P_{m_x} + A_s^x}{2a^2} & \frac{\alpha_s P_{m_y} + A_s^y}{2a^2} & \frac{\alpha_s P_{m_z} + A_s^z}{2a^2} \\
\frac{\alpha_s P_{\rho_1} + \vec{v}\cdot\vec{\mathcal{A}}_s}{2a^2} & \cdots & \frac{\alpha_s P_{\rho_n} + \vec{v}\cdot\vec{\mathcal{A}}_s}{2a^2} & \frac{\alpha_s P_{m_x} - A_s^x}{2a^2} & \frac{\alpha_s P_{m_y} - A_s^y}{2a^2} & \frac{\alpha_s P_{m_z} - A_s^z}{2a^2} \\
-\frac{(\vec{v}\times\vec{\beta})\cdot\hat{n}}{2} & \cdots & -\frac{(\vec{v}\times\vec{\beta})\cdot\hat{n}}{2} & -\frac{(\hat{n}\times\vec{\beta})_x}{2} & -\frac{(\hat{n}\times\vec{\beta})_y}{2} & -\frac{(\hat{n}\times\vec{\beta})_z}{2} \\
\frac{(\vec{v}\times\vec{\beta})\cdot\hat{n}}{2} & \cdots & \frac{(\vec{v}\times\vec{\beta})\cdot\hat{n}}{2} & \frac{(\hat{n}\times\vec{\beta})_x}{2} & \frac{(\hat{n}\times\vec{\beta})_y}{2} & \frac{(\hat{n}\times\vec{\beta})_z}{2} \\
P_{e\rho_1} - \frac{\gamma_e p_e P_{\rho_1}}{\rho a^2} & \cdots & P_{e\rho_n} - \frac{\gamma_e p_e P_{\rho_n}}{\rho a^2} & -\frac{\gamma_e p_e P_{m_x}}{\rho a^2} & -\frac{\gamma_e p_e P_{m_y}}{\rho a^2} & -\frac{\gamma_e p_e P_{m_z}}{\rho a^2} \\
0 & \cdots & 0 & 0 & 0 & 0
\end{array} \right.
$$

$$
\left. \begin{array}{ccccc}
-y_1 \frac{P_{B_x} - n_x P_{B_n}}{a^2} & -y_1 \frac{P_{B_y} - n_y P_{B_n}}{a^2} & -y_1 \frac{P_{B_z} - n_z P_{B_n}}{a^2} & -y_1 \frac{P_E}{a^2} & -y_1 \frac{P_{S_e}}{a^2} \\
\vdots & \vdots & \vdots & \vdots & \vdots \\
-y_n \frac{P_{B_x} - n_x P_{B_n}}{a^2} & -y_n \frac{P_{B_y} - n_y P_{B_n}}{a^2} & -y_n \frac{P_{B_z} - n_z P_{B_n}}{a^2} & -y_n \frac{P_E}{a^2} & -y_n \frac{P_{S_e}}{a^2} \\
\frac{\alpha_f (P_{B_x} - n_x P_{B_n}) + \sqrt{\rho/\mu_\circ}\,\Delta_f^x}{2a^2} & \frac{\alpha_f (P_{B_y} - n_y P_{B_n}) + \sqrt{\rho/\mu_\circ}\,\Delta_f^y}{2a^2} & \frac{\alpha_f (P_{B_z} - n_z P_{B_n}) + \sqrt{\rho/\mu_\circ}\,\Delta_f^z}{2a^2} & \frac{\alpha_f P_E}{2a^2} & \frac{\alpha_f P_{S_e}}{2a^2} \\
\frac{\alpha_f (P_{B_x} - n_x P_{B_n}) + \sqrt{\rho/\mu_\circ}\,\Delta_f^x}{2a^2} & \frac{\alpha_f (P_{B_y} - n_y P_{B_n}) + \sqrt{\rho/\mu_\circ}\,\Delta_f^y}{2a^2} & \frac{\alpha_f (P_{B_z} - n_z P_{B_n}) + \sqrt{\rho/\mu_\circ}\,\Delta_f^z}{2a^2} & \frac{\alpha_f P_E}{2a^2} & \frac{\alpha_f P_{S_e}}{2a^2} \\
\frac{\alpha_s (P_{B_x} - n_x P_{B_n}) + \sqrt{\rho/\mu_\circ}\,\Delta_s^x}{2a^2} & \frac{\alpha_s (P_{B_y} - n_y P_{B_n}) + \sqrt{\rho/\mu_\circ}\,\Delta_s^y}{2a^2} & \frac{\alpha_s (P_{B_z} - n_z P_{B_n}) + \sqrt{\rho/\mu_\circ}\,\Delta_s^z}{2a^2} & \frac{\alpha_s P_E}{2a^2} & \frac{\alpha_s P_{S_e}}{2a^2} \\
\frac{\alpha_s (P_{B_x} - n_x P_{B_n}) + \sqrt{\rho/\mu_\circ}\,\Delta_s^x}{2a^2} & \frac{\alpha_s (P_{B_y} - n_y P_{B_n}) + \sqrt{\rho/\mu_\circ}\,\Delta_s^y}{2a^2} & \frac{\alpha_s (P_{B_z} - n_z P_{B_n}) + \sqrt{\rho/\mu_\circ}\,\Delta_s^z}{2a^2} & \frac{\alpha_s P_E}{2a^2} & \frac{\alpha_s P_{S_e}}{2a^2} \\
\sqrt{\frac{\rho}{\mu_\circ}} \frac{(\hat{n}\times\vec{\beta})_x}{2} & \sqrt{\frac{\rho}{\mu_\circ}} \frac{(\hat{n}\times\vec{\beta})_y}{2} & \sqrt{\frac{\rho}{\mu_\circ}} \frac{(\hat{n}\times\vec{\beta})_z}{2} & 0 & 0 \\
\sqrt{\frac{\rho}{\mu_\circ}} \frac{(\hat{n}\times\vec{\beta})_x}{2} & \sqrt{\frac{\rho}{\mu_\circ}} \frac{(\hat{n}\times\vec{\beta})_y}{2} & \sqrt{\frac{\rho}{\mu_\circ}} \frac{(\hat{n}\times\vec{\beta})_z}{2} & 0 & 0 \\
-\frac{\gamma_e p_e P_{B_x}}{\rho a^2} & -\frac{\gamma_e p_e P_{B_y}}{\rho a^2} & -\frac{\gamma_e p_e P_{B_z}}{\rho a^2} & -\frac{\gamma_e p_e P_E}{\rho a^2} & P_{eS_e} - \frac{\gamma_e p_e P_{S_e}}{\rho a^2} \\
n_x & n_y & n_z & 0 & 0
\end{array} \right) \qquad \text{(A.31)}
$$

APPENDIX B

ISOPARAMETRIC ELEMENTS

In order to obtain a high-order solution in the finite-volume scheme, it is necessary to *reconstruct* the cell-average values to obtain more a accurate representation of the data. The method of undetermined coefficients is one such technique, that requires the basis functions to be integrated over the area of the cell. In general coordinates or on unstructured meshes, integration over irregular cells becomes a necessity which can be handled by the use of shape functions, which are used to transform between the physical and natural coordinate systems,

$$\int_{x_1}^{x_2} u(x)\ dx \underset{\text{physical}}{\overset{\text{natural}}{\rightleftharpoons}} \int_{-1}^{1} u(\xi)|J|\ d\xi. \tag{B.1}$$

B.1 One-Dimensional Shape Functions

B.1.1 Linear Elements

The shape functions for the linear isoparametric element are as follows.

$$H_1(\xi) = \frac{1}{2}(1-\xi) \tag{B.2a}$$

$$H_2(\xi) = \frac{1}{2}(1+\xi) \tag{B.2b}$$

A point ξ within the natural element is mapped into a point x within the physical element using the shape functions given in Eq. B.2.

$$x = H_1(\xi)x_1 + H_2(\xi)x_2 \tag{B.3a}$$

$$= \frac{1}{2}(1-\xi)x_1 + \frac{1}{2}(1+\xi)x_2 \tag{B.3b}$$

The Jacobian is given by

$$J = \frac{dx}{d\xi} = \sum_{i=1}^{2} \frac{dH_i(\xi)}{d\xi} x_i = \frac{1}{2}(x_2 - x_1). \tag{B.4}$$

B.2 Two-Dimensional Shape Functions

B.2.1 Bilinear Elements

The shape functions for the bilinear isoparametric element are given below.

$$H_1(\xi,\eta) = \frac{1}{4}(1-\xi)(1-\eta) \tag{B.5a}$$

$$H_2(\xi,\eta) = \frac{1}{4}(1+\xi)(1-\eta) \tag{B.5b}$$

$$H_3(\xi,\eta) = \frac{1}{4}(1+\xi)(1+\eta) \tag{B.5c}$$

$$H_4(\xi,\eta) = \frac{1}{4}(1-\xi)(1+\eta) \tag{B.5d}$$

A point (ξ, η) within the natural element is mapped into a point (x, y) within the physical element using the shape function given in Eq. B.5.

$$x = \sum_{i=1}^{4} H_i(\xi,\eta)x_i \tag{B.6a}$$

$$y = \sum_{i=1}^{4} H_i(\xi,\eta)y_i \tag{B.6b}$$

Similarly, any physical variable can be interpolated using the same shape functions.

$$\phi = \sum_{i=1}^{4} H_i(\xi,\eta)\phi_i \tag{B.7}$$

The Jacobian matrix is given by

$$J = \begin{pmatrix} \dfrac{\partial x}{\partial \xi} & \dfrac{\partial y}{\partial \xi} \\ \dfrac{\partial x}{\partial \eta} & \dfrac{\partial y}{\partial \eta} \end{pmatrix}, \tag{B.8}$$

with Jacobian,

$$|J| \equiv \det(J) = \frac{\partial x}{\partial \xi}\frac{\partial y}{\partial \eta} - \frac{\partial y}{\partial \xi}\frac{\partial x}{\partial \eta}. \tag{B.9}$$

The components of the Jacobian matrix are as follows:

$$J_{11} = \frac{\partial x}{\partial \xi} = \sum_{i=1}^{4} \frac{\partial H_i(\xi,\eta)}{\partial \xi} x_i \tag{B.10a}$$

$$J_{12} = \frac{\partial y}{\partial \xi} = \sum_{i=1}^{4} \frac{\partial H_i(\xi,\eta)}{\partial \xi} y_i \tag{B.10b}$$

$$J_{21} = \frac{\partial x}{\partial \eta} = \sum_{i=1}^{4} \frac{\partial H_i(\xi,\eta)}{\partial \eta} x_i \tag{B.10c}$$

$$J_{22} = \frac{\partial y}{\partial \eta} = \sum_{i=1}^{4} \frac{\partial H_i(\xi,\eta)}{\partial \eta} y_i \tag{B.10d}$$

$$J_{11} = -\frac{1}{4}(1-\eta)x_1 + \frac{1}{4}(1-\eta)x_2 + \frac{1}{4}(1+\eta)x_3 - \frac{1}{4}(1+\eta)x_4 \tag{B.11a}$$

$$J_{12} = -\frac{1}{4}(1-\eta)y_1 + \frac{1}{4}(1-\eta)y_2 + \frac{1}{4}(1+\eta)y_3 - \frac{1}{4}(1+\eta)y_4 \tag{B.11b}$$

$$J_{21} = -\frac{1}{4}(1-\xi)x_1 + \frac{1}{4}(1+\xi)x_2 + \frac{1}{4}(1+\xi)x_3 - \frac{1}{4}(1-\xi)x_4 \tag{B.11c}$$

$$J_{22} = -\frac{1}{4}(1-\xi)y_1 + \frac{1}{4}(1+\xi)y_2 + \frac{1}{4}(1+\xi)y_3 - \frac{1}{4}(1-\xi)y_4 \tag{B.11d}$$

$$J_{11} = \frac{1}{4}[(1-\eta)(x_2 - x_1) + (1+\eta)(x_3 - x_4)] \tag{B.12a}$$

$$J_{12} = \frac{1}{4}[(1-\eta)(y_2 - y_1) + (1+\eta)(y_3 - y_4)] \tag{B.12b}$$

$$J_{21} = \frac{1}{4}[(1-\xi)(x_4 - x_1) + (1+\xi)(x_3 - x_2)] \tag{B.12c}$$

$$J_{22} = \frac{1}{4}[(1-\xi)(y_4 - y_1) + (1+\xi)(y_3 - y_2)] \tag{B.12d}$$

This leads to a more precise form of the Jacobian,

$$\begin{aligned} |J| = A &+ (x_1y_4 - x_1y_3 + x_2y_3 + x_4y_2 - x_2y_4 + x_3y_1 - x_4y_1 - x_3y_2)\xi \\ &+ (x_4y_2 - x_3y_1 + x_1y_3 - x_1y_2 - x_2x_4 + x_3y_4 + x_2y_1 - x_4y_3)\eta, \end{aligned} \tag{B.13}$$

or

$$|J| = \frac{1}{8}[2A + (\vec{12} \times \vec{43})\xi + (\vec{23} \times \vec{14})\eta], \tag{B.14}$$

where the area, A, is given by the cross product

$$A = \frac{1}{2}(\vec{13} \times \vec{24}). \tag{B.15}$$

APPENDIX C

VISUALIZATION

Many of the two-dimensional numerical results in the work have been presented in the form of Schlierens and interferograms. Such visualization techniques not only accentuate key flow feautures such as strong gradients but also allow direct comparison with experimental results (see Figure C.1).

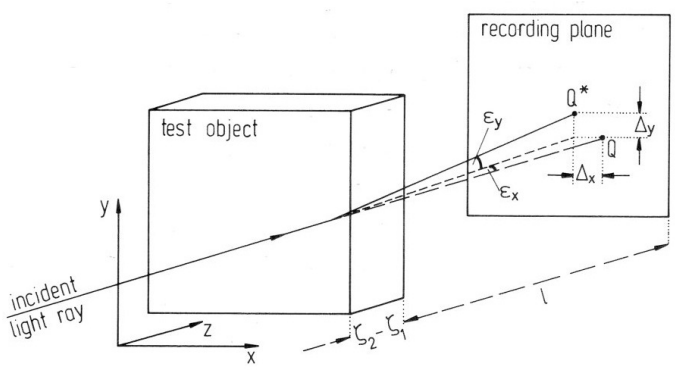

Figure C.1: Generalized visualization setup and geometric reference. Taken from [77].

Such techniques are based on gradients of the refractive index of the fluid and for a plasma, the electron contribution is significant and must be accounted for. The composite refractive index can be found from a linear combination of all species[1],

$$n - 1 = \sum \rho_i K_i \tag{C.1}$$

For a singly-ionized, monatomic plasma, we have

$$n - 1 = \rho\{(1 - \alpha)K_a + \alpha K_i\} + N_e K'_e \tag{C.2}$$

[1]Here n is used to denote the refractive index while N denotes the number density.

and specifically for argon, we have $K_{Ar^+} = \frac{2}{3}K_{Ar}$ ([77]),

$$n - 1 = \rho K(1 - \alpha/3) - 4.46 \times 10^{-16}\lambda^2 N_e \tag{C.3}$$

with the electronic refractive index,

$$n_e - 1 = -4.46 \times 10^{-16}\lambda^2 N_e \tag{C.4}$$

With the refractive index computed from a numerical snapshot, a simulated interferogram can easily be calculated from

$$\frac{\Delta\phi}{2\pi} = \frac{1}{\lambda}\int_{\zeta_1}^{\zeta_2} \{n(x, y, z) - n_\infty\}\, dz. \tag{C.5}$$

Alternatively, the refractive index can be used to construct a simulated Schlieren by computing its gradient throughout the flowfield by

$$\frac{\Delta I}{I} = \int_{\zeta_1}^{\zeta_2} \frac{1}{n}\frac{\partial n}{\partial y}\, dz. \tag{C.6}$$

APPENDIX D

IMPLICIT CR FORMULATION

The collisional-radiative source term is integrated independently of the convective terms at each time step, assuming the conserved variables to be frozen within the time step. The governing equations for the CR kinetics then reduce to a system of ODE's,

$$\left(\frac{dQ}{dt}\right)_{CR} = \dot{\Omega}, \tag{D.1}$$

that can be integrated in time using a standard Euler implicit method,

$$\left(\frac{\Delta Q}{\Delta t}\right)_{CR} = \dot{\Omega}^{n+1}. \tag{D.2}$$

Upon expanding the RHS via a Taylor series expansion,

$$\left(\frac{\Delta Q}{\Delta t}\right)_{CR} = \dot{\Omega}^{n} + \frac{\partial \dot{\Omega}^{n}}{\partial Q^{n}}(Q^{n+1} - Q^{n}) \tag{D.3}$$

an expression is obtained for that change in conserved quantities[1],

$$\Delta Q = (I - \Delta t J)^{-1} \Delta t \dot{\Omega}, \tag{D.4}$$

with the Jacobian,

$$J = \frac{\partial \dot{\Omega}}{\partial Q}. \tag{D.5}$$

As was done for the case of heat conduction[2], the source term may be expressed as a

[1] Note that the subscript n has been dropped.

[2] To facilitate derivation of the stability condition (see Chapter 7)

matrix-vector product,

$$\dot{\Omega} = \Phi Q \tag{D.6}$$

such that the Jacobian can also be written as

$$J = \frac{\partial(\Phi Q)}{\partial Q} \tag{D.7}$$

$$= \Phi + \frac{\partial \Phi}{\partial Q} Q \tag{D.8}$$

$$= \Phi + \Psi, \tag{D.9}$$

the elements of which take on the following form,

$$J = \left(\begin{array}{ccc|cc} \ddots & \vdots & \iddots & \vdots & \vdots \\ \cdots & \frac{\partial \dot{\omega}_{n_i}}{\partial n_j} & \cdots & \frac{\partial \dot{\omega}_{n_i}}{\partial E_h} & \frac{\partial \dot{\omega}_{n_i}}{\partial E_e} \\ \iddots & \vdots & \ddots & \vdots & \vdots \\ \hline \cdots & \frac{\partial \dot{\omega}_{E_h}}{\partial n_j} & \cdots & \frac{\partial \dot{\omega}_{E_h}}{\partial E_h} & \frac{\partial \dot{\omega}_{E_h}}{\partial E_e} \\ \cdots & \frac{\partial \dot{\omega}_{E_e}}{\partial n_j} & \cdots & \frac{\partial \dot{\omega}_{E_e}}{\partial E_h} & \frac{\partial \dot{\omega}_{E_e}}{\partial E_e} \end{array} \right). \tag{D.10}$$

This leads to a natural block matrix decomposition of the Jacobian,

$$J = \begin{pmatrix} J^{(1)} & J^{(2)} \\ J^{(3)} & J^{(4)} \end{pmatrix} = \begin{pmatrix} \Phi^{(1)} & \Phi^{(2)} \\ \Phi^{(3)} & \Phi^{(4)} \end{pmatrix} + \begin{pmatrix} \Psi^{(1)} & \Psi^{(2)} \\ \Psi^{(3)} & \Psi^{(4)} \end{pmatrix} \tag{D.11}$$

In what follows, the form of matrix Φ is given along with the components of the Jacobian J. The matrix Ψ can be found by subtracting Φ from J. It is emphasized here that the rates associated with ionization and recombination processes are functions of j_c, such that

$$S_i,\ O_i,\ W_i,\ V_i,\ R_i = f(j_c). \tag{D.12}$$

Also, the electron density is given from consideration of charge neutrality, $n_e = n_{Ar^+(j_c=3/2)} + n_{Ar^+(j_c=1/2)}$.

Sub-matrices of Φ

$$\Phi^{(2)} = \begin{pmatrix} & & \\ & & \\ \vdots & \vdots & \\ 0 & 0 & \\ \vdots & \vdots & \\ & & \\ & & \end{pmatrix} \tag{D.13}$$

$$\Phi^{(4)} = \begin{pmatrix} n_e \frac{2m_e}{m_{Ar}}((\alpha-1)k_{en} - \alpha k_{ei}) & \frac{2m_e}{m_{Ar}}(n_n k_{en} + n_e k_{ei}) \\ -n_e \frac{2m_e}{m_{Ar}}((\alpha-1)k_{en} - \alpha k_{ei}) & -\frac{2m_e}{m_{Ar}}(n_n k_{en} + n_e k_{ei}) \\ & -9.5 \times 10^{-41} \frac{n_e Z_{\text{eff}}^2}{(k_{\text{B}} T_e)^{1/2}} \end{pmatrix}, \quad \alpha = \frac{n_e}{n_h} \tag{D.14}$$

$$\Phi^{(1)} = \begin{pmatrix} -\sum_{i\neq 1} A_{i1}^{(1)} & n_e F_{21} + n_1 L_{21} & n_e F_{31} + n_1 L_{31} & n_e F_{41} + n_1 L_{41} & n_e\left(n_1 W_1\right. & n_e\left(n_1 W_1\right. \\ & +A_{21} & +A_{31} & +A_{41} & \left.+n_e O_1 + R_1\right) & \left.+n_e O_1 + R_1\right) \\ n_e C_{12} + n_1 K_{12} & -\sum_{i\neq 2} \Phi_{i2}^{(1)} & n_e F_{32} + n_1 L_{32} & n_e F_{42} + n_1 L_{42} & n_e\left(n_1 W_2\right. & n_e\left(n_1 W_2\right. \\ +(1-\Lambda_{21})A_{21} & & +A_{32} & +A_{42} & \left.+n_e O_2 + R_2\right) & \left.+n_e O_2 + R_2\right) \\ n_e C_{13} + n_1 K_{13} & n_e C_{23} + n_1 K_{23} & -\sum_{i\neq 3} \Phi_{i3}^{(1)} & n_e F_{43} + n_1 L_{43} & n_e\left(n_1 W_3\right. & n_e\left(n_1 W_3\right. \\ +(1-\Lambda_{31})A_{31} & +(1-\Lambda_{32})A_{32} & & +A_{43} & \left.+n_e O_3 + R_3\right) & \left.+n_e O_3 + R_3\right) \\ n_e C_{14} + n_1 K_{14} & n_e C_{24} + n_1 K_{24} & n_e C_{34} + n_1 K_{34} & -\sum_{i\neq 4} \Phi_{i4}^{(1)} & n_e\left(n_1 W_4\right. & n_e\left(n_1 W_4\right. \\ +(1-\Lambda_{41})A_{41} & +(1-\Lambda_{42})A_{42} & +(1-\Lambda_{42})A_{42} & & \left.+n_e O_4 + R_4\right) & \left.+n_e O_4 + R_4\right) \\ n_e S_1 + n_1 V_1 & n_e S_2 + n_1 V_2 & n_e S_3 + n_1 V_3 & n_e S_4 + n_1 V_4 & -\sum_{i\neq 5} \Phi_{i5}^{(1)} & 0 \\ +(1-\Lambda_i)R_1 & +(1-\Lambda_i)R_2 & +(1-\Lambda_i)R_3 & +(1-\Lambda_i)R_4 & & \\ n_e S_1 + n_1 V_1 & n_e S_2 + n_1 V_2 & n_e S_3 + n_1 V_3 & n_e S_4 + n_1 V_4 & 0 & -\sum_{i\neq 6} \Phi_{i6}^{(1)} \\ +(1-\Lambda_i)R_1 & +(1-\Lambda_i)R_2 & +(1-\Lambda_i)R_3 & +(1-\Lambda_i)R_4 & & \end{pmatrix} \tag{D.15}$$

$$\Phi^{(3)} = \begin{pmatrix} & n_1 \sum_{i<2} \varepsilon_{i2} L_{2i} & n_1 \sum_{i<3} \varepsilon_{i3} L_{3i} & & & \\ -n_1 \sum_{j>1} \varepsilon_{1j} K_{1j} & -n_1 \sum_{j>2} \varepsilon_{2j} K_{2j} & -n_1 \sum_{j>3} \varepsilon_{3j} K_{3j} & n_1 \sum_{i<4} \varepsilon_{i4} L_{4i} & n_1 n_e \sum_k I_k W_k & n_1 n_e \sum_k I_k W_k \\ -n_1 I_1 V_1 & -n_1 I_2 V_2 & -n_1 I_3 V_3 & -n_1 I_4 V_4 & & \\ & n_e \sum_{i<2} \varepsilon_{i2} F_{2i} & n_e \sum_{i<3} \varepsilon_{i3} F_{3i} & & & \\ -n_e \sum_{j>1} \varepsilon_{1j} C_{1j} & -n_e \sum_{j>2} \varepsilon_{2j} C_{2j} & -n_e \sum_{j>3} \varepsilon_{3j} C_{3j} & n_e \sum_{i<4} \varepsilon_{i4} F_{4i} & n_e n_e \sum_k I_k O_k & n_e n_e \sum_k I_k O_k \\ -n_e I_1 S_1 & -n_e I_2 S_2 & -n_e I_3 S_3 & -n_e I_4 S_4 & -n_e R'_k & -n_e R'_k \end{pmatrix} \tag{D.16}$$

D.1 Jacobian Elements

$$\frac{\partial \dot{\omega}_{Ar^+}}{\partial n_1} = n_1 V_1 + \sum_k n_k V_k + n_e S_1 - n_e \sum_k n_{Ar^+} W_k + (1 - \Lambda_1) R_1 \tag{D.17}$$

$$\frac{\partial \dot{\omega}_{i>1}}{\partial n_1} = \sum_{k<i} (n_k K_{ki} - n_i K_{ik}) + \sum_{k>i} (n_k L_{ki} + n_1 K_{1i} - n_i K_{ik}) - n_i V_i + n_e n_{Ar^+} W_i + n_e C_{1i} + n_1 K_{1i} + (1 - \Lambda_{i1}) A_{i1} \tag{D.18}$$

$$\frac{\partial \dot{\omega}_{Ar^+(j_c)}}{\partial n_{j>1}} = n_e S_j(j_c) + n_1 V_j + (1 - \Lambda_j) R_j \tag{D.19}$$

$$\frac{\partial \dot{\omega}_i}{\partial n_{j>1}} = n_e F_{ji} + n_1 L_{ji} + A_{ji} \tag{D.20}$$

$$\frac{\partial \dot{\omega}_{i>j}}{\partial n_{j>1}} = n_e C_{ji} + n_1 K_{ji} + (1 - \Lambda_{ij}) A_{ij} \tag{D.21}$$

$$\frac{\partial \dot{\omega}_i}{\partial n_{Ar^+}} = \sum_{k>i} (n_k F_{ki} - n_i C_{ik}) + \sum_{k<i} (n_k C_{ki} - n_i F_{ik}) + 2 n_e n_{Ar^+} O_i + n_{Ar^+} R_i - n_1 S_i + n_1 n_{Ar^+} W_i + n_e^2 O_i + n_e R_i + n_1 n_e W_i \tag{D.22}$$

$$\frac{\partial \dot{\omega}_{E_e}}{\partial n_j} = n_+ \sum_{k<j} \varepsilon_{kj} F_{jk} - n_+ \sum_{k>j} \varepsilon_{jk} C_{jk} - n_+ S_j \varepsilon_j + 3 \rho_e k_{\mathrm{B}} (T_h - T_e) \frac{k_{en}}{m_j} + \sum_i ((1 - \Lambda_i) R_i') \tag{D.23}$$

$$\frac{\partial \dot{\omega}_{E_e}}{\partial n_+} = \sum \varepsilon_k (3n_+^2 O_k - n_k S_k) + \sum_i \sum_{j>i} \varepsilon_{ij}(n_j F_{ji} - n_i C_{ij}) + 3\rho_e k_{\mathrm{B}}(T_h - T_e)\frac{\bar{k}_{ei}}{m_{Ar^+}} - 2n_e \sum_i R_i' \quad \text{(D.24)}$$

$$\frac{\partial \dot{\omega}_{E_e}}{\partial E_e} = \frac{2}{3}\frac{1}{k_B}\sum_i \sum_{j>i} \varepsilon_{ij}\left(n_j \frac{\partial F_{ji}}{\partial T_e} - n_i \frac{\partial C_{ij}}{\partial T_e}\right) + \frac{2}{3}\frac{1}{k_B}\sum_i \varepsilon_i \left(n_e n_+ \frac{\partial O_i}{\partial T_e} - n_i \frac{\partial S_i}{\partial T_e}\right) + n_n \frac{2m_e}{m_{Ar}}\left((T_h - T_e)\frac{\partial k_{en}}{\partial T_e} - k_{en}\right) + n_e \frac{2m_e}{m_{Ar^+}}\left((T_h - T_e)\frac{\partial \bar{k}_{ei}}{\partial T_e} - \bar{k}_{ei}\right) + \sum_i \left((n_i(1-\Lambda_i) - n_e n_+)\frac{\partial R_i'}{\partial T_e}\frac{2}{3}\frac{1}{n_e k_{\mathrm{B}}}\right) - 4.75 \times 10^{-41}\frac{Z_{\mathrm{eff}}^2}{k_{\mathrm{B}} T_e^{1/2}} n_+ \quad \text{(D.25)}$$

$$\frac{\partial \dot{\omega}_{E_e}}{\partial E_h} = \frac{n_e n_n}{n_h}\frac{2m_e}{m_{Ar}}k_{en} + \frac{n_e^2}{n_h}\frac{2m_e}{m_{Ar^+}}\bar{k}_{ei} \quad \text{(D.26)}$$

$$\frac{\partial \dot{\omega}_{E_h}}{\partial n_1} = \sum_i \sum_{j>i} \varepsilon_{ij}(n_j L_{ji} - n_i K_{ij}) - \sum_{j>1} \varepsilon_{1j}(n_1 K_{1j}) + \sum_i \varepsilon_i (n_e n_+ W_i - n_i V_i) - n_1 V_1 \varepsilon_1 - \frac{3}{2} n_e k_{\mathrm{B}}(T_h - T_e)\frac{2m_e}{m_{Ar}}k_{en} \quad \text{(D.27)}$$

$$\frac{\partial \dot{\omega}_{E_h}}{\partial n_k} = n_1 \sum_{i<k} L_{ki}\varepsilon_{ik} - n_1 \sum_{j>k} K_{kj}\varepsilon_{kj} - n_1 V_k \varepsilon_k - \frac{3}{2} n_e k_{\mathrm{B}}(T_h - T_e)\frac{2m_e}{m_{Ar}}k_{en} \quad \text{(D.28)}$$

$$\frac{\partial \dot{\omega}_{E_h}}{\partial n_+} = 2n_1 n_+ \sum_i \varepsilon_i W_i - \frac{3}{2} n_n k_{\mathrm{B}}(T_h - T_e)\frac{2m_e}{m_{Ar}}k_{en} - 3n_e k_{\mathrm{B}}(T_h - T_e)\frac{2m_e}{m_{Ar^+}}\bar{k}_{ei} \quad \text{(D.29)}$$

$$\frac{\partial \dot{\omega}_{E_h}}{\partial E_e} = \frac{2n_1 n_+^2}{3k_B} \sum_i \varepsilon_i \frac{\partial W_i}{\partial T_e} - n_n \frac{2m_e}{m_{Ar}} \left((T_h - T_e) \frac{\partial k_{en}}{\partial T_e} - k_{en} \right) - n_e \frac{2m_e}{m_{Ar^+}} \left((T_h - T_e) \frac{\partial \bar{k}_{ei}}{\partial T_e} - \bar{k}_{ei} \right) \quad \text{(D.30)}$$

$$\frac{\partial \dot{\omega}_{E_h}}{\partial E_h} = \frac{2n_1}{3k_B} \sum_i \sum_{j>i} \varepsilon_{ij} (n_j \frac{\partial L_{ji}}{\partial T_h} - n_i \frac{\partial K_{ij}}{\partial T_h}) + \frac{2n_1}{3k_B} \sum_i \varepsilon_i (n_e n_+ \frac{\partial W_i}{\partial T_h} - n_i \frac{\partial V_i}{\partial T_h}) - \frac{n_e n_n}{n_h} \frac{2m_e}{m_{Ar}} k_{en} - \frac{n_e^2}{n_h} \frac{2m_e}{m_{Ar^+}} \bar{k}_{ei} \quad \text{(D.31)}$$

D.2 Conditioning

Note that matrices $J^{(1)}$ and $J^{(4)}$ are nondimensional. This is an ideal situation for optimal numerical condition of the Jacobian matrix. Matrices $J^{(2)}$ and $J^{(3)}$, however, have units of Joules and Joules^{-1}, respectively, which may lead to an ill-conditioned Jacobian under certain conditions. To remedy this, these matrices are normalized by a scaling factor which leaves the Jacobian well-conditioned for numerical inversion while simultaneously maintaining diagonal dominance[3]. The scaling factor, which can be thought of as an idealized energy unit, takes the form

$$SF = \left(\frac{\max J^{(2)}}{\max J^{(3)}} \right)^{1/2} \quad \text{(D.32)}$$

which is used to update $J^{(2)}$ and $J^{(3)}$ according to

$$J^{(2)} \rightarrow J^{(2)}/SF \quad \text{(D.33)}$$

$$J^{(3)} \rightarrow J^{(3)} \cdot SF. \quad \text{(D.34)}$$

[3]A necessary condition for Gaussian elimination without partial pivoting.

In addition, the energy source terms Eqs. (**??**) must also be transformed,

$$\dot{\omega}_{E_h} \rightarrow \dot{\omega}_{E_h} \cdot SF \tag{D.35}$$

$$\dot{\omega}_{E_e} \rightarrow \dot{\omega}_{E_e} \cdot SF. \tag{D.36}$$

Once the changes in the heavy particle and electron energies have been obtained, the units are transformed back to Joules via

$$\Delta E_h \rightarrow \Delta E_h / SF \tag{D.37}$$

$$\Delta E_e \rightarrow \Delta E_e / SF. \tag{D.38}$$

APPENDIX E

ADDITIONAL STEADY-STATE RESULTS

Results of the Mach 16.1, 16.5, and 13.0 ionizing shock test cases as computed under steady-state conditions are provided here.

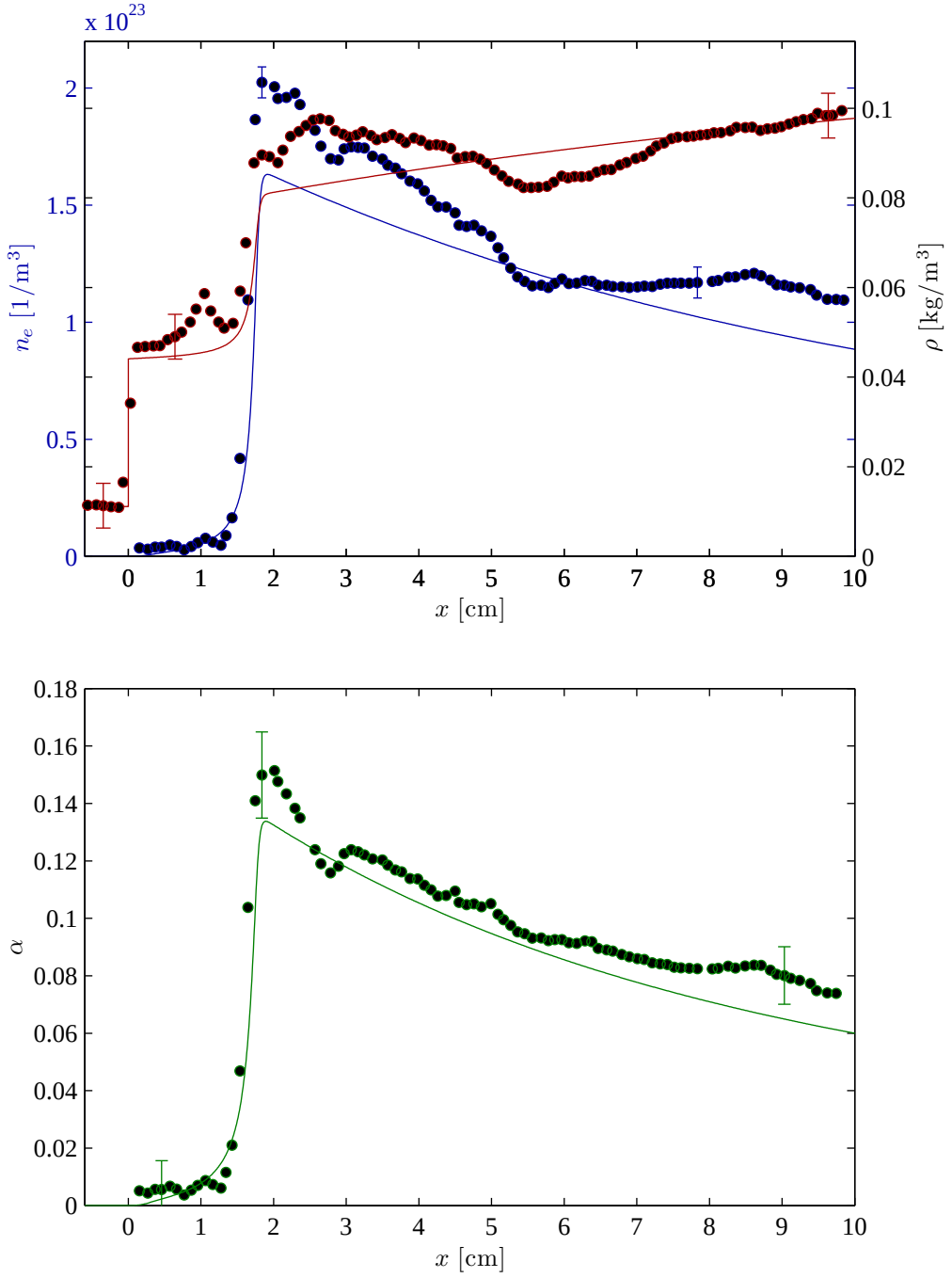

Figure E.1: Ionizing shock structure as detailed by (a) ρ and n_e, and (b) α for case 2: $p_\circ = 5.15$ torr, $T_\circ = 295.9$ K, Ma $= 16.1$.

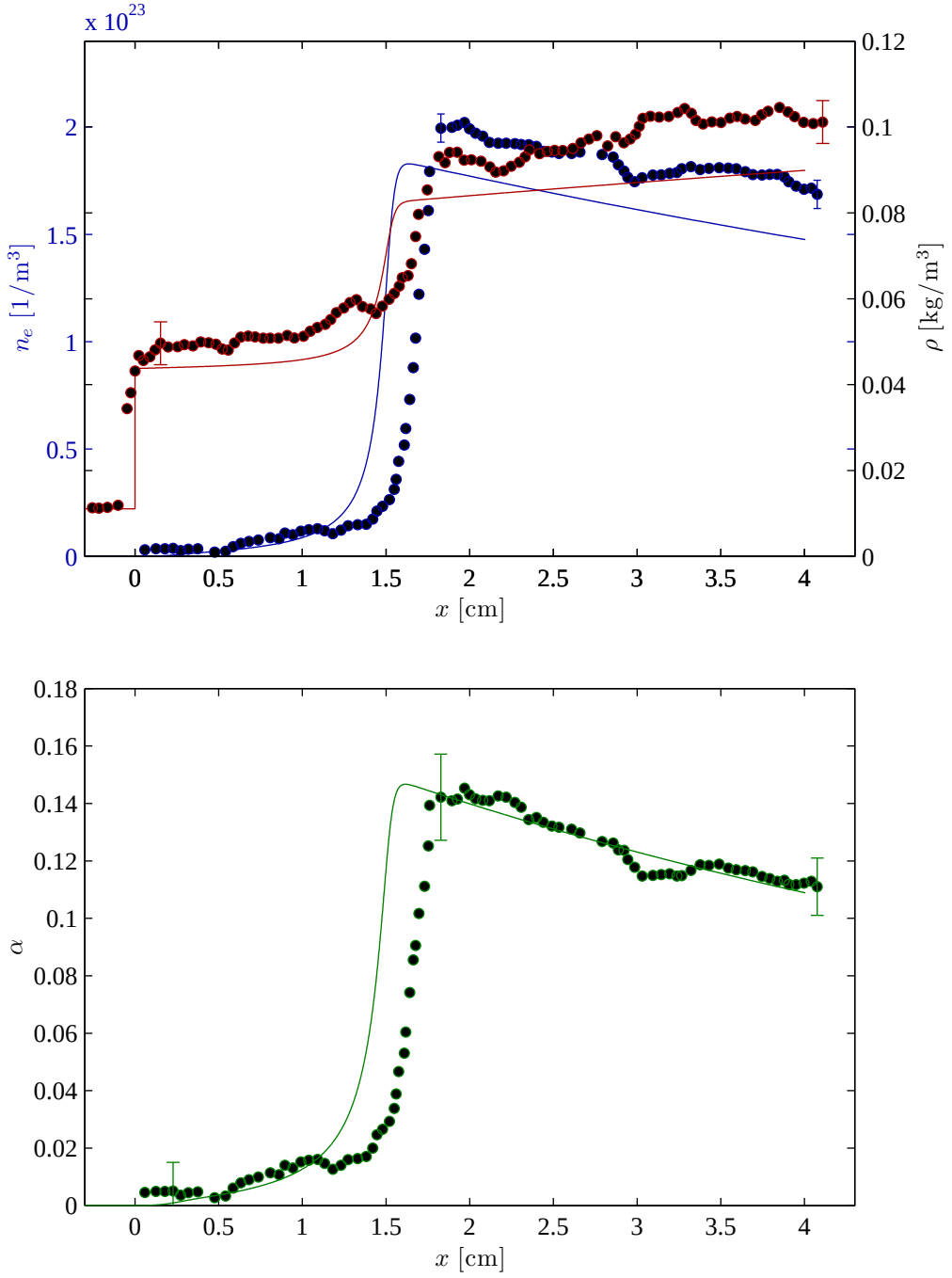

Figure E.2: Ionizing shock structure as detailed by (a) ρ and n_e, and (b) α for case 3: $p_\circ = 5.12$ torr, $T_\circ = 296.6$ K, Ma $= 16.5$.

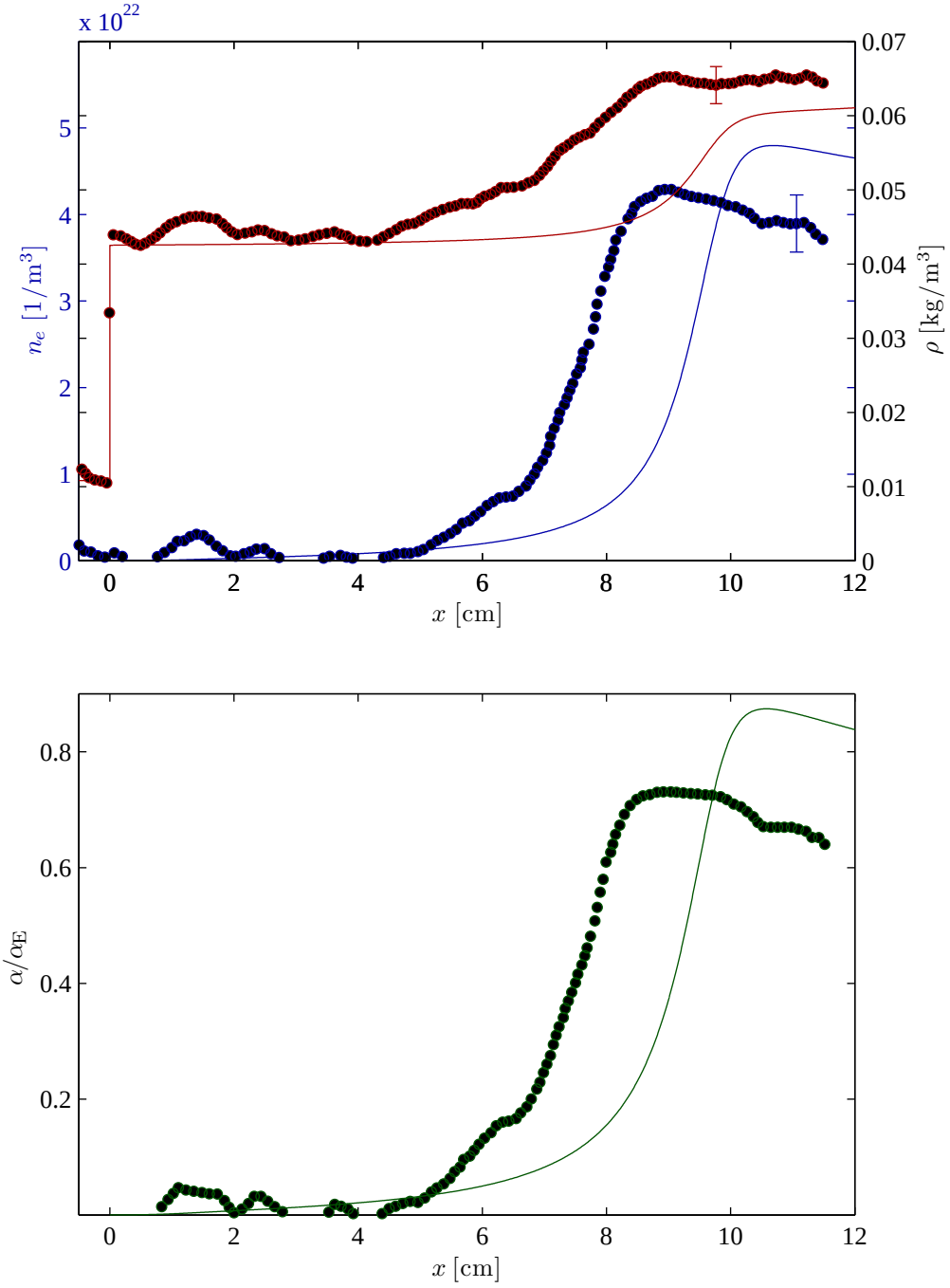

Figure E.3: Ionizing shock structure as detailed by (a) ρ and n_e, and (b) α for case 4: $p_\circ = 5.01$ torr, $T_\circ = 296.6$ K, Ma $= 13.0$.

Bibliography

[1] H. Alfvén. On the existence of electromagnetic-hydrodynamic waves. *Arkiv för Matematik, Astronomie, och Fysik*, 29B(2):1–7, 1943.

[2] R. L. Alpert and T. Y. Toong. Periodicity in exothermic hypersonic flows about blunt projectiles. *Acta Astronautica*, 17:538–560, 1972.

[3] M. Arora and P. L. Roe. On postshock oscillations due to shock capturing schemes. *Journal of Computational Physics*, 130(1):25–40, 1997.

[4] P. Atkins. *Physical Chemistry*. W. H. Freeman and Company, New York, sixth edition, 1998.

[5] G. R. Baker and E. A. Overman II. *The Art of Scientific Computing*. The Ohio State University Bookstore, Columbus, draft xii edition, 2006.

[6] T. J. Barth. Numerical methods for gasdynamic systems. In D. Kroner, M. Ohlberger, and C. Rohde, editors, *An Introduction to Recent Developments in Theory and Numerics for Conservation Laws*, pages 195–285. Springer-Verlag, New York/Berlin, first edition, 1999.

[7] D. R. Bates, A. E. Kingston, and R. W. P. McWhirter. Recombination between electrons and atomic ions. I: Optically thin plasmas. *Proceedings of the Royal Society A*, 267:297–312, 1962.

[8] D. R. Bates, A. E. Kingston, and R. W. P. McWhirter. Recombination between electrons and atomic ions. II: Optically thick plasmas. *Proceedings of the Royal Society A*, 270:155–167, 1962.

[9] D. R. Bates, A. E. Kingston, and R. W. P. McWhirter. Collisional-radiative recombination at low temperatures and densities. *Proceedings of the Royal Society A*, 83:43–47, 1964.

[10] T. V. Bazhenova, L. G. Gvozdeva, and M. G. Nettleton. Unsteady interaction of shock waves. *Aerosp. Sci.*, 21:249–331, 1984.

[11] L. M. Biberman and I. T. Yakubov. Approach to ionization equilibrium behind the front of a shock wave in an atomic gas. *Soviet Physics-Technical Physics (English Translation)*, 8:1001–1007, 1964.

[12] J. B. Boffard, G. A. Piech, M. F. Gehrke, L. W. Anderson, and C. C. Lin. Measurement of electron-impact excitation cross sections out of metastable levels of argon and comparison with ground-state excitation. *Physical Review A*, 59(4):2749–2763, 1999.

[13] I. N. Bogatu, D. H. Edgell, J. S. Kim, R. C. Pardo, and R. Vondrasek. Argon ionization cross sections for charge state distribution modeling in electron cyclotron resonance ion source. *Review of Scientific Instruments*, 73(2):638–640, 2002.

[14] J. U. Brackbill and D. C. Barnes. The effect of nonzero $\nabla \cdot \mathbf{B}$ on the numerical solution of the magnetohydrodynamic equations. *Journal of Computational Physics*, 35:426–430, 1980.

[15] S. Brassier and G. Gallice. A Roe scheme for the bi-temperature model of magnetohydrodynamics. *Computers and Mathematics with Applications*, 41:257–267, 1998.

[16] P. I. Brimelow. An interferometric invesigation of shock structure and its induced shock-tube boundary layer in ionized argon. Technical Report 187, UTIAS, July 1974.

[17] M. Brio and C. C. Wu. An upwind differencing scheme for the equations of ideal magnetohydrodynamics. *Journal of Computational Physics*, 75:400–422, 1987.

[18] M. P. F. Bristow and I. I. Glass. Polarizability of singly ionized argon. *Physics of Fluids*, 15(11):2066–2067, 1972.

[19] A. Bultel, B. van Ootegem, A. Bourdon, and P. Vervisch. Influence of Ar_2^+ in an argon collisional-radiative model. *Physical Review E*, 65:1–16, 2002.

[20] J.-L. Cambier. Numerical methods for TVD transport and coupled relaxing processes in gases and plasmas. In *Proceedings of the 21st Fluid Dynamics, Plasma Dynamics, and Lasers Conference*, Seattle, WA, June 1990. AIAA.

[21] J.-L. Cambier. Numerical simulations of a nonequilibrium argon plasma in a shock-tube experiment. In *Proceedings of the 22nd Fluid Dynamics, Plasma Dynamics, and Lasers Conference*, Honolulu, HI, June 1991. AIAA.

[22] J.-L. Cambier, M. Carroll, and M. Kapper. Development of a hybrid model for non-equilibrium high-energy plasmas. In *Proceedings of the 35th Plasmadynamics and Lasers Conference*, Portland, OR, June 2004. AIAA.

[23] J.-L. Cambier and S. Moreau. Simulations of a molecular plasma in collisional-radiative nonequilibrium. In *Proceedings of the 24th Plasmadynamics and Lasers Conference*, Orlando, FL, July 1993. AIAA.

[24] J. P. Cocchi, R. Saurel, and J. C. Loraud. Some remarks about the resolution of high velocity flows near low density. *Shock Waves*, 8:119–125, 1998.

[25] P. Colella and P. R. Woodward. The piecewise parabolic method (PPM) for gas-dynamical simulations. *Journal of Computational Physics*, 54:174, 1984.

[26] R. Courant and K. O. Friedrichs. *Supersonic Flow and Shock Waves*. Interscience Publishers, Inc., New York, third edition, 1961.

[27] T. G. Cowling. *Magnetohydrodynamics*. Interscience Publishers, Inc., New York, first edition, 1957.

[28] R. K. Crockett, P. Colella, R. T. Fisher, R. I. Klein, and C. F. McKee. An unsplit, cell-centered Godunov method for ideal MHD. *Journal of Computational Physics*, 203(2):422–448, 2005.

[29] W. Dai and P. R. Woodward. Extension of the piecewise parabolic method (PPM) to multidimensional magnetohydrodynamics. *Journal of Computational Physics*, 111:354, 1994.

[30] W. Dai and P. R. Woodward. On the divergence-free condition and conservation laws in numerical simulations for supersonic magnetohydrodynamic flows. *The Astrophysical Journal*, 494:317, 1998.

[31] W. Dai and P. R. Woodward. A simple finite-difference scheme for multidimensional magnetohydrodynamic equations. *Journal of Computational Physics*, 142:331, 1998.

[32] P. J. Davis. *Circulant Matrices*. AMS Chelsea Publishing Company, New York, second edition, 1994.

[33] P. Deb and R. Agarwal. Numerical study of compressible viscous MHD equations with a bi-temperature model for supersonic blunt body flows. In *AIAA 38th Aerospace Sciences Meeting and Exhibit, Reno NV, January 10–13, 2000*, January 2000.

[34] H. Deutsch, K. Becker, A. N. Grum-Grzhimailo, K. Bartschat, H. Summers, M. Probst, S. Matt-Leubner, and T. D. Mark. Calculated cross sections for the electron-impact ionization of excited argon atoms using the DM formalism. *International Journal of Mass Spectrometry and Ion Processes*, 233:39–43, 2004.

[35] H. Deutsch, K. Becker, S. Matt, and T. D. Mark. Theoretical determination of absolute electron-impact ionization cross sections of molecules. *International Journal of Mass Spectrometry and Ion Processes*, 197:37–69, 2000.

[36] M. Van Dyke. *An Album of Fluid Motion*. The Parabolic Press, Stanford, tenth edition, 2005.

[37] B. Einfeldt, C. D. Munz, P. L. Roe, and B. Sjogreen. On Godunov-type methods near low densities. *Journal of Computational Physics*, 92:273–295, 1991.

[38] C. R. Evans and J. F. Hawley. Simulation of magnetohydrodynamic flows: A constrained transport method. *The Astrophysical Journal*, 332:659, 1988.

[39] W. Fickett and W. C. Davis. *Detonation*. University of California Press, Berkeley, first edition, 1972.

[40] H. H. Fleischmann and R. C. Dehmel. On Drawin's formula for ionization in atom-atom collisions. *Zeitschrift für Physik*, 252:435–442, 1972.

[41] A. I. Gavrikov, A. A. Efimenko, and S. B. Dorofeev. A model for detonation cell size prediction ffrom chemical kinetics. *Combustion and Flame*, 120:19–33, 2000.

[42] I. I. Glass and W. S. Liu. Effects of hydrogen impurities on shock structure and stability in ionizing monatomic gases. Part 1. Argon. *Journal of Fluid Mechanics*, 84:55–77, 1978.

[43] R. M. Gray. *Toeplitz and Circulant Matrices: A Review*. Now Publishers, Norwell, Massachusetts, first edition, 2006.

[44] H. R. Griem. *Plasma Spectroscopy*. McGraw-Hill, Inc., New York, first edition, 1964.

[45] W. Grosso. *Java RMI*. O'Reilly & Associates, Inc., New York, 2002.

[46] A. Harten. High resolution schemes for hyperbolic conservation laws. *Journal of Computational Physics*, 49:357–393, 1983.

[47] A. Harten. On a class of high resolution total-variation-stable finite-difference methods. *SIAM Journal on Numerical Analysis*, 21:1–23, 1984.

[48] A. Harten. ENO schemes with subcell resolution. *Journal of Computational Physics*, 83:148–184, 1989.

[49] K. E. Harwell and R. C. Jahn. Initial ionization rates in shock-heated argon, krypton, and xenon. *Physics of Fluids*, 7(2):214–222, 1964.

[50] P. Haugsjaa and R. Amme. Ionization and metastable excitation in low-energy collisions of ground-state argon atoms. *Journal of Chemical Physics*, 52(9):4874–4877, 1970.

[51] X. Y. Hu and B. C. Khoo. Kinetic energy fix for low internal energy flows. *Journal of Computational Physics*, 193:243–259, 2003.

[52] H. T. Huynh. Accurate monotone cubic interpolation. *SIAM Journal on Numerical Analysis*, 30(1):57–100, 1993.

[53] H. T. Huynh. Accurate upwind methods for the Euler equations. *SIAM Journal on Numerical Analysis*, 32(5):1565–1619, 1995.

[54] H. T. Huynh. *Schemes and Constraints for Advection*, volume 490 of *Lecture Notes in Physics*, pages 498–503. Springer, Berlin, 1997.

[55] P. Hyde. *Java thread programming*. Howard W. Sams, New York, 2000.

[56] Jr. J. D. Anderson. *Hypersonic and High Temperature Gas Dynamics*. McGraw-Hill Book Company, San Francisco, first edition, 1989.

[57] A. Jeffrey. *Applied Partial Differential Equations*. Academic Press, San Diego, first edition, 2003.

[58] A. Jeffrey and T. Taniuti. *Non-Linear Wave Propagation*. Academic Press, New York, first edition, 1964.

[59] K. Katsonis and H. W. Drawin. Transition probabilities for argon(I). *Journal of Quantitative Spectroscopy and Radiative Transfer*, 23:1–55, 1980.

[60] A. J. Kelly. Atom-atom ionization cross sections of the noble gases—argon, krypton, and xenon. *Journal of Chemical Physics*, 45(5):1723–1732, 1966.

[61] A. Kimura, H. Kobayashi, M. Nishida, and P. Valentin. Transition probabilities for argon(I). *Journal of Quantitative Spectroscopy and Radiative Transfer*, 34:189–215, 1985.

[62] S. Kudriakov and W. H. Hui. On a new defect of shock-capturing schemes. *Journal of Computational Physics*, 227:2105–2117, 2008.

[63] K. K. Kuo. *Principles of Combustion*. John Wiley & Sons, Inc., New Jersey, second edition, 2005.

[64] H. F. Lehr. Experiments on shock-induced combustion. *Acta Astronautica*, 17:589–597, 1972.

[65] G. Lin and E. Karniadakis. A discontinuous Galerkin method for two-temperature plasmas. *Computer Methods in Applied Mechanics and Engineering*, 195:3504–3527, 2006.

[66] T. Linde. A practical, general-purpose, two-state HLL Riemann solver for hyperbolic conservation laws. *International Journal for Numerical Methods in Fluids*, 40:391–402, 2002.

[67] T. Linde and P. Roe. On a mistaken notion of "proper upwinding". *Journal of Computational Physics*, 142:611–614, 1998.

[68] H. Lomax, T. H. Pulliam, and D. W. Zingg. *Fundamentals of Computational Fluid Dynamics*. Springer-Verlag, New York, first edition, 2000.

[69] B. Marder. A method for incorporating Gauss' law into electromagnetic PIC codes. *Journal of Computational Physics*, 68:48–55, 1987.

[70] R. Matsuzaki. Quasi-one-dimensional nonequilibrium flow of partially ionized argon with different species temperatures. *Journal of the Physical Society of Japan*, 38:1488–1493, 1975.

[71] R. P. McEachran and A. D. Stauffer. Relativistic effects in low-energy electron-argon scattering. *Australian Journal of Physics*, 50:511–524, 1997.

[72] T. I. McLaren and R. M. Hobson. Initial ionization rates and collision cross sections in shock-heated argon. *Physics of Fluids*, 11(10):2162–2172, 1968.

[73] D. A. McQuarrie and J. D. Simon. *Physical Chemistry: A Molecular Approach*. University Science Books, Sausalito, first edition, 1997.

[74] B. J. McVey and T. Y. Toong. Mechanism of instabilities of exothermic hypersonic blunt-body flows. *Combustion Science and Technology*, 17:538–560, 1972.

[75] R. Menikoff. Errors when shock waves interact due to numerical shock width. *SIAM Journal on Scientific Computing*, 15(5):1227–1242, 1994.

[76] M. Merilo and E. J. Morgan. Ionization rates behind shock waves in argon. *Journal of Chemical Physics*, 52(5):2192–2198, 1970.

[77] W. Merzkirch. *Flow Visualization*. Academic Press, Inc., San Diego, second edition, 1987.

[78] M. Mitchner and C. H. Kruger. *Partially Ionized Gases*. John Wiley and Sons, Inc., New York, first edition, 1973.

[79] M. F. Modest. *Radiative Heat Transfer*. Academic Press, San Francisco, second edition, 2003.

[80] E. J. Morgan and R. D. Morrison. Ionization rates behind shock waves in argon. *Physics of Fluids*, 8:1608–1615, 1965.

[81] J.-M. Moschetta and D. I. Pullin. A robust low diffusive kinetic scheme for the Navier-Stokes/Euler equations. *Journal of Computational Physics*, 133:193–204, 1997.

[82] W. Noh. Errors for calculations of strong shocks using an artificial viscocity and an artificial heat flux. *Journal of Computational Physics*, 72:79, 1978.

[83] E. S. Oran and J. P. Boris. *Numerical Simulation of Reactive Flow*. Elsevier Science Publishing Co., Inc., New York, first edition, 1987.

[84] A. Orszag and C. M. Tang. Small-scale structure of two-dimensional magnetohydrodynamic turbulence. *Journal of Fluid Mechanics*, 90:129, 1979.

[85] H. Petschek and S. Byron. Approach to equilibrium ionization behind strong shock waves in argon. *Annals of Physics*, 1:270–315, 1957.

[86] K. G. Powell, P. L. Roe, T. J. Linde, T. I. Gombosi, and D. L. Zeeuw. A solution-adaptive scheme for ideal magnetohydrodynamics. *Journal of Computational Physics*, 154:284–309, 1999.

[87] K. G. Powell, P. L. Roe, and R. S. Myong. An upwind scheme for magnetohydrodynamics. In *AIAA 12th Computational Fluid Dynamics Conference, San Diego, June 19-22*, pages 661–674, June 1995.

[88] J. J. Quirk. An alternative to unstructured grids for computing gas dynamic flows around arbitrarily complex two-dimensional bodies. Technical Report ICASE-92-7, NASA, 1992.

[89] J. J. Quirk. A contribution to the great Riemann solver debate. Technical Report ICASE-92-64, NASA, 1992.

[90] J. J. Quirk. Godunov-type schemes applied to detonation flows. Technical Report ICASE-93-15, NASA, 1993.

[91] J. J. Quirk. A Cartesian grid approach with hierarchical refinement for compressible flows. Technical Report ICASE-94-51, NASA, 1994.

[92] J. J. Quirk. A contribution to the great Riemann solver debate. *International Journal for Numerical Methods in Fluids*, 18:555–574, 1994.

[93] J. J. Quirk and U. R. Hanebutte. A parallel adaptive mesh refinement algorithm. Technical Report ICASE-93-63, NASA, 1993.

[94] J. J. Quirk and S. Karni. On the dynamics of a shock-bubble interaction. Technical Report ICASE-94-75, NASA, 1994.

[95] Yu. Ralchenko, A. E. Kramida, J. Reader, and NIST ASD Team. NIST atomic spectral database (version 3.1.5). `http://physics.nist.gov/asd3`, 2008.

[96] P. L. Roe. Approximate Riemann solvers, parameter vectors, and difference schemes. *Journal of Computational Physics*, 43:357–372, 1981.

[97] P. L. Roe and D. S. Balsara. Notes on the eigensystem of magnetohydrodynamics. *SIAM Journal on Applied Mathematics*, 56:57–67, 1996.

[98] R. Samtaney. Computational methods for self-similar solutions of the compressible Euler equations. *Journal of Computational Physics*, 132:327–345, 1997.

[99] R. Scott Schappe, M. Bruce Schulman, L. W. Anderson, and C. C. Lin. Measurement of cross sections for electron-impact excitation into the metastable levels of argon and number densities of metastable argon atoms. *Physical Review A*, 50(1):444–461, 1994.

[100] K. Sermeus and H. Deconinck. An entropy fix for multi-dimensional upwind residual distribution schemes. *Computers and Fluids*, 34:617–640, 2005.

[101] G. S. Settles. *Schlieren and Shadowgraph Techniques*. Springer-Verlag, Berlin, second edition, 2006.

[102] A. H. Shapiro. *The Dynamics and Thermodynamics of Compressible Flow*, volume I. The Ronald Press Company, New York, first edition, 1953.

[103] A. H. Shapiro. *The Dynamics and Thermodynamics of Compressible Flow*, volume II. The Ronald Press Company, New York, first edition, 1953.

[104] Chi-Wang Shu and Stanley Osher. Efficient implementation of essentially non-oscillatory shock capturing schemes. *Journal of Computational Physics*, 145:458–485, 1998.

[105] B. M. Smirnov. *Physics of Ionized Gases*. John Wiley and Sons, Inc., New York, first edition, 2001.

[106] G. D. Smith. *Numerical Solution of Partial Differential Equations: Finite Difference Methods*. Clarendon Press, Oxford, second edition, 1978.

[107] A. Suresh and H. T. Huynh. Accurate monotonicity-preserving schemes with Runge-Kutta time stepping. *Journal of Computational Physics*, 136(1):83–99, 1997.

[108] M. A. Sussman and G. J. Wilson. Computation of chemically reacting flow using a logarithmic form of the species conservation equations. In *Proceedings of the 4th International Symposium on Computational Fluid Dynamics*, pages 1113–1118, Davis, CA, September 1991. AIAA.

[109] G. W. Sutton and A. Sherman. *Engineering Magnetohydrodynamics*. McGraw-Hill Book Company, San Francisco, first edition, 1965.

[110] J. C. Tannehill, D. A. Anderson, and R. H. Pletcher. *Computational Fluid Mechanics and Heat Transfer*. Taylor and Francis, Philadelphia, second edition, 1997.

[111] E. F. Toro. *Riemann Solvers and Numerical Methods for Fluid Dynamics: A Practical Introduction*. Springer, Berlin, second edition, 1999.

[112] G. Tóth. The $\nabla \cdot \mathbf{B}$ constraint in shock-capturing magnetohydrodynamics codes. *Journal of Computational Physics*, 161:605–652, 2000.

[113] B. van Leer. Towards the ultimate conservative difference scheme. II. monotonicity and conservation combined in a second-order scheme. *Journal of Computational Physics*, 14:361–370, 1974.

[114] B. van Leer. Towards the ultimate conservative difference scheme. III. upstream-centered finite-difference schemes for ideal compressible flow. *Journal of Computational Physics*, 23:263–275, 1977.

[115] B. van Leer. Towards the ultimate conservative difference scheme. IV. A new numerical approach to numerical convection. *Journal of Computational Physics*, 23:276–299, 1977.

[116] B. van Leer. Towards the ultimate conservative difference scheme. V. A second order sequel to Godunov's method. *Journal of Computational Physics*, 32:101–136, 1979.

[117] J. Vlček. A collisional-radiative model applicable to argon discharges over a wide range of conditions. I: Formualtion and basic data. *Journal of Physics D: Applied Physics*, 22:623–631, 1989.

[118] J. Vlček and V. Pelikán. Excited level populations of argon atoms in a non-isothermal plasma. *Journal of Physics D: Applied Physics*, 19:1879–1888, 1986.

[119] J. Vlček and V. Pelikán. A collisional-radiative model applicable to argon discharges over a wide range of conditions. II: Application to low-pressure, hollow-cathode arc and low-pressure glow discharges. *Journal of Physics D: Applied Physics*, 22:632–643, 1989.

[120] Z. U. A. Warsi. *Fluid Dynamics: Theoretical and Computational Approaches*. CRC Press, New York, second edition, 1999.

[121] P. R. Woodward. Piecewise-parabolic methods for astrophysical fluid dynamics. In K.-H. A. Winkler and M. L. Norman, editors, *Astrophysical Radiation Hydrodynamics*, pages 245–326. D. Reidel Publishing, 1986.

[122] Z. Xu and C.-W. Shu. Anti-diffusive flux corrections for high order finite difference WENO schemes. *Journal of Computational Physics*, 205:458–485, 2005.

[123] A. Yanguas-Gil, J. Cotrino, and L. L. Alves. An update of argon inelastic cross sections for plasma discharges. *Journal of Physics D: Applied Physics*, 38:1588–1598, 2005.

[124] A. L. Zachary, A. Malagoli, and P. Colella. The effect of nonzero $\nabla \cdot \mathbf{B}$ on the numerical solution of the magnetohydrodynamic equations. *SIAM Journal on Scientific and Statistical Computing*, 15:263, 1994.

[125] O. Zatsarinny. 2009. private communication.

[126] O. Zatsarinny and K. Bartschat. B-spline Breit-Pauli R-matrix calculations for electron collisions with argon atoms. *Journal of Physics B: Atomic, Molecular and Optical Physics*, 37:4693–4703, 2004.

[127] O. Zatsarinny and K. Bartschat. B-spline calculations of oscillator strengths in neutral argon. *Journal of Physics B: Atomic, Molecular and Optical Physics*, 39:2145–2158, 2006.

[128] Ya. B. Zel'dovich and Yu. P. Raizer. *Physics of Shock Waves and High Temperature Hydrodynamic Phenomena*. Dover Publications, Inc., New York, third edition, 2002.